

1. Report No. FHWA/TX-12/0-5997-1	2. Government Accession No.	3. Recipient's Catalog No.	
4. Title and Subtitle STRUCTURAL ASSESSMENT OF "D" REGIONS AFFECTED BY PREMATURE CONCRETE DETERIORATION: TECHNICAL REPORT		5. Report Date Published: November 2012	6. Performing Organization Code
		8. Performing Organization Report No. Report 0-5997-1	
7. Author(s) John B. Mander, Joseph M. Bracci, Stefan Hurlbaus, Zachary Grasley, Madhu M. Karthik, Shih-Hsiang Liu, and Reece M. Scott		10. Work Unit No. (TRAIS)	
9. Performing Organization Name and Address Texas C( O "Transportation Institute College Station, Texas 77843-3135		11. Contract or Grant No. Project 0-5997	
		13. Type of Report and Period Covered Technical Report: September 2007–August 2014	
12. Sponsoring Agency Name and Address Texas Department of Transportation Research and Technology Implementation Office P.O. Box 5080 Austin, Texas 78763-5080		14. Sponsoring Agency Code	
		15. Supplementary Notes Project performed in cooperation with the Texas Department of Transportation and the Federal Highway Administration. Project Title: Structural Assessment of "D" Region Affected by Premature Concrete Deterioration URL: <a href="http://tti.tamu.edu/documents/0-5997-1.pdf">http://tti.tamu.edu/documents/0-5997-1.pdf</a>	
16. Abstract The effects of ASR/DEF on the D-regions of structures are investigated by means of a dual experimental and analytical modeling program. Four near full scale specimens that represent cantilever and straddle pier bents, that are representative of typical bridges in Texas, are constructed, conditioned over time, and tested to failure. The undamaged first specimen serves as the control specimen, while the next two are tested after eight months and two years of field conditioning through the Texas heat along with supplemental water aimed at promoting ASR/DEF. The fourth remains to be tested within the next three years. In the two specimens subjected to deterioration, early formation of ASR gel is observed, and with time load-induced cracks along with other additional cracks are observed. These additional cracks are a result of the continued formation of ASR gel, which causes the concrete to swell, and in turn puts the reinforcing steel into a state of active prestress. It is observed that the failure mechanism in all the specimens is a brittle shear failure through the beam-column joint. Specimens with ASR/DEF deterioration show greater stiffness and strength, and slightly greater ductility. A <i>Compatibility Strut-and-Tie</i> (C-STM) technique is developed as a suitable minimalist analysis technique to model the force-deformation behavior of reinforced concrete bridge piers with significant D-regions that may be deteriorated through ASR/DEF effects. The C-STM simulates the overall and the internal behavior of the structure very well. In spite of the disturbing appearances of the ASR/DEF damage arising from concrete swelling and cracking, the performance and strength of the specimens are not impaired. Damage that appears in the cover concrete region is offset by the mild level of confinement to the core concrete induced by the reinforcing steel.			
17. Key Words Bridge Bent; ASR/DEF Deterioration; Force-Deformation Modeling; Strut-and-Tie Modeling; Compatibility Strut-and-Tie Modeling		18. Distribution Statement No restrictions. This document is available to the public through NTIS: National Technical Information Service Alexandria, Virginia 22312 <a href="http://www.ntis.gov">http://www.ntis.gov</a>	
19. Security Classif. (of this report) Unclassified	20. Security Classif. (of this page) Unclassified	21. No. of Pages 304	22. Price



# **STRUCTURAL ASSESSMENT OF "D" REGIONS AFFECTED BY PREMATURE CONCRETE DETERIORATION: TECHNICAL REPORT**

by

John B. Mander  
Zachry Professor of Design and  
Construction Integration  
Zachry Department of Civil Engineering

Madhu M. Karthik  
Graduate Assistant Researcher  
Zachry Department of Civil Engineering

Joseph M. Bracci  
Professor  
Zachry Department of Civil Engineering

Shih-Hsiang Liu  
Graduate Assistant Researcher  
Zachry Department of Civil Engineering

Stefan Hurlebaus  
Associate Professor  
Zachry Department of Civil Engineering

and

Zachary Grasley  
Assistant Professor  
Zachry Department of Civil Engineering

Reece M. Scott  
Graduate Assistant Researcher  
Zachry Department of Civil Engineering

Report 0-5997-1

Project 0-5997

Project Title: Structural Assessment of "D" Region Affected by Premature Concrete  
Deterioration

Performed in cooperation with the  
Texas Department of Transportation  
and the  
Federal Highway Administration

Published: November 2012

TEXAS A&M TRANSPORTATION INSTITUTE  
College Station, Texas 77843-3135



## **DISCLAIMER**

This research was performed in cooperation with the Texas Department of Transportation (TxDOT) and the Federal Highway Administration (FHWA). The contents of this report reflect the views of the authors, who are responsible for the facts and the accuracy of the data presented herein. The contents do not necessarily reflect the official view or policies of the FHWA or TxDOT. This report does not constitute a standard, specification, or regulation.

The United States Government and the State of Texas do not endorse products or manufacturers. Trade or manufacturers' names appear herein solely because they are considered essential to the object of this report.

## **ACKNOWLEDGMENTS**

This project was conducted at Texas A&M University in conjunction with the Texas Transportation Institute. The experiments were conducted in the High Bay Structures and Material Testing Laboratory. Mr. Matthew Potter is thanked for his assistance.

Funding for this project was provided via a contract with the Texas Department of Transportation (TxDOT) (Project 0-5997) with Mr. Dingyi Yang serving as Project Director. The guidance of Mr. Yang and the project control group is gratefully acknowledged.

## TABLE OF CONTENTS

List of Figures.....	xiii
List of Tables.....	xvii
1 Introduction.....	1
1.1 Background and Motivation.....	1
1.2 Scope.....	2
1.3 What Then Is Particularly New in This Work?.....	4
2 Literature Review.....	5
2.1 Scope of Chapter.....	5
2.2 Historic Developments on Concrete Deterioration Mechanisms.....	5
2.2.1 Alkali-Silica Reaction.....	5
2.2.2 Delayed Ettringite Formation.....	6
2.3 Historic Developments on Truss Modeling.....	7
2.3.1 Beam Shear Models.....	7
2.3.2 Plastic Truss (Strut-and-Tie) Modeling.....	9
2.3.3 Shear Panel Modeling.....	10
2.3.4 Compatibility Truss Modeling.....	11
3 Analysis Schema.....	13
3.1 Scope.....	13
3.2 Stage 1: Analysis Using Beam Theory.....	15
3.3 Stage 2: Strut-and-Tie Analysis.....	21
3.4 Stage 3: Analysis Using Compatibility Strut-and-Tie Methods.....	27
3.4.1 Stage 3.1: C-STM Based on Undamaged Material Properties.....	27

3.4.2	Stage 3.2: C-STM Allowing for ASR/DEF Damage and Its Effects.....	27
3.5	Stage 4: Establish Acceptability of Structure.....	28
3.6	Key Steps in the Strength Assessment of Concrete Structures Deteriorated with ASR/DEF Effects .....	29
4	Compatibility Strut-and-Tie Formulation.....	31
4.1	Scope .....	31
4.2	Truss and Arch Action .....	31
4.3	Modeling Truss Action.....	31
4.4	Modeling Arch Action.....	36
4.5	Modeling the Combined Truss and Arch Action .....	36
4.6	Stress and Strain Transformation for Flexural Equivalence .....	39
4.7	C-STM Geometry and Axial Rigidity Assignments .....	44
4.7.1	Truss Geometry.....	44
4.7.2	Axial Rigidity.....	44
4.8	Element Constitutive Material Relations .....	46
4.8.1	Reinforcing Steel .....	46
4.8.2	Diagonal Concrete Struts .....	46
4.8.3	Concrete Tensile Strength.....	48
4.8.4	Concrete Compression Chord Members.....	51
4.8.5	Modified Material Properties to Account for ASR/DEF .....	51
4.9	Ultimate Strength and Softening of Constitutive Relations .....	56
4.9.1	SAT Strength Checks.....	58



4.10	Computational Implementation .....	58
4.11	Experimental Verification .....	63
4.11.1	The Structure.....	63
4.11.2	Present Code-Based Strength Predictions.....	65
4.11.3	Strength and Deformation Capacity Using C-STM Computational Modeling .	71
4.11.4	C-STM Results and Discussion .....	76
4.12	Concluding Remarks and Key Findings on Experimental Validation .....	83
5	Experimental Program – Specimen Design, Construction, and Deterioration Phase ....	85
5.1	Summary .....	85
5.2	Introductory Background .....	85
5.2.1	Alkali-Silica Reaction.....	87
5.2.2	Delayed Ettringite Formation .....	88
5.3	Experimental Specimen Development .....	90
5.3.1	Representative Prototypes.....	90
5.3.2	Specimen Design .....	90
5.3.3	Specimen Construction and Curing.....	92
5.3.4	Thermal Effects.....	93
5.3.5	Pre-Loading Setup .....	95
5.3.6	Weather Conditioning.....	95
5.3.7	The Supplemental Watering System.....	97
5.3.8	Summary of Experimental Specimen Development.....	97
5.4	Visual Observation over Time .....	98
5.5	Surface Concrete Strains .....	101

5.5.1	Mohr’s Circle .....	104
5.6	Internal Concrete Strains .....	104
5.7	Reinforcing Steel Strains .....	104
5.8	Post-Test Cores.....	107
5.9	Discussion .....	109
5.10	Closure and Key Findings .....	111
6	Controlling the Internal Temperature of Curing Concrete .....	113
6.1	Scope .....	113
6.2	Estimating Required Internal Heat Supply.....	113
6.3	Novel Method for Supplying Internal Heat.....	119
6.4	Results .....	120
6.5	Closure and Key Findings .....	123
7	Experimental Investigation of Large-Scale Specimens without and with ASR/DEF Deterioration Effects .....	125
7.1	Background and Scope.....	125
7.2	Experimental Investigation.....	126
7.2.1	Representative Prototype, Test Setup, and Deterioration Conditions.....	126
7.2.2	Concrete Compressive Strength.....	129
7.2.3	Experimental Test Setup .....	130
7.2.4	Instrumentation .....	135
7.2.5	Experimental Testing Procedure and Loading History.....	138
7.2.6	Experimental Performance.....	149

7.2.7	Force-Displacement Behavior .....	151
7.3	Discussion .....	151
7.3.1	Failure Assessment .....	151
7.3.2	Longitudinal Steel Behavior .....	157
7.3.3	Out-of-Plane Behavior .....	161
7.4	Key Findings from the Experimental Observations .....	161
8	Force-Deformation Modeling of Experimental Results .....	165
8.1	Scope .....	165
8.2	The Structure .....	166
8.3	Present Code-Based Strength Predictions .....	168
8.4	Strength and Deformation Capacity Using C-STM .....	175
8.4.1	The C-STM Model .....	175
8.4.2	Results of C-STM Analysis .....	178
8.4.3	Interrogation of Internal Strains from C-STM and Comparison with Experimental Results .....	181
8.4.4	Failure Analysis .....	188
8.5	Discussion .....	192
8.6	Key Findings from C-STM Modeling .....	194
9	C-STM Application to Texas Bridge Piers .....	197
9.1	Background and Scope .....	197
9.2	Analysis of Pier I5C .....	197
9.2.1	The Structure .....	197

9.2.2	The C-STM Model.....	199
9.2.3	C-STM Results and Discussion .....	202
9.3	Analysis of Pier H19C.....	204
9.3.1	The Structure.....	204
9.3.2	Loading .....	204
9.3.3	The C-STM Model.....	210
9.3.4	C-STM Results and Discussion .....	214
9.4	Key Findings .....	218
10	Summary, Conclusions, and Recommendations.....	219
10.1	Summary .....	219
10.2	Conclusions .....	223
10.3	Recommendations and Future Work.....	226
	References .....	227
	Appendix A: Details of Heat Flow Analysis.....	237
	Appendix B: Stage 1–3 Analysis–Bent Cap Specimen .....	245
	Appendix C: Stage 1–3 Analysis–C-Beam Specimen.....	249

## LIST OF FIGURES

Figure 3–1: Flowchart for Analysis Procedure of Bridge Piers.....	14
Figure 3–2: Bridge Pier and Equivalent Beam Model for Flexure Analysis.....	16
Figure 3–3: Joint Arch Mechanism in Beam-Column Joint. ....	22
Figure 3–4: SAT Model of (a) Cantilever Bent (b) Straddle Bent. ....	24
Figure 4–1: Truss Model Idealization for a Fixed-Fixed Beam-Kim and Mander (1999). ....	33
Figure 4–2: Results of Convergence Study for Different Numerical Integration Schemes for C-STM Analysis.....	35
Figure 4–3: Composition of Classic Arch and Truss Action That Leads to the Overall C-STM.	37
Figure 4–4: Constitutive Stress-Strain Relationship for Compression Chord Elements. ....	41
Figure 4–5: Diagonal Concrete Web Elements. ....	49
Figure 4–6: Concrete Tension Stiffening Ties.....	49
Figure 4–7: Assumed Arching Mechanism between Hoops for Rectangular Sections (Mander et al., 1988). ....	55
Figure 4–8: Confined Strength Determination from Lateral Confining Stresses for Rectangular Sections (Mander et al., 1988). ....	55
Figure 4–9: Modified Stress-Strain Model for Steel to Account for Prestressing Effects due to ASR/DEF.....	57
Figure 4–10: SAP2000 Screenshot: Steel Truss (Top); Concrete Truss (Bottom).....	59
Figure 4–11: Nonlinear Constitutive Material Properties (a) Diagonal Web Members, (b) Compression Chord Elements, and (c) Tension Stiffened Elements.....	61
Figure 4–12: Elevation and Cross Section of Selected Specimens (Bracci et al., 2000).....	64
Figure 4–13: Shear Force and Bending Moment Diagram of Equivalent Beam Model of Bent Cap Specimens.....	68
Figure 4–14: SAT Model of Reinforced Concrete Bridge Cap Specimen 2A. ....	69
Figure 4–15: Experimental, Stage 1, and Stage 2 Results. ....	72
Figure 4–16: C-STM Model for Bent Cap Specimen.....	73
Figure 4–17: Cracked Reinforced Concrete Material Properties.....	75
Figure 4–18: Comparison of Experimental and C-STM Results.....	77
Figure 4–19: Progression of Nonlinear Behavior for Specimen 2A.....	78

Figure 4–20: Experimental vs. Analytical Results for Specimen 5D (top row) and 8G (bottom row).....	80
Figure 4–21: Failure Analysis of Specimen 2A.....	81
Figure 5–1: Prototype Reinforced Concrete Bridge Bents. ....	86
Figure 5–2: Experimental Specimen.....	91
Figure 5–3: Gravity Loading Applications. ....	94
Figure 5–4: Field Environment for the Specimens in Bryan, Texas.....	96
Figure 5–5: Crack Patterns over Time.....	99
Figure 5–6: Crack Patterns over Time – Specimen 4. ....	100
Figure 5–7: Surface Concrete Strain in Longitudinal and Transverse Directions from DEMEC Readings – Specimen 4. ....	102
Figure 5–8: Surface Concrete Strain in Joint and Across the Diagonals of the DEMEC Grid – Specimen 4. ....	103
Figure 5–9: Mohr’s Circle. ....	105
Figure 5–10: Mid-Depth Strain Behavior of the Concrete as Measured by Concrete Gages – Specimen 4. ....	105
Figure 5–11: Reinforcing Steel Strain from Strain Gages – Specimen 4. ....	106
Figure 5–12: Petrographic Results of Specimen 2 after Eight Months’ Exposure.....	108
Figure 5–13: Performance without and with ASR/DEF Expansions.....	110
Figure 6–1: Model Conditions for Heat Flow Analysis Used to Predict Temperature History in Hydrating Concrete Beams. ....	117
Figure 6–2: Measured and Modeled Concrete Temperatures When No External Devices Were Used to Increase/Control Internal Temperature. ....	117
Figure 6–3: Layout of Electrical Resistive Wiring to Raise Concrete Temperature. ....	121
Figure 6–4: Cross-Section View of ERW Heating Plan for Increasing/Controlling Concrete Temperature in Order to Promote DEF. ....	121
Figure 6–5: Measured Temperature History at the Top and Middle of Concrete Element Heated with Electrical Resistive Wiring. ....	122
Figure 7–1: Prototype Reinforced Concrete Bridge Bents with ASR/DEF Deterioration. ....	127
Figure 7–2: Experimental Specimens.....	128
Figure 7–3: Comparison of Cured and Field Cylinders.....	131

Figure 7–4: Experimental Setup for Specimens 1 and 2.....	133
Figure 7–5: Experimental Setup for Specimen 4.....	134
Figure 7–6: External Instrumentation Layout.....	136
Figure 7–7: Internal Instrumentation Layout.....	137
Figure 7–8: Test of Specimen 1: Phase I – Serviceability Loading at 200 kip.....	139
Figure 7–9: Test of Specimen 1: Phase I – Yield at 440 kip. ....	140
Figure 7–10: Test of Specimen 1: Phase II – Ultimate Load at 474 kip.....	141
Figure 7–11: Test of Specimen 2: Serviceability Loading at 200 kip. ....	143
Figure 7–12: Test of Specimen 2: Load at 400 kip.....	144
Figure 7–13: Test of Specimen 2: Ultimate Load at 500 kip.....	145
Figure 7–14: Test of Specimen 4: Serviceability Loading at 200 kip. ....	146
Figure 7–15: Test of Specimen 4: Load at 400 kip.....	147
Figure 7–16: Test of Specimen 4: Ultimate Load at 503 kip.....	148
Figure 7–17: Force-Displacement Behavior of Specimens 1, 2, and 4. ....	152
Figure 7–18: Joint Behavior of Specimens 1, 2, and 4. ....	153
Figure 7–19: Parallel and Perpendicular to Strut (Crack) LVDT Readings. ....	155
Figure 7–20: Failure Mechanism of Specimen 1.....	156
Figure 7–21: Failure Mechanism of Specimen 2.....	158
Figure 7–22: Failure Mechanism of Specimen 4.....	159
Figure 7–23: Strain Gage Readings in Main Flexural Reinforcing Steel. ....	160
Figure 7–24: Out-of-Plane Strains of Specimens 2 and 4.....	162
Figure 8–1: Elevation and Cross-Section of the C-Beam Specimens.....	167
Figure 8–2: Modeling Approach Based on Code-Based Beam and SAT Methods.....	171
Figure 8–3: Experimental, Stage 1, and Stage 2 Results. ....	174
Figure 8–4: Modeling the C-Beam Specimens without and with ASR/DEF Damage.....	176
Figure 8–5: Cracked Reinforced Concrete Material Properties.....	177
Figure 8–6: Actual and Modified Stress-Strain Models for Reinforcing Steel to Account for Prestressing Effects in C-Beam Specimens.....	179
Figure 8–7: Comparison of Experimental and C-STM Results for C-Beam Specimens. ....	180
Figure 8–8: Failure Pattern Observed at the Beam-Column Joint of C-Beam Specimen 1. ....	182

Figure 8–9: Experimental vs. C-STM Comparison of Nonlinear Response and Early Concrete Cracking Effects: Specimen 1 .....	184
Figure 8–10: Experimental vs. C-STM Comparison of Nonlinear Concrete and Steel Response: Specimen 1 .....	185
Figure 8–11: Experimental vs. C-STM Comparison of Nonlinear Concrete and Steel Response: Specimen 2 .....	186
Figure 8–12: Experimental vs. C-STM Comparison of Nonlinear Concrete and Steel Response: Specimen 4 .....	187
Figure 8–13: Computed Sequence of Non-Linear Behavior Events. ....	189
Figure 8–14: Comparison of Strains Parallel and Perpendicular to Crack in the Joint and Beam Region. ....	191
Figure 8–15: Force-Deformation Results for C-Beam Specimens. ....	193
Figure 9–1: Layout and Reinforcement Detail of Pier I5C .....	198
Figure 9–2: C-STM Model of Pier I5C .....	200
Figure 9–3: Cracked Reinforced Concrete Material Properties .....	201
Figure 9–4: Force-Deformation of Pier I5C without and with ASR/DEF Damage. ....	203
Figure 9–5: Layout and Reinforcement Detail of Pier H19C–Sheet 1. ....	205
Figure 9–6: Layout and Reinforcement Detail of Pier H19C–Sheet 2. ....	206
Figure 9–7: Loads on Pier H19C. ....	208
Figure 9–8: Bending Moment Diagrams for Normal Service Regime. ....	209
Figure 9–9: Column Interaction Diagram with Different Load Cases. ....	211
Figure 9–10: Bending Moment Diagrams for (a) the Design Ultimate Strength and (b) for Overload at Incipient Mechanism Formation .....	212
Figure 9–11: C-STM Model for Pier H19C .....	213
Figure 9–12: Cracked Reinforced Concrete Material Properties .....	215
Figure 9–13: Force-Deformation for Case 1 and Case 2 Live Load .....	217



## LIST OF TABLES

Table 3–1: Summary of Notations Used.....	13
Table 4–1: Convergence Study of Higher Order Truss Models for a Cantilever Beam.....	33
Table 4–2: Elastic Truss Member Axial Rigidities.....	45
Table 4–3: Material Properties, Stage 1 and 2 Analyses, and Experimental Results.....	66
Table 4–4: Axial Rigidity Assignments for Specimen 2A.....	74
Table 4–5: Summary of Results for Bent Cap.....	83
Table 5–1: Summary of Experimental Specimen Development.....	97
Table 6–1: Material Properties and Empirical Constants Utilized in Predicting Concrete Temperature History.....	118
Table 7–1: Material Properties of Concrete.....	130
Table 8–1: Material Properties, Stage 1 and 2 Analyses, and Experimental Results.....	169
Table 8–2: Result for C-Beam Specimens.....	194
Table 9–1: Column Axial Load and Moment for Various Load Combinations.....	210



# 1 INTRODUCTION

## 1.1 BACKGROUND AND MOTIVATION

Over the past decade, the structural longevity of a large number of reinforced concrete bridge piers has been compromised as a result of premature concrete deterioration that is generally attributed to alkali-silica reaction (ASR) and delayed ettringite formation (DEF). The aim of this research is to investigate the adverse effects of ASR/DEF on structural performance with particular attention to the disturbed regions that are commonly referred to as D-regions. In this regard an experimental program is designed where near full-scale specimens are built, subjected to the various factors leading to the accelerated formation of ASR/DEF, and destructively tested to assess the performance of the structure. The specimens are subjected to varying amounts of ASR/DEF deterioration in order to study what effects slight, moderate, and heavy damage would have on the D-regions of the structure.

It is well-known that the behavior of deep beams, or disturbed (or “D”) regions, in a structural system cannot be accurately described according to conventional beam theory due to the high irregularity of internal stress and strain distributions, accompanied by the interaction of flexure and shear. As a result, the shear analysis of structural concrete deep beams has been a contentious issue to both researchers and structural engineers for decades.

Conventional U.S. design standards for D-regions have historically been based on empirically derived expressions. The concept of strut-and-tie modeling (SAT) was first introduced as a design method in the *AASHTO LRFD Bridge Design Specification* in 1994 and the *ACI 318 Building Code Requirements for Structural Concrete* in 2002. However, as SAT only satisfies force equilibrium and is intentionally formulated as a lower bound (plastic) solution, the critical mode of failure (i.e., element or nodal failure) is often elusive to the designers. Thus, the ultimate failure mechanism obtained using any of the code-based analysis methodologies might lead to an undesirable brittle collapse when imposed to overload scenarios.

Current nonlinear shear analysis models for structural concrete deep beams are generally complicated to use and have limited applicability or appeal to practicing engineers. Clearly, it is desirable to have a model derived from rational mechanics and validated with experimental

evidence that can be implemented into commercially available structural analysis software. The intention of this research is to provide design engineers with a supplementary analysis tool that can be used to augment the design process by accurately assessing the force-deformation response and nonlinear failure modes of deep beams with small span-to-depth ratios or D-regions.

A *Compatibility Strut-and-Tie Model* (C-STM) that is intended for the nonlinear analysis of shear critical reinforced concrete structures is developed through the course of this research. This report presents the background theory, formulation, and validation of the proposed C-STM modeling technique. The C-STM approach is then applied to the experimental results of the control and ASR/DEF damaged specimens that are presented herein.

## **1.2 SCOPE**

This report is divided into 10 chapters on relatively distinct topics. Following this introductory chapter, Chapter 2 presents a literature review in two parts. First, a review of ASR and DEF effects on the performance of concrete structures is conducted. Second, four truss modeling approaches pertaining to the analysis of reinforced concrete members are discussed, with a particular emphasis on D-regions.

Chapter 3 presents the recommended analysis schema for the strength and deterioration assessment of bridge piers. The analysis can be divided into four stages: Stage 1 pertains to analysis using the normal beam theory; Stage 2 of the analysis uses the SAT analysis method; Stage 3 analysis relates to performing a C-STM analysis which is a minimalist analysis procedure developed in Chapter 4; and Stage 4 of the analysis deals with making recommendations and establishing the acceptability criteria of an existing structure based on the first three stages of analysis.

Chapter 4 presents the development of the C-STM approach. It also explains in detail how to model the truss and arch action and the constitutive material relations. Modifications that need to be made to the material properties to account for ASR/DEF damages in the structure are also presented. The C-STM developed is verified with the results of a large-scale experiment with respect to the overall and internal behavior.

Chapter 5 presents the experimental program including the specimen design, construction, and deterioration phases in detail. Visual observations and concrete and steel strain measurements that are collected over time from the different specimens are presented and inferences are drawn. From the observations made, a hypothesis on what may actually be going on within the specimen due to ASR/DEF deterioration is postulated.

In Chapter 6, a heat flow modeling strategy is set forth to enable an estimation of the amount of supplemental heat that is required to raise the curing temperature of the specimens to above 160°F. The purpose of this supplemental heating is to promote the formation of DEF in the specimens. A simple and efficient method is developed to supply the required amount of electrical energy and hence heat the concrete during the curing process.

Chapter 7 contains the experimental test setup and the instrumentation details. The experimental testing procedure and the load history are also presented in this chapter. The performance, force-deformation behavior, and various other important observations made during the destructive testing of the control and the age-deteriorated specimens are discussed in detail.

Chapter 8 presents the application of the analysis methodology that was developed in Chapter 3 to the specimens tested in Chapter 7. The application of the C-STM technique developed in Chapter 4 to the specimens tested is also presented. Chapter 8 also studies the internal strains obtained from the C-STM model and the corresponding failure analysis results, in addition to modeling the overall force-deformation behavior of the specimens, without and with ASR/DEF deterioration. All C-STM results are compared with the experimental results.

Chapter 9 presents case studies of two Texas bridge piers that are part of the downtown San Antonio *Y* located along I-10 and I-35, that are subjected to ASR/DEF damage. The C-STM analysis of these bridge piers is performed, and conclusions regarding the structural safety without and with ASR/DEF deterioration are drawn accordingly.

Chapter 10 gives a final summary of the dual experimental and analytical modeling program and the key findings from this study. Major conclusions from each of the chapters are presented, and recommendations for future work are made.

### **1.3 WHAT THEN IS PARTICULARLY NEW IN THIS WORK?**

The major contributions from this work toward the existing pool of knowledge can be summarized as below:

- Development of a heating technique to promote DEF by raising the curing temperature to above 160°F.
- Observation of large-scale reinforced concrete members fully exposed to the field environment with wet-dry cycles over time allows for examining the evolution of ASR and DEF effects and the time-dependent quantification of the associated swelling strains.
- Large-scale tests through failure of reinforced concrete members with D-regions, and a comparison of specimens with mild and moderate ASR/DEF damage with an undamaged control specimen.
- C-STM technique is developed as a minimalist analysis technique. The analyses are performed in displacement control to better capture the true failure state and loading. This enables the post-peak falling branch of the force-deformation response to be captured. The C-STM also shows good agreement with previously conducted experimental investigation and the present experimental results, not only in the macro-level, but also in the micro-level behavior.

## 2 LITERATURE REVIEW

### 2.1 SCOPE OF CHAPTER

A review of the past studies done on the effects of ASR and DEF on concrete is given first. This is followed by a historical overview of four shear modeling approaches that are considered applicable to this research.

### 2.2 HISTORIC DEVELOPMENTS ON CONCRETE DETERIORATION MECHANISMS

#### 2.2.1 Alkali-Silica Reaction

It is well-known that high alkali contents in Portland cement used with reactive siliceous aggregates in concrete can result in ASR, particularly when exposed to moisture. ASR results in the formation of expansive products that generally form around aggregates, which in turn leads to cracking of the concrete.

Chemical reactions between alkalis in the cement of concrete and reactive silica found in aggregates can result in ASR when exposed to moisture (Swamy and Al-Asali, 1989 and 1998; Chana and Korobokis, 1991; Poole, 1992; Swamy, 1992; Ahmed et al., 1998, 1999a and 1999b; Fan and Hanson, 1998a and 1998b; Berube et al., 2002; Jensen, 2003). Conditions required for ASR include reactive silica phases in the aggregates, alkali hydroxides in the pore solution ( $[Na^+]$ ,  $[K^+]$ , and  $[OH^-]$ ), and sufficient moisture. The reaction between the reactive silica in the aggregates and the alkali in the pore solution produce a gel, commonly referred to as the ASR gel, which over time expands and causes cracking of the concrete. As the alkalis and reactive silica are consumed with time, the ASR process stops unless these constituents are provided from external sources. Berube et al. (2002) reported that the exposure conditions of concrete greatly influence the development of surface cracking and the expansion of the ASR-affected concrete. It was pointed out that wetting and drying cycles significantly promote surface cracking even though the surface expansion due to ASR may reduce when the concrete is allowed to dry. It is believed that the amount of ASR gel is reduced when the alkali content on the surface layer is reduced due to the inter-leaching of the alkalis from the surface layer. This reduction leads to differential strains between the interior and surface layers and then results in cracking of the surface layer (Deschenes et al., 2009).

As the ASR gel starts to form, tensile stresses are imposed internally within the concrete system and lead to cracking. It was found that the hydrated cement paste is weaker than the aggregates and the cracking usually occurs in the hydrated cement paste or along the interface of the aggregate, and the hydrated cement paste (Poole, 1992 and Swamy, 1992). Jensen (2003) indicated that eventual expansion due to ASR can cause cracking of the aggregates although it initiates in the hydrated cement paste.

### **2.2.2 Delayed Ettringite Formation**

It has also been found that rapid hardening cements in large-volume concrete structures can lead to a very high heat of hydration during concrete curing. This process can cause cracking due to thermal effects and late-age cracking (Kelham, 1996; Odler and Chen, 1996; Scrivener and Lewis, 1997; Grattan-Bellew et al., 1998; Zhang et al., 2002; Deschenes et al., 2009). Ettringite forms within concrete after the high heat condition during initial concrete curing. The reformation of ettringite, commonly known as DEF, can lead to later expansion and cracking. It has been found that DEF can develop as a result of high temperatures at an early age in concrete. Temperature ranges from 148 to 160 °F (64 to 71 °C) during the early age of concrete curing have been reported as the cause. In general, it is believed that structures first exhibit cracking due to ASR and then due to DEF. Both ASR and DEF can lead to cracking of the concrete even though they are different mechanisms of deterioration (Deschenes et al., 2009).

Generally, ettringite forms at an early age in fresh concrete. The sulfate is consumed while reacting with the calcium-aluminates in the presence of calcium hydroxide. Once the sulfate concentration in the pore solution reaches specific lower value, the calcium-aluminates react with the already formed ettringite to produce monosulfoaluminate. Furthermore, if sulfates are reintroduced either from external or internal sources to the pore solution, the monosulfoaluminate can revert back to ettringite, causing expansive forces and cracking. Research has found that if the concrete is subjected to high early heat, the sulfate ions are physically attached to the calcium silicate hydrate (C-S-H) and are available as a source of sulfate at late age of the concrete (Odler and Chen, 1996; Scrivener and Lewis, 1997). Thus, concrete experiencing high temperature during hydration either from high cement contents or large volume structures can lead to the occurrence of DEF.



While ASR initiates at the interface of the hydrated cement paste and the aggregates, introducing tensile stress and resulting in cracking, DEF typically occurs at void locations in the hydrated cement paste and then causes internal stresses. Although ASR and DEF initiate at different areas, both mechanisms can lead to cracking of the hydrated cement paste and the aggregates. It is believed that it takes longer for DEF to take place than ASR, and the damage caused by DEF, in general, may reduce the capacity of a structure (Deschenes et al., 2009). However, both deterioration processes result in similar damage types, and both can affect the strength of a concrete structure. However, the extent of strength reduction is generally unknown.

### **2.3 HISTORIC DEVELOPMENTS ON TRUSS MODELING**

A comprehensive review on the historical developments of truss modeling approaches was presented by the ASCE-ACI Committee 445 (1998). Based on the pre-existing body of knowledge, four truss modeling approaches were considered to be applicable to this research.

- (i) Beam shear models (sectional theories).
- (ii) Plastic truss (strut-and-tie) models.
- (iii) Shear panel models (such as Modified Compression Field Theory and Softened Truss Model).
- (iv) Compatibility truss models.

#### **2.3.1 Beam Shear Models**

For homogenous (uncracked) concrete the shear stress across a section can be found from the well-known formula

$$\tau = \frac{VA\bar{y}}{Ib} \quad (2-1)$$

in which  $V$  = shear force on the cross section,  $A\bar{y}$  = first moment of area about the centroidal axis of the part of the cross-sectional area lying either above or below the point at which the shear is being computed,  $I$  = moment of inertia of the cross section, and  $b$  = width of the member at the section where the stresses are being calculated.

This approach when coupled with the longitudinal flexural stresses can be combined to give the total principal stresses in a beam. Such an approach was historically adapted by AASHTO's *Standard Specifications for Highway Bridges* (2002) and other codes to assess the degree of loading in a prestressed concrete beam to cause shear cracking in narrow-web prestressed concrete members. However, it has little relevance for reinforced concrete as such members crack at low levels of load.

For cracked reinforced concrete beams the total shear resistance is given by

$$V_u = V_s + V_c \quad (2-2)$$

in which  $V_s$  = shear carried by the transverse reinforcing steel and  $V_c$  = the shear carried by concrete given by

$$V_c = v_c b_w d \quad (2-3)$$

where  $b_w$  = web width;  $d$  = effective depth, and  $v_c$  = shear stress carried by concrete given as  $v_c = 0.0632\sqrt{f'_c} \text{ (ksi)} = 2\sqrt{f'_c} \text{ (psi)} = 0.17\sqrt{f'_c} \text{ (MPa)}$ , where  $f'_c$  = concrete strength.

Truss approaches have been known for more than a century (Ritter, 1899; Morsch, 1909). Ritter used a substitute truss (discussed below) with diagonal web members oriented at an angle  $\theta$ . Shear resistance was provided by transverse ties that can be shown to be

$$V_{s\theta} = A_{sh} f_y \frac{jd}{s} \cot \theta \quad (2-4)$$

in which  $A_{sh}$  = area of one set of stirrups;  $f_y$  = yield strength of steel;  $jd$  = internal lever arm where  $j = (1 - d'/d)$  is the internal lever arm coefficient and  $s$  = stirrup spacing. This formula

gives the component of shear carried by steel and is the same as that used in the present AASHTO LRFD (2010) sectional model design approach.

From Eq. (2–1), it can be shown that at the neutral axis of a non-prestressed beam  $\theta = 45$  degrees. Using this in Eq. (2–4) and approximating  $jd = d$  one obtains

$$V_{s,45} = A_{sh}f_y \frac{d}{s} \quad (2-5)$$

This formula is the well-known steel component of shear resistance that has historically been used in ACI-318 (2008) and the AASHTO *Standard Specifications for Highway Bridges* (2002).

### **2.3.2 Plastic Truss (Strut-and-Tie) Modeling**

For concrete structures, the difficulty in dealing with flexure-shear interaction has long been recognized. More than a century ago, Ritter (1899) and Morsch (1909) independently dealt with the problem by converting a reinforced concrete beam into a substitute truss. This design approach is arguably the commencement of early plastic truss methods and led to the development of the SAT, providing a consistent modeling solution for the design of deep beams, D-regions, and anchorage regions in prestressed concrete (Marti, 1985; Schlaich et al., 1987; MacGregor, 1992; Collins and Mitchell, 1991).

Sritharan and Ingham (2003) developed a force transfer method (FTM) for the design and assessment of bridge joints subjected to in-plane seismic actions. This method was based on similar principles to SAT but was specifically used in the seismic performance of bridge joints subjected to shear and bending, as well as accounting for post-tensioning.

Alcocer and Uribe (2008) investigated the monolithic and cyclic behavior of four simply supported deep beams in order to validate the adequacy of using SAT approaches for seismic design. They concluded that the response of each specimen exceeded the SAT expectations in terms of strength, stiffness, and deformation capacity, and hence SAT is appropriate for seismic design provided that the reversed cyclic shear and inelastic deformation demands do not exceed a specified criterion. This conclusion is flawed because only strength-based predictions were made

in comparison to experimental results, thus demonstrating that SAT is insufficient for assessing the deformation demands of a structure. Instead, the present research shows that inherent conservatism in SAT design procedures was the reason for the acceptable cyclic response. This conservative approach should not be blindly used to design structural elements subjected to seismic conditions as deep beams are typically shear critical, hence brittle failure mechanisms may occur if not carefully identified and accommodated for accordingly through capacity design principles.

Typically used as a design tool, SAT is purely a force-based approach that implicitly assumes a lower-bound solution by establishing a plastic truss consisting of concrete compression struts and steel tension ties, satisfying both equilibrium and ultimate material strength requirements. Consequently the eventual mode of failure and associated deformations are often elusive to the designer, as deformation compatibility requirements are not part of the design or analysis process. If incorrectly applied, SAT and other typical sectional shear analysis methods can lead to the formation of a brittle shear collapse mechanism in overload scenarios instead of an anticipated flexural failure (Collins et al., 2008). Hence, the treatment of shear problems should correspond to the context to which they are applied, where different methods can be used to supplement each other in order to provide a consistent and rational means of evaluating the structural shear strength (Marti, 1999).

### **2.3.3 Shear Panel Modeling**

The MCFT (Collins, 1978; Collins and Mitchell, 1980; Vecchio and Collins, 1986) was developed to solve the unknown variables associated with the variable-angle truss model for an idealized reinforced concrete element. By applying equilibrium, compatibility, and constitutive stress-strain relationships of cracked reinforced concrete materials, the angle of inclination of concrete struts  $\theta$  and thus the internal stresses and strains can be determined. In parallel to this, the Softened Truss Model (Mau and Hsu, 1987; Hsu, 1994 and 1996) was developed assuming a uniform state of stress in a web shear element and idealizes the concrete compressive stresses as a series of parallel compressive struts. This model is also based on axioms of equilibrium and compatibility, and can be used to analyze a member subjected to any combination of bending, axial load, shear, and torsion.

These models have been experimentally validated and proven to accurately model the behavior of reinforced concrete *panel elements* subjected to different applied states of stress. However, these models are typically based on the premise that the crack angle rotates as the analysis proceeds, whereas this is not typical of deep beam type elements. Moreover, the well-known arch and truss actions (Park and Paulay, 1975) for shear resistance in beams cannot be easily uncoupled when the analysis essentially takes place on small panel elements.

#### **2.3.4 Compatibility Truss Modeling**

Compatibility truss modeling considers truss member deformations in order to formulate the shear stiffness of reinforced concrete beams using strain energy concepts of the analogous truss (Dilger, 1966). The elastic components of deformation for a deep coupling beam can be characterized as: truss action, arch action, flexural deformations, and beam elongation. The transfer of shear forces to the transverse reinforcement through the diagonal concrete struts is known as the truss action. Arch action pertains to the shear force resisted by a single diagonal corner-to-corner concrete strut. The strain differences in the top and bottom longitudinal reinforcements lead to flexural deformations; and the average strains in the top and bottom longitudinal reinforcements result in beam elongation (Paulay, 1971).

Using structural analysis software, the nonlinear force-deformation response of a reinforced concrete structure can be computationally modeled by extending these principles to account for the nonlinear constitutive material relationships as shown by Kim and Mander (1999, 2000, and 2007). Other models based on SAT modeling principles have also been developed and accurately validated against experimental results (Hwang et al., 2000; To et al., 2001, 2002, 2003, and 2009; Salem and Maekawa, 2006). These models can be used as powerful analysis tools for predicting the coupled flexure and shear force-deformation behavior of deep beams and D-regions in comparison to the foregoing plastic truss solutions. However, the majority of these models either are computationally involved and difficult for practicing engineers to replicate, require nonlinear structural analysis software not commonly available to engineering firms, are not versatile and thus cannot be applied to a variety of structures, or require some empirical calibration with experimental results (To et al., 2009).

In light of this, the primary objective of this research is to develop a displacement-based analysis that adopts a compatibility-based strut and tie model that is sufficiently accurate to capture the nonlinear force-deformation response of reinforced concrete structures. Moreover, the approach needs to be sufficiently simple to be implemented by practicing engineers as a supplemental design tool using commonly accepted software. This research is an extension of the earlier work of Kim and Mander (1999, 2000, and 2007) and is adapted specifically for modeling the behavior of the “D-region” of deep cantilevered beams with small span-to-depth ratios that may or may not be affected by premature concrete deterioration due to the effects of ASR/DEF.

### 3 ANALYSIS SCHEMA

#### 3.1 SCOPE

This section presents a methodology for determining the structural capacity of cracked concrete bridge piers. The method is considered to be particularly useful for those portions of the bridge piers where disturbed regions may govern the behavior. The method is not really intended to be a substitute for existing design procedures, but rather a check on the capacity of new designs or existing sub-structures that may be showing signs of distress.

The flowchart given in Figure 3–1 depicts the procedure and the branching decision points that either terminate the analysis or trigger additional analyses to provide additional insights into expected behavior of bridge piers. A summary of the notations used in the following sections along with what they represent are presented in Table 3–1.

**Table 3–1: Summary of Notations Used.**

Notation	Comments
$P_y^b = M_y^b / L_b$	Externally applied load causing first yield
$P_n^f = M_n^f / L_b$	Externally applied load causing flexural moment in the critical beam-column face
$V_n^s = V_c + V_s + V_p$	Nominal shear capacity provided by the section
$\phi V_n^s$	Factored shear capacity
$V_n^j = V_{arch} + V_{truss}$	Joint shear capacity
$V_{jv}$	Vertical shear in beam-column joint caused by $P_n^f$
$V_{jh}$	Horizontal shear in beam-column joint caused by $P_n^f$
$P_y^{SAT}$	Externally applied load causing first yield from SAT analysis
$P_n^{SAT}$	Externally applied load causing flexural shear demand from SAT analysis

As a prelude to the analysis, material properties are determined from the records, plans, in situ testing, or through non-destructive evaluations, which form an input for the various stages of analysis. After, a preliminary structural analysis, the first yield flexure capacity ( $M_y^b$ ), the

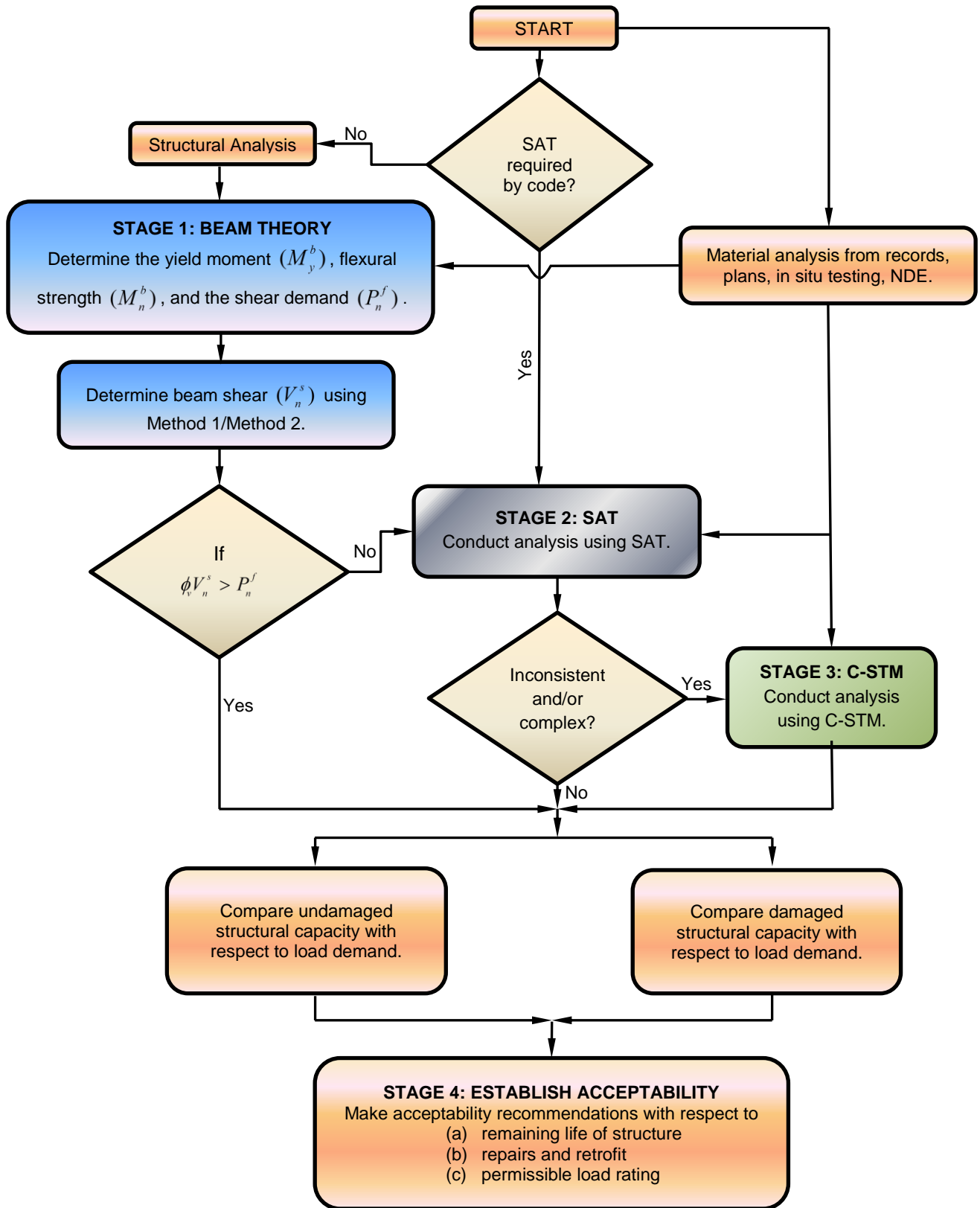


Figure 3–1: Flowchart for Analysis Procedure of Bridge Piers.



nominal flexural moment ( $M_n^f$ ), the externally applied load causing first yield and beam flexure ( $P_y^b = M_y^b / L_b$  and  $P_n^f = M_n^f / L_b$ , respectively, where  $L_b$  = length to the nearest inflexion point), and the beam shear ( $V_n^s$ ) are determined as part of Stage 1 of the analysis. From Stage 1, if the factored shear capacity ( $\phi_v V_n^s$  where  $\phi_v = 0.90$ ) is greater than the nominal external load causing beam flexure ( $P_n^f$ ), then there is a measure of reserve shear capacity; therefore the beam should fail in flexure. However, if the factored shear capacity is insufficient, or when the code mandates, additional analysis of the structure may be required. In the first instance this can be done using the strut-and-tie method, which forms Stage 2 of the analysis schema. If Stage 2 leads to conclusive results, further analysis may be unnecessary. However, in the event of inconsistent and/or complex results from Stage 2 analysis, Stage 3 analysis comprising a C-STM analysis may be required. Based on these analysis results, the acceptability of the structure can be established, which forms Stage 4 of the analysis. A detailed analysis procedure follows.

### 3.2 STAGE 1: ANALYSIS USING BEAM THEORY

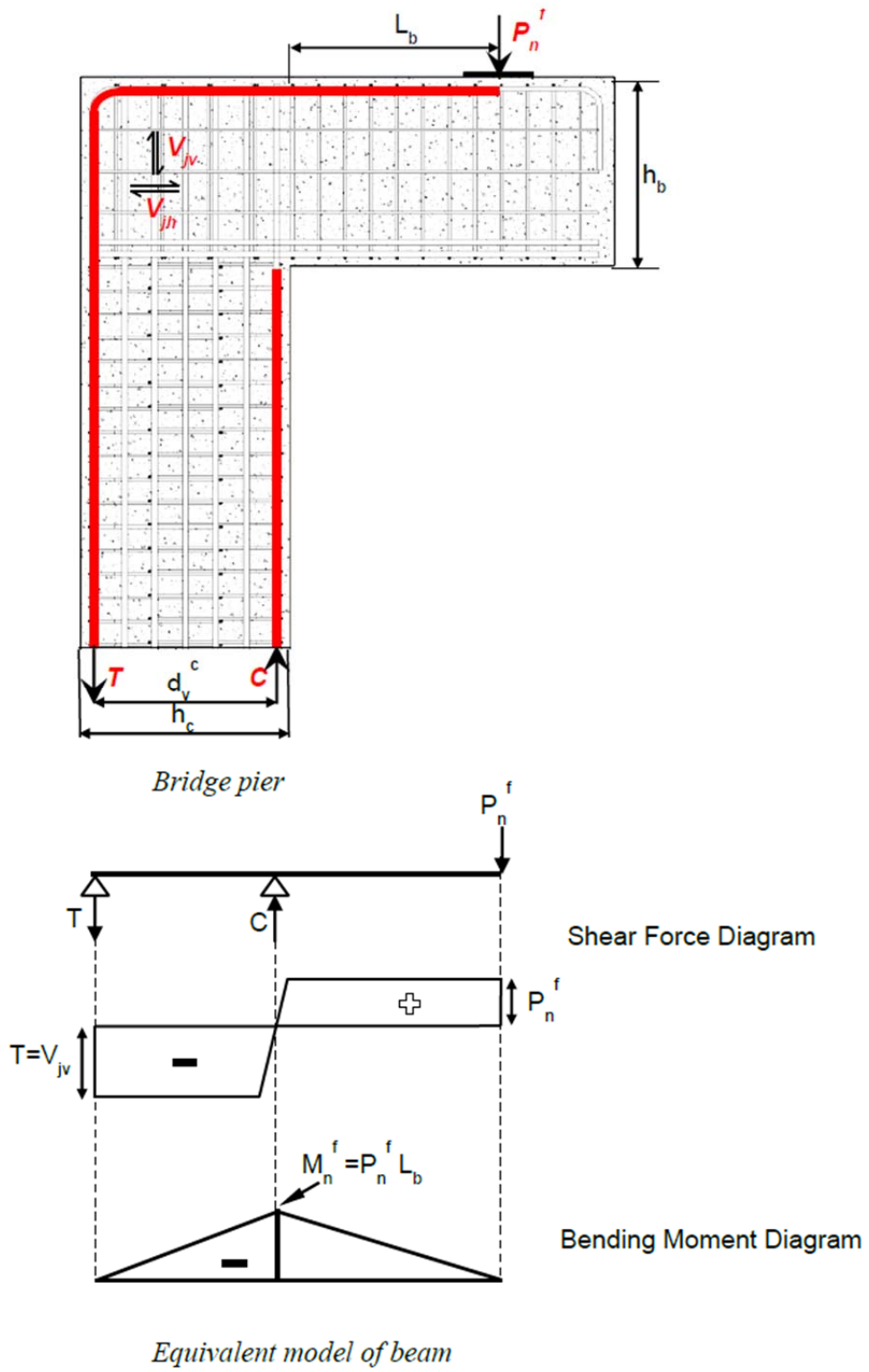
As a first step in the analysis of a bridge pier as shown in Figure 3–2, it is assumed flexural plastic hinge forms first, and the analysis is conducted based on flexural bending theory. The following steps summarize this analysis technique:

*Step 1:* Determine first yield flexural capacity,  $M_y^b$ .

Calculate the beam yield moment ( $M_y^b$ ) at first yield of longitudinal steel given by:

$$M_y^b = C_s(d - d') + C_c(d - kd / 3) \quad (3-1)$$

in which  $d$  = depth to the centroid of tensile reinforcement from the extreme compression fiber;  $d'$  = depth to the centroid of compression steel from the extreme compression fiber;  $C_s = A_s' f_s$  when  $f_s \leq f_y$  and  $C_c = 0.85 f_c' ab$  where  $A_s'$  = the area of compression reinforcement;  $f_s$  = stress in steel corresponding to strain  $\epsilon_s$ ;  $f_y$  = yield stress of reinforcing steel;  $f_c'$  = concrete compressive strength;  $b$  = width of the section; and  $k$  is the elastic compression zone coefficient as given by Park and Paulay (1975):



**Figure 3–2: Bridge Pier and Equivalent Beam Model for Flexure Analysis.**

$$k = \sqrt{(\rho_L + \rho'_L)^2 n^2 + 2(\rho_L + \rho'_L d'/d)n} - (\rho_L + \rho'_L)n \quad (3-2)$$

in which  $\rho_L$  = the ratio of tension reinforcement;  $\rho'_L$  = the ratio of compression reinforcement; and  $n$  = the modular ratio of steel to concrete.

The externally applied load causing first yield is given by:

$$P_y^b = M_y^b / L_b \quad (3-3)$$

where  $L_b$  = distance from the point of application of the load to the face of the column.

*Step 2:* Determine nominal flexural moment,  $M_n^f$ .

The flexural moment ( $M_n^f$ ) of the beam is calculated as:

$$M_n^f = C_s(d - d') + C_c(d - a/2) \quad (3-4)$$

in which  $a = \beta_1 c$  is the depth of the equivalent rectangular stress-block for which  $c$  is the neutral axis depth and  $\beta_1$  = the equivalent rectangular stress-block parameter given as:

$$0.65 \leq \beta_1 = 0.85 - 0.05(f'_c(\text{ksi}) - 4) \leq 0.85 \quad (3-5)$$

*Step 3:* Determine externally applied load based on flexure,  $P_n^f$ .

Based on the flexural capacity ( $M_n^f$ ), the external load causing beam flexure ( $P_n^f$ ) is determined:

$$P_n^f = M_n^f / L_b \quad (3-6)$$

*Step 4:* Determine beam shear capacity,  $V_n^s$ .

The shear capacity ( $V_n^s$ ) of the beam is computed as:

$$V_n^s = V_c + V_s + V_p \quad (3-7)$$

in which  $V_p$  = component of shear carried by prestressing tendons, if any;  $V_s$  = shear carried by steel; and  $V_c$  = shear carried by concrete given by:

$$V_c = 0.0316 \beta \sqrt{f'_c} b_v d_v \quad (3-8)$$

where  $f'_c$  = concrete strength is in *ksi* units;  $b_v$  = section web width across shear plane;  $d_v$  = effective shear depth taken as  $d_v = jd$  or not less than the greater of  $0.9d$  (where  $d$  = effective depth), or  $0.72h$  (where  $h$  = overall depth).

For sections with steel transverse to the longitudinal axis of the member ( $\alpha = 90^\circ$ ), the shear carried by the hoops and /or cross ties is given by:

$$V_s = A_v f_y \frac{d_v}{s} \cot \theta \quad (3-9)$$

where  $A_v$  = cross-sectional area of hoopset;  $s$  = hoopset spacing; and  $\theta$  = shear crack angle inclined from the longitudinal axis.

AASHTO LRFD (2010) specifications permit  $\beta$  and  $\theta$  in Eq. (3-8) and (3-9) to be calculated by one of the following two methods:

Method 1: Simplified Procedure

For reinforced (non-prestressed) concrete members, values of  $\beta = 2.0$  and  $\theta = 45^\circ$  can be used. Thus, the shear carried by concrete is the same as the well-known historic ACI-318 (2011) method.

Method 2: General Sectional Procedure

This method is based on the simplified version of the MCFT (Bentz et al., 2006). In this method the parameters  $\beta$  and  $\theta$  can be determined as described below.

For sections containing the minimum amount of transverse reinforcement as specified in AASHTO LRFD (2010),  $\beta$  is determined as:

$$\beta = \frac{4.8}{1 + 750\varepsilon_s} \quad (3-10)$$

where  $\varepsilon_s$  = net longitudinal tensile strain in the section at the centroid of the tensile reinforcement determined as explained later.

For sections that do not contain the minimum amount of shear reinforcement as specified in AASHTO LRFD (2010),  $\beta$  is determined as:

$$\beta = \frac{4.8}{(1+750\varepsilon_s)} \frac{51}{(39+s_{xe})} \quad (3-11)$$

where  $s_{xe}$  = the crack spacing parameter is given by:

$$12.0(in.) \leq s_{xe} = s_x \frac{1.38}{a_g + 0.63} \leq 80.0(in.) \quad (3-12)$$

where  $a_g$  = maximum aggregate size in inches;  $s_x$  = the lesser of either  $d_v$  (effective shear depth) or the maximum distance between layers of longitudinal crack control reinforcement, where the area of the reinforcement in each layer is not less than  $0.003b_v s_x$ .

The crack angle  $\theta$  for any of the above cases is given by:

$$\theta = 29 + 3500\varepsilon_s \quad (3-13)$$

In Eqs. (3-10), (3-11), and (3-13),  $\varepsilon_s$  can be determined from the following expression:

$$\varepsilon_s = \frac{\left( \frac{|M_u|}{d_v} + 0.5N_u + |V_u - V_p| - A_{ps}f_{po} \right)}{E_s A_s + E_p A_{ps}} \quad (3-14)$$

where  $|M_u|$  = factored moment, not to be taken less than  $|V_u - V_p| d_v$ ;  $V_u$  = factored shear force;  $V_p$  = component of shear carried by prestressing tendon;  $N_u$  = factored axial force taken as positive if tensile and negative if compressive;  $A_s$  = area of non-prestressing tensile steel;  $A_{ps}$  = area of prestressing steel on the flexural tension side of the member;  $f_{po}$  (pretensioned members) = stress in strands when concrete is cast around them, and  $f_{po}$  (post-tensioned members) = average stress in the tendons when the post-tensioning is completed, or for usual levels of prestressing  $f_{po} = 0.7f_{pu}$  for both pre- and post-tensioning;  $f_{pu}$  = ultimate stress in the prestressing tendon;  $E_s$  and  $E_p$  = modulus of elasticity of reinforcing steel and prestressing steel, respectively; and  $A_s$  = area of reinforcing steel.

Step 5: Check strength hierarchy.

Once the externally applied load causing beam flexure ( $P_n^f$ ) and the shear capacity ( $V_n^s$ ) are calculated, the strength hierarchy can be determined based on:

$$\text{IF} \quad \phi V_n^s > P_n^f$$

THEN shear has a measure of reserve capacity and the beam should fail in flexure.

$$\text{IF} \quad \phi V_n^s < \phi_f P_n^f$$

THEN the factored shear capacity may be insufficient leading to a shear failure of the bridge pier.

In the above,  $\phi = 0.90$  and  $\phi_f = 0.90$  are the strength reduction factors for shear and flexure, respectively, as per AASHTO LRFD *Bridge Design Specifications* (2010).

Step 6: Determine the shear capacity of the beam-column joint regions.

In the beam-column joint zones, the code is silent on the amount of reinforcement needed. However, the seismic provisions (clause 5.10.11.4 AASHTO LRFD *Bridge Design Specifications*, 2010) note that the transverse reinforcement from the column should be continued into the cap and the shear resistance from normal weight concrete be limited to the following check:

$$V_h < 0.380bd\sqrt{f_c'}(ksi) \quad (3-15)$$

The commentary notes: “The (shear) strength of the column connections in a column cap is relatively insensitive to the amount of transverse reinforcement, provided that there is a minimum amount and that the shear resistance is limited to the values specified.”

However, for the beam-column joint regions in bent caps, the joint shear capacity needs to be determined in the direction in which the shear steel (hoops) are oriented. Thus, the vertical shear in the joint ( $V_{jv}$ ) determined from the shear force diagram (Figure 3–2) of the bridge bent cap, can be transformed as follows to obtain the horizontal shear in the joint:

$$V_{jh} = \frac{h_c}{h_b} V_{jv} \quad (3-16)$$

in which  $h_b$  and  $h_c$  are the overall depth of the beam and column, respectively.

The joint capacity can be assessed as:

$$V_n^j = V_{arch} + V_{truss} \quad (3-17)$$

where  $V_{arch}$  = shear carried by the corner-to-corner diagonal concrete arch (defined later); and  $V_{truss} = \sum A_{sv} f_y =$  the shear carried by the hoops and/or cross ties, in which  $\sum A_{sv}$  = the total area of steel given by all hoops/ties within the joint region.

There is a parabolic distribution of stress in the corner-to-corner arch in the beam-column zone which can further be simplified as shown in Figure 3-3a and b. From Figure 3-3c,  $V = P \sin \alpha$ . The total tensile force across the arch equals  $P/2 = (jd / \sin \alpha) b_w f_t'$ , which implies the shear contribution from the corner-to-corner joint arch is given by:

$$V_{arch} = 0.253 \sqrt{f_c' (ksi)} b_v jd = 8 \sqrt{f_c' (psi)} b_v jd \quad (3-18)$$

taking  $f_t' = 0.126 \sqrt{f_c' (ksi)} = 4 \sqrt{f_c' (psi)}$ .

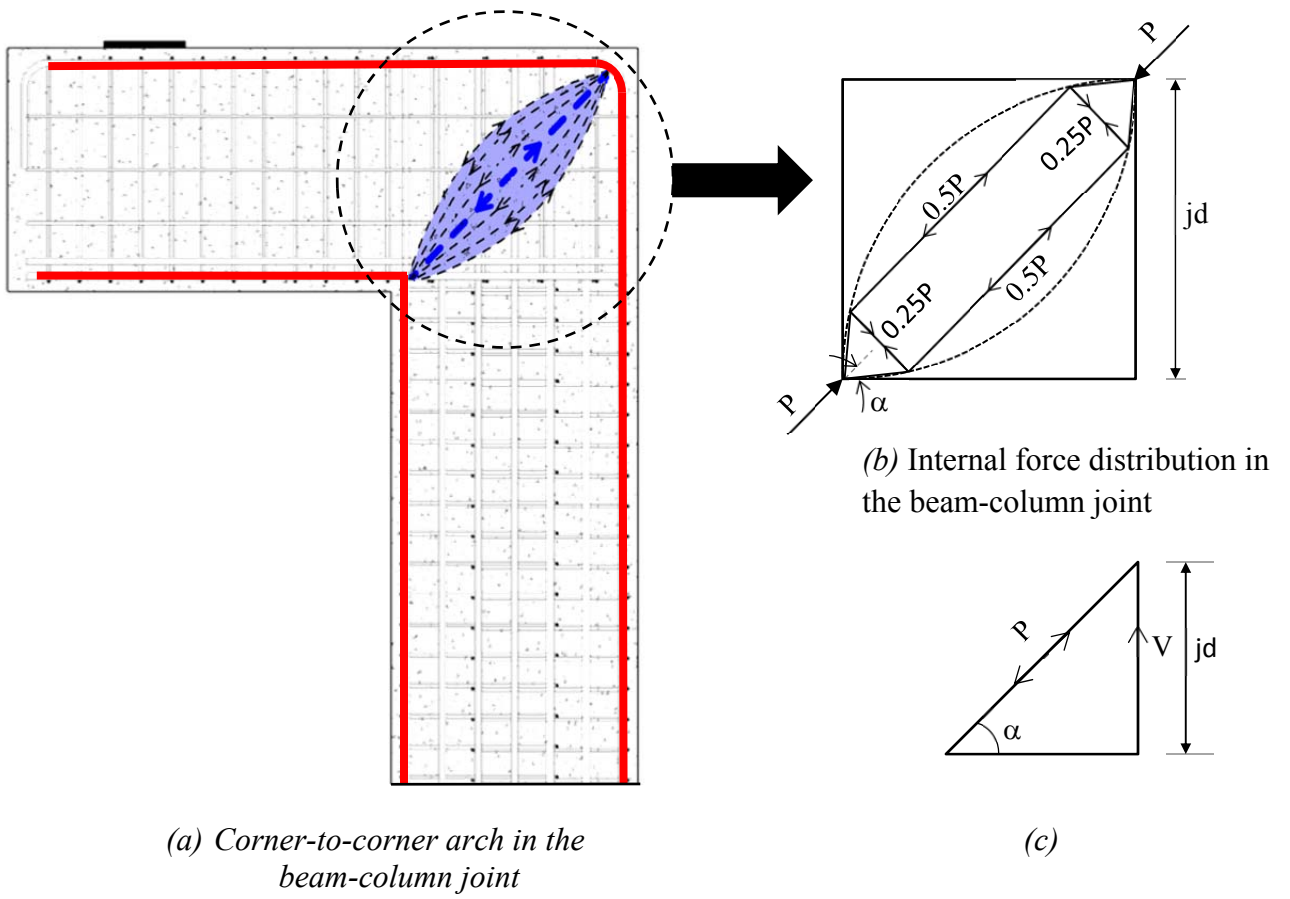
For the beam-column joint to be safe in shear, the following should be satisfied:

$$\phi_n V_n^j > V_{jv} \quad (3-19)$$

From the above analysis, if it is determined that the beam has a measure of reserve capacity, then the analysis can essentially be stopped at this point. However, if either the beam or the beam-column joint is a shear critical section, then further investigation is warranted. In such a case or when as required by the code, the SAT technique of analysis can be used for further analysis, which is discussed in the next section.

### 3.3 STAGE 2: STRUT-AND-TIE ANALYSIS

The SAT modeling technique is a lower-bound plastic truss model that is particularly useful for design. It can also be adopted for strength analysis and may be particularly useful for structures



**Figure 3–3: Joint Arch Mechanism in Beam-Column Joint.**



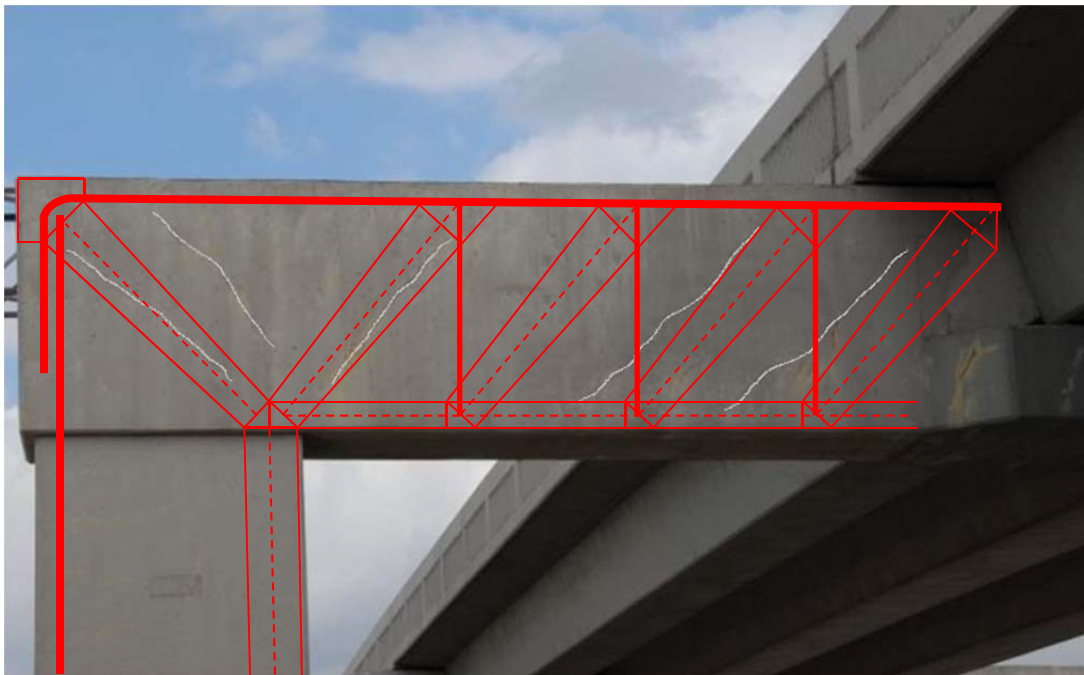
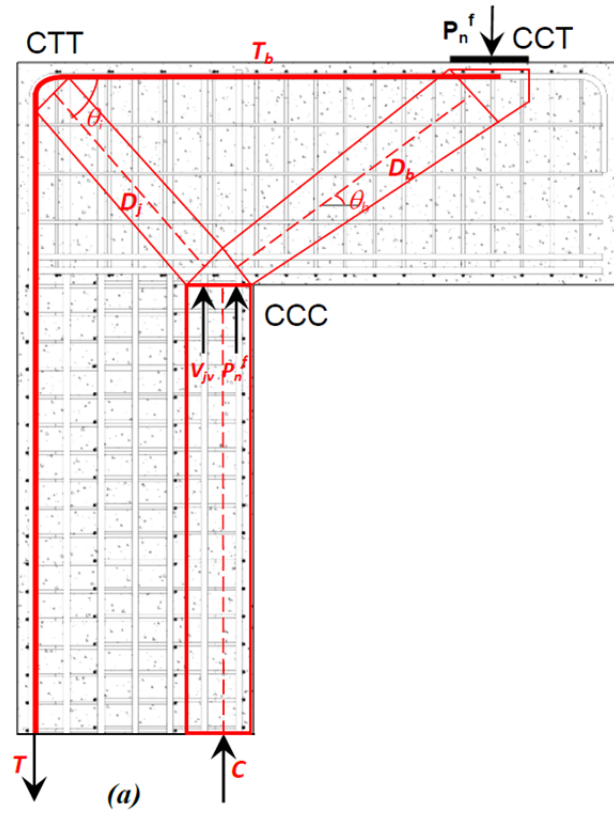
that possess stocky members and a significant number of D-regions. Using an SAT approach, a structure with D-regions is modeled as a truss, which consists of three types of elements: struts, ties, and nodes. Struts represent concrete that carries compressive loads, while tensile loads are carried by ties representing steel reinforcements. Struts and ties intersect at nodes. Nodes are labeled by the element forces intersecting at the nodes; “C” represents compression, while “T” stands for tension. Based on the type of member forces at the node, the nodes can be classified as CCC, CCT, CTT, and so on.

The truss geometry of the SAT model is based on the direction of stress flow in the D-region. The ties are aligned along the reinforcement layout, whereas the struts are oriented based on the compressive stress flow trajectories. It is also reasonable to determine the truss geometry based on the cracks that can be seen on a structural member as illustrated in Figure 3–4b.

Once the truss geometry is determined, the nodal geometries must be established in order to calculate the stresses on each of the nodal faces. These calculated stresses must not exceed the allowable stresses for each nodal face. The nodes can be proportioned either as a hydrostatic node or as a non-hydrostatic node. In a hydrostatic node, the principal stresses are equal on all sides of the node; hence, the ratio of each nodal face is directly proportional to the force being applied to the nodal face. However, often the nodal dimensions are inconsistent with the beam details such as the location of the reinforcement and depth of the flexural compression zone. In the case of non-hydrostatic nodes, the stresses applied to each nodal face are different as the node is sized based on the beam details. As a result of this, the nodal geometry is synchronized with the beam details. Additionally, higher values of shear span-to-depth ratio can also lead to unrealistically large struts in the case of hydrostatic nodes.

Based on the above concepts, a SAT model for a cantilever bent and a straddle bent are shown in Figure 3–4. The forces in the truss elements can be determined by a simple truss analysis. The stresses in each of the truss elements and nodes are then checked against the allowable stresses.

The allowable concrete compressive stresses on the nodal face depend on the type of node. The allowable stresses in the nodal regions are defined as follows:



(b)

Figure 3-4: SAT Model of (a) Cantilever Bent (b) Straddle Bent.

For	CCC nodes	$f_{cu} = 0.85 f_c'$	
	CCT nodes	$f_{cu} = 0.75 f_c'$	(3-20)
	CTT nodes	$f_{cu} = 0.65 f_c'$	

The limiting compressive stress within a strut ( $f_{cu}$ ) is given by:

$$f_{cu} = \frac{f_c'}{0.8 + 170\varepsilon_1} \leq 0.85 f_c' \quad (3-21)$$

in which  $\varepsilon_1$  = principal tension strain given by:

$$\varepsilon_1 = \varepsilon_s + (\varepsilon_s + 0.002) \cot^2 \alpha_s \quad (3-22)$$

where  $\varepsilon_s$  = tensile strain in the direction of the tension tie; and  $\alpha_s$  = the smallest angle between the compressive strut and adjoining tension tie.

The nominal resistance of a strut/node is given as:

$$P_n = f_{cu} A_{cs} \quad (3-23)$$

where  $A_{cs}$  = effective cross-sectional area of the strut/node.

The nominal resistance of a tension tie is given by:

$$P_n = f_y A_{st} + A_{ps} [f_{pe} + f_y] \quad (3-24)$$

where  $f_y$  = yield strength of reinforcing steel;  $A_{st}$  = area of reinforcing steel in the tension tie;  $A_{ps}$  = area of prestressing steel;  $f_{pe}$  = stress in prestressing steel after losses.

A generalized stepwise procedure on how to determine the capacity of a bridge pier using a SAT model follows, and is also illustrated in Figure 3-4.

*Step 1: Determine the truss and node geometry.*

The first step in conducting a SAT analysis is to determine the geometry of the truss and the nodes. The width of the compression chords in the column and the beam can be determined based on the depth of the triangular stress-block or the equivalent rectangular stress-block. The base of the CCC node can be proportioned based on the externally applied load that causes beam flexure ( $P_n^f$ ) and the vertical component of shear in the beam-column joint ( $V_{jv}$ ). The width of the CCT node is taken to be equal to the width of the bearing pad, and the CTT node is dimensioned based on the bending radius of longitudinal reinforcement. The struts can be drawn based on the dimension of the nodes. This will also provide the inclination angle of the diagonal struts.

*Step 2: Solve the determinate truss.*

It is assumed that the tensile reinforcement of the beam yields, that is,  $T_b = A_s f_y$ . Considering equilibrium of forces at the nodes, the forces in all the members of the truss can be determined.

*Step 3: Determine minimum applied load causing node failure.*

Based on the nodal dimensions and the allowable stress (Eq. 3–20), the nodal capacity of each node can be determined. The minimum applied load causing node failure can then be back calculated.

*Step 4: Determine shear demand.*

The shear demand on the bridge pier can be determined based on the most critical strut/tie or nodal zone.

While the SAT method is a relatively simple approach it suffers from two major drawbacks. First and foremost, the SAT approach is a lower bound plastic truss that gives no sense of what the related deformations are under a given set of applied loads. Second and related to this, is the fact that SAT does not give a unique solution. This feature was brought out strongly in research by Ley et al. (2007) who designed and tested several specimens with different reinforcing layouts, all designed by SAT methods. Ley et al. (2007) concluded that the ultimate failure load and mode cannot be predicted by the SAT method.

This calls for a more advanced analysis technique that adopts the concepts of the SAT method and gives an idea about the overall behavior of the structure. One such technique, the C-STM, is developed in the next chapter.

### **3.4 STAGE 3: ANALYSIS USING COMPATIBILITY STRUT-AND-TIE METHODS**

As mentioned above, SAT analysis methods are strictly lower bound solutions. Such solutions adhere to the principles of equilibrium, but are both silent on and unable to predict deformations of the structure.

#### **3.4.1 Stage 3.1: C-STM Based on Undamaged Material Properties**

To obtain a more holistic view of structural behavior that provides a complete force vs. deformation pathway to failure, compatibility of member deformations must be incorporated into the analysis. This approach is referred to as the C-STM.

As this approach is relatively new, a complete background and theoretical formulation is presented in the next chapter. As keeping track of this class of nonlinear analysis can be time consuming, it is suggested that nonlinear structural analysis software (e.g., SAP2000<sup>TM</sup>, 1995) be used for the analysis. In this stage of analysis, the undamaged material properties are used in evaluating the behavior of the structure.

#### **3.4.2 Stage 3.2: C-STM Allowing for ASR/DEF Damage and Its Effects**

It is well-known that ASR/DEF may cause the concrete to deteriorate. The effects of ASR/DEF on the structure can be explained as follows:

- ASR/DEF effects cause the concrete to swell.
- This in turn may cause the cover concrete to badly crack and in some cases cause spalling.
- Meanwhile, swelling of the core concrete occurs, but this is constrained in part by the presence of longitudinal and transverse reinforcement.
- Tensile strains that are induced put the reinforcing steel into a state of prestress.

- In turn, this prestress effect, which is similar to adding an axial force, increases the stiffness and can slightly enhance the strength of the members most affected by ASR/DEF.

The effects of ASR/DEF on the structure can be modeled in C-STM by introducing the effects of concrete deterioration and swelling. The latter causes confinement of the core concrete and prestressing of the reinforcing steel. Therefore, the stress-strain relation for concrete and steel need to be modified accordingly.

Based on an assessment of the extent of damage due to ASR/DEF effects observed in the structure, the damage can be categorized into three classes: slight, moderate, and heavy damage. Based on the damage class, the deteriorated concrete properties, and the prestressing forces in the longitudinal and transverse reinforcing steel are determined. A C-STM analysis with the modified properties gives the behavior of the structure with ASR/DEF damage.

Based on the results from the three stages of analysis presented above, the structural capacity of the damaged/undamaged structure can be compared to the load demand on the structure. Based on these comparisons, acceptability criterion can be set for a structure; this constitutes Stage 4 of the analysis schema.

### **3.5 STAGE 4: ESTABLISH ACCEPTABILITY OF STRUCTURE**

Based on the analysis conducted on the structure in the above three stages, a structural engineer must be able to make recommendations and establish the acceptability of an existing structure that may or may not be subjected to any form of deterioration/damage. The engineer must be able to make acceptability recommendations with respect to:

- The remaining life of the structure: This would essentially give ample time for the state DOTs to plan ahead on how to deal with the existing structure and/or plan alternate strategies.
- Repairs or retrofit: Such remediation can be done in order to strengthen the existing structure and give it added service life to enable it to perform as designed.
- Permissible load rating: By limiting the permissible loads on the structure, the service life of the structure can be extended.

The first two stages of analysis, using beam theory and SAT analysis, would give the structural engineer just an idea about the maximum load that the structure can withstand before it starts to show signs of distress or even fails. However, Stage 3 of the analysis (where the C-STM technique is adopted) gives the overall force-deformation of the structure, which helps to better predict/model its behavior and make a more definitive engineering judgment on the structure's acceptability condition. The C-STM analysis technique will aid the structural engineer to make a more accurate educated prediction about the behavior of the structure.

### **3.6 KEY STEPS IN THE STRENGTH ASSESSMENT OF CONCRETE STRUCTURES DETERIORATED WITH ASR/DEF EFFECTS**

The following key observations can be drawn from the analysis schema developed in this chapter:

- Stage 1 analysis that employs the well-known beam theory can be used to determine the capacity of structures assuming a plastic hinge forms first. In fact, it may not be required to do a SAT/C-STM analysis if it is deemed that the structure is critical in flexure. However, this theory breaks down if D-regions are critical and thus becomes invalid. Nevertheless, the approach is still an important step in an overall assessment of the structure. For example, the shear-force diagram can be used to inform the analyst in Stage 2 on how nodal geometry should be apportioned.
- Stage 2 (SAT) can be used for analysis of structures with D-regions and as a further analysis technique if Stage 1 of the analysis leads to inconclusive results. However, SAT methods are strictly lower bound solutions and are both silent on and unable to predict deformations of the structure.
- The effects of ASR/DEF cannot be dealt with using Stage 1 and 2 of the analysis as these are based on the performance of sound concrete. ASR/DEF causes concrete swelling to occur; therefore a compatibility method is required.
- C-STM is a minimalist analysis procedure. It can be used to obtain a holistic behavior of the structure and to incorporate the effects of ASR/DEF in predicting the structural performance.





## **4 COMPATIBILITY STRUT-AND-TIE FORMULATION**

### **4.1 SCOPE**

This chapter describes the various aspects in the development of the Compatibility Strut-and-Tie analysis technique, including validation of this analysis technique with experimental results.

To obtain a more holistic view of structural behavior that provides a complete force vs. deformation pathway to failure, compatibility of member deformations must be incorporated into the analysis. This approach is referred to as the C-STM. While, the normal SAT methods only require force equilibrium, the C-STM must also maintain displacement compatibility. Additionally this must be ensured between the parallel systems consisting of the truss and the arch.

### **4.2 TRUSS AND ARCH ACTION**

It is well-known that the shear resistance in structural concrete elements is resisted by a combination of truss and arch action (Park and Paulay, 1975). Truss action is associated with the shear resistance provided by the transverse reinforcement (Ritter, 1899; Morsch, 1909; Dilger, 1966; Paulay, 1971; Kim and Mander, 1999, 2000, and 2007). Arch action becomes prevalent in squat-reinforced concrete members, particularly those with wide webs where a direct compression load path (arch) exists between the applied load and the supports. These two primary mechanisms are further considered in what follows.

### **4.3 MODELING TRUSS ACTION**

Figure 4–1a illustrates a variable angle crack pattern that typically forms in the disturbed regions of a fixed-fixed reinforced concrete deep beam. After the development of first cracking, diagonal concrete compression struts are tied together by the longitudinal and transverse reinforcing steel, thus resembling a truss. Starting with a differential portion of this truss, Kim and Mander (1999, 2007) integrated this over the beam length to develop a “continuum truss” model where cracking was implicitly smeared in order to obtain the shear stiffness in a numerical form.

Alternative numerical integration schemes were then considered by Kim and Mander (1999, 2007) to model the discrete crack patterns typically observed in reinforced concrete

beams and are explored further herein. For a fixed-fixed beam, the simplest of these numerical integration schemes uses a two-point Gaussian quadrature solution leading to a so-called two-point Gauss Truss shown in Figure 4–1b. Note the solid lines represent tension ties (reinforcing steel), and the dashed lines represent diagonal compression struts (concrete). Through experimental and analytical validation, Kim and Mander (1999, 2007) found the two-point Gauss Truss to be a suitably accurate numerical integration scheme for capturing both shear and flexure deformations of disturbed regions with fixed-fixed end conditions. Higher order numerical schemes were also considered; however, the two-point Gauss Truss model has the appeal of being statically determinate (due to anti-symmetry).

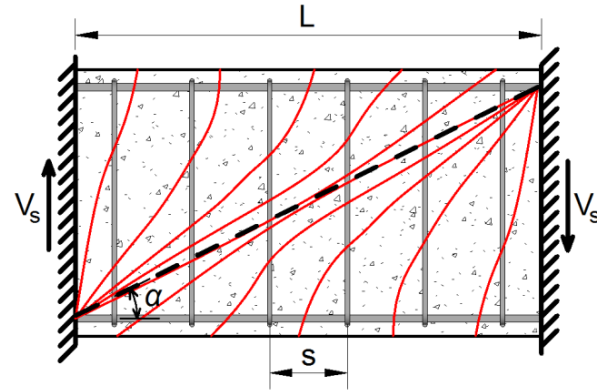
By taking only one-half of an anti-symmetric fixed-fixed beam that is represented by the two-point Gauss Truss, a statically determinant cantilever remains, which can be represented by a so-called *Single-Point Gauss Truss*. In order to confirm the numerical accuracy of the proposed single-point Gauss Truss, a convergence study of higher order numerical integration schemes was conducted. Based on recommendations of Kim and Mander (1999, 2000), the axial rigidities assigned to each truss member at the  $i^{th}$  integration point are given by:

$$(EA)_{Ti} = \omega_i E_s A_{sh} \frac{L}{s} \quad (4-1)$$

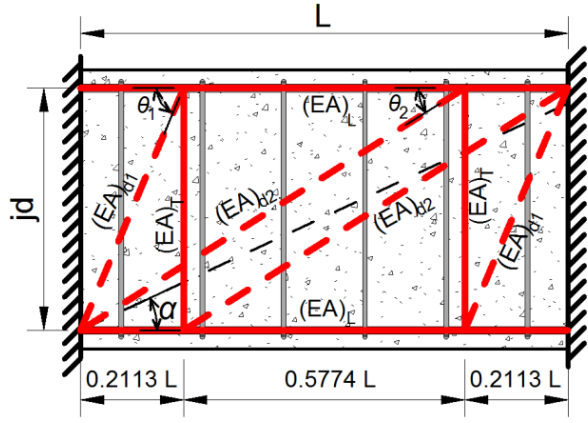
$$(EA)_{di} = \frac{0.5\omega_i}{\sqrt{x_i + \tan^2 \theta_i}} E_c A_v \quad (4-2)$$

$$(EA)_L = A_L E_s \quad (4-3)$$

in which  $(EA)_{Ti}$  = axial rigidity of the transverse reinforcement ties (where  $\omega_i$  = numerical weight factor for transverse reinforcement defined in Table 4–1,  $E_s$  = Young's Modulus for steel,  $A_{sh}$  = area of one set of stirrups,  $L$  = member length; and  $s$  = stirrup spacing);  $(EA)_{di}$  = axial rigidity of the diagonal concrete struts (where  $x_i$  = normalized coordinate of the  $i^{th}$  integration point,  $\theta_i$  = strut angle relative to longitudinal steel,  $E_c$  = Young's Modulus for concrete,  $A_v = b_w d$  is the shear area of concrete,  $b_w$  = beam width, and  $d$  = the effective depth of the beam from the extreme concrete compression fiber to the centroid of the tension steel); and



(a) Discrete representation



(b) Two-point Gauss Truss

Figure 4–1: Truss Model Idealization for a Fixed-Fixed Beam-Kim and Mander (1999).

Table 4–1: Convergence Study of Higher Order Truss Models for a Cantilever Beam.

Numerical Scheme	$i$	$x_i$	$\omega_i$	$\frac{K_{Truss}}{K_{2-point}}$
Single-Point Gauss	1	0.42265	1	1.0429
	2	0.57735	1	
Two-Point Gauss	1	0.21132	0.5	<b>1.0000</b>
	2	0.78868	0.5	
Three-Point Gauss	1	0.11270	5/18	1.0007
	2	0.50000	8/18	
	3	0.88730	5/18	
Boole's Rule	1	0.00	7/90	0.9371
	2	0.25	32/90	
	3	0.50	12/90	
	4	0.75	32/90	
	5	1.00	7/90	

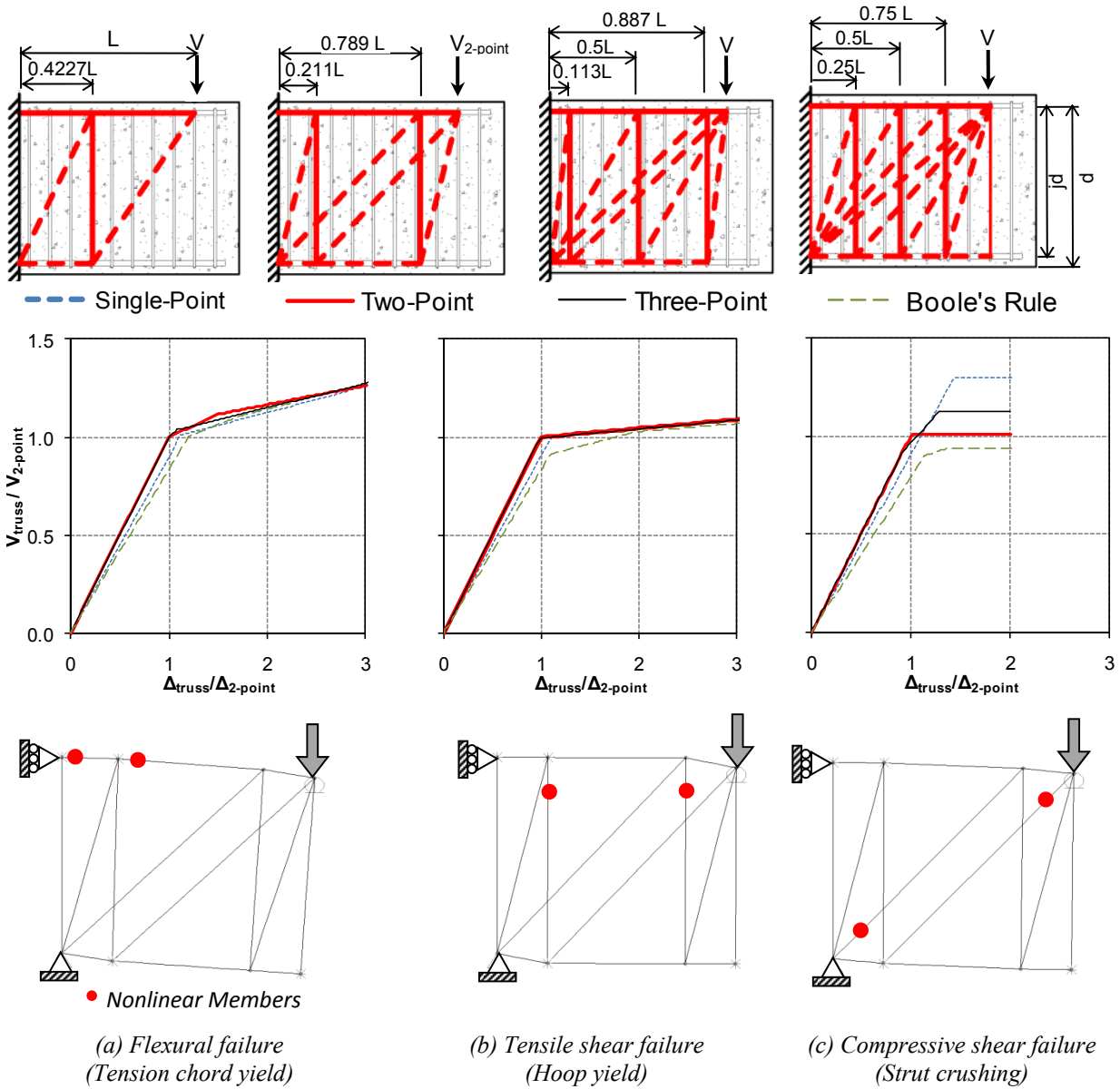
$(EA)_L$  = axial rigidity the longitudinal reinforcement ties (where  $A_L$  = is the sectional area of steel assigned to the longitudinal tension tie).

Table 4–1 presents four different numerical integration schemes that were considered in this convergence study: single, two, and three-point Gauss quadrature, and Boole’s rule. A 3 ft by 2 ft (900 x 600 mm) cantilevered beam was used as an illustrative example with a span to depth ratio of 1, and longitudinal and transverse reinforcing ratios of 0.010 and 0.003, respectively, where each integration scheme is depicted at the top of Figure 4–2. The right column of Table 4–1 presents the relative elastic shear stiffness ( $K$ ) of each truss normalized with respect to the two-point Gauss Truss. Although some variability between schemes exists, it can be concluded that any reasonable integration scheme may be used to provide a satisfactory representation of shear stiffness. However, a more in-depth study should be considered to compare the flexure-shear interaction between truss models.

Figure 4–2 shows the force-deformation response of each truss model normalized with respect to the two-point Gauss Truss solution considering the following nonlinear mechanisms: (a) flexural steel yielding; (b) transverse steel yielding; and (c) concrete strut crushing. Each truss is modeled using well-known commercial structural analysis software SAP2000 (1995), and considers a bilinear stress-strain relationship with 3 percent strain hardening stiffness for steel and an elasto-plastic response with a maximum compression stress of  $0.85f'_c$  for the concrete struts.

When nonlinear behavior is governed by longitudinal tensile steel yielding (Figure 4–2a), the post-yield force-deformation response is ductile. Despite similar yield strengths, the single-point Gauss Truss model resulted in a slightly more flexible elastic stiffness than the higher order Gauss quadrature truss models. The Boole’s truss was the most flexible of the truss models and provided slightly lower initial yield strength, but had a similar post yield response.

When nonlinear behavior is governed by transverse steel yielding (Figure 4–2b), similar stiffness results were obtained. However, the post yield stiffness was less than that with longitudinal steel yielding. This shows that yielding of the transverse reinforcement can lead to large shear deformations with small increases in applied load.



**Figure 4-2: Results of Convergence Study for Different Numerical Integration Schemes for C-STM Analysis.**

When nonlinear behavior is governed by strut crushing (Figure 4–2c), the ultimate strength had a variation up to 30 percent with the single-point truss giving the largest difference. An elasto-plastic response of concrete was used for illustrative purposes only and does not accurately model concrete crushing; hence, the response of each was stopped at a ductility of two.

In summary, for cantilever modeling, the single-point Gauss Truss is evidently a sufficiently accurate model for considering the nonlinear flexure-shear interaction relative to the higher-order truss models when the failure mechanism is controlled by longitudinal and transverse steel yielding. However, for mechanisms controlled by strut crushing, a convergence study is recommended to ensure the single-point Gauss Truss does not over-estimate the failure mechanism.

#### **4.4 MODELING ARCH ACTION**

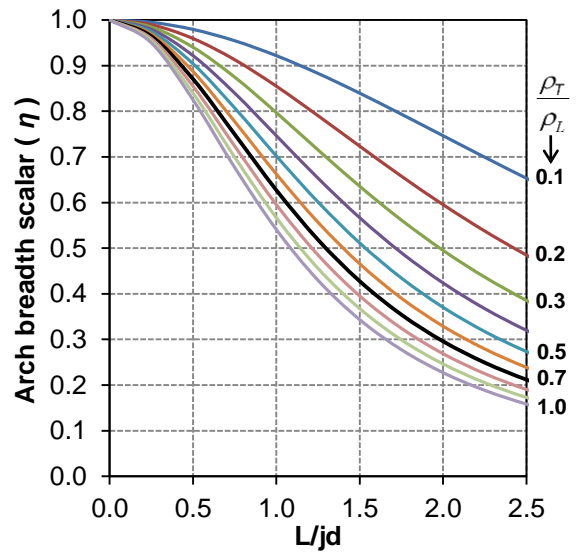
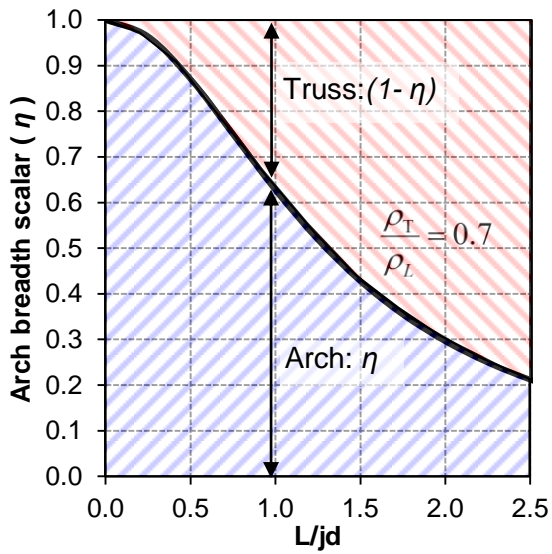
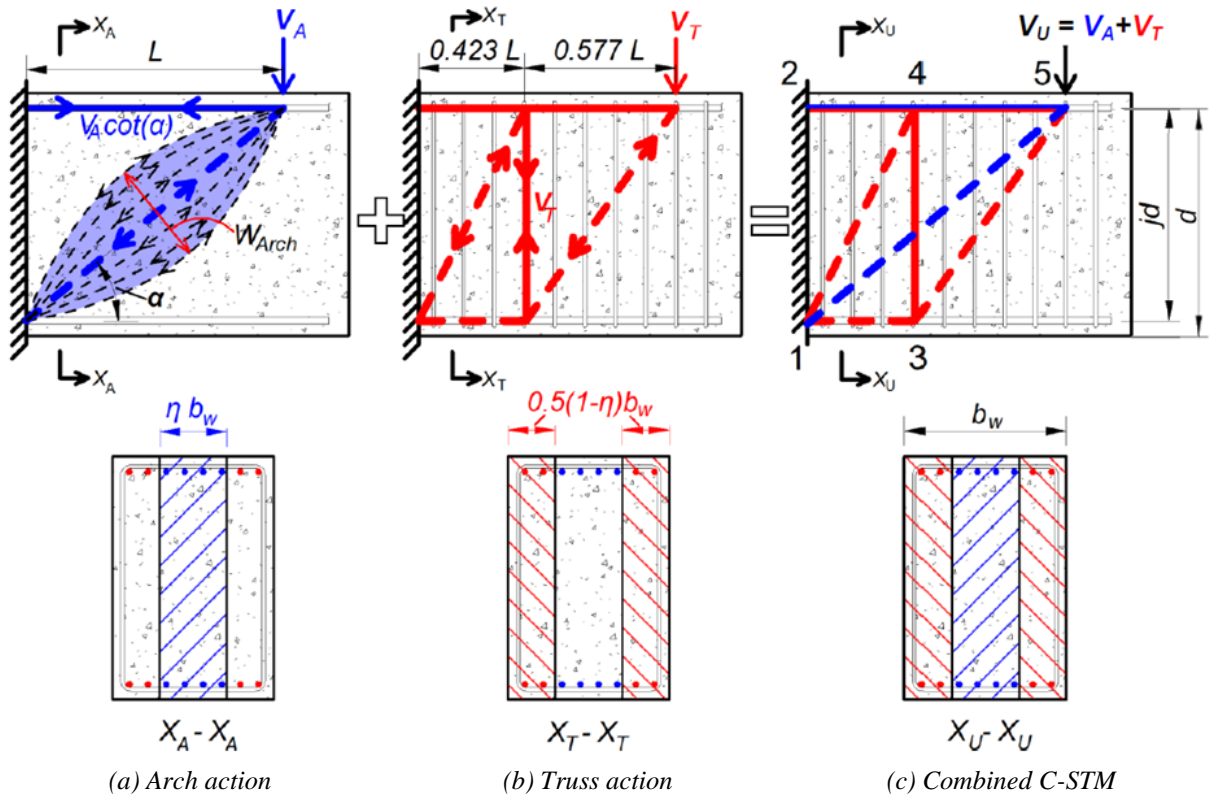
Arch action consists of a compressive stress field forming a diagonal corner-to-corner concrete strut that is tied back by the longitudinal reinforcement as shown in Figure 4–3a. The strut is assumed to have a parabolic stress distribution with a strut width that is proportional to the depth and length of the beam given below (Holden et al., 2003):

$$W_A = 0.375jd / \cos\alpha \quad (4-4)$$

This approach is similar to that proposed for coupling beams by Paulay (1971).

#### **4.5 MODELING THE COMBINED TRUSS AND ARCH ACTION**

Figure 4–3 presents the combined C-STM that is comprised of: (a) arch action acting through the center of the beam cross section; and (b) truss action acting along the outside stirrup legs. Figure 4–3c shows the amalgamated response of arch and truss action, where displacement compatibility is inherently accounted for such that the two mechanisms work in parallel to one another. A method of apportioning the relative contributions of arch and truss action is described in what follows.



**Figure 4-3: Composition of Classic Arch and Truss Action That Leads to the Overall C-STM.**

Different methods of allocating the shear resisting mechanisms have previously been proposed based on the following parameters: (i) strength (Paulay, 1971; Kim and Mander, 1999); (ii) stiffness (Zhu et al., 2003); (iii) geometry (Hwang et al., 2000); and (iv) the shear span-to-internal lever arm ratio (FIP-Commission 3, 1996). An investigation into the merits of each of these strategies was conducted, and the following conclusion was drawn: varying the proportions of arch and truss action resulted in minimal differences of the elastic force-deformation response. However, significant differences in the nonlinear response of the flexure and shear failure mechanisms were observed. Hence, to accurately model the flexure-shear interaction, it is considered necessary to apportion the arch and truss mechanisms according to the longitudinal and transverse reinforcement ratios to account for strength and  $L/jd$  to account for geometry.

An arch breadth scalar  $\eta$  is proposed to apportion the section width (shown in the cross-sections of Figure 4–3) and is defined by the following ratio:

$$\eta = \frac{V_{Arch}}{V_{Arch} + V_{Truss}} = \frac{\rho_L f_y}{\rho_L f_y + \rho_T f_{yh} j \cot^2 \alpha} \quad (4-5)$$

in which  $V_{Arch}$  = maximum shear force resisted by arch action that is proportional to the longitudinal reinforcement given below; and  $V_{Truss}$  = maximum shear force resisted by truss action that is proportional to the transverse reinforced given as:

$$V_{Arch} = f_y A_L \tan \alpha = \rho_L f_y b_w d \tan \alpha \quad (4-6a)$$

$$V_{Truss} = f_{yh} A_{sh} L / s = \rho_T f_{yh} b_w j d \cot \alpha \quad (4-6b)$$

where  $\alpha$  = the corner-to-corner diagonal angle;  $\rho_L = A_L / b_w d$  is the volumetric ratio of longitudinal steel to concrete;  $A_L$  = is the area of longitudinal reinforcement contributing to the tension tie;  $\rho_T = A_{sh} / b_w s$  is the volumetric ratio of transverse steel to concrete over one hoop spacing;  $f_y$  = yield strength of the longitudinal steel;  $f_{yh}$  = yield strength of the transverse steel; and  $j = (1 - d' / d)$  the internal lever arm coefficient.



The total shear resistance of the combined C-STM  $V_U$ , as shown in Figure 4–3c, can now be defined as:

$$V_U = V_A + V_T \quad (4-7)$$

where  $V_A$  = is the shear resistance from arch action; and  $V_T$  = is the shear resistance from truss action.

In order to maintain deformation compatibility and equilibrium between the arch and truss mechanisms, it is assumed that the section width  $b_w$  is proportioned according to the component strength as follows:

$$\frac{V_A}{V_U} = \frac{\eta b_w}{b_w} \quad ; \quad \frac{V_T}{V_U} = \frac{(1-\eta)b_w}{b_w} \quad (4-8)$$

where  $\eta b_w$  = the arch breadth, and  $(1-\eta)b_w$  = the truss breadth as shown in the cross sections of Figure 4–3a and b, respectively.

Figure 4–3d and e illustrate the results of the arch breadth scalar  $\eta$  (Eq. 4–5) when plotted against  $L/jd$  with varying ratios of transverse to longitudinal reinforcement. As one might intuitively expect, this relationship shows that arch action is more prominent in beams with smaller  $L/jd$  and  $\rho_T/\rho_L$  ratios, while truss action has more of an effect in beams with larger  $L/jd$  and  $\rho_T/\rho_L$  ratios. Others have made similar conclusions (Hsu, 1996).

#### 4.6 STRESS AND STRAIN TRANSFORMATION FOR FLEXURAL EQUIVALENCE

A primary difficulty associated with truss modeling approaches is the limitation of selecting a single truss model geometry that captures the full elastic and inelastic force-deformation response. For doubly reinforced sections, it is proposed that the longitudinal C-STM flexural chords (members 1-3 [compression] and 2-4-5 [tension] in Figure 4–3c) be aligned with the respective compression steel centroids so that the internal lever arm is represented as  $jd = d - d'$ , where  $d$  and  $d'$  are the respective centroids of the tension and compression steel. A similar

approach was used and validated by Kim and Mander (1999, 2000) in order to incorporate cyclic behavior. However, because the centroids of the steel compression force ( $C_s$ ) and the concrete compression force ( $C_c$ ) may not coincide, it is necessary to transform the concrete constitutive material properties accordingly so that the transposition of the concrete element force ( $C_c$ ) will provide a similar moment in order to satisfy the sectional moment capacity throughout the analysis.

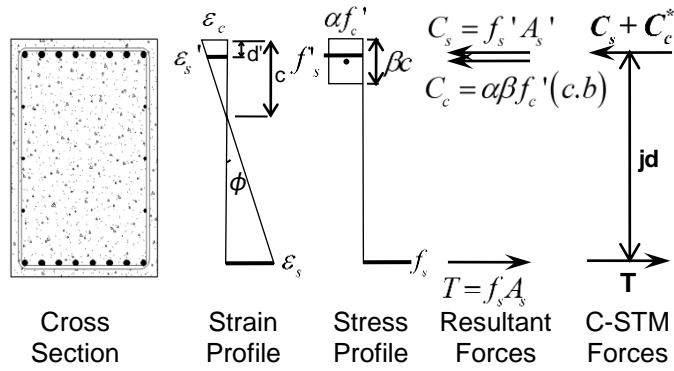
Historically, the truss geometry for SAT models has been mostly based on an elastic stress field analysis and typically ignores the presence of compression steel (Hwang et al., 2000; Drucker, 1961; Thürlimann et al., 1983). Other researchers contend that the use of elastic stress analysis is inappropriate when assessing the ultimate limit state of a structure due to highly nonlinear development of strains associated with D-regions (MacGregor, 1992; Salem and Maekawa, 2006; Yun, 2000; Sritharan and Ingham, 2003). The proposed transformation theory (described below) provides a method that accounts for both compression steel and the nonlinear behavior of concrete compression chord element in accordance with standard stress-block analysis that is incorporated over the entire range of loading. Figure 4–4a illustrates a standard flexural stress block analysis performed on a doubly reinforced concrete section, assuming plane sections remain plane purely for the purposes of defining the concrete compression force, where the concrete tensile strength is assumed as zero. The neutral axis depth  $c$  can be defined such that  $c = kd$ , where  $k$  is the elastic compression zone coefficient given by Park and Paulay (1975) as:

$$k = \sqrt{(\rho_L + \rho'_L)^2 n^2 + 2(\rho_L + \rho'_L d'/d)n} - (\rho_L + \rho'_L)n \quad (4-9 \text{ a})$$

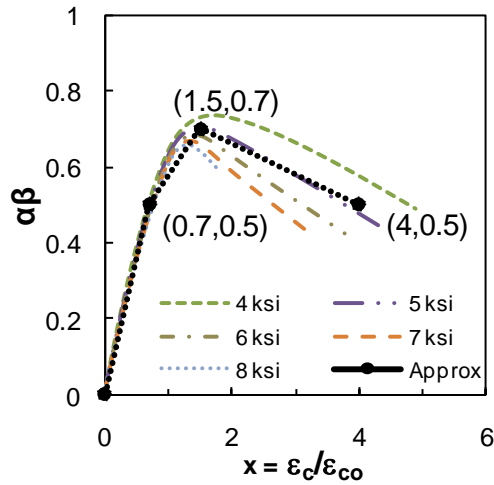
For column members an additional modification is made to allow for the axial force given by Eq. (4–9b) (Arnold, 2004).

$$k = \sqrt{\left(\rho_L + \rho'_L + \left(\frac{P}{f_c'bd}\right)\left(\frac{f_c'}{f_s}\right)\right)^2 n^2 + 2\left(\rho_L + \rho'_L\left(\frac{d'}{d}\right) + \left(\frac{P}{f_c'bd}\right)\left(\frac{f_c'}{f_s}\right)\right)n} - \left(\rho_L + \rho'_L + \left(\frac{P}{f_c'bd}\right)\left(\frac{f_c'}{f_s}\right)\right)n \quad (4-9 \text{ b})$$

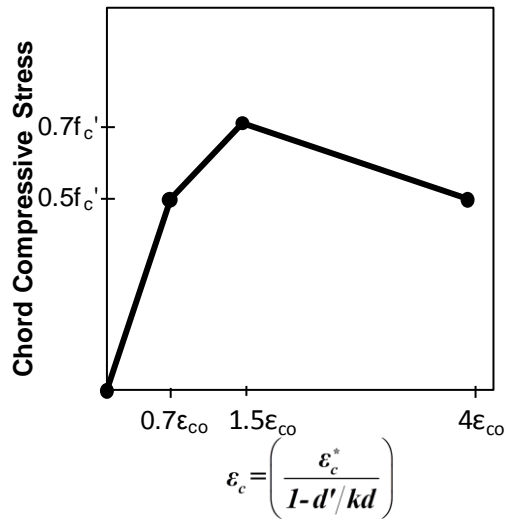
where  $d$  = the effective depth of the beam from the extreme concrete compression fiber to the centroid of the tension steel;  $d'$  = the depth from the extreme compression fiber to the centroid of



(a) Doubly reinforced stress block analysis



(b) Stress block parameters (Karthik and Mander, 2011)



(c) Key stress-strain parameters

Figure 4-4: Constitutive Stress-Strain Relationship for Compression Chord Elements.

the compression reinforcement;  $\rho$  = the ratio of tension reinforcement;  $\rho'$  = the ratio of compression reinforcement;  $n$  = the modular ratio of steel to concrete;  $b$  = the section width;  $f_c'$  = concrete compression strength; and  $P$  = axial force plus prestressing force (if any).

Because the C-STM compression chord member is located at the steel centroid, a transformation of the concrete stress block force  $C_c$  is required to convert it to an equivalent C-STM force that coincides with C-STM compression chord member. Section equilibrium requires:

$$P = (C_s + C_c^*) - T \quad (4-10)$$

in which  $P$  = the applied axial load ( $P = 0$  for beams);  $T = A_s E_s \varepsilon_s$  (where  $A_s$  = representative area of longitudinal tension steel, and  $\varepsilon_s$  = tensile steel strain);  $C_s = A'_s E_s \varepsilon'_s$  (where  $A'_s$  = representative area of longitudinal compression steel, and  $\varepsilon'_s$  = compression steel strain); and  $C_c^*$  = transformed concrete force discussed below.

The effective concrete strain  $\varepsilon_c^*$  measured by the C-STM chord member can be defined in terms of the extreme compressive concrete strain using the strain compatibility relationships:

$$\varepsilon_c^* = \varepsilon'_s = \varepsilon_c \left( 1 - \frac{d'}{kd} \right) \quad (4-11)$$

Hence, the concrete compression force can be expressed in terms of equivalent concrete stress block and related to  $\varepsilon'_s = \varepsilon_c^*$  as follows:

$$C_c = \alpha \beta f_c' (kd \cdot b) = \varepsilon_c^* \psi E_c A_c \quad (4-12)$$

in which  $\alpha \beta$  = the stress block parameters used to define the equivalent stress block, where  $\alpha$  = effective average concrete stress ratio and  $\beta$  = effective stress block depth factor;  $f_c'$  = concrete strength;  $\varepsilon_c^*$  = C-STM concrete compression chord strain;  $\psi$  = a compatibility correction scalar; and  $A_c = kd b$  is the area assigned to the concrete chord element.

Rearranging Eq. (4-12) and substituting Eq. (4-11), the compatibility correction scalar can be expressed as:

$$\psi = \frac{\alpha\beta f'_c}{\varepsilon_c^* E_c} = \frac{\alpha\beta}{(1-d'/kd)xn} \quad (4-13)$$

in which  $x = \varepsilon_c / \varepsilon_{co}$  is the normalized concrete compression strain at the extreme compression fiber;  $\varepsilon_{co} = 0.002$  for unconfined concrete; and  $n = E_c \varepsilon_{co} / f'_c$  (where  $E_c = 60000\sqrt{f'_c(\text{psi})} = 5000\sqrt{f'_c(\text{MPa})}$  is the initial tangent modulus) (Mander et al., 1988).

The only remaining unknown variables in Eq. (4-13) are  $\alpha\beta$  and the nonlinear strain,  $x$ . The nonlinear relationship between these two stress block variables is shown in Figure 4-4b (Karthik and Mander, 2011), where a tri-linear relationship is used to approximate the stress block parameters. The key stress-strain parameters for obtaining the concrete chord members constitutive relationship can be obtained through a direct axis transformation as shown in Figure 4-4c, where stress is a function of  $\alpha\beta f'_c$ , and the strain is a function of  $x\varepsilon_{co}$ , as derived from Eq. (4-13). The transformed constitutive relation used for concrete chord members is then derived by substituting appropriate values of  $f'_c$  and  $(1-d'/kd)$  into Figure 4-4c. An application of this is presented later.

A similar analysis for singly reinforced beams may be applied where the location of the compression chord member can be defined as follows. For members that do not exceed the elastic limit in the concrete compression stress block, the internal lever arm may be defined such that  $jd = d - kd/3$  (where  $k$  = the elastic compression zone coefficient defined in Eq. (4-9)). For members that do exceed the elastic stresses, a more appropriate representation of the internal lever arm may be defined using an ultimate limit state analysis such that  $jd = d - \beta_1 c / 2$  (where  $\beta_1$  is the standard code-based stress block factor, and  $c$  is the neutral axis depth calculated by satisfying section equilibrium).

## 4.7 C-STM GEOMETRY AND AXIAL RIGIDITY ASSIGNMENTS

The C-STM shown in Figure 4–3c can be adapted for any deep beam or disturbed region and modeled using structural analysis software. Each member in the C-STM is comprised of two elements that model the individual behavior of steel and concrete in that member. The two elements are constrained together in order to give the combined steel-concrete response. The C-STM requires the following parameters to be defined in order to model the constitutive behavior of truss members: (i) truss geometry to define the member force; and (ii) axial rigidities of the steel and concrete elements to define elastic deformations.

### 4.7.1 Truss Geometry

As previously discussed, the primary difficulty associated with accurate truss modeling is the limitation of selecting a single truss model geometry that captures the force-deformation over a range of both elastic and inelastic response. The truss geometry is defined by first locating the node coordinates for the compression and tension chord members. This is done in accordance with the foregoing section, where the location of the compression chord member varies for doubly and singly reinforced sections.

The horizontal coordinates of the boundary nodes are either defined by: (i) an applied load/bearing support (i.e., Node 5 in Figure 4–3c is defined by the centroid of the applied load); or (ii) at the intersecting lines of thrust from the beam and column members (i.e., Node 1 in Figure 4–3c is defined at the intersection of the compression steel in the beam and supporting column represented as a fixed boundary). The transverse tension ties in the truss mechanism are then located according to the selected numerical truss as defined in Figure 4–2 (i.e., Nodes 3 and 4 in Figure 4–3c are defined by single-point Gauss quadrature).

### 4.7.2 Axial Rigidity

For each C-STM member, the expected composite steel-concrete response is modeled using separate elements for steel and concrete, respectively. Each element is assigned elastic axial rigidities as specified in Table 4–2, where the member numbers refer to Figure 4–3c. Some comments on Table 4–2 follow.

**Table 4–2: Elastic Truss Member Axial Rigidities.**

Member	Steel		Concrete		Comments
	$E$	$A$	$E$	$A$	
2–4 4–5	$E_s$	$A_s$	$E_c$	$b.kd$	Tension Chord
1–3	$E_s$	$A_s'$	$\psi_E E_c$	$b.kd$	* Compression Chord
3–4	$E_s$	$N_h A_{sh}$	$E_c$	$(4c + 2d_h) N_h s$	<sup>†</sup> Active Hoop steel including tension stiffening effect
1–5	–	–	$E_c$	$\frac{0.375 \eta b_w j d}{\cos \alpha}$	Concrete Strut in Arch Mechanism
1–4	–	–	$E_c$	$\frac{0.5(1-\eta)b_w j d}{\sqrt{0.423 + \tan^2 \alpha}}$	Concrete Strut in Truss Mechanism
3–5	–	–	$E_c$	$\frac{0.5(1-\eta)b_w j d}{\sqrt{0.577 + \tan^2 \alpha}}$	Concrete Strut in Truss Mechanism

$$*\psi_E = \text{strain compatibility coefficient} = \frac{\sqrt{f'_c(\text{psi})}}{168(1-d'/kd)} = \frac{\sqrt{f'_c(\text{MPa})}}{14(1-d'/kd)}$$

In lieu of a more precise analysis it is recommended that  $\psi_E = 0.6$

<sup>†</sup> $N_h = \text{int}[L/s-1]$  is the integer part of active hoops in truss mechanism

For tension chord members (row 1 of Table 4–2), the presence of longitudinal distribution steel along the web may be accounted for by using an effective steel area:

$$A_s^* = \frac{\bar{A}_s \bar{d}}{d} \quad (4-14)$$

where  $\bar{A}_s$  = the total area of longitudinal plus distribution reinforcement acting in tension;  $\bar{d}$  = the effective depth to the centroid of  $\bar{A}_s$ ; and  $d$  = section depth to the longitudinal tension reinforcement.

For tension and compression chord members (row 1 and 2 of Table 4–2), the concrete area is assumed to be the same so that cyclic effects can to be accounted for, if necessary.

For transverse truss members (row 3 of Table 4–2), the total area of transverse reinforcement is evaluated as the number or hoops actively participating in the truss mechanism

$N_h$ , where  $N_h = \text{int}[L/s - 1]$  is the number of hoopsets. Also, the effective tension area of concrete for the transverse tie is taken as twice the cover depth ( $c_c$ ) plus the stirrup hoop diameter ( $d_h$ ), multiplied over the length of actively participating hoops ( $N_h s$ ), thus defining the area of concrete surrounding the stirrup legs.

For the concrete arch member (row 4 of Table 4–2), the strut width is given by Eq. (4–4) and is multiplied by the apportioned arch strut width  $\eta b_w$  to obtain the strut area.

For the concrete strut members in the truss mechanism (row 5 and 6 of Table 4–2), the strut width is defined using Eq. (4–2) (Kim and Mander, 1999, 2000), where the normalized coordinate of the  $i^{\text{th}}$  integration point  $x_i$  is taken as 0.423 and 0.577 (in accordance with Table 4–1) for the concrete elements 1–4 and 3–5, respectively. These are multiplied by the apportioned truss strut width  $(1-\eta)b_w$  to obtain the respective strut areas.

## **4.8 ELEMENT CONSTITUTIVE MATERIAL RELATIONS**

The elastic parameters of the C-STM model are defined by the truss geometry and axial rigidities. In order to define the strength of each element, nonlinear constitutive material relationships for cracked reinforced concrete are applied as follows.

### **4.8.1 Reinforcing Steel**

For simplicity, the reinforcing steel is approximated using a bi-linear stress-strain relationship with 3 percent strain hardening beyond yielding. Where necessary, a more accurate material model may be applied in order to allow for bond slip or where a bilinear slope does not provide suitable accuracy.

### **4.8.2 Diagonal Concrete Struts**

From the works of Vecchio and Collins (1986), Mau and Hsu (1987), and Hsu and Zhang (1997), it is well-known that the compression strength of diagonal concrete struts in reinforced concrete beams and panel elements is reduced as a result of the tensile strain acting orthogonal to the compression strain. This concrete softening phenomenon was investigated by Collins and his



research group; one rendition of their work is modeled by the following relationship (Vecchio and Collins, 1986):

$$\zeta = \frac{f_{2,\max}}{f'_c} = \frac{1}{0.8 + 0.34 \left| \frac{\varepsilon_1}{\varepsilon_{co}} \right|} \leq 1.0 \quad (4-15)$$

where  $\zeta$  = the softening coefficient;  $f_{2,\max}$  = the “softened” concrete strength;  $\varepsilon_{co}$  = the principal compression strain typically taken as 0.002; and  $\varepsilon_1$  = the principal tensile strain acting perpendicular to compression strut.

This relationship is typically incorporated in each step of a hand analysis or directly embedded into a nonlinear Finite Element Modeling (FEM) formulation where the softening coefficient is continuously updated to satisfy equilibrium (Rots et al., 1985). However, when applying this in commercial structural analysis software (such as SAP2000, 1995), the user is restricted to the initial input parameters and hence a more direct approximation is required. Accordingly, Eq. (4-15) can be conveniently recast as:

$$\zeta = \frac{1}{1 + \left\langle \frac{\varepsilon_1 - 0.0012}{3 \varepsilon_{co}} \right\rangle} \quad (4-16)$$

where  $\langle \bullet \rangle$  are Macaulay brackets, and the value 0.0012 can be thought of as a fracture strain such that only when  $\varepsilon_1 > 0.0012$  the concrete softens.

The strain  $\varepsilon_1$  can be assessed from dummy strain elements (with  $EA = I$ ) perpendicular to the diagonal concrete struts as described later. An alternate to Eq. (4-16), based on the compression softening data obtained from panel test results presented in Vecchio (2000), is given by:

$$\zeta = \frac{1}{1 + 0.25 \frac{\varepsilon_1}{\varepsilon_2}} \quad (4-17)$$

where  $\varepsilon_2$  is the strain in the diagonal member. However, it is noted that the softened model for concrete is somewhat sensitive to  $\varepsilon_1$ , and the value of  $\varepsilon_1$  is dependent on where the transverse strain member is placed relative to the diagonal concrete element.

The softened constitutive relations for the diagonal concrete struts can now be defined by modifying the Mander et al. (1988) model to reduce the concrete stress and strain given by:

$$f_c = \frac{\zeta f'_c x^r}{r-1+x^r} \quad (4-18)$$

in which  $\zeta f'_c$  = softened concrete stress;  $x = \varepsilon_c / (\zeta \varepsilon_{co})$  is the softened concrete strain coefficient (where  $\varepsilon_{co} = 0.002$ ); and  $r = E_c / (E_c - E_{sec})$  (where  $E_{sec} = f'_c / \varepsilon_{co}$ ). The softened concrete stress-strain relationship is shown in Figure 4-5 by the dotted line and approximated as a linear response in accordance with Vecchio and Collins (1993).

### 4.8.3 Concrete Tensile Strength

The contribution provided by the concrete tensile strength, commonly referred to as “tension stiffening” (Vecchio and Collins, 1986), is typically ignored in many force-based SAT models (MacGregor, 1992; Collins and Mitchell, 1991; Collins, 1978; Hwang et al., 2000). By assuming strain compatibility between concrete and steel, the overall member tensile force is simply the summation of the steel and concrete forces for a given strain (Collins and Mitchell, 1991; Vecchio and Collins, 1986). Thus the combined steel and concrete elements that make up the tension members 2-4-5, and 3-4 in Figure 4-3c, intrinsically provide the overall tension stiffened response.

Tension stiffening models vary for different situations and structures; hence the following three approaches are recommended for the C-STM:

- For longitudinal and transverse reinforcing steel bars, tension stiffening is modeled by considering a fracture energy method (Pettersson, 1980) as shown in Figure 4-6. The fracture energy  $G_f$  is defined as the energy required to create one unit area of cracking in

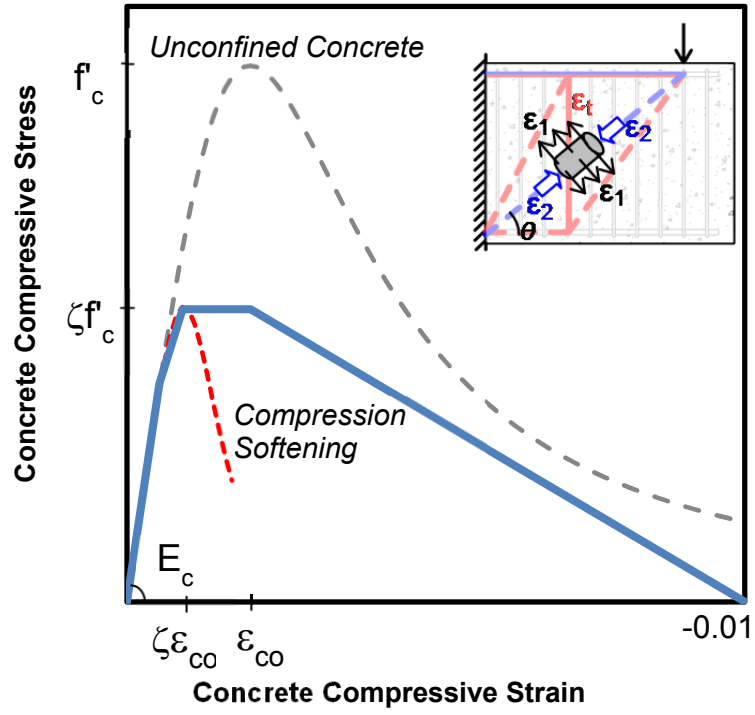


Figure 4-5: Diagonal Concrete Web Elements.

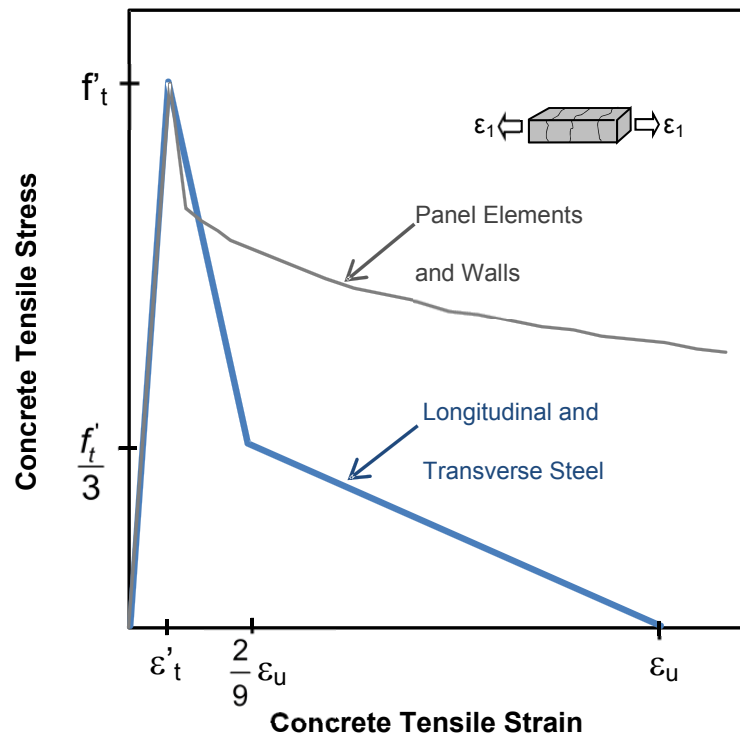


Figure 4-6: Concrete Tension Stiffening Ties.

which  $G_f = h g_f$ , where  $h = 3d_a$  is the crack band width taken as three aggregate diameters, and  $g_f =$  the area under the stress-strain softening diagram. The stress-strain relationship is defined using a tri-linear stress-strain relationship given by:

$$f_t = E_c \varepsilon_t \quad \text{for} \quad \varepsilon_t \leq \varepsilon_t' \quad (4-19a)$$

$$f_t = \frac{f_t'}{3} \quad \text{for} \quad \varepsilon_t = \frac{2}{3} \varepsilon_u \quad (4-19b)$$

$$f_t = 0 \quad \text{for} \quad \varepsilon_t = \varepsilon_u \quad (4-19c)$$

in which  $f_t =$  average concrete tensile stress;  $\varepsilon_t =$  average concrete tensile strain;  $\varepsilon_t' =$  strain at peak tensile stress;  $f_t' = 4\sqrt{f_c'}$  (psi) is typically used to define the concrete tensile strength (Collins and Mitchell, 1991); and  $\varepsilon_u =$  ultimate tensile strain where stress can no longer be transferred given below.

$$\varepsilon_u = \frac{18 G_f}{5 f_t' h} \quad (4-20)$$

Based on experimental results, Petersson (1980) noted that the fracture energy  $G_f$  for normal-weight concrete typically ranges from  $0.343 - 0.571$  (lbs/in) =  $60 - 100$  (N/m). Alternatively, for simplicity,  $\varepsilon_u$  is assumed as the steel yield strain in this work.

- In the case of panel and wall structures with a dense network of reinforcing steel, the descending branch model proposed by Vecchio and Collins (1986) may be more appropriate as shown in Figure 4-6. That is:

$$f_t = \frac{\alpha_1 \alpha_2 f_t'}{1 + \sqrt{500 \varepsilon_t}} \quad \text{for} \quad \varepsilon_t > \varepsilon_t' \quad (4-21)$$

where  $\alpha_1$  and  $\alpha_2 =$  factors to account for bond characteristics of reinforcement.

- For structures with experimental results, parameterized models can be applied to model the stress-strain relations used for concrete tension stiffening.

#### 4.8.4 Concrete Compression Chord Members

As previously discussed, the transformed constitutive relation used for concrete chord members is derived by substituting appropriate values of  $f'_c$  and  $(1-d'/kd)$  into Figure 4-4c to obtain the stress-strain relationship of the concrete compression chord member.

#### 4.8.5 Modified Material Properties to Account for ASR/DEF

The effects of ASR/DEF on the structure can be taken into account in the C-STM analysis technique by modifying the material properties based on observations and experimental data. Based on visual inspection and discretion of the field engineer, the extent of damage on the structure can be categorized into three classes: *slight*, *moderate*, and *heavy* damage. Based on this assessment the following material properties should be adopted in the analysis. In lieu of more definitive empirical data, these values have been assumed based on the observations made to date in this experimental program presented in sections 5.5 through 5.7.

- *Diagonal truss concrete:*

The concrete strength in the diagonal truss members have to be factored to account for the damages in cover concrete due to deterioration of concrete by ASR/DEF effects. The modified concrete strength is given as:

$$f'_{cASR} = \lambda f'_c \quad (4-22)$$

where  $\lambda$  = the strength reduction factor defined according to the extent of damage observed. From the deterioration data that is presented later in section 5.5, the average surface concrete strains perpendicular to the beam-column joint ( $\epsilon_1$ ) for slight, moderate, and heavy (inferred) damage is observed to be around 0.0025, 0.004, and 0.006 (extrapolated), respectively. Substituting the values for ( $\epsilon_1$ ) in Eq. (4-16) gives the strength reduction factors  $\lambda$  as follows:

- slight damage  $\lambda = 0.85$
- moderate damage  $\lambda = 0.70$
- heavy damage  $\lambda = 0.60^*$

\*Caveat: This value is assessed based on incomplete trends in data at the time of writing (2012). Results of experiments currently in progress are expected in 2014 and will provide a final value.

- *Assess concrete core confinement and modify the concrete properties:*

ASR/DEF effect causes the concrete to swell. The swelling of core concrete is constrained by longitudinal and transverse reinforcement, which effectively confines the core concrete. To account for this effect, the confinement ratio ( $K_{cc} = f'_{cc} / f'_{co}$  where  $f'_{co}$  = in situ concrete strength) has to be determined to obtain the confined concrete stress ( $f'_{cc}$ ). The procedure to evaluate the confinement ratio is as described below (Mander et al., 1988).

The effective confining stress in the x and y direction  $f'_{lx}$  and  $f'_{ly}$  are given as:

$$\begin{aligned} f'_{lx} &= k_e \rho_x f_y \\ f'_{ly} &= k_e \rho_y f_y \end{aligned} \quad (4-23)$$

where  $k_e$  = confinement effectiveness coefficient (defined below);  $f_y$  = yield stress of reinforcing steel;  $\rho_x$  and  $\rho_y$  are the volumetric ratio of lateral confining steel parallel to the x and y axis, respectively, given as:

$$\begin{aligned} \rho_x &= \frac{A_{sx}}{sd_c} \\ \rho_y &= \frac{A_{sy}}{sb_c} \end{aligned} \quad (4-24)$$

in which  $A_{sx}$  and  $A_{sy}$  = total area of lateral reinforcement parallel to the x and y axes, respectively;  $s$  = spacing of hoop sets;  $d_c$  = core dimension in y direction; and  $b_c$  = core dimension in the x direction. The confinement effectiveness coefficient ( $k_e$ ) is the ratio of area of effectively confined core concrete ( $A_e$ ) to the concrete core area of the section ( $A_{cc}$ ).

$$k_e = \frac{A_e}{A_{cc}} \quad (4-25)$$

In rectangular sections the transverse steel bows outward between the longitudinal bars; hence, arching action will occur between the longitudinal bars that are fully supported in position by an angle bend in the transverse steel as shown in Figure 4-7. The arching action is assumed to take the form of a second-degree parabola with an initial tangent slope of 45°. The area of one such parabola is given by  $(w_i')^2 / 6$ , where  $w_i'$  is the  $i^{th}$  clear transverse spacing between longitudinal bars in which arching action of concrete develops. In the case of a lightly confined rectangular section, the parameter  $w'$  along the y axis is taken as the depth of the neutral axis ( $kd$ ) minus the distance from the extreme compression fiber to the longitudinal bar. The net area of ineffectively confined concrete for the  $n$  longitudinal bars supported in the corners of the bent transverse hoops is given by:

$$\sum_{i=1}^n (w_i')^2 / 6 \quad (4-26)$$

The total effectively confined core concrete area is defined as:

$$A_e = \left[ b_c d_c - \sum_{i=1}^n (w_i')^2 / 6 \right] \left( 1 - 0.5 \frac{s'}{b_c} \right) \left( 1 - 0.5 \frac{s'}{d_c} \right) \quad (4-27)$$

in which  $s'$  = clear longitudinal spacing between hoop bars in which arching action of concrete develops.

The concrete core area of the rectangular section is given by:

$$A_{cc} = b_c d_c (1 - \rho_{cc}) \quad (4-28)$$

where  $\rho_{cc}$  = volumetric ratio of longitudinal steel in the confined core. Note that the term  $(1 - \rho_{cc})$  in the above equation effectively removes the presence of longitudinal bars from the confined concrete area. From these, the confinement effectiveness coefficient ( $k_e$ ) can be determined from Eq. (4-25).

The ratios  $f'_{lx} / f'_{co}$  and  $f'_{ly} / f'_{co}$  are determined, the smaller of these ratios is taken as  $f'_{l1} / f'_{co}$ , and the larger is taken as  $f'_{l2} / f'_{co}$ . The confinement ratio ( $K_{cc} = f'_{cc} / f'_{co}$ ) is determined from the chart shown in Figure 4-8. Thus, the confined concrete stress is then determined as  $f'_{cc} = K_{cc} f'_{co}$ , where  $f'_{co}$  = in situ concrete strength.

The strain ( $\varepsilon_{cc}$ ) corresponding to the maximum confined concrete stress ( $f'_{cc}$ ) is defined as:

$$\varepsilon_{cc} = \varepsilon_{co} (1 + 5(K_{cc} - 1)) \quad (4-29)$$

in which  $\varepsilon_{co}$  = the strain corresponding to the unconfined concrete strength (usually  $\varepsilon_{co} = 0.002$ ).

- *Prestress effects in longitudinal bars and hoops:*

The constraint offered by longitudinal reinforcement and transverse hoops to the swelling of core concrete puts tensile strains on the reinforcing steel. This effectively puts the longitudinal and transverse reinforcement in a state of prestress.

The prestressing forces on the reinforcement can be evaluated from the prestressing stresses, which depend on the extent of damage (slight, moderate, or heavy) due to ASR/DEF effects. Based on experimental observations (presented later in section 5.7) the



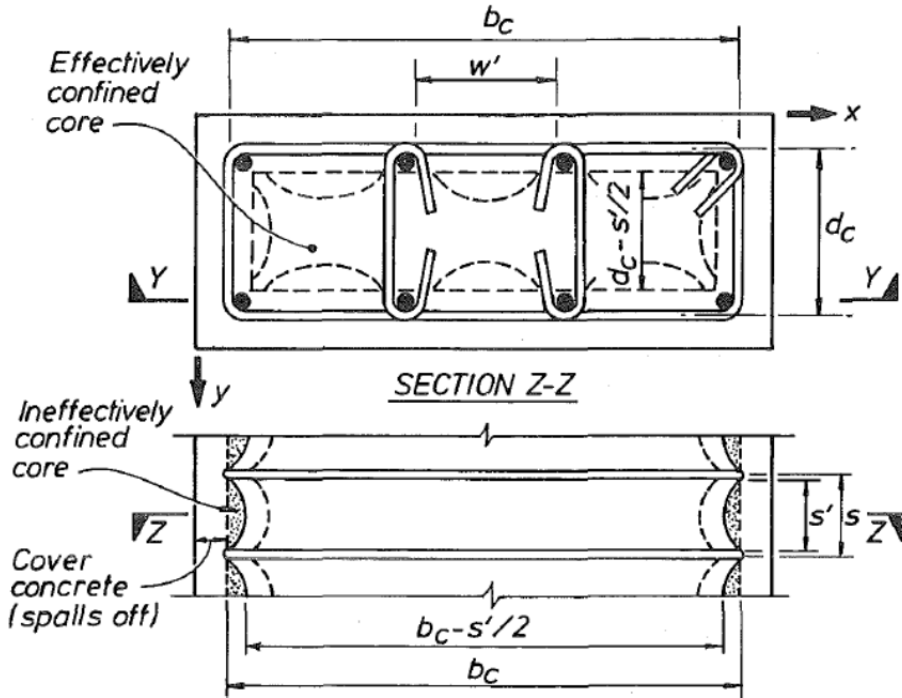


Figure 4-7: Assumed Arching Mechanism between Hoops for Rectangular Sections (Mander et al., 1988).

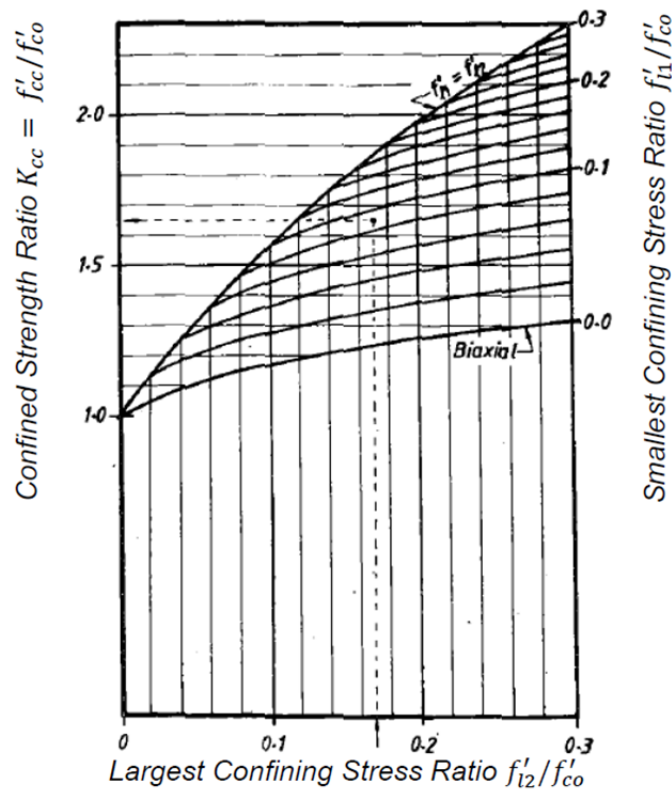


Figure 4-8: Confined Strength Determination from Lateral Confining Stresses for Rectangular Sections (Mander et al., 1988).

following recommendations are made for prestressing stresses ( $f_{ps}$ ) in longitudinal reinforcement:

- slight damage  $f_{ps} = 0.3 f_y$
- moderate damage  $f_{ps} = 0.5 f_y$
- heavy damage  $f_{ps} = 0.8 f_y^*$

in which  $f_y$  = yield stress of longitudinal reinforcement.

Recommendations for prestressing stresses in hoops based on experimental observations presented in section 5.7 are:

- slight damage  $f_{ps} = 0.5 f_{yh}$
- moderate damage  $f_{ps} = 1.0 f_{yh}$
- heavy damage  $f_{ps} = 1.1 f_{yh}^*$

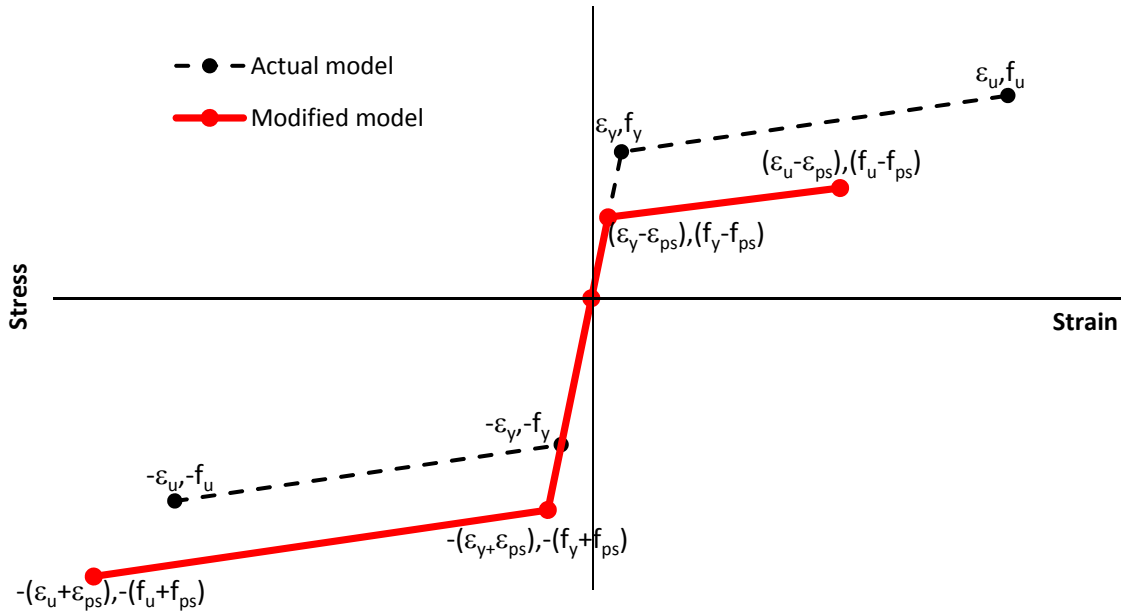
in which  $f_{yh}$  = yield stress of transverse hoops.

\*Caveat: This value is assessed based on incomplete trends in data at the time of writing (2012). Results of experiments currently in progress are expected in 2014 and will provide a final value.

Appropriate modifications to the stress-strain behavior of the reinforcing steel have to be made to account for the prestressing effects. The modified stress-strain relation of steel is shown in Figure 4–9 in which  $\epsilon_{ps}$  = prestrain corresponding to prestressing stress ( $f_{ps}$ ).

#### 4.9 ULTIMATE STRENGTH AND SOFTENING OF CONSTITUTIVE RELATIONS

The exact failure mechanism for deep beams or D-regions is difficult to define due to unknown (a priori) hierarchy of failure mechanisms, particularly given the fact that shear failure alone can be of four types: diagonal tension, web crushing, nodal failure, or sliding shear. In reality the type of failure is heavily dependent on the member geometry and reinforcement detailing and is often a combination of events that lead to the formation of the final collapse mechanism. In the C-STM, steel yielding, concrete crushing, and concrete softening are intrinsically accounted for through the material constitutive relationships previously described. However a more thorough



**Figure 4-9: Modified Stress-Strain Model for Steel to Account for Prestressing Effects due to ASR/DEF.**

post analysis assessment may be required in order to assess other possible critical failure mechanisms.

#### **4.9.1 SAT Strength Checks**

SAT modeling predisposes itself to defining failure as either: yielding of reinforcing ties, crushing of a strut, anchorage failure of reinforcing ties, or nodal failure. The member forces in the C-STM can be used to check that the force does not exceed the strength defined using conventional SAT design procedures for anchorage and nodal failures.

#### **4.10 COMPUTATIONAL IMPLEMENTATION**

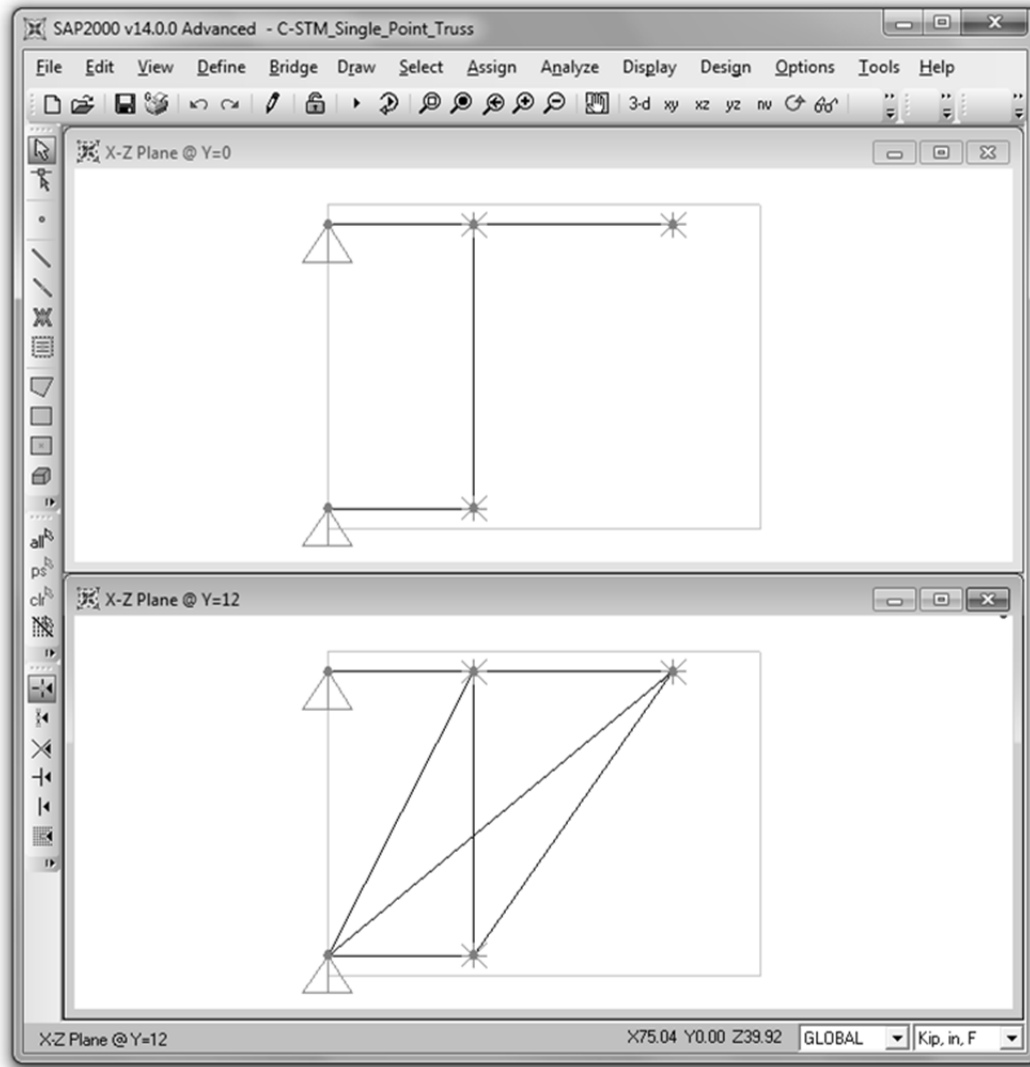
The computational analysis of the C-STM described in the above sections can be implemented using structural analysis software and carried out in 6 steps as discussed in what follows.

##### *Step 1: Assign node coordinates*

For doubly reinforced sections, the longitudinal chord members (members 2–4–5 tension and 1-3 compression of Figure 4–3c) are defined at the respective longitudinal steel centroids. The horizontal coordinates of the boundary nodes are either defined by: *(i)* an applied load/bearing support (i.e., Node 5 in Figure 4–3c is defined by the centroid of the applied load); or *(ii)* at the intersecting lines of thrust from the beam and column members (i.e., Node 1 in Figure 4–3c is defined at the intersection of the compression steel in the beam and supporting column represented as a fixed boundary). The transverse tension ties in the truss mechanism are then located according to the selected numerical truss scheme (i.e., Nodes 3 and 4 in Figure 4–3c are defined by single-point Gauss quadrature).

##### *Step 2: Assign steel and concrete elements*

The steel and concrete elements of the C-STM can be modeled using separate trusses with nodes constrained together to give the combined steel-concrete member response. This is most easily simulated by duplicating the assigned nodes in the out-of-plane axis to form two separate trusses, and constraining the degrees of freedom for each of the duplicate nodes. Steel and concrete elements are then drawn with pinned-end connections between the appropriate node points as shown in Figure 4–10.



**Figure 4–10: SAP2000 Screenshot: Steel Truss (Top); Concrete Truss (Bottom).**

The expressions presented in Table 4–2 are used to define the stiffness and axial area assignments for each steel and concrete element of the C-STM model. The arch breadth scalar  $\eta$  is used to apportion the contributions of the arch and truss actions, defined as a function of the longitudinal and transverse reinforcement and members' span-to-depth ratio given by Eq. (4–5).

Alternatively, the arch breadth scalar can be obtained graphically using Figure 4–3e, where the span-to-depth ratio is used to determine the arch breadth scalar according to the ratio of transverse to longitudinal reinforcement. Once defined, element areas are assigned as axial cross-sectional areas with an associated material property that defines the elastic stiffness, thus defining the element's axial rigidity.

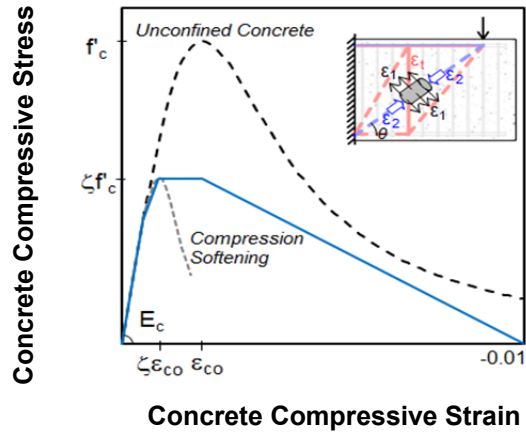
*Step 3: Assign nonlinear constitutive material relationships*

At this stage, the elastic response of the C-STM is defined by steps 1 and 2; hence nonlinear constitutive material relations for cracked reinforced concrete are now used to define the element's nonlinear behavior. Figure 4–11 shows the theoretical stress-strain relationships used to define the concrete constitutive relations for:

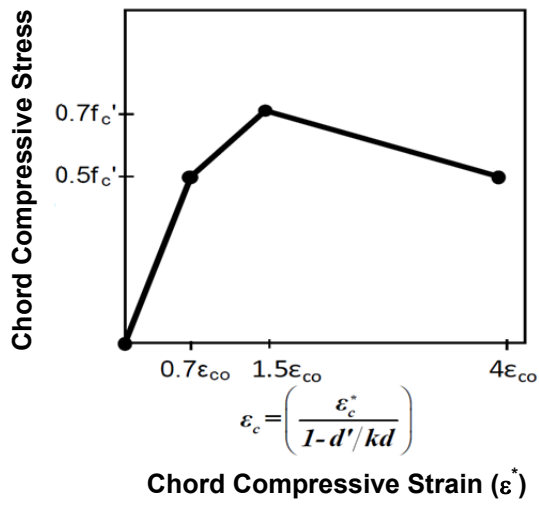
- (a) Diagonal concrete struts.
- (b) Concrete chord members.
- (c) Concrete tension behavior used in conjunction with all truss elements that also possess steel.

*Step 4: Assign load cases*

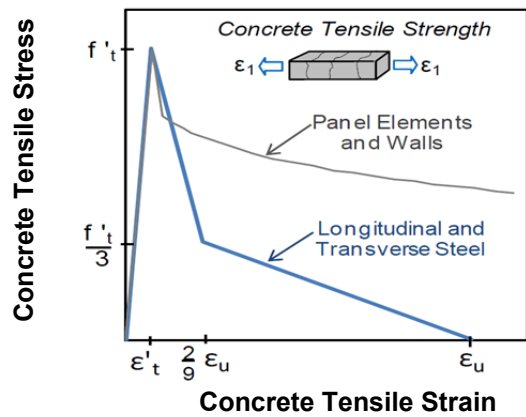
Load patterns are assigned at node locations as either forces or displacements in order to replicate the structure's loading pattern. Other parameter inputs include: loading control either specified as *load* or *displacement* control; incremental step size; results saved at final load or incremental load steps; and other nonlinear parameters. However with SAP2000 (1995), in order to perform an analysis in displacement control, additional joints have to be introduced without altering the structural behavior of the system. Joint displacements are provided at these joints, and the corresponding forces are calculated to obtain the overall force-deformation behavior of the system.



(a)



(b)



(c)

Figure 4–11: Nonlinear Constitutive Material Properties (a) Diagonal Web Members, (b) Compression Chord Elements, and (c) Tension Stiffened Elements.

### *Step 5: Run analysis*

The analysis can now be run for the desired load cases as input by the user. Once complete, the user can progressively step through the deformed shape to review the formation of nonlinear behavior.

### *Step 6: Post analysis investigation*

Axial forces, displacements, and other output parameters can then be exported to a spreadsheet, so that a post analysis investigation can be conducted. The axial force in each member can be individually assessed in order to ensure that the force does not exceed any other strength failure criteria (i.e., anchorage failure, nodal crushing, concrete softening, etc.). Because element strains are not given as an explicit output in SAP2000 (1995), an alternative means of defining the strain is required. This can be done using one of the following techniques:

- The element strain can be defined in terms of the element force divided by the axial rigidity as shown below:

$$\varepsilon = \frac{F}{EA} \quad (4-30)$$

where  $EA$  is constant in the elastic range, hence this can only be applied prior to nonlinear behavior.

- For members that reach nonlinear deformations, the strain can be obtained from the link deformations. The link deformations can be divided by their actual member length to obtain the strain in that member.
- Alternatively to the above methods, a third truss called a “strain-meter truss,” can be defined in the out-of-plane axis similar to the steel and concrete trusses such that each node is constrained accordingly. Truss elements with a unit axial rigidity (i.e.,  $EA = 1$ ) can be drawn between the desired nodes as “strain members” so that the (small) force resisted is equal to the strain as shown in Eq. (4-30). This will provide the composite steel-concrete axial strain associated between the selected two node points. (Note: this method was verified in this research using the previously mentioned methods providing



identical comparisons for vertical and horizontal members. However, some minor numerical discrepancies were observed in the diagonal concrete members where the results from the above technique would deviate with highly nonlinear behavior.)

#### **4.11 EXPERIMENTAL VERIFICATION**

In this section three specimens tested by Bracci et al. (2000), Young et al. (2002), and Powanusorn and Bracci (2006) to investigate the causes of excessive cracking in deep reinforced concrete bent caps are used to illustrate the analytical procedures and to verify the accuracy of the proposed C-STM. The C-STM is used to simulate the force-deformation and internal strain behavior of the three specimens. The selection of these three specimens from a total of 16 tested specimens was based on a variety of transverse to longitudinal reinforcement ratios and clarity of results reported. The structures are first analyzed using beam theory, and from this a SAT model is developed. Finally, the structures are modeled using the C-STM technique. All results are compared with the experimental results.

##### **4.11.1 The Structure**

Full-scale models of prototype bents used in Texas that had shown sign of distress near the column-to-bent cap negative moment connection were tested in order to determine their performance and investigate the causes of the cracks. Figure 4–12 presents the reinforcing layout and cross-section of the three specimens selected for the analysis. The specimen has compression reinforcement consisting of eight No. 8 (25 mm) bars and a specified cover concrete depth of 2.25 inches (57 mm).

The reported force-deformation responses are based on the actuator forces that were run in parallel to one another in a stepped force-controlled configuration, versus the average displacement of the two experimental beam displacement responses. This was justified using the FEM model presented by Bracci et al. (2000), Young et al. (2002), and Powanusorn and Bracci (2006), as well as the C-STM (described below), where the end displacements of the two cantilevered ends were calculated within 1 percent of each other.

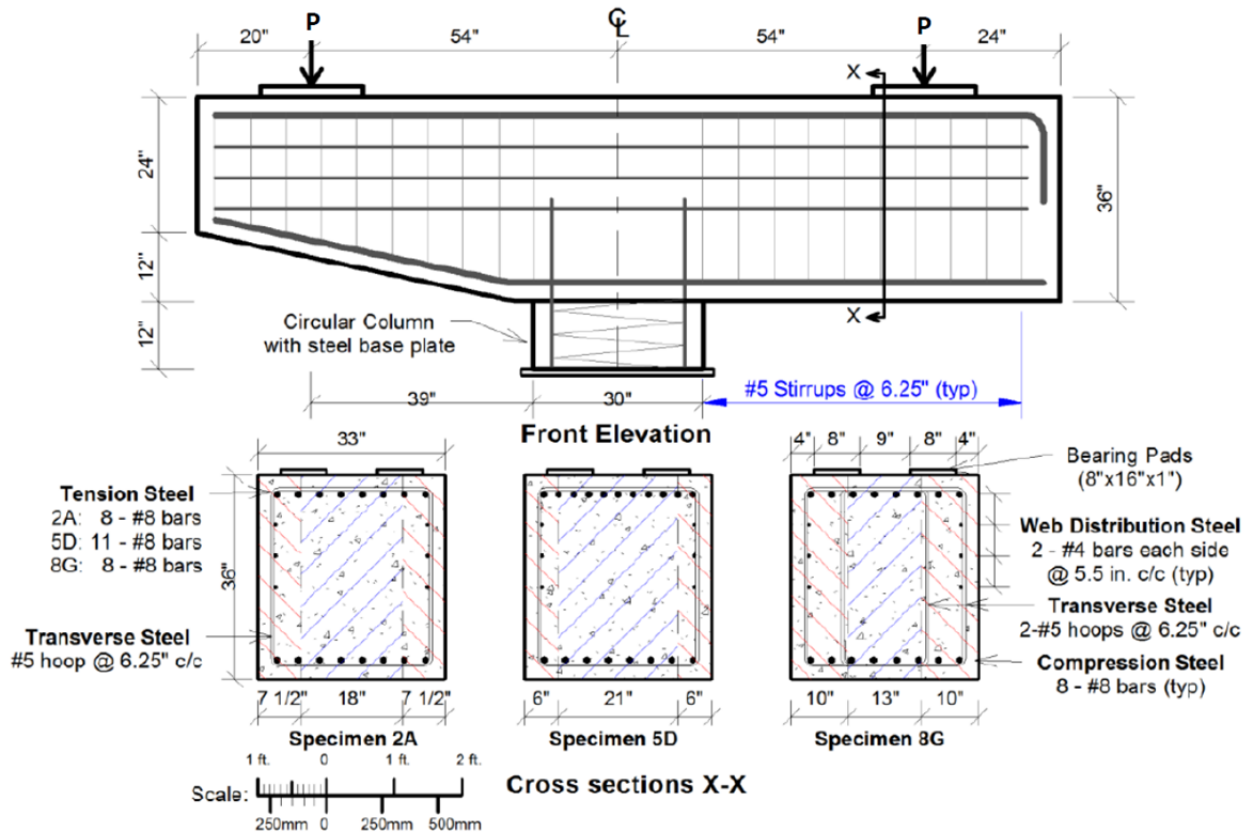


Figure 4–12: Elevation and Cross Section of Selected Specimens (Bracci et al., 2000).

Table 4–3 presents the reported material strength data and experimental test results for the three specimen (Bracci et al., 2000), in which:  $P_{Yield}^{Expt}$  and  $P_{Failure}^{Expt}$  = applied load at first yield and ultimate failure, respectively;  $\Delta_{Yield}^{Expt}$  and  $\Delta_{Failure}^{Expt}$  = vertical tip displacement at first yield and ultimate failure, respectively; and  $\mu = \Delta_{Failure}^{Expt} / \Delta_{Yield}^{Expt}$  = structural displacement ductility. (Note: as no test day strength results were provided, the 28–day strength was assumed for the analysis of the specimen.)

General observations reported during testing where as follows:

- Vertical flexural cracking initiated near the column face at the top of the bent cap around 100 kip.
- At approximately 160 kip, the vertical flexural cracks began to incline toward the applied load.
- With increased loading, inclined flexure-shear cracks initiated, propagated, and widened, while the original flexural cracks stabilized.
- Ultimate failure was very sudden and typically occurred along the diagonal shear plane, extending from the load point inclined toward the column support (Bracci et al., 2000).

#### 4.11.2 Present Code-Based Strength Predictions

The code-based design approaches that use the AASHTO *LRFD Bridge Design Specifications* (2010) that were also described in detail in Chapter 3 are used to predict the response of the three specimens.

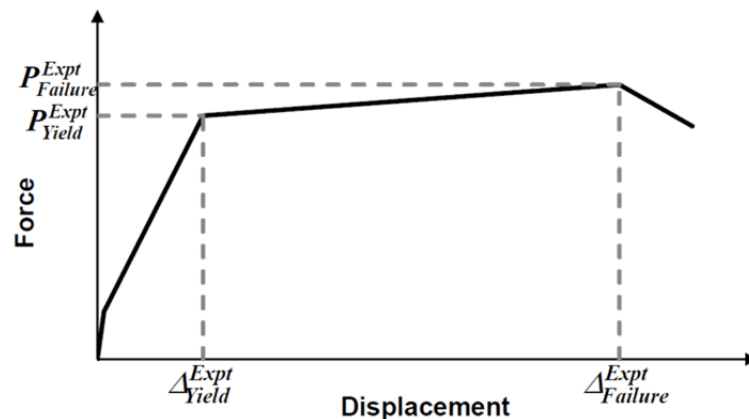
Analysis results are presented in Table 4–3 and discussed in what follows.

Stage 1 of the analysis considered only normal beam theory. The yield moment ( $M_y^b$ ) and the externally applied load at first yield ( $P_y^b$ ) are calculated using Eqs. (3–1) and (3–3), respectively. The analysis results in a yield moment of  $M_y^b = 1028$  kip-ft and an external yield load of  $P_y^b = 316$  kip for Specimen 2A. Results for Specimen 5D and 8G are presented in Table 4–3. The nominal flexural moment ( $M_n^f$ ) was calculated by normal practice as per the AASHTO *LRFD Bridge Design Specifications* (2010) and Eq. (3–4). The flexural capacity for

**Table 4–3: Material Properties, Stage 1 and 2 Analyses, and Experimental Results.**

		Specimen 2A	Specimen 5D	Specimen 8G	Comments
Material Properties	$f'_c$ (ksi) <sup>#</sup>	6.20	5.50	5.30	
	$f'_t$ (ksi)	0.32	0.30	0.29	
	$E_c$ (ksi)	4490	4225	4150	
Stage 1 Analyses (Sectional)	$M_y^b$ (kip.ft)	1028	1396	1024	Eq. (3–1)
	$P_y^b$ (kip)	<b>316</b>	<b>430</b>	<b>315</b>	Eq. (3–3)
	$M_n^f$ (kip.ft)	1197	1566	1197	Eq. (3–4)
	$P_n^f$ (kip)	<b>368</b>	<b>482</b>	<b>368</b>	Eq. (3–6)
	$\phi_f P_n^f$ (kip)	331	434	331	$\phi_f = 0.9$
	$V_n^s$ (kip)	<b>339</b>	<b>331</b>	<b>515</b>	Eq. (3–7)
Stage 2 Analyses (SAT)	$P_y^{SAT}$ (kip)	<b>306*</b>	<b>421*</b>	<b>306*</b>	Based on longitudinal steel yield.
	$\phi_v P_y^{SAT}$ (kip)	214	295	214	
	$P_n^{SAT}$ (kip)	368	483	369	Based on node capacity.
	$\phi_n P_n^{SAT}$ (kip)	258	338	259	
Experimental Results	$P_{Yield}^{Expt}$ (kip)	330	425	345	
	$P_{Failure}^{Expt}$ (kip)	<b>404</b>	<b>465</b>	<b>433</b>	
	$\Delta_{Yield}^{Expt}$ (in)	0.25	0.32	0.32	
	$\Delta_{Failure}^{Expt}$ (in)	0.77	0.50	1.26 <sup>†</sup>	
	$\mu$	3.08	1.56	>3.94	
Theory/ Experiment	$P^{SAT} / P_{Failure}^{Expt}$	0.76	0.97	0.71	

<sup>#</sup> TxDOT Class C Concrete-Average compression strength of three 28-day cylinder tests (Section 15.3, ACI 318-99). \* Expected critical failure mode capacity. <sup>†</sup> Specimen was not loaded to ultimate failure. Superscript: *b*=beam; *f*=flexure; *s*=shear; *SAT*=strut-and-tie; *Expt*=Experiment. Notations for experimental results:



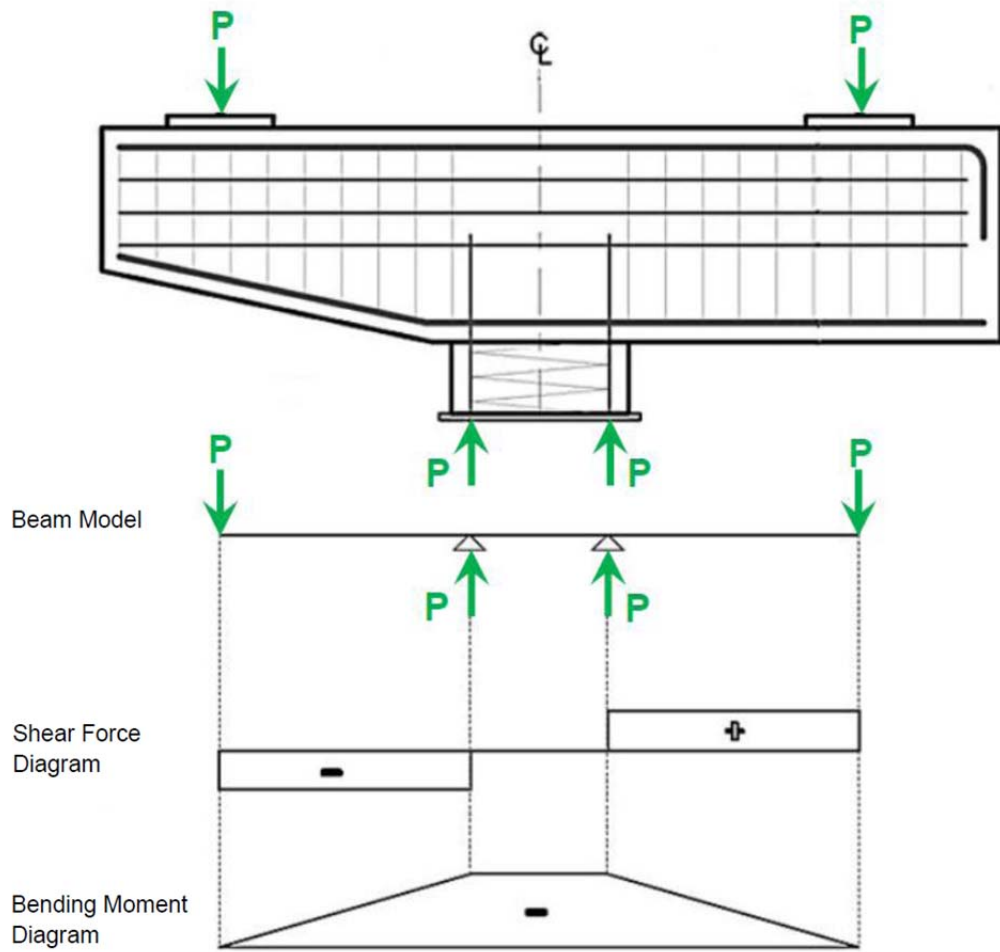
Specimen 2A was found to be  $M_n^f = 1197$  kip-ft. Based on the nominal flexural moment ( $M_n^f$ ), and knowing that the shear span to the face of the column  $L_b = 39$  inches, the external load causing flexure on the bent cap for Specimen 2A was found to be  $P_n^f = 368$  kip. The shear capacity ( $V_n^s$ ) is calculated from Eq. (3-7). Since there are no prestressing tendons, the component of shear carried by tendons is  $V_p = 0$ . The parameters  $\beta$  and  $\theta$  are calculated based on Method 1 of the AASHTO LRFD *Bridge Design Specifications* (2010). The beam shear capacity was found to be  $V_n^s = 339$  kip for Specimen 2A. The results for the other two specimens are presented in Table 4-3.

The next step of the analysis is to determine the strength hierarchy. The strength reduction factors for shear and flexure are  $\phi_v = 0.90$  and  $\phi_f = 0.90$ , respectively. It is observed that  $\phi_v V_n^s = 0.90 \times 339 = 305$  kip is less than  $\phi_f P_n^f = 0.90 \times 368 = 331$  kip for Specimen 2A. A similar observation is made for Specimen 5D. That is, the factored shear capacity is insufficient, which could lead to a shear failure of the bridge pier.

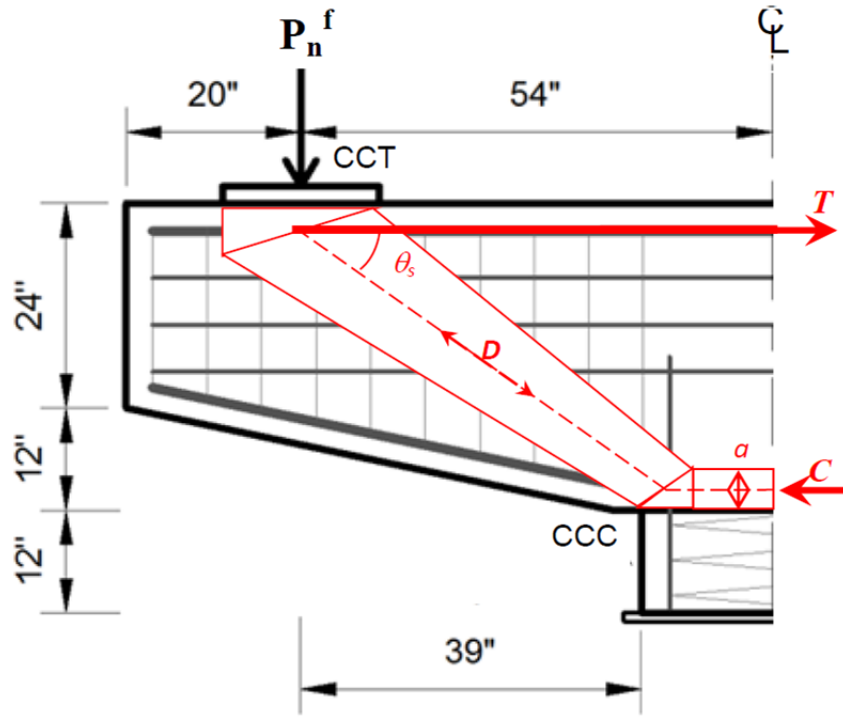
It is important to investigate the shear in the beam-column joint, as this can be a critical section. From the shear force diagram of the equivalent beam model of the bent cap shown in Figure 4-13, it is observed that there is no shear in the beam-column joint. Hence, the beam-column joint is determined not to be critical.

From the above computations it is observed that the factored shear capacity of the bent cap is insufficient. This warrants further investigation, and the strut-and-tie technique is used for further analysis.

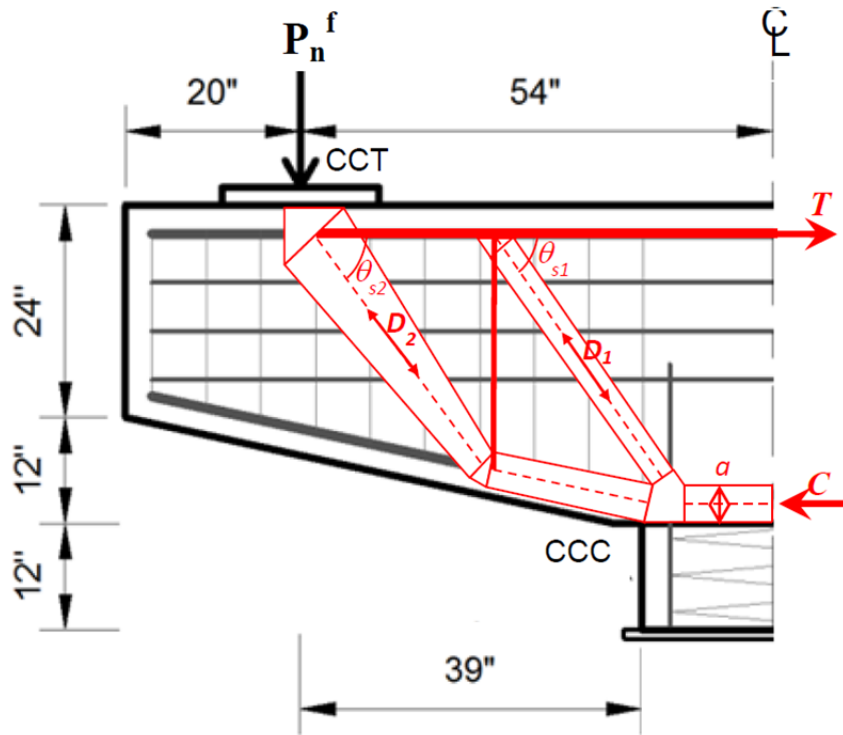
Stage 2 of the analysis considers a SAT model developed for the bent cap as shown in Figure 4-14. The strut-and-tie model predictions are based on the procedure detailed in Chapter 3. No reduction factors are used in order to predict the actual response. Both the single panel and two panel SAT models are shown. The steps involved in the construct and analysis of the single panel SAT method is described below.



**Figure 4–13: Shear Force and Bending Moment Diagram of Equivalent Beam Model of Bent Cap Specimens.**



(a) One panel model



(b) Two panel model

Figure 4-14: SAT Model of Reinforced Concrete Bridge Cap Specimen 2A.

As an important first step in the strut-and-tie analysis to construct the SAT model it is required to determine the truss and node geometry. By equating the horizontal forces  $C$  and  $T$  in Figure 4–14a, the height ( $a$ ) of the CCC node is:

$$a = \frac{T}{0.85f'_c b_w} = \frac{A_s f_y}{0.85f'_c b_w} \quad (4-31)$$

where the variables are as described earlier. The width of the CCT node equals the width of the bearing pad, which is 16 inches. The depth of the back face of the CCT node is taken as twice the distance from near face of the beam to the centroid of the tension reinforcement = 6.75 inches. The angle of inclination of the compression strut  $\theta_s = \tan^{-1}\left(\frac{jd}{shear\ span}\right) = 36.8^\circ$ .

Taking moment equilibrium about the CCC node, the external load on the beam  $P_n^f = T(\tan \theta_s)$  can be determined. Thus,  $P_n^{SAT}$  based on longitudinal steel yield for each of the specimen is evaluated. Based on equilibrium of vertical forces at the CCT node, the strut force  $D$  can be determined. The bottom face of the CCC node is proportioned based on the vertical component of the strut force  $D$  and compressive force  $C$ . An example on how to size the CCC node for Specimen 2A follows, with reference to Figure 4–14a:  $a = A_s f_y / 0.85f'_c b_w = 2.35$  inches,  $\theta_s = \tan^{-1}(jd / L_b) = 36.8^\circ$ . Taking moments about C gives  $P_n^f = T \times jd / L_b = 306$  kip. The diagonal force  $D = P_n^f / \sin \theta_s = 510$  kip. By proportion the width of the bottom face of the CCC node is  $D \sin \theta_s (a / C) = 1.76$  inches. Thus knowing the two vertical faces of the node, the slant face can be determined. The values for the other two specimens can be found in Appendix B.

Based on the geometry of the nodes, it is evident that the CCC node is the most critical node. As per AASHTO LRFD Design Specifications (2010) the strength of the critical CCC node is found from  $0.85f'_c A_{node}$ , where  $A_{node}$  = the cross-sectional area of the inclined face of the CCC node.

Incidentally it is found that the strut force  $D$  is equal to the node strength of the CCC node. Therefore, the externally applied load based on node capacity  $P_n^{SAT} = P_n^f$ . However, the



factored capacity  $\phi_v P_n^{SAT} < \phi_f P_n^f$ . The results obtained from the SAT analysis are presented in Table 4–3.

Figure 4–15 shows the experimentally obtained force-deformation response along with each of the code-based predictions. As each of the code-based techniques is only a strength-based approach, no predictions of the structure’s global deformation can be made; hence, the predicted forces are represented by horizontal lines.

From the SAT analysis, it can be concluded that the joint capacity is undependable, even though  $P_n^{SAT} = P_n^f$ . The results are inconclusive, and this warrants a more advanced analysis be conducted using C-STM. Clearly it is desirable to have a more insightful analysis that can overcome these shortcomings. This is now the subject of the following section.

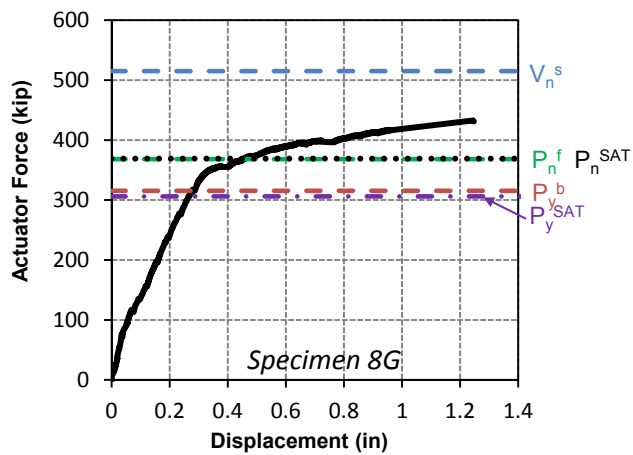
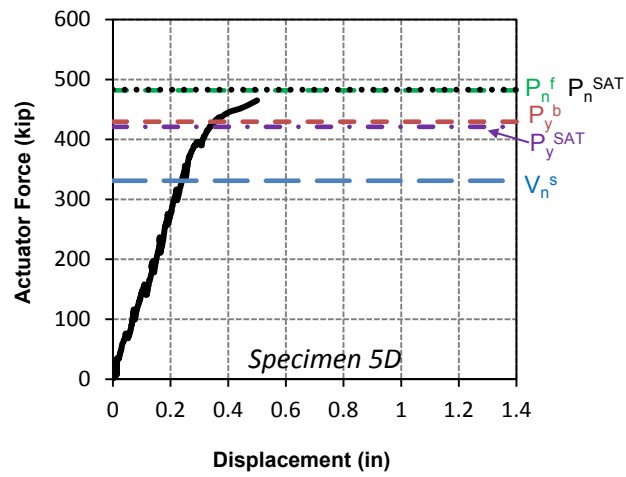
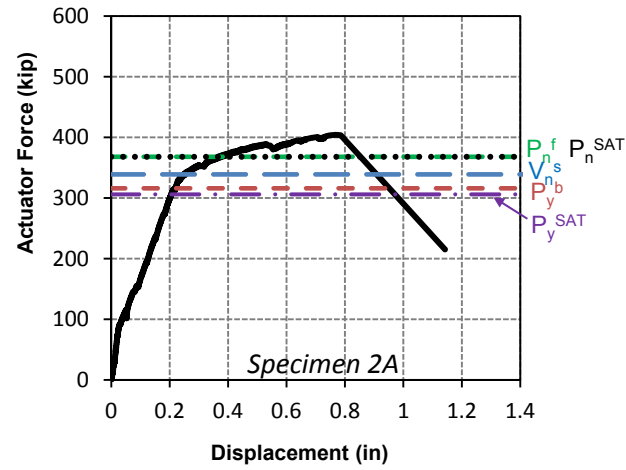
#### **4.11.3 Strength and Deformation Capacity Using C-STM Computational Modeling**

Using the modeling procedure described in detail in Chapter 4, the proposed C-STM can be applied to the experimental reinforced concrete bent caps in order to provide a more informative analysis. Figure 4–16 shows the C-STM model developed for the bent cap. The numbered node points in Figure 4–16 correspond to the cantilevered example shown in Figure 4–3c, and the suffixes *C* and *B* refer to the tapered cantilever and beam ends, respectively.

The representative area of longitudinal tension reinforcement labeled 5C–5B (Figure 4–16) was defined as the centroid of the No. 8 longitudinal bars plus the three sets of two No. 4 web distribution bars. The internal lever arm of the column support was taken as the internal diameter of the longitudinal reinforcement, thus defining the horizontal coordinates of nodes 1 and 2. The horizontal coordinates of the vertical transverse reinforcement member (member 3-4) were defined according to the single-point Gauss quadrature model.

As an example, Table 4–4 presents the variables used for Specimen 2A to calculate the area assignments of each element described earlier. For a  $L / jd$  ratio of 1.52 and a transverse to longitudinal reinforcement ratio of 0.41, the corresponding arch breadth scalar can be calculated as 0.55 using Eq. (4–5), or graphically interpolated as illustrated in Figure 4–3e.

- $P_y^b$  = External load causing flexural yield
- $P_n^f$  = External load causing beam flexure
- $V_n^s = V_s + V_c$  = Nominal beam shear
- $P_y^{SAT}$  = External load based on longitudinal steel yield from SAT
- $P_n^{SAT}$  = External load based on node capacity from SAT



**Figure 4–15: Experimental, Stage 1, and Stage 2 Results.**

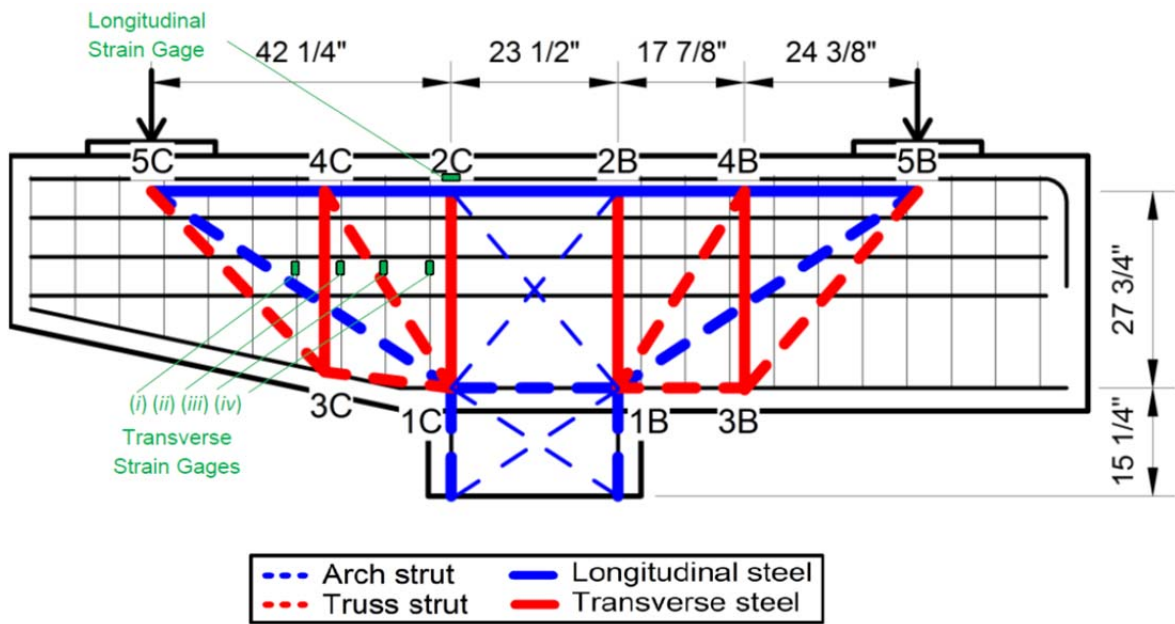


Figure 4-16: C-STM Model for Bent Cap Specimen.

**Table 4–4: Axial Rigidity Assignments for Specimen 2A.**

Member	Steel		Concrete		Comments
	$E - ksi$ (GPa)	$A - in.^2$ (mm <sup>2</sup> )	$E - ksi$ (MPa)	$A - in.^2$ (mm <sup>2</sup> )	
2 – 4 4 – 5	$E_s = 29000$ (200)	$A_s = 7.46$ (4813)	$E_c = 4490$ (30,960)	$b.kd = 250.7$ (161,740)	† Tension Chord
1 – 3	$E_s = 29000$ (200)	$A_s' = 6.28$ (4051)	$\psi_E E_c = 3680$ (25,373)	$b.kd = 250.7$ (161,740)	†* Compression Chord
3 – 4	$E_s = 29000$ (200)	$N_h A_{sh} = 2.46$ (1584)	$E_c = 4490$ (30,960)	$(4c + 2d_h) N_h s = 256.3$ (165,350)	Active Hoop steel including tension stiffening effect
1 – 5	–	–	$E_c = 4490$ (30,960)	$\frac{0.375 \eta b_w j d}{\cos \alpha} = 224.2$ (144,645)	Concrete Strut in Arch Mechanism
1 – 4	–	–	$E_c = 4490$ (30,960)	$\frac{0.5(1-\eta)b_w j d}{\sqrt{0.423 + \tan^2 \alpha}} = 220.7$ (145,390)	Concrete Strut in Truss Mechanism
3 – 5	–	–	$E_c = 4490$ (30,960)	$\frac{0.5(1-\eta)b_w j d}{\sqrt{0.577 + \tan^2 \alpha}} = 203.2$ (131,100)	Concrete Strut in Truss Mechanism

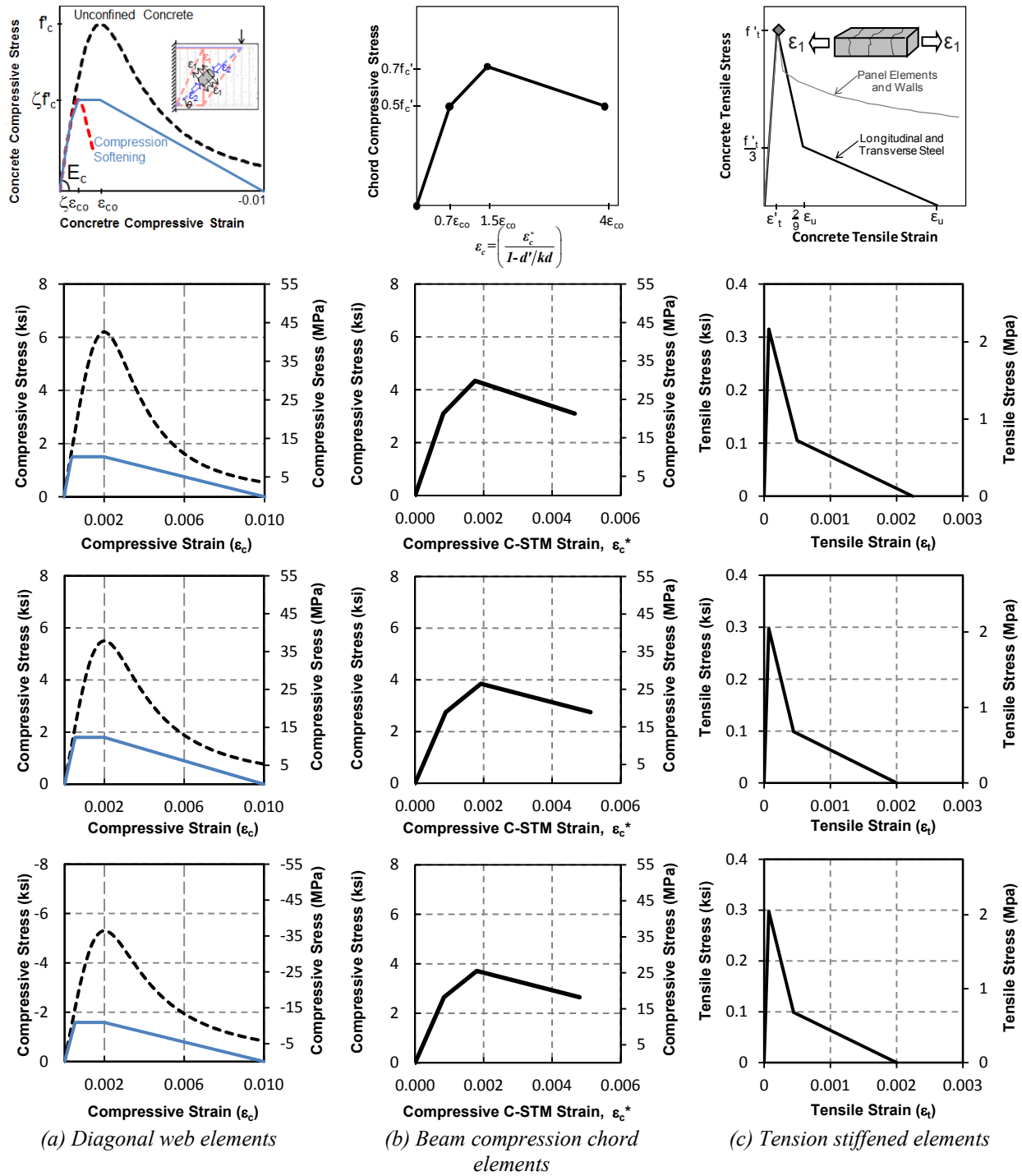
**Variables**

$L$ in (mm)	$jd$ in (mm)	$L/jd$	$\rho_T$	$\rho_L$	$\eta$	$A_s$ in <sup>2</sup> (mm <sup>2</sup> )	$A_s'$ in <sup>2</sup> (mm <sup>2</sup> )	$N_h$	$A_{sh}$ in <sup>2</sup> (mm <sup>2</sup> )	$b_w$ in (mm)	$d$ in (mm)	$kd$ in (mm)	$d'$ in (mm)	$\alpha$
42.25 (1073)	27.76 (705)	1.52	0.0030	0.0073	0.55	7.46 (4813)	6.28 (4051)	4	0.614 (396)	33 (838)	31 (787)	7.60 (193)	3.25 (83)	33.3°

$$\dagger k = \sqrt{(\rho_L + \rho_L')^2 n^2 + 2(\rho_L + \rho_L' d'/d)n} + (\rho_L + \rho_L')n = 0.245 * \psi_E = \frac{\sqrt{f_c'}(\text{psi})}{168(1-d'/kd)} = \frac{\sqrt{f_c'}(\text{MPa})}{14(1-d'/kd)} = 0.82$$

Row 2 of Figure 4–17 shows the three different nonlinear concrete stress-strain relationships derived for Specimen 2A from the material properties presented in Table 4–3 and are described as follows.

Figure 4–17a shows the softened stress-strain relationship for the diagonal concrete struts that were applied to the diagonal web elements. This was obtained by first running an analysis with strain truss members perpendicular to the diagonal concrete strain elements. This provides the strain transverse to the diagonal concrete members,  $\epsilon_1$ . Using Eq. (4–16) the concrete softening coefficient is evaluated, and the softened stress-strain relation is obtained using Eq. (4–18). The resulting softened stress-strain model may then be simplified in a tri-linear form for ease of implementation in SAP2000 (1995), as shown in Figure 4–17a.



**Figure 4–17: Cracked Reinforced Concrete Material Properties.**

**Row 1: Theoretical nonlinear behavior.**

**Row 2: Specimen 2A modeled behavior.**

**Row 3: Specimen 5D modeled behavior.**

**Row 4: Specimen 8G modeled behavior.**

Figure 4–17b shows the transformed concrete chord stress-strain relationship applied to the longitudinal compression chord members. This was obtained by multiplying the tri-linear stress ( $\sigma_c$ ) and strain ( $\varepsilon_c$ ) coefficients by  $f'_c$  and  $\varepsilon_{co}$ , respectively; where  $\varepsilon_{co} = 0.002$  is typically used for unconfined concrete. A further strain transformation of  $\varepsilon_c$  is then required to obtain the compressive C-STM strain ( $\varepsilon_c^*$ ) that applies to the actual position of the C-STM compression chord member. This is achieved by multiplying the values of  $\varepsilon_c$  by  $(1 - d'/kd)$ .

Figure 4–17c shows the concrete tensile strength, which is directly related to the concrete's material strength properties, as well as the type of structure under consideration.

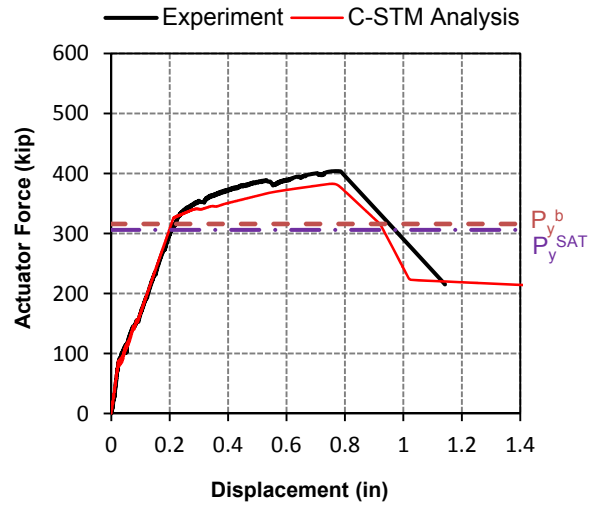
Rows 3 and 4 of Figure 4–17 show the nonlinear concrete stress-strain relationship for Specimen 5D and 8G, respectively.

#### **4.11.4 C-STM Results and Discussion**

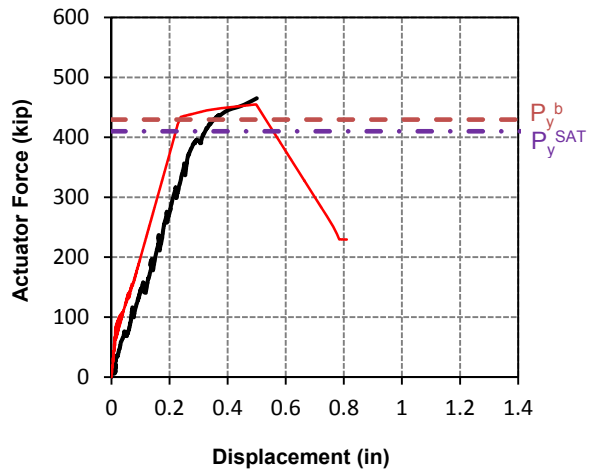
Figure 4–18 shows a comparison of the experimental results with the modeled analytical C-STM response for the three bent cap specimens. These comparisons illustrate the interaction of flexural and shear behavior that occurs in deep beams. It can be observed that the analytical results are in good agreement with the experimental results. The C-STM was also able to accurately simulate the failure of the specimen. However, it was also observed that this failure point was dependent on the softened stress-strain model of concrete that was used for the arch elements.

##### *Interrogation of Internal Strains from C-STM and Comparison with Experimental Results*

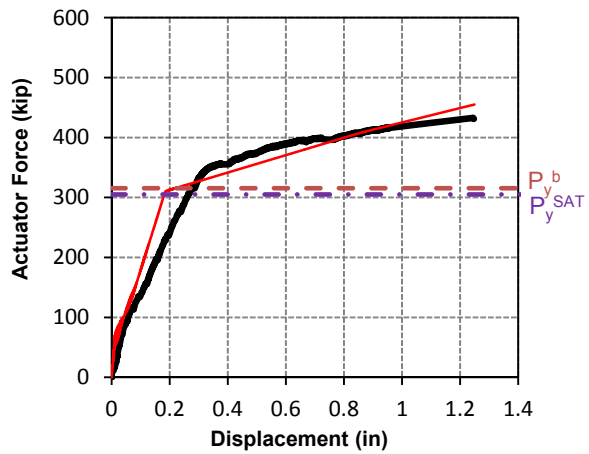
Figure 4–19 shows the major events in the progression of failure in Specimen 2A. It is to be noted that the strains obtained experimentally from strain gages and LVDT compare well with the corresponding member strains obtained from the C-STM analysis. Additionally, the C-STM concluded that the responses of each end were within 1 percent of each other despite their geometric differences, hence only the cantilevered end is reported from the C-STM analysis. A detailed description on the events in Figure 4–19 is described below. (FEM in Figure 4–19 refers to the analytical model proposed by Bracci et al., 2000).



*Specimen 2A*



*Specimen 5D*



*Specimen 8G*

**Figure 4–18: Comparison of Experimental and C-STM Results.**

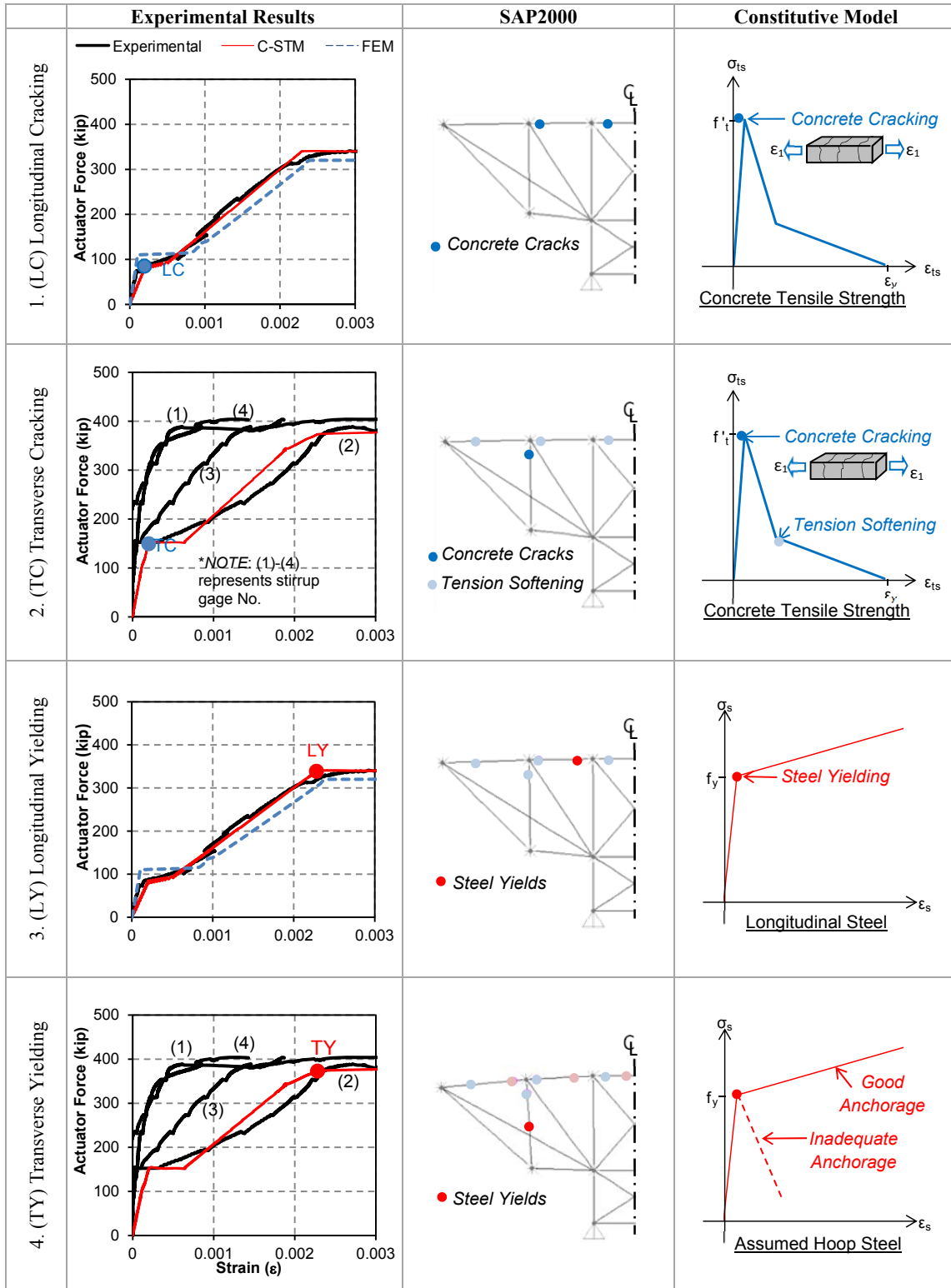


Figure 4-19: Progression of Nonlinear Behavior for Specimen 2A.

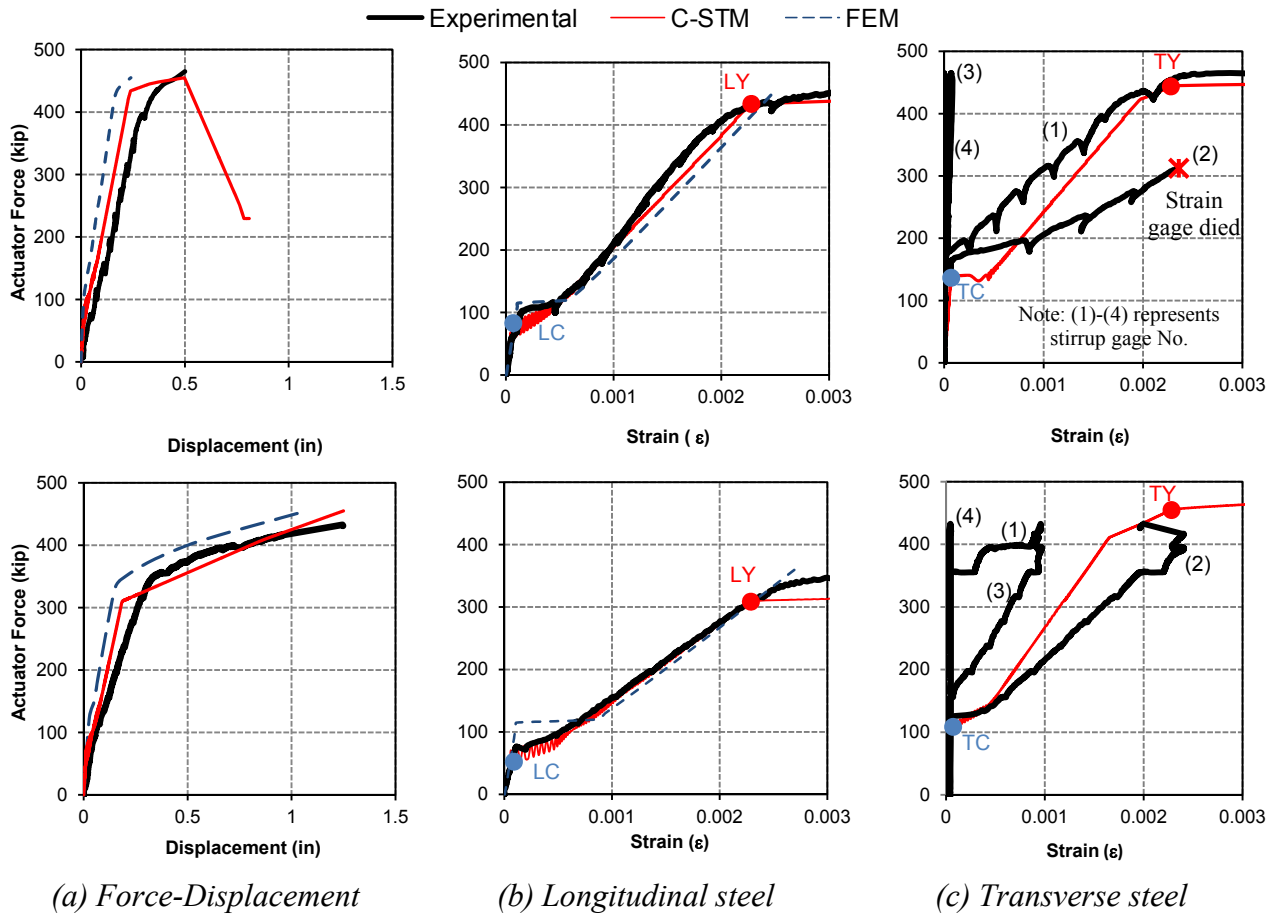


- LC*: Longitudinal cracking (row 1 of Figure 4–19) first occurs in the longitudinal concrete elements when the member stress exceeds the concrete tensile strength  $f_t'$ , thus indicating vertical flexural cracking in the top chord. As the force increases, the longitudinal tension-stiffened members exhibit tension softening effects where the concrete between cracks still has some ability to contribute in resisting tensile strains.
- TC*: Transverse cracking (row 2 of Figure 4–19) then occurs in the tension stiffened transverse truss elements. This correlates to the diagonal shear cracking observed as a result of the flexure-shear interaction.
- LY*: Longitudinal steel yielding (row 3 of Figure 4–19) occurs when the reinforcing steel yield stress  $f_y$  is exceeded and correlates to the flexural moment capacity of the member.
- TY*: Transverse steel yielding (row 4 of Figure 4–19) occurs when the stress in the transverse hoops exceeds the yield stress. Post-yield behavior of transverse reinforcement is governed by the anchorage of the hoops: if open 90° hooks or U-bars are used then loss of anchorage may occur at high strains; if closed 135° hooks are used then a full post-yield behavior may be assumed.

Figure 4–20 presents a summary of experimental versus C-STM results for the overall force-deformation, longitudinal, and transverse responses of Specimens 5D and 8G. The force versus longitudinal and transverse strain diagrams (column [b] and [c] of Figure 4–20 respectively) identify the nonlinear behavior in a similar manner to Figure 4–19. FEM in Figure 4–20 refers to the analytical model proposed by Bracci et al. (2000). It is observed that the overall force-deformation behavior and the member force-strain responses from C-STM are in good agreement with the experimental results. However, the simulated overall response of Specimens 5D and 8G tends to be a little stiffer than the experimental response.

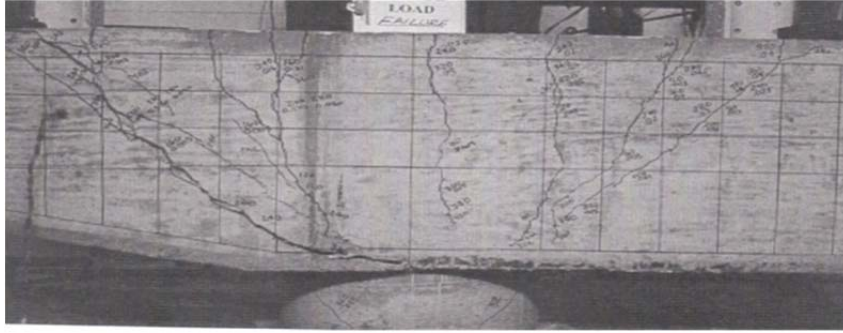
### *Failure Analysis*

The photograph showing the crack pattern of Specimen 2A is presented in Figure 4–21a. Figure 4–21b shows the order of nonlinear hinge formation observed by the C-STM analysis. These points are indicated on the force-deformation curve (Figure 4–21c), which gives an insight

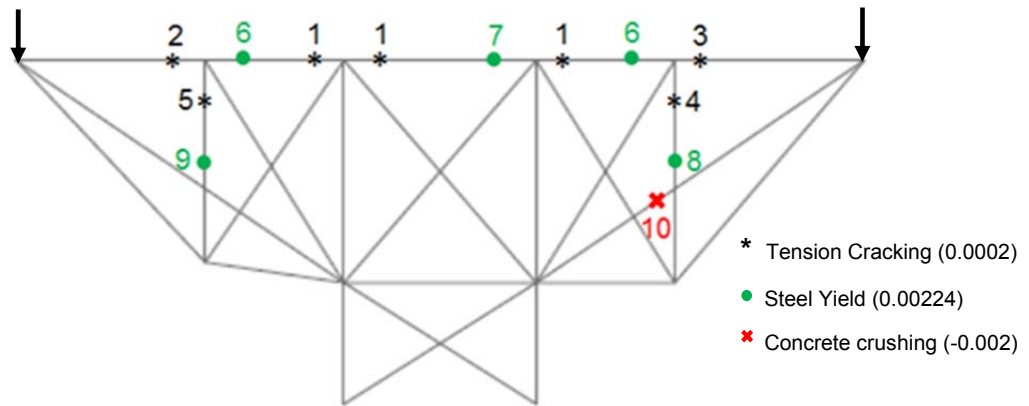


**Figure 4–20: Experimental vs. Analytical Results for Specimen 5D (top row) and 8G (bottom row).**

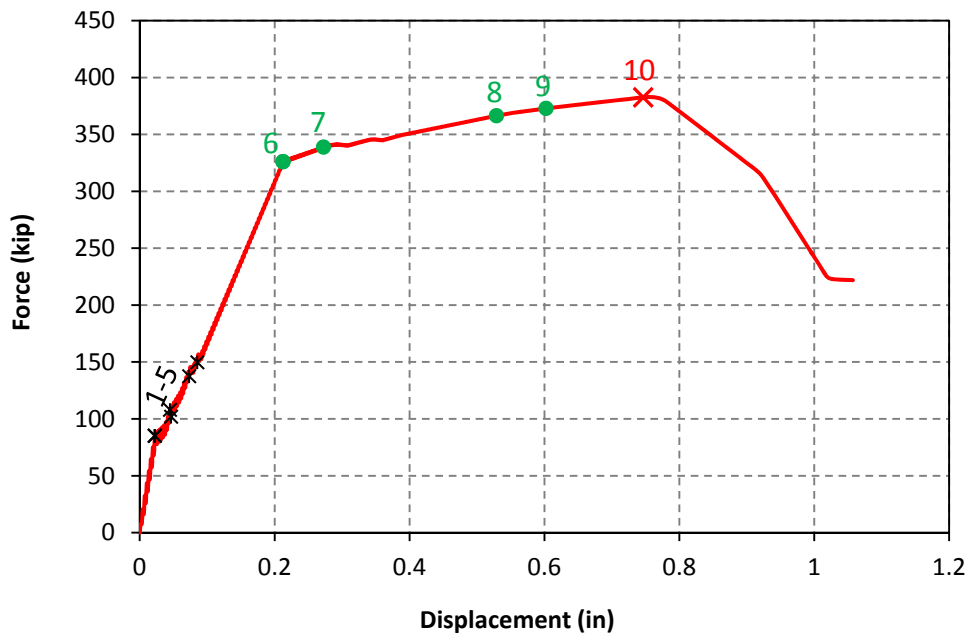
Note: LC = Longitudinal Cracking, TC = Transverse Cracking, LY = Longitudinal Yield, and TY = Transverse Yield.



(a) Experimental photo showing failure crack pattern



(b) Order of nonlinear hinge formation



(c) Force-deformation with nonlinear hinge formation events

**Figure 4-21: Failure Analysis of Specimen 2A.**

into the progression of the nonlinear hinges relative to the global force-deformation behavior of the structure. Each member is comprised of steel and concrete elements. Chronological progression of nonlinear behavior for Specimen 2A is described as follows:

- Concrete cracking first occurs in the longitudinal concrete element closest to the center-line when the concrete tensile strength  $f'_t$  is exceeded. This signifies the vertical flexural cracking at the column face of the beams observed in Figure 4–21a.
- Concrete cracking slowly extends along the longitudinal concrete element as the applied load increases. This indicates the formation of small vertical flexural cracks observed along the beam closer to the applied load.
- Concrete cracking of the transverse concrete element shortly follows. This signifies the propagation of shear cracking across the diagonal shear plane, where the cracks incline toward the column support. These cracks were typically observed at approximately 160 kip.
- Steel yielding first occurs in the longitudinal steel elements closest to the center-line when the yield stress  $f_y$  is exceeded. This corresponds to the flexural moment capacity of the critical section and drastically changes the member's force-deformation response resulting in the nonlinear bilinear slope observed.
- Steel yielding extends along the longitudinal steel elements with increased loading.
- Steel yielding of the transverse steel elements occurs when the average stress of the stirrups exceeds the yield stress  $f_y$ . This results in large shear deformations and indicates the widening of the diagonal shear crack observed close to the ultimate load.
- Once the transverse steel yields, the load-carrying capacity of the truss reduces. Stress flow occurs mainly through the corner-to-corner arch diagonal. This mechanism of stress flow provides additional load-carrying capacity (point 9 to 10 in Figure 4–21c) to the specimen. With further loading, the peak stresses are reached in the softened diagonal arch member.
- It was observed that after the arch diagonal on the beam side of the specimen reached its peak softened stress, the strains in the arch diagonal on the cantilever portion of the beam increased. The specimen finally failed when the strains in this member started dropping,

leading to the final collapse of the specimen, which is in agreement with the photograph of the specimen shown in Figure 4–21a.

#### 4.12 CONCLUDING REMARKS AND KEY FINDINGS ON EXPERIMENTAL VALIDATION

The computational C-STM results along with the experimental observations for the three specimens are summarized in Table 4–5.

**Table 4–5: Summary of Results for Bent Cap.**

		Stage 3: C-STM	Experiment
		$P_{C-STM}^{++}$	$P_{Failure}^{Expt \#}$
<b>2A</b>	Capacity (kip)	383*	404
	Factored Capacity (kip)	268	---
<b>5D</b>	Capacity (kip)	455*	465
	Factored Capacity (kip)	319	---
<b>8G</b>	Capacity (kip)	Not loaded to failure.	
	Factored Capacity (kip)		

++ Compression failure due to diagonal splitting/compression in the cantilever beam zone.  $\phi = 0.70$  (assumed).

# Maximum load at incipient failure due to failure in cantilever beam zone.

The code-based prediction shows the difficulties associated with trying to predict the failure mechanism using present conventional strength-based analysis techniques. Hence when used alone, these strength-based approaches are unable to provide satisfactory insight into the expected behavior in order to identify the progression of failure modes along with any post-yield capacity. Interestingly, the flexural analysis methods provided the most consistent predictions of the yield force despite the common perception that plane sections no longer remain plane in D-regions.

The C-STM technique developed in this chapter was validated against laboratory experiments, and the following two key observations can be made:

- The C-STM simulates the overall behavior of the specimen fairly accurately and gives the entire force versus deformation behavior of the specimen. The C-STM also models the internal behavior of the structure quite well. In order to capture the true failure state

and loading, the analysis must be conducted in “displacement control.” This enables the post-peak falling branch of the force-deformation response to be captured.

- The C-STM overcomes the difficulties associated with trying to model the failure mechanism using present conventional strength-based analysis techniques that rely mostly on equilibrium. The C-STM has a clear advantage when compared to the code-based analysis techniques and is a sound minimalist analysis technique that can be used to predict/model the behavior of structures.

## 5 EXPERIMENTAL PROGRAM – SPECIMEN DESIGN, CONSTRUCTION, AND DETERIORATION PHASE

### 5.1 SUMMARY

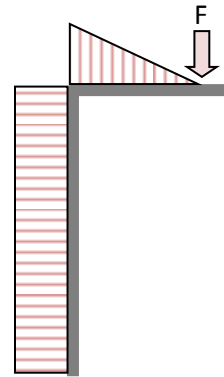
The effect of concrete deterioration due to evolving ASR and DEF is examined on large-scale specimens that represent typical modern Texas reinforced concrete bridge piers. Specimens are designed and constructed with a special mix that aims at promoting ASR/DEF effects. Following loading, that mimics prototype gravity effects, the specimens have a moderate amount of cracking that permits moisture ingress. Therefore, the specimens are conditioned outdoors in the Texas heat under daily wetting and drying cycles. Over a two-year period, substantial crack progression due to the effect of ASR/DEF results. While map cracking of concrete that indicates the formation of ASR gel is observed at an early age, over time the surface and internal concrete strains as well as reinforcing steel strains show substantial evidence of dilation due to ASR effects. This is also verified using post-test petrographic analysis. Results show that much of the ASR-induced damage is concentrated in the concrete cover, while the reinforcing cage tends to restrain the ASR expansion due to its confining effect.

### 5.2 INTRODUCTORY BACKGROUND

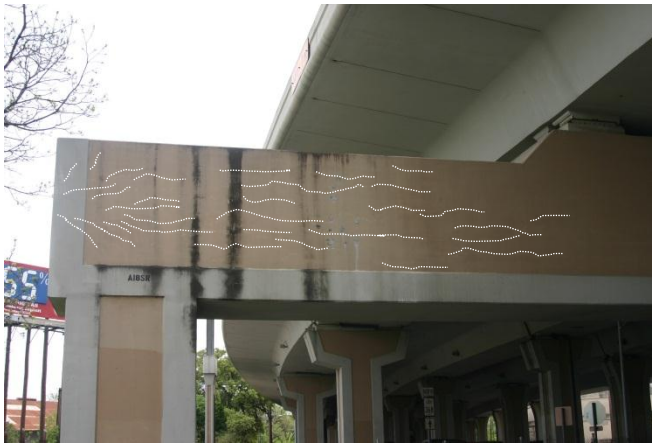
Over the past decade, the structural longevity of a large number of reinforced concrete bridge piers has been compromised as a result of premature concrete deterioration that is generally attributed to ASR and DEF. The aim of this research is to investigate the adverse effects of ASR/DEF on structural performance with particular reference to so-called disturbed regions that are commonly referred to as D-regions. Figure 5–1 shows two types of reinforced concrete bridge piers in Texas that are showing signs of ASR or DEF distress in their D-regions. The *cantilever bent* on I–10 in San Antonio, Texas, shown in Figure 5–1a, exhibits flexural cracking within the flexural tension zone on the left side of the column, plus one significant flexure shear crack propagating from the applied load near the knee joint as indicated by the staining patterns shown as white dotted lines. The *bent* on I–45 and Beltway 8 in Houston, Texas, shown in Figure 5–1b, exhibits distinct cracks through the potential plastic hinge zones in the beam and beam-column joint, also indicated by the white dotted lines. These cracks exist mostly in the



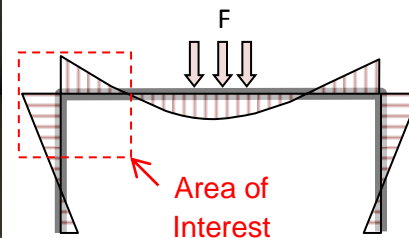
(a) *Cantilevered bent*



Schematic BMD



(b) *Straddle bent*



Schematic BMD

Note that the white dotted lines signify concrete cracking

**Figure 5–1: Prototype Reinforced Concrete Bridge Bents.**



D-regions where both flexural and shear demands are high. Although cracks are expected in such zones in reinforced concrete structures, by design, the crack-widths are somewhat larger than what one would normally expect to observe from service loads alone. This therefore may be particularly alarming to bridge inspectors who would invariably wonder whether such cracking is a sign of strength impairment.

### **5.2.1 Alkali-Silica Reaction**

It is well-known that high alkali contents in Portland cement used with reactive siliceous aggregates in concrete can result in ASR particularly when exposed to moisture. ASR results in the formation of expansive products that generally form around aggregates, which in turn leads to cracking of the concrete. Although a significant amount of research has been conducted on deciphering the mechanism of ASR deterioration, neither the identification of the critical variables which lead to ASR, nor the mitigation of the damage caused by ASR, nor the assessment of the capacity of structures experiencing ASR deterioration have been investigated thoroughly. One such issue, which is also one of the objectives of this study, is the validity and accuracy of SAT modeling in D-regions of large-scale structural elements subject to different conditions of premature concrete deterioration.

Chemical reactions between alkalis in the cement of concrete and reactive silica found in aggregates can result in ASR when exposed to moisture (Swamy and Al-Asali, 1989 and 1998; Chana and Korobokis, 1991; Poole, 1992; Swamy, 1992; Ahmed et al., 1998, 1999a, and 1999b; Fan and Hanson, 1998a and 1998b; Berube et al., 2002; Jensen, 2003). Conditions required for ASR include reactive silica phases in the aggregates, alkali hydroxides in the pore solution ( $[Na^+]$ ,  $[K^+]$ , and  $[OH^-]$ ), and sufficient moisture. The reaction between the reactive silica in the aggregates and the alkali in the pore solution produce a gel, commonly referred to as the ASR gel, which over time expands and causes cracking of the concrete. As the alkalis and reactive silica are consumed with time, the ASR process stops unless these constituents are provided from external sources. Berube et al. (2002) reported that the exposure conditions of concrete greatly influence the development of surface cracking and the expansion of ASR affected concrete. It was pointed out that wetting and drying cycles significantly promote surface cracking even though the surface expansion due to ASR may decrease when the concrete

is allowed to dry. It is believed that the amount of ASR gel is reduced when the alkali content on the surface layer is reduced due to the inter-leaching of the alkalis from the surface layer. This leads to differential strains between the interior and surface layers and then results in cracking of the surface layer (Deschenes et al., 2009).

As the ASR gel starts to form, tensile stresses are imposed internally within the concrete system and lead to cracking. It was found that the hydrated cement paste is weaker than the aggregates, and the cracking usually occurs in the hydrated cement paste or along the interface of the aggregate and the hydrated cement paste (Poole, 1992; Swamy, 1992). Jensen (2003) indicated that eventual expansion due to ASR can cause cracking of the aggregates although it initiates in the hydrated cement paste. Since shear capacity partly relies on the nature of the aggregate interlock, cracking of the aggregates may decrease the shear capacity and can further affect the bond strength of the reinforcement and strut strength in D-regions.

### **5.2.2 Delayed Ettringite Formation**

It has also been found that rapid hardening cements in large-volume concrete structures can lead to a very high heat of hydration during concrete curing. This can cause cracking due to thermal effects and late-age cracking (Kelham, 1996; Odler and Chen, 1996; Scrivener and Lewis, 1997; Grattan-Bellew et al., 1998; Zhang et al., 2002; Deschenes et al., 2009). Ettringite forms within concrete after the high heat condition during initial concrete curing. The reformation of ettringite, commonly known as DEF, can lead to later expansion and cracking. It has been found that DEF can develop as a result of high temperatures at an early age in concrete. Temperature ranges from 148 to 160 °F (64 to 71 °C) during the early age of concrete curing have been reported as the cause. In general, it is believed that structures first exhibit cracking due to ASR and then DEF. Both ASR and DEF can lead to cracking of the concrete even though they are different mechanisms of deterioration (Deschenes et al., 2009).

Generally, ettringite forms at an early age in fresh concrete. The sulfate is consumed while reacting with the calcium-aluminates in the presence of calcium hydroxide. Once the sulfate concentration in the pore solution reaches specific lower value, the calcium-aluminates react with the already formed ettringite to produce monosulfoaluminate. Furthermore, if sulfates are reintroduced either from external or internal sources to the pore solution, the

monosulfoaluminate can revert back to ettringite, causing expansive forces and cracking. Research has found that if the concrete is subjected to high early heat, the sulfate ions are physically attached to the calcium silicate hydrate (C-S-H) and are available as a source of sulfate at late age of the concrete (Odler and Chen, 1996; Scrivener and Lewis, 1997). Thus, concrete experiencing high temperature during hydration either from high cement contents or large-volume structures can lead to the occurrence of DEF.

While ASR initiates at the interface of the hydrated cement paste and the aggregates, introducing tensile stress and resulting in cracking, DEF typically occurs at void locations in the hydrated cement paste and then causes internal stresses. Although ASR and DEF initiate at different areas, both mechanisms can lead to cracking of the hydrated cement paste and the aggregates. It is believed that it takes longer for DEF to take place than ASR, and the damage caused by DEF, in general, may reduce the capacity of a structure (Deschenes et al., 2009). However, both deterioration processes result in similar damage types, and both can affect the strength of a concrete structure. However, the extent of strength reduction is generally unknown. The purpose of this work is to make an attempt at quantifying the degree of strength reduction with a particular emphasis on the massive bridge piers and bents with D-regions that are commonplace in Texas and elsewhere. Because these structures tend to possess stocky members with low shear-to-span ratios ( $M/Vd < 2$ ), their behavior may be governed by the performance in their D-regions. It is evident from the abovementioned literature that structural behavior under adverse ASR/DEF condition falls into a knowledge gap.

This chapter presents an experimental investigation on the concrete deterioration of large-scale reinforced concrete specimens specifically designed to emulate D-regions in typical Texas bridge structures that exhibit such ASR/DEF effects in their D-regions. To promote the two most common concrete deterioration mechanisms, ASR and DEF, a custom construction procedure, a special concrete mix, and post-curing treatment were used. This research, therefore, is intended to provide insight into the evolution of crack progression and apparent concrete deterioration. Destructive testing is not considered in this chapter. Rather, the evolution of expansive strains is investigated over time. The main aim is to quantify what a bridge inspection may observe in the field but not have the instrumentation in place to confirm the extent of the suspicious-looking behavior.

## **5.3 EXPERIMENTAL SPECIMEN DEVELOPMENT**

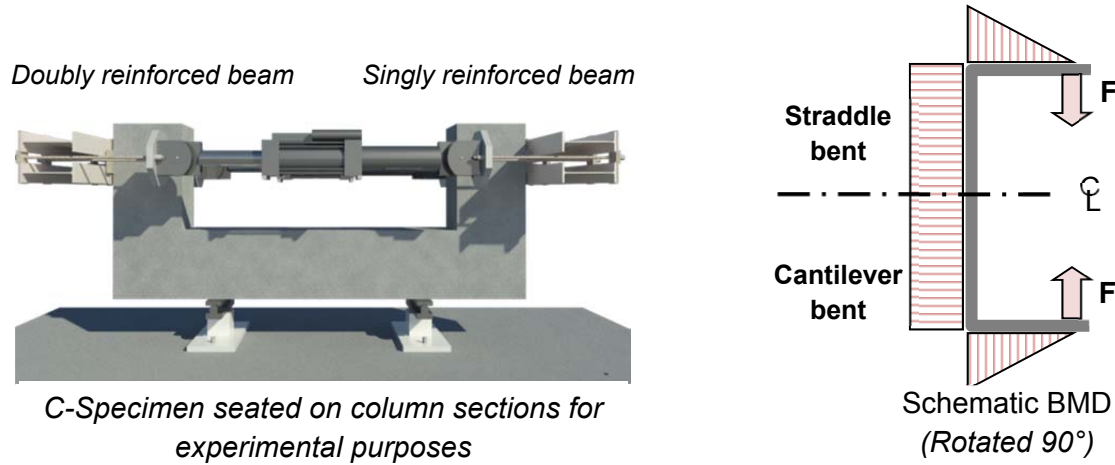
### **5.3.1 Representative Prototypes**

As shown in Figure 5–1, the two bridge bents selected as the basis for designing the specimens to be tested in this research were based on current bridge structures in Texas. Cantilever bents, as shown in Figure 5–1a, are typically constructed with minimal compression steel in the bent cap using bending theory or SAT design methods. Therefore, a similar singly reinforced bent cap was considered in the specimen design. Straddle bents, as shown in Figure 5–1b, typically have both tension and compression steel in the bent cap to accommodate the alternating negative and positive moments along the cap beam. The bottom (positive moment) reinforcement needed for the mid-span region of the cap beam is normally terminated inside the column face within the beam-column joint zone. This generally leads to a fully doubly reinforced cap beam where the top and bottom reinforcement areas are similar.

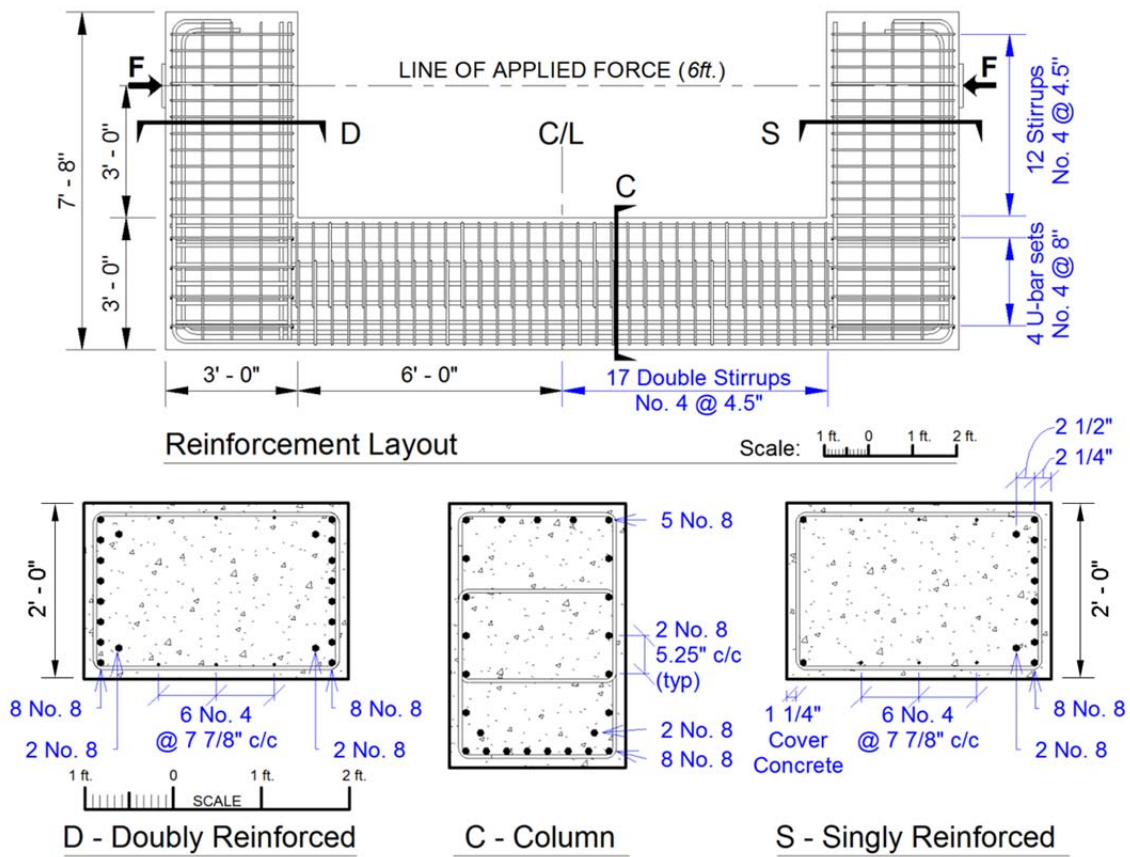
### **5.3.2 Specimen Design**

Figure 5–2 presents the experimental specimens adopted for this research. Four specimens with the same design were constructed as C-shaped sub-assemblages consisting of two D-regions. Due to their large size, an important feature was to ensure the specimens could be structurally tested using a self-reacting system as shown in Figure 5–2a. This test setup provided an axis of symmetry at the specimen’s centerline. The C-shaped sub-assemblage specimens had a constant cross-section, 24 inches wide by 36 inches deep throughout. The only deviation from symmetry was the varying compression steel in the bent caps near the D-regions. Considering the prototype structures shown in Figure 5–1, the scale factor for the specimens in this research is approximately 50 to 75 percent of full-scale for the cantilever bent and straddle bent, respectively.

Figure 5–2b presents the specimen dimensions and the reinforcing details of the C-shaped specimens. The longitudinal reinforcement, scaled to replicate the cantilever and straddle bents described previously, consisted of 10 No. 8 rebars (1.0 inch/25 mm diameter) running continuously on the tension side of the specimen and hooked at the end of each bent. The singly



(a) Experimental C-Specimen



(b) Reinforcement details

Figure 5-2: Experimental Specimen.

reinforced bent cap section (S) had only two No. 8 bars on the compression face. These bars are necessary for construction purposes in order to tie the transverse steel and form an enclosed cage. The doubly reinforced bent cap section (D) had 10 No. 8 bars in both the tension and compression faces of the beam.

The longitudinal side face bent reinforcement (distributed along the bent cap web) consisted of three sets of equally spaced No. 4 rebars (0.5 inch/13 mm diameter). Transverse bent cap reinforcement consisted of closed stirrups with a center-to-center spacing of 4.5 inches (115 mm) starting at the column face. The longitudinal column reinforcement, in addition to the 10 No. 8 rebars used in the tension region, consisted of five sets of equally spaced No. 8 rebars throughout the mid-region of the column section and five No. 8 rebars along the compression face. Transverse column reinforcement consisted of 4.5 inch center-to-center spaced No. 4 overlapping hoops. The beam-column joint was reinforced with four No. 4 U-bars with 8 inch spacing continuing from the transverse bent reinforcement.

### **5.3.3 Specimen Construction and Curing**

For the construction of each of the four specimens, the concrete mix used in this research was designed for a target concrete compressive strength of 5000 psi (35 MPa). Type III cement with a high alkali content (from Lehigh Cement in Evansville, Pennsylvania) was used in the mix for the specimens in order to promote both the ASR and DEF deterioration mechanisms in the concrete. The saturated-surface dry (SSD) weight of cement for the concrete mix was 752 pcy (445 kg/m<sup>3</sup>). Coarse river gravel aggregate (from Hanson Aggregates in Garwood, Texas) with a maximum size of 1 inch (25 mm) was mixed with fine aggregate (from Wright Materials in Robstown, Texas) with SSD proportions for coarse and fine aggregates of 1350 pcy (799 kg/m<sup>3</sup>) and 1439 pcy (851 kg/m<sup>3</sup>), respectively. Sodium hydroxide (NaOH) solution with a target density in the specimens of 5.7 pcy (3.4 kg/m<sup>3</sup>) was added to accelerate the premature concrete deterioration mechanisms. The water/cement ratio for the concrete mix used in this research was  $w/c = 0.48$ .

To promote the development of DEF in the specimens of the experimental program, the specimens were heated with electrical resistive wiring (ERW) to remain above the threshold temperature of 170 °F (77 °C) for at least 2 days during the curing phase. Each side of the

formwork was insulated to better maintain the internal curing temperature and supplemental heat. The ERW was pre-installed in the top and bottom faces of the formwork and covered with stainless sheets. Additionally, to create a more uniform heat distribution, ERW was fed through cross-linked polyethylene tubes located in the mid-depth region of the specimens. In order to ensure that the temperature of the specimens was above 170 °F and maintained for at least 2 days, thermocouples were attached in the specimens to record the temperature during the curing phase and used in a feedback loop to actively control the internal concrete temperatures throughout the specimen. Additional details on the development of the ERW system can be found in Chapter 6.

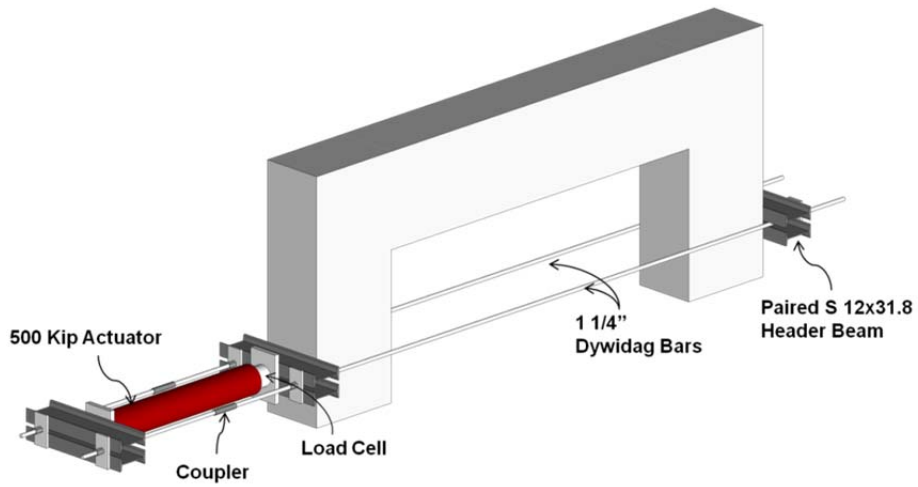
#### **5.3.4 Thermal Effects**

Suppose the concrete of a bridge pier is cast on a hot summer's day in Texas with an ambient temperature of 100 °F. The next day is also hot and humid, and meanwhile, due to heat of hydration effects, the internal concrete temperature has risen to some 170 °F. Then as stripping of the formwork commences, there is a torrential thunderstorm with hail stones. The temperature on the surface of the concrete drops suddenly to 50 °F (10 °C). This shock leads to cracking. The fine cracking due to the thermal effect is one of the concerns in this research. The temperature gradient on the concrete surface caused by removing the formwork can result in the initiation of the fine cracking.

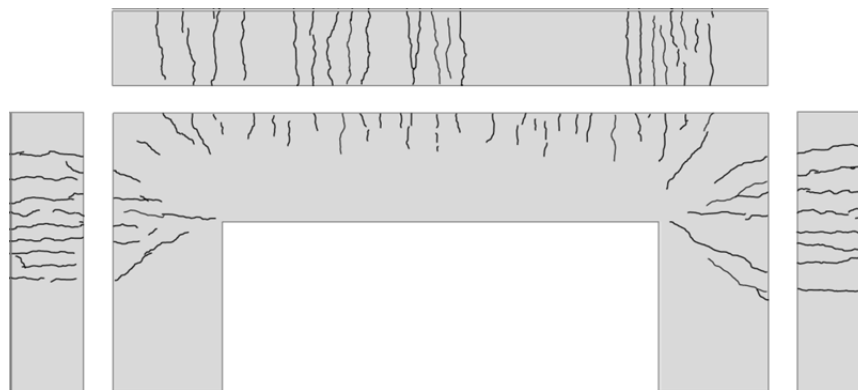
In order to investigate and to amplify such an abovementioned thermal scenario, the beam area of one side of Specimen 4 was deliberately thermally shocked using packed ice bags immediately after the removal of top formwork at 70 hours after pouring the concrete. After a two-hour application of thermal shock, the temperature of the surface of concrete dropped 100 °F (56 °C). Map cracking arising from thermal distress was observed as shown in Figure 5–3a. The initiation of map-cracking provides the access for moisture and may subsequently lead to the accelerated formation of ASR/DEF when in field conditions. The thermal effect acts as a trigger and becomes an initial driver of subsequent ASR/DEF mechanisms—significantly more pathways for moisture ingress exist due to the thermal shock. The thermal shock effect is discussed in more detail in the next chapter.



(a) Map-cracking due to thermal effect



(b) Gravity loading setup



(c) Crack pattern induced by gravity load

**Figure 5–3: Gravity Loading Applications.**



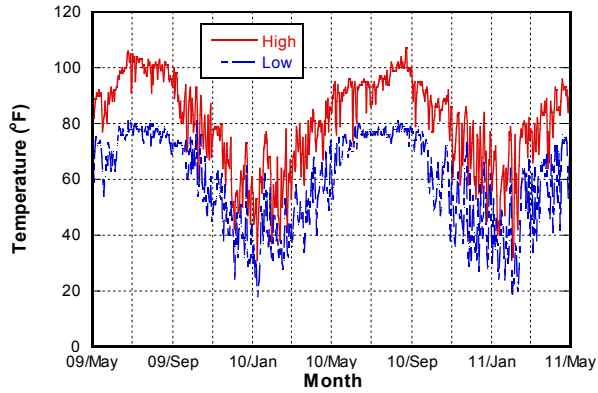
### 5.3.5 Pre-Loading Setup

In Figure 5–3b the application of the prestress applied to Specimens 2, 3, and 4 is shown. Two 1.25 inch (32 mm) high strength (DYWIDAG<sup>TM</sup>) high-alloy threadbars were located at a distance of 3 ft (915 mm) from the column face along with two groups of paired S 12 × 31.8 header beams to create an equal and opposite load condition as shown in Figure 5–3b. Strain gages were placed on the threadbars to monitor the applied prestress force over time. The total force exerted on both bars was obtained with calculations of the recorded strains. This provided a reference during the preloading procedure and the tendency of the remaining preload over time. A 500-kip capacity actuator was connected with a load cell to record the force exerted on the system. The reading of the load cell provided the true force and a reference for the calculations of the recorded strains in the bars. Flexural cracking was observed at a load of 200 kip during the first pre-loading procedure. A load of 200 kip was then determined as the load for mimicking gravity loads. With the expectation of the force loss immediately after preloading, the whole system was loaded to near 215 kip (956 kN). The remaining force after initial set losses according to the threadbar strain gages was 200 kip (890 kN). This operation was undertaken in the lab and once complete the prestressing threadbars were locked off, the hydraulic jack was removed, and the specimen was shipped to the field.

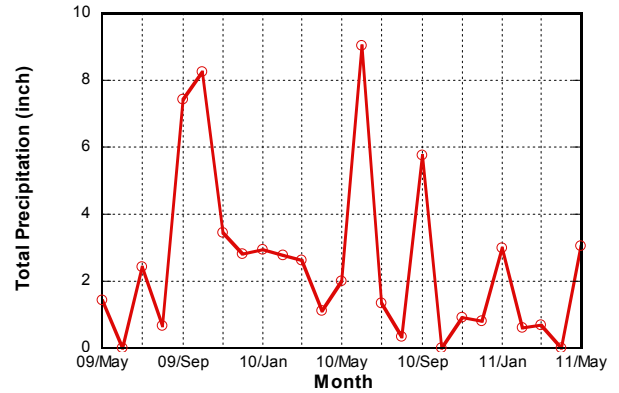
The crack pattern induced by the prestress load prior to any field deterioration is shown in Figure 5–3c. The preload created a tension field such that initial cracking was generated near the tension side of the specimens. According to a crack comparator card, the observed cracks were merely hairline and less than 0.005 inch ( $\leq 0.13$  mm) in width. These initial cracks permitted the absorption of moisture into the specimen. Such moisture is known to accelerate the deterioration mechanisms once the specimens were transported to the field.

### 5.3.6 Weather Conditioning

Figure 5–4a shows the observed daily maximum and minimum temperatures, while Figure 5–4b presents the monthly precipitation throughout the two-year period from May 2009 to May 2011. This exposure was in an open field at the Texas A&M University Riverside Campus, west of Bryan, Texas. The average high temperature exceeded 80 °F from about April to October. Over



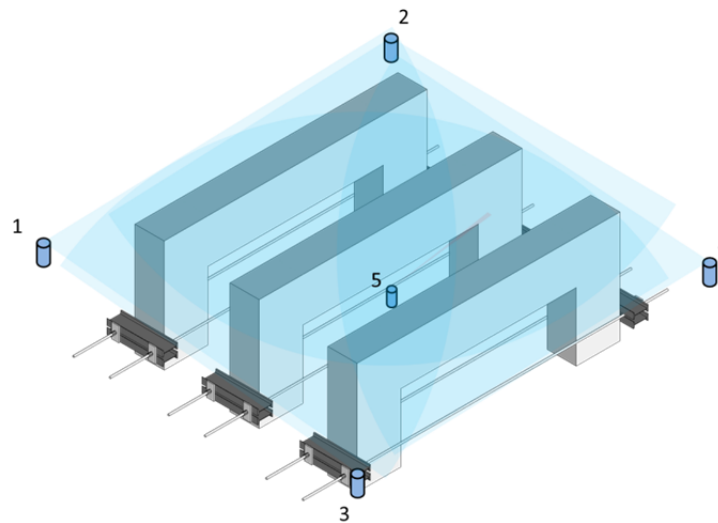
(a) Daily temperature



(b) Monthly precipitation



(c) C-Specimens exposed to environmental conditions



(d) Water coverage from the irrigation system

**Figure 5–4: Field Environment for the Specimens in Bryan, Texas.**

this Texas heat period, any surface water dried off quickly; evidently this helped to promote the ASR/DEF deterioration mechanism.

### 5.3.7 The Supplemental Watering System

After construction, Specimens 2, 3, and 4 were transported and placed at the Riverside Campus (Figure 5–4c). To provide sufficient water to accelerate the formation of ASR and DEF, a sprinkler system was built that applied water for 15 minutes four times a day. As shown in Figure 5–4d, five sprinklers were installed to ensure uniform coverage of this system. The specimens were placed with a clear space of around 6 ft to ensure coverage of each face of each specimen with water.

### 5.3.8 Summary of Experimental Specimen Development

Table 5–1 presents a summary of cast date, age when prestress was applied, age at the beginning of wetting and drying cycles, age when specimen was shipped back to the structural testing lab, and age when testing was conducted for each specimen. Note that prestress was removed before the specimens were shipped back to the structural testing lab.

The specimens were heated with ERW to maintain the temperature above 170 °F (77 °C) for at least 2 days. The top formwork was removed after shutting off the heat, while the side formwork remained in place for at least 1 day. The beam area of one side of Specimen 4 was thermally shocked immediately after the removal of top formwork.

**Table 5–1: Summary of Experimental Specimen Development.**

	<i>Lab</i>		<i>Field</i>	<i>Lab</i>	
	<b>Cast Date</b>	<b>Prestress Applied</b>	<b>Wetting and Drying Cycles</b>	<b>Moved to lab with prestress removed</b>	<b>Testing</b>
Specimen		Age (days)	Age (days)	Age (days)	Age (days)
1	11/24/08	N/A	N/A	N/A	392
2	01/13/09	97	112	364	499
3	02/13/09	66	81	-	-
4	03/06/09	45	60	808	888

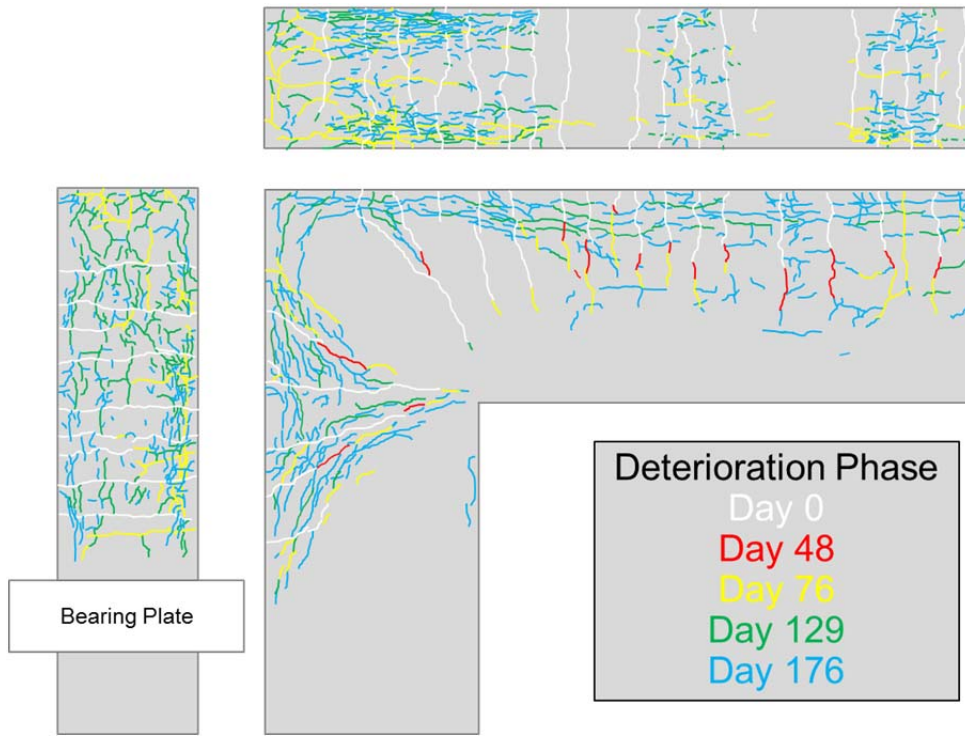
#### 5.4 VISUAL OBSERVATION OVER TIME

On the one D-region of Specimen 4 that was intentionally thermally shocked, fine map cracking was observed almost immediately. Figure 5–3a presents a photograph of the region affected by the thermal shock. Similar map cracking, but less pronounced, was observed at an early age in the other specimens in most locations as well. However, for both cases without and with thermal shock, the fine map cracking grew over time. Eventually some of these cracks merged with the load-induced cracks that developed when the post-tensioned prestress loads were applied; these were intended to emulate the gravity load effects on the prototype structure as depicted in Figure 5–3c. These cracks also continued to grow and widen as a result of creep effects in the first few months.

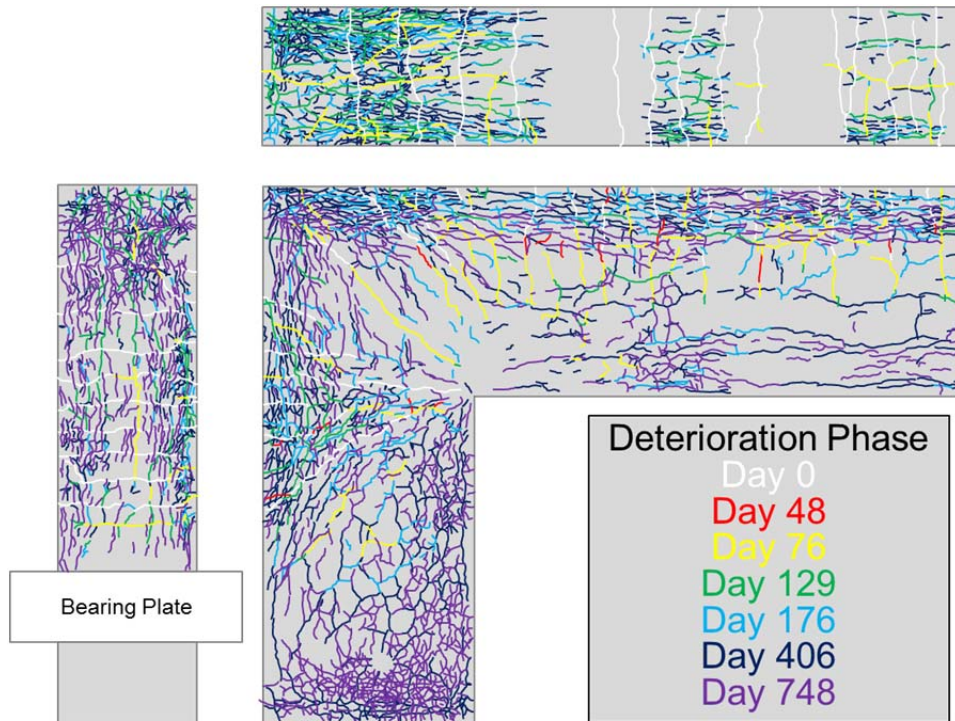
Figure 5–5 presents the crack patterns as recorded over time. Figure 5–5a presents the crack pattern of Specimen 2 after a 25-week (Day 176) exposure before physical testing. Longitudinal cracks were observed and merged with prestress load-induced cracking. For Specimen 4, a significant amount of cracks were observed after a 2-year (Day 748) exposure (Figure 5–5b). Map cracking due to the ASR effect merged with the load-induced and longitudinal cracks. At the time of writing, Specimen 3 remains in the field with weather conditioning and will be tested after some five years of total exposure to investigate DEF effect.

Figure 5–6a plots the first crack pattern of Specimen 4 of field observations at 48 days. In addition to the growth of the load-induced cracks, some new map cracking was noticed over the first 75 days along with some new cracks that aligned themselves with the longitudinal rebars, as show in Figure 5–6b. These new cracks may be interpreted as the indicator of incipient ASR formation. This view is supported by the measured surface and internal strains as presented and discussed below. The widening of the load-induced cracks provided additional access for the concrete to imbibe moisture.

In the field, the specimens were oriented as shown in Figure 5–4. As a consequence of the sprinkler system, water tended to saturate on the top side of joint and column. This provided sufficient water as an ingredient to promote the ASR/DEF formation. As shown in Figure 5–6c to Figure 5–6e, over time the initial thermal-induced map cracking grew in length and width and spread due to ASR effects and merged with the load-induced cracks. Such cracks gave an

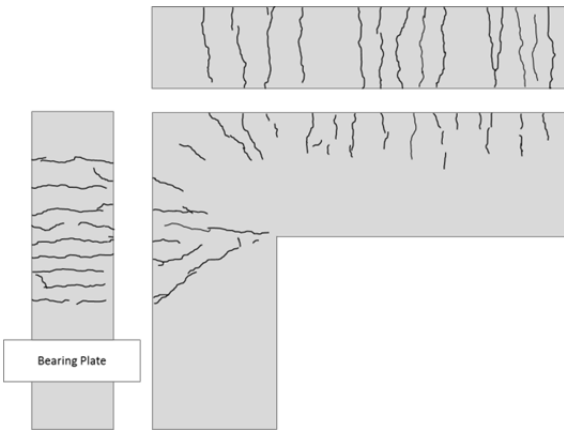


(a) Specimen 2

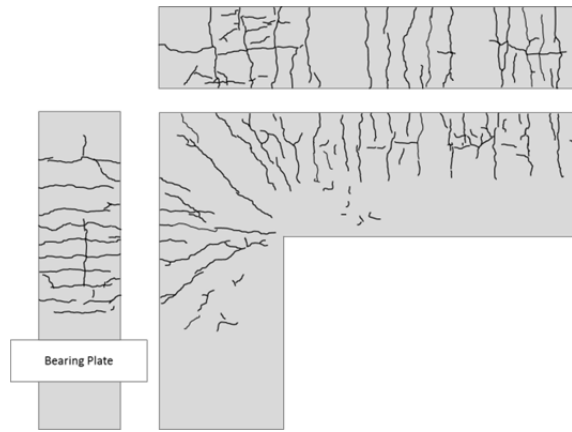


(b) Specimen 4

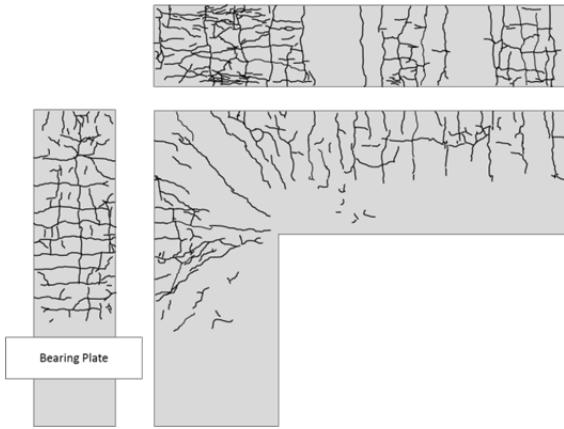
**Figure 5-5: Crack Patterns over Time.**



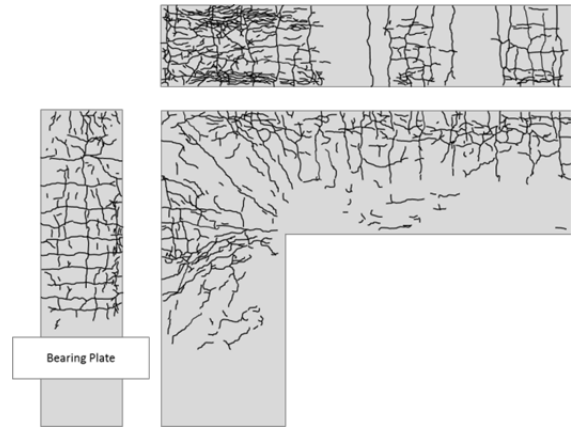
(a) Deterioration phase – Day 48



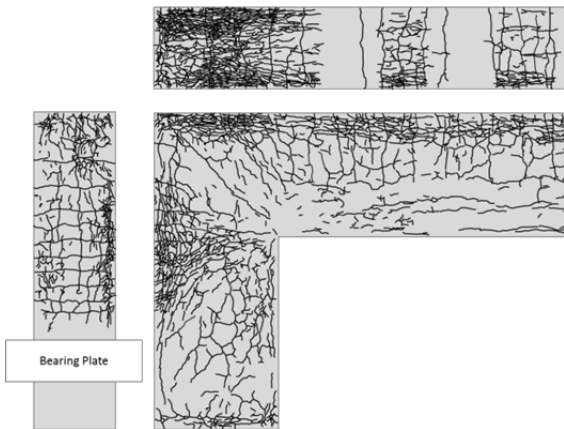
(b) Deterioration phase – Day 76



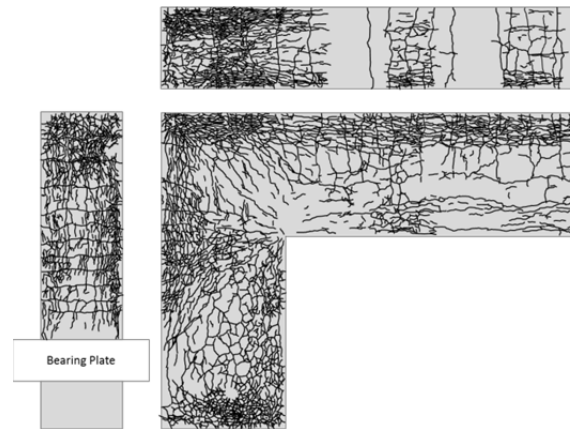
(c) Deterioration phase – Day 129



(d) Deterioration phase – Day 176



(e) Deterioration phase – Day 406



(f) Deterioration phase – Day 748

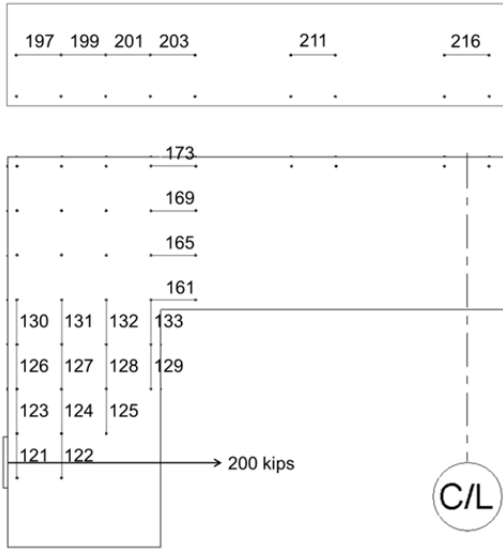
**Figure 5–6: Crack Patterns over Time – Specimen 4.**

appearance of cause for concern after 6 months, while after 15 months their appearance would give cause for alarm. These results are consistent with the evolution of ASR effects observed in laboratory studies (Swamy and Al-Asali, 1989 and 1998; Chana and Korobokis, 1991; Poole, 1992; Swamy, 1992; Ahmed et al., 1998, 1999a, and 1999b; Fan and Hanson, 1998a and 1998b; Berube et al., 2002; Jensen, 2003).

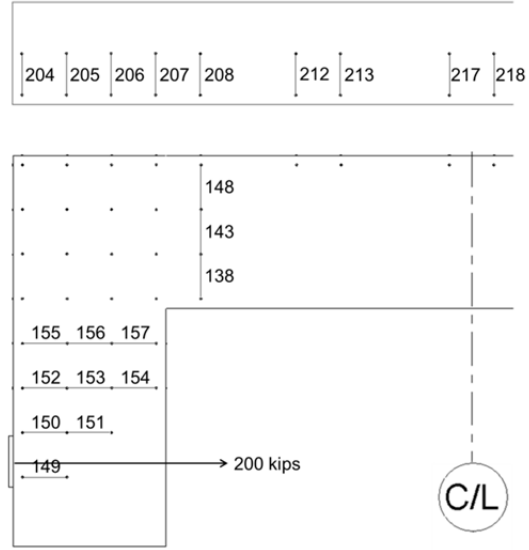
## **5.5 SURFACE CONCRETE STRAINS**

Figure 5–7 and Figure 5–8 present the time-dependent progression of strains at the surface in the beam, the beam column joint, and the column of Specimen 4. These strains are averaged as measured between two DEMEC points, normally 10.5 inch apart (267 mm), except when on a diagonal near the beam and the joint areas. After the initial loading that emulated the self-weight of a prototype bridge, all surface strains in each direction were less than the steel yield strain (0.0021). Nevertheless, over the first 2 months, some minor expansion was observed.

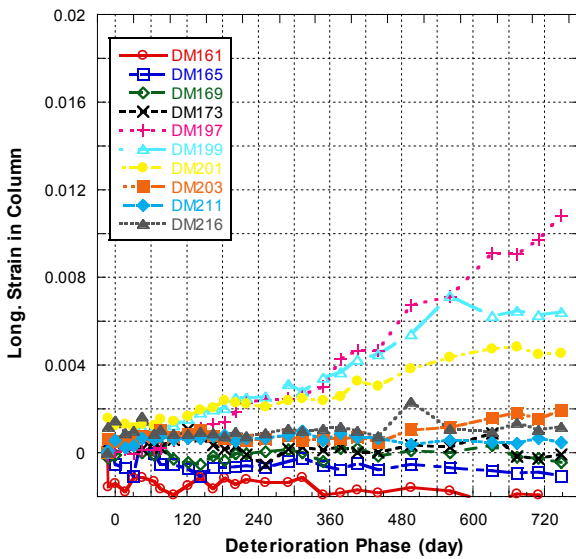
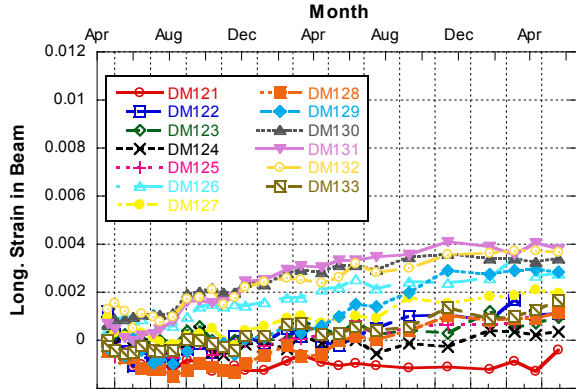
When the heat of Texas summer took effect in subsequent months, a higher deterioration rate was observed. Following the summertime exposure during the first year in the field, the side surface transverse strains at the joint reached 0.010 (DM205 and 206), while the longitudinal strains were less than 0.003 (DM197 and 199, Figure 5–7). Clearly the greater amount of longitudinal reinforcement close to the side surface at the joint was influential in restraining the concrete expansion. As the high heat plus wetting and drying effect subsided over the winter months, the rate of deterioration declined. Then once the heat returned in April, the deterioration rate increased and the surface strains grew at a greater rate over the summer months. Over the two-year period of field curing, strains in excess of 0.010 were observed in beam and joint areas, while the outer surface strains of the joint significantly enlarged to over 0.020. These observations verified the well-known assumption that the wetting and drying mechanism induced by high temperature were the drivers for ASR/DEF formation. Since the deterioration rate was rapid from April to October, from the observed results it may be inferred that the ASR/DEF mechanism damage accelerated once temperatures exceed 80 °F (Figure 5–4a).



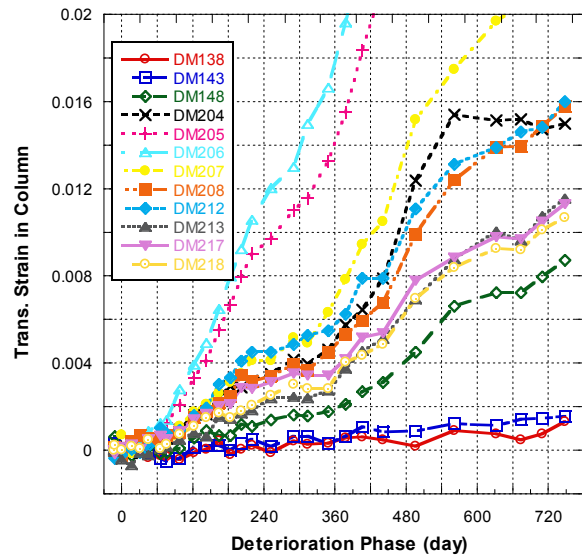
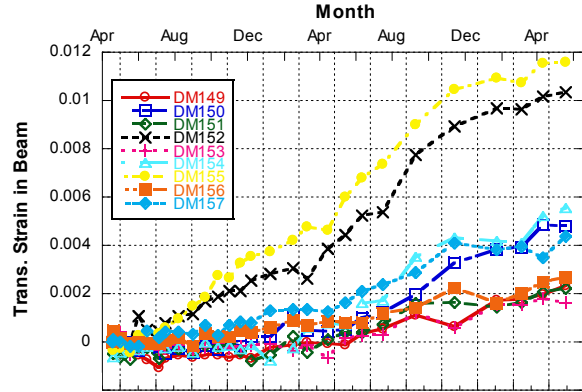
(a) Longitudinal readings



(b) Transverse readings



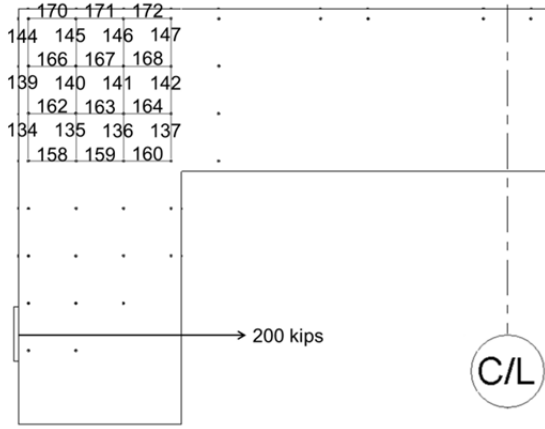
(c) Longitudinal strain



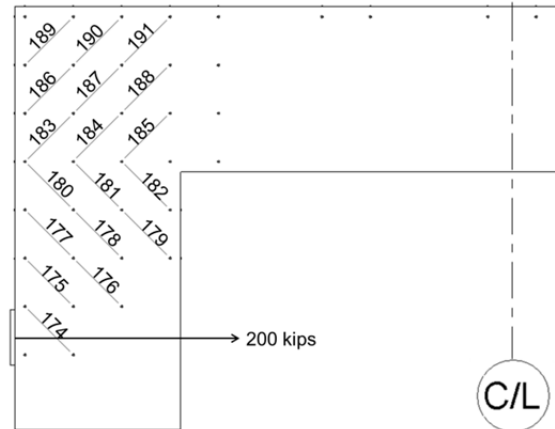
(d) Transverse strain

**Figure 5-7: Surface Concrete Strain in Longitudinal and Transverse Directions from DEMEC Readings – Specimen 4.**

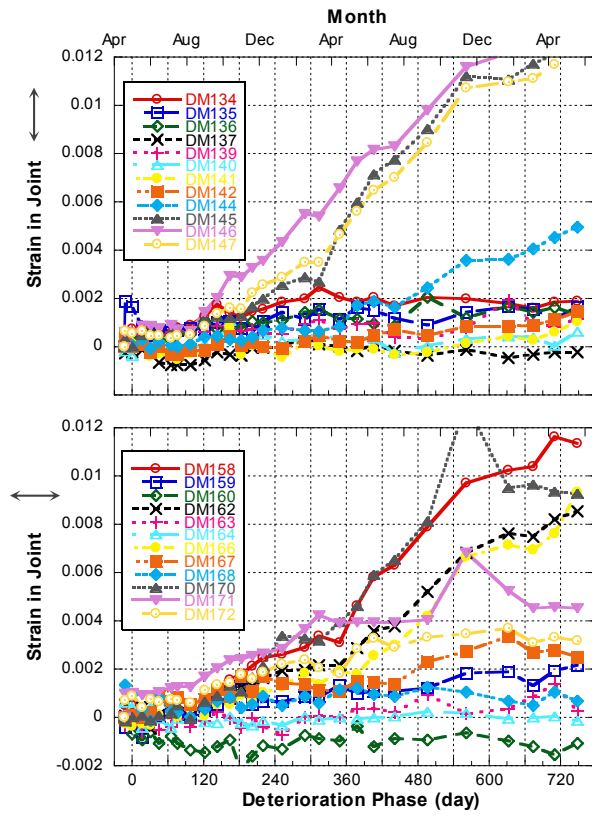




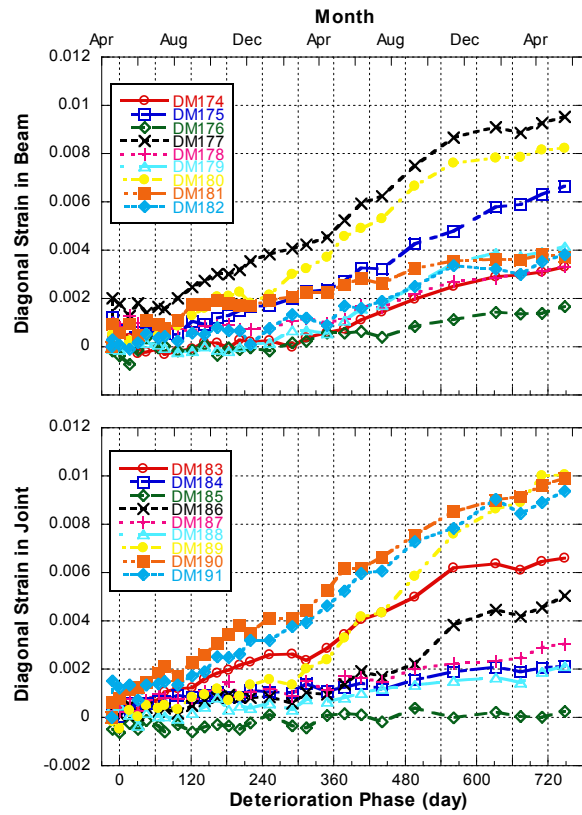
(a) Joint readings



(b) Diagonal readings



(c) Joint strain



(d) Diagonal strain

**Figure 5–8: Surface Concrete Strain in Joint and Across the Diagonals of the DEMEC Grid – Specimen 4.**

### 5.5.1 Mohr's Circle

As shown in Figure 5–8, it may be observed that at 20 months (Dec 2010) the longitudinal surface concrete strains at the outer beam column joint (DM144 and 170) were approximately 0.004 and 0.012, respectively. Plotting this result on Mohr's circle of strain, as shown in Figure 5–9, the strain in the diagonal ( $\theta = 45^\circ$ ) direction may be obtained by rotating ( $2\theta = 90^\circ$ ). Thus, the diagonal strain in the strut would be  $\epsilon = 0.008$ . This result is keeping with an average of the diagonal strains measured in the joint (DM189), as shown in Figure 5–8d.

### 5.6 INTERNAL CONCRETE STRAINS

In order to detect the behavior of core concrete, six concrete gages (KM) for each side of the specimens were embedded in the specimen core. Figure 5–10 depicts the concrete strains measured over the first two years of the specimen life within the central region of the beam (gages KM1-KM3) and beam column joint (gages KM4-KM6). The concrete strains of the SAT diagonal struts in the directions from loading point to the inner corner of the joint (gage KM1) and from outer corner to the inner corner of the joint (gage KM4) remained in compression and varied little over time. However, it was observed that the concrete strains perpendicular to these struts (gages KM2 and KM5) reached 0.001 after the first summer and increased to over 0.002 over two years. In the out of plane direction (gages KM3 and KM6), however, the concrete strains expanded significantly during the second summer and reached over 0.005 after a two-year period. It was observed that the core concrete tended to expand more across the width of the specimen. This is considered to be the case because the transverse hoops (restricted to the perimeter of the cross-section) provided relatively little restraint against the ASR expansion effects (i.e., minimal confinement).

### 5.7 REINFORCING STEEL STRAINS

Figure 5–11 shows the reinforcing steel strains over a two-year period for Specimen 4. Once loaded by the prestress (15 days prior to deterioration phase), the strains in the main longitudinal bar were immediately within the range of 0.0005 to 0.0008 (22 to 36 percent of yield strain, Figure 5–11b and c) before the specimens were shipped to the field. The reinforcing strains then

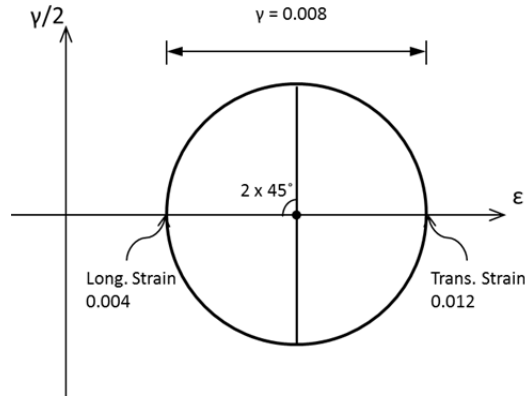
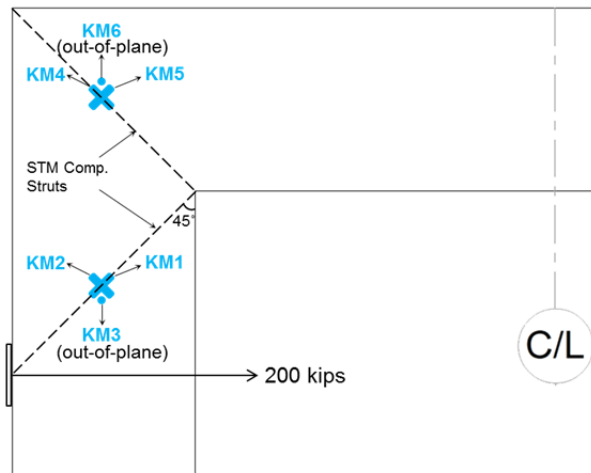
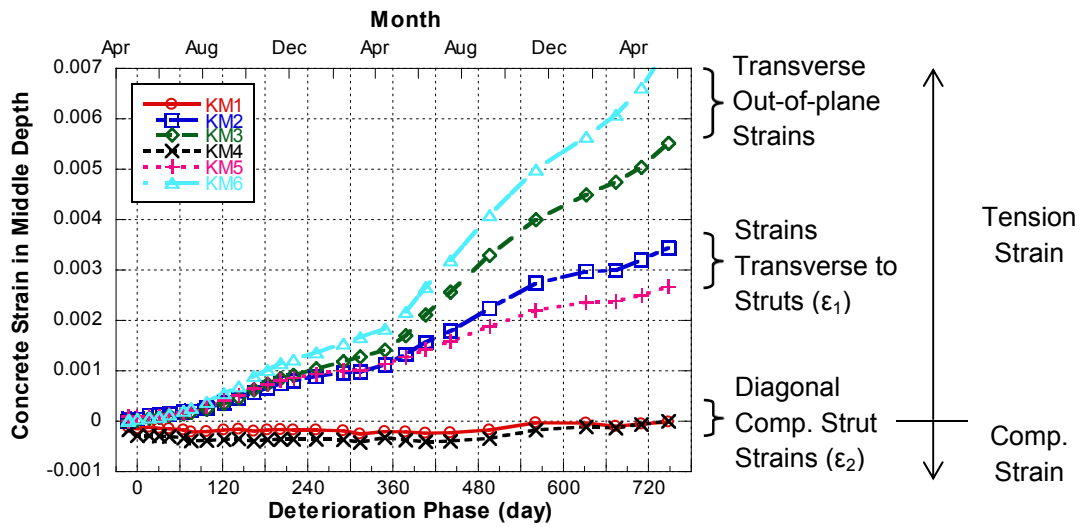


Figure 5-9: Mohr's Circle.

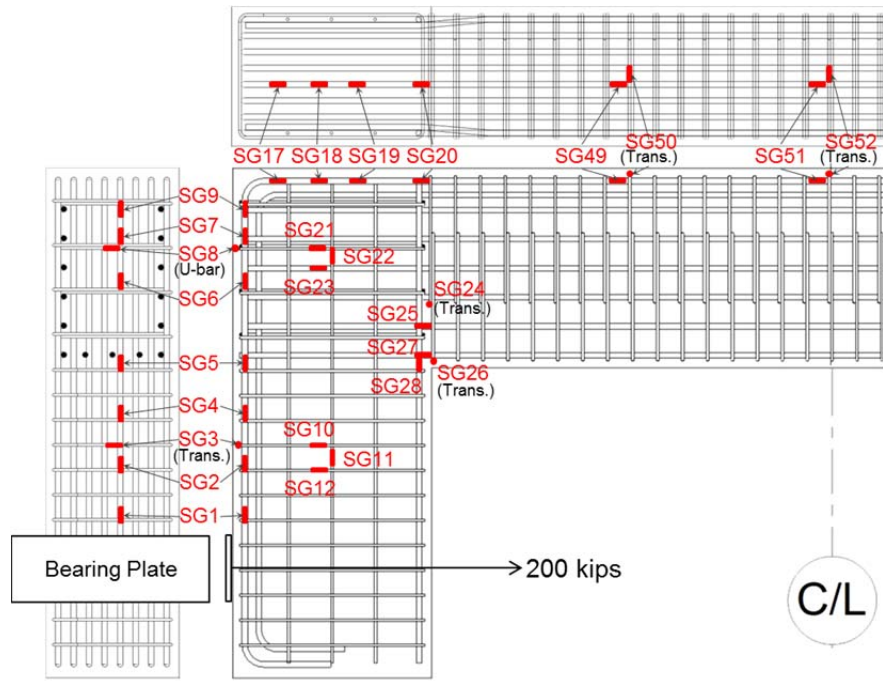


(a) Orientations of concrete gages in middle depth

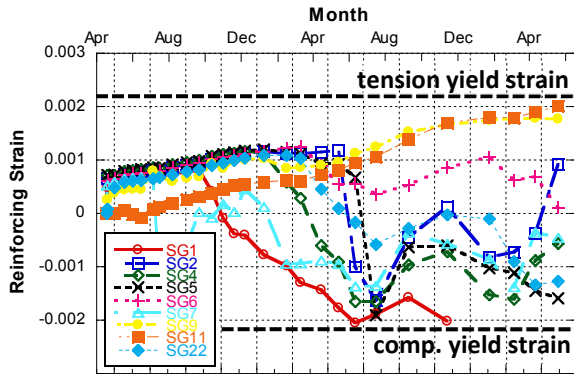


(b) Concrete strain in middle depth

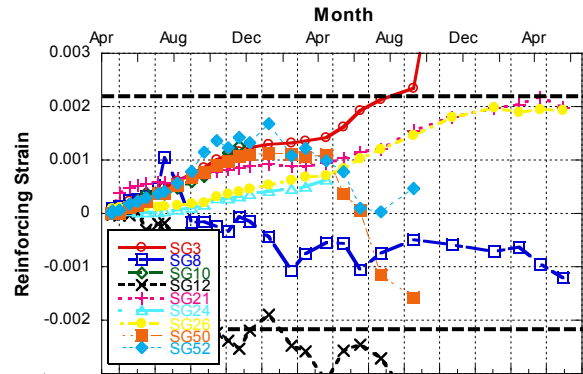
Figure 5-10: Mid-Depth Strain Behavior of the Concrete as Measured by Concrete Gages – Specimen 4.



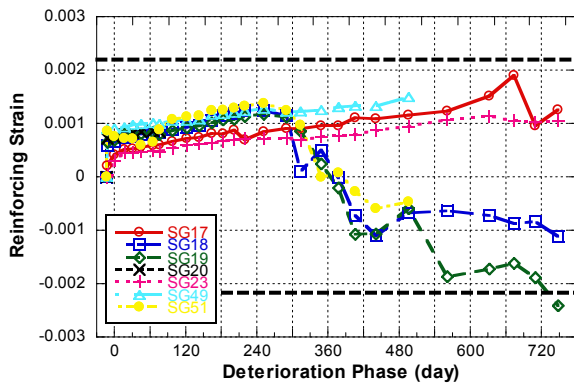
(a) Layout of strain gages attached to reinforcing steel



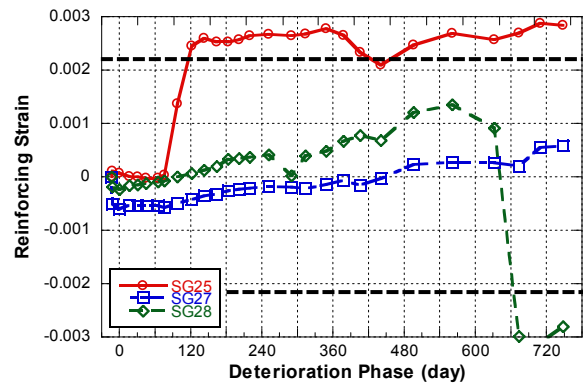
(b) Longitudinal steel in beam



(d) Transverse steel and U-bar



(c) Longitudinal steel in column



(e) Compression zone

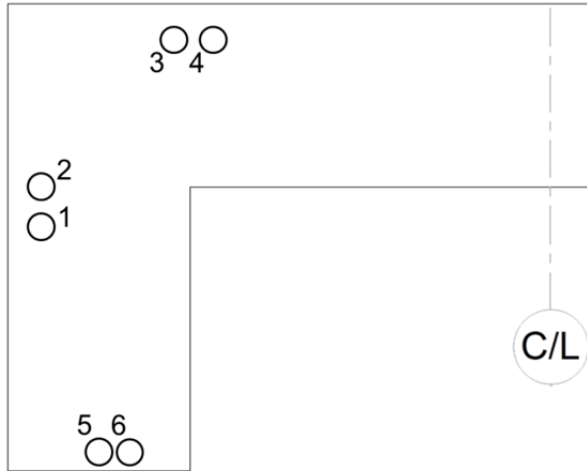
Figure 5–11: Reinforcing Steel Strain from Strain Gages – Specimen 4.

gradually increased in the first four months. In the subsequent period, compression strains were recorded. This most likely indicated force re-distribution between the main longitudinal rebars. Also, formation of ASR gel around the rebars may cause de-bonding between the concrete and steel and resulted in local compression strains. Note that there was a longitudinal crack right above the longitudinal rebar that was instrumented with strain gages. This crack possibly introduced more moisture, promoted local formation of ASR gel, and caused the unpredictability of measured reinforcing steel strains. Also, faulty readings may have been recorded due to the development of faulty gages over time from the ASR/DEF deterioration. Note that several gages failed (stopped reading) due to the ASR/DEF deterioration over time.

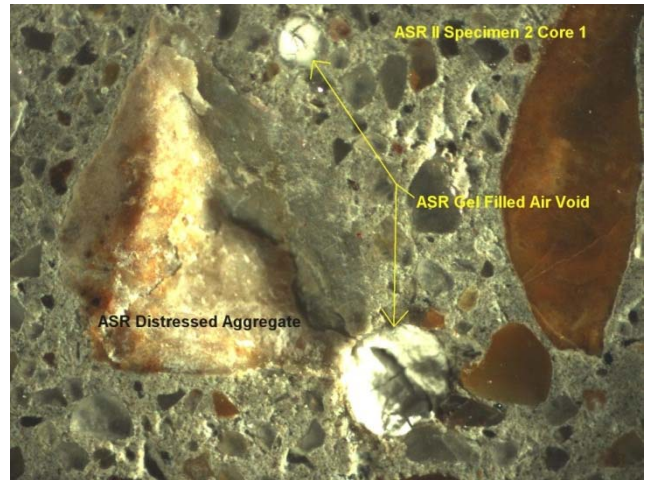
The strain in the hoop steel (gage SG3) gradually increased during the summer and reached the tensile yield strain at about 70 weeks (Figure 5–11d). It is evident that the ASR expansion introduced some confining effect to core concrete and eventually led the hoop steel reach yield strain. It is also evident that the ASR-induced deterioration in the cover concrete would offset any beneficial confining effect in the core concrete. Due to the unpredictability of the locations of ASR gel formation, other reinforcing strains as recorded appeared to have random patterns (Figure 5–11d and e). This might result from local force re-distribution and de-bonding between concrete and reinforcing steel.

## **5.8 POST-TEST CORES**

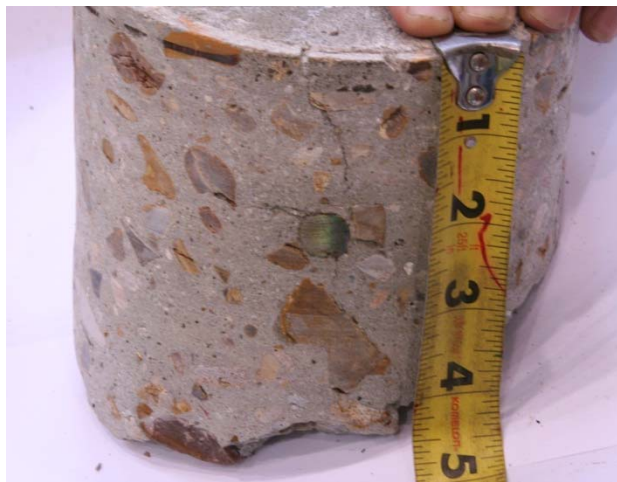
A post-test petrographic analysis of cores of Specimens 1 and 2 with no/minor damage that followed the destructive test was conducted by TxDOT personnel. For Specimen 1, it was reported that ASR gel was observed at the paste aggregate interface but the amount was sparse. The gel did not exhibit shrinkage cracking indicating that the gel had not absorbed much water. Figure 5–12a depicts the core locations of Specimen 2. It was reported that surface cracks with a maximum width of 0.016 inches were traced from the surface to a depth of 2.5 inches (64 mm) (Figure 5–12b and c). Figure 5–12d and e shows two photographs of the cores taken for the petrographic analysis. Figure 5–12d shows where ASR gel was observed in air voids adjacent to reactive particles, consequently the neighboring aggregates showed signs of distress due to the ASR expansion. The ASR-distressed level was reported as moderate to high. This petrographic evidence confirmed the formation of ASR in the concrete.



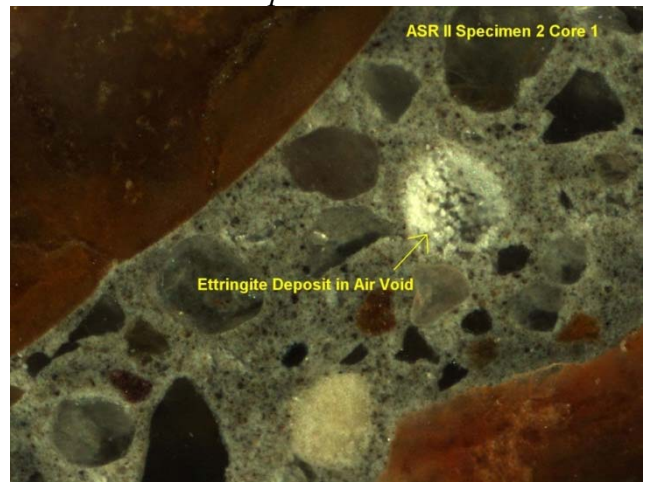
(a) Core locations



(d) ASR filled air voids adjacent to reactive particle



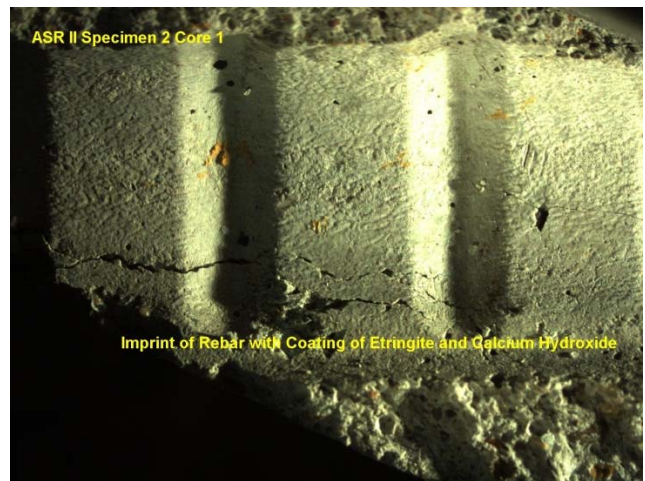
(b) Crack from the surface to reinforcing steel (Core 1)



(e) Accumulation of ettringite in air void



(c) Crack from the surface to reinforcing steel (Core 2)



(f) Imprint of rebar with accumulation of ettringite

**Figure 5–12: Petrographic Results of Specimen 2 after Eight Months' Exposure.**

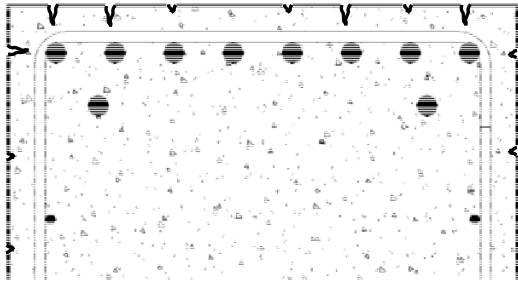
In Figure 5–12e, petrographic analysis showed signs of ettringite formation within voids and cracks. DEF was also found at the interface of aggregates and cement paste plus coating at the steel bar imprint (Figure 5–12f). Although only minor accumulation of ettringite was observed, this indicated that the onset of DEF commenced within the first eight months of age; this effect would be expected to develop somewhat further over time. At the time of reporting, the cores of Specimen 4 are under analysis by TxDOT personnel.

## 5.9 DISCUSSION

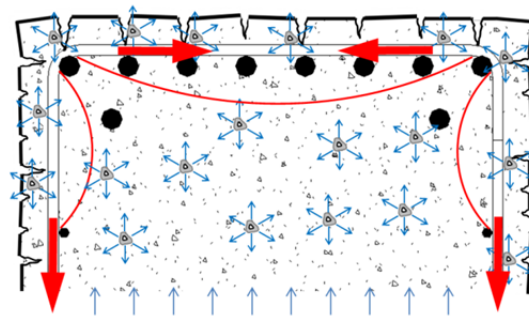
Figure 5–13 presents a hypothesis that attempts to explain the performance of structures affected by ASR/DEF. After construction, various reasons such as rapid temperature drop (thermal shock) after removing formwork and subsequent structural/constructional loading may cause fine (map) cracking mostly on the surface and in the cover region (Figure 5–13a). The cracks, albeit very fine, serve as an avenue for moisture ingress. If active aggregates are present in the concrete mix or if the curing temperature was high, there is the possibility of either ASR and/or DEF effects.

Once cracking has formed in the cover region, a pathway for moisture penetration is formed, thus leading to the possibility of ASR/DEF formation within both the cover and core concrete regions, as depicted in Figure 5–13b. ASR/DEF effects lead to expansive strains. In the unconfined cover concrete this evidently leads to further cracking while within the core concrete, expansive strains induce tension forces on the reinforcing steel. These forces tend to restrain further ASR/DEF expansion effects due to the provision of a passive confining action. It is postulated that this beneficial confining effect inhibits or offsets further ASR/DEF deterioration. It is for this reason that the damage to the concrete is mostly restricted to about a 5 inch band around the perimeter of the section.

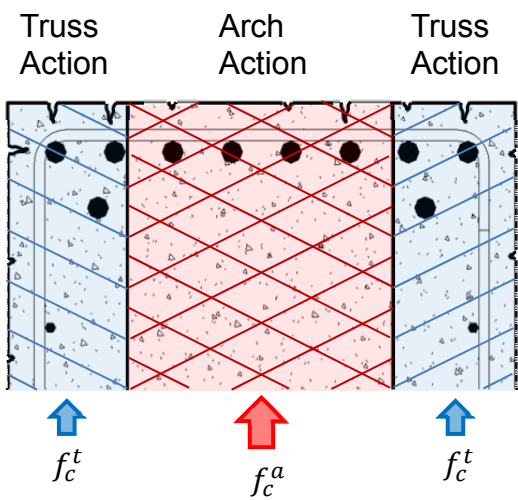
Once damaged, the ASR/DEF expansion in the cover causes incipient spalling such that the resistance contribution of cover concrete diminishes. However, the expansion in the core also causes a confining effect that provides more compressive strength in the core. This offsets some of the damage in the cover and may provide a substantially beneficial effect to the structure. Although significant visual damage would seriously concern engineers and owners, the performance in terms of the strength of the structure may not be significantly impaired, if at all.



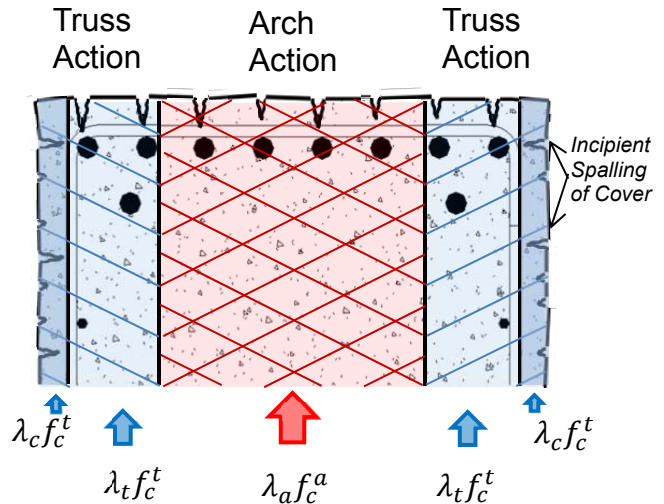
(a) Structure without ASR/DEF



(b) Partially pre-confined due to ASR/DEF



(c) No confining effect



(d) Actively confined due to ASR/DEF effects

**Figure 5–13: Performance without and with ASR/DEF Expansions.**



As shown in Figure 5–13c, the strength of the truss and arch concrete at incipient failure may be respectively assigned as  $f_c^t$  and  $f_c^a$  for the case without concrete material damage. If, however, ASR/DEF deterioration takes place over time, the material strengths may be adjusted by a scalar depending on the location in the cross section. For this purpose, let  $\lambda_c$ ,  $\lambda_t$ , and  $\lambda_a$  be the material reduction parameters for the cover, the truss (within the core concrete), and the arch, respectively, as shown in Figure 5–13d. These parameters need to be evaluated through experimental tests and analysis, which follows in Chapter 8. It is expected that both  $\lambda_c$  and  $\lambda_t < 1$  because of excessive cracking and spalling of the cover concrete, and  $0.85 < \lambda_a < 1.15$ . For the latter, when  $\lambda_a > 1$ , this signifies a beneficial biaxial stress field exists that is induced by the expansion of the core but restrained and confined by the hoops. This hypothesis is examined further through physical testing and advanced analysis using a new SAT approach in the following chapters.

## 5.10 CLOSURE AND KEY FINDINGS

By combining high reactive aggregates along with a mix dosage of a sodium hydroxide solution and Type III cement, large-scale reinforced concrete specimens representative of modern bridge piers with D-regions constructed in Texas were successfully constructed and aged for up to two years in the field to promote ASR/DEF effects. Substantial map micro-cracking was observed. On one face of Specimen 4, that was thermally shocked, the map micro-cracking was more pronounced. The specimens were loaded via external prestress to emulate the self-weight effects of the entire bridge structure and then transported to the field for conditioning under accelerated wetting and drying cycles. The specimens were “irrigated” with water for 15 minutes four times per day to observe the long-term conditioning in the Texas heat.

In this study, the premature concrete deterioration (ASR/DEF) damage levels of affected specimens were defined by monitoring the surface concrete strains, internal concrete strains, and reinforcing steel strains over time. Without embedded instrumentation, the damage levels can only be determined by external observation and measurement. The recorded strains were correlated to the external cracking pattern and measured crack width. The applied loads to mimic upper structure gravity caused the bridge bents and piers to develop initial cracks with less than 0.005 inch ( $\leq 0.13$  mm) in width. With ASR/DEF effects, new map cracking was observed and

merged with the initial cracks over time. The initial cracks propagated and expanded in width. The maximum crack of 0.020 inch (0.50 mm) in width was measured for the specimen with minor damage (Specimen 2). For the specimen with moderate damage (Specimen 4), more map cracking was observed and spread all over the concrete surface. New map cracking was perceived in the compression side of the bridge bents and piers. The maximum measured crack width was 0.050 inch (1.3 mm). At the time of reporting, Specimen 3 is still in the field with weathering condition and supplemental watering. Severe damage is expected with more field exposure. The correlated cracking pattern and crack width will be reported in the final report.

The key findings from the experimental program are as follows:

- Early formations of ASR gel were observed, and then over the next two years considerable growth of the load-induced cracks plus numerous new cracks were observed.
- Crack widths of some 0.020 inch (0.5 mm) and 0.050 inch (1.3 mm) were noticed at six months and 15 months, respectively. With this evolving rate of ASR effects, it may be postulated that at six months bridge inspectors would become very *concerned*. However, after 15 months and certainly by the time of the first required biannual inspection, bridge inspectors would be potentially *alarmed by the poor appearance and condition* of the piers. It should be noted, however, that the mix used in the experiments led to an aggressive progression of ASR/DEF deterioration; not all structures with ASR/DEF reactions will progress this rapidly.
- Tensile yield strain in the hoop steel was observed at 70 weeks. It is postulated that this may well provide a beneficial confining effect to the core concrete offsetting the more visible evidence of ASR-induced deterioration in the cover concrete.

However, whether these visually disturbing signs are indicative of deterioration in strength and/or deformation capacity is the subject of the experimental investigation presented in Chapter 7 in conjunction with computational modeling of the force-deformation behavior through failure in Chapter 8.

## **6 CONTROLLING THE INTERNAL TEMPERATURE OF CURING CONCRETE**

### **6.1 SCOPE**

It is well-documented that DEF either requires or is most prevalent when the internal temperature of concrete exceeds about 150 – 160 °F (about 65-70 °C) for several hours during the 24 hours following initial mixing (Thomas et al., 2008; Barbarulo et al., 2005; Taylor et al., 2001; Ronne and Hammer, 1999; Lawrence 1995). Research has indicated that the high temperatures result in increased adsorption of sulfate ions by the calcium silicate hydrate phase (Taylor et al., 2001; Shimada and Young, 2004; Fu et al., 1994 and 1995). After the concrete begins to cool, these sulfate ions are released back into the pore solution and are thus available to convert the previously formed monosulfoaluminate (monosulfate) into ettringite. The formation of the ettringite results in expansive pressure and subsequent damage.

Concrete within large field structures (e.g., bridge substructures, etc.) may readily achieve sustained temperatures greater than 160 °F (about 70 °C). However, in temperature-controlled laboratories where solar radiation is not present, it is more difficult to achieve such temperatures while maintaining representative mixture and structural designs. Therefore, in order to replicate concrete temperatures experienced in field structures in controlled lab environments for the purpose of generating DEF, it is necessary to devise a means for heat generation and control within the concrete.

The objectives of this portion of the research project were to

- Estimate or model the amount of heat required to raise (and sustain) concrete to the appropriate temperature for DEF to occur.
- Devise a simple means of supplying the necessary heat to the concrete.
- Evaluate the model efficacy by comparison of predicted temperature history to measured temperature history in experiments.

### **6.2 ESTIMATING REQUIRED INTERNAL HEAT SUPPLY**

In order to estimate the internal heat supply required to boost the internal concrete temperature of the structural elements to the appropriate level for the appropriate period of time, it was first

necessary to estimate the temperature of the concrete if no actions were taken to control it. To this end, a simple 1-D thermal model was developed. Assuming no other sources of energy present other than thermal, the conservation of energy may be expressed according to:

$$\frac{dq}{dt} = -\text{div}(j_q) + q_{gen} \quad (6-1)$$

where  $t$  is elapsed time,  $q$  is the volume-specific thermal energy (units of  $\text{J}/\text{m}^3$ ),  $j_q$  is the heat flux density (units of  $\text{J}/(\text{m}^2\text{-s})$ ), and  $q_{gen}$  is the *rate* of local heat production (units of  $\text{J}/(\text{m}^3\text{-s})$ ). If we assume a linear constitutive relationship between the heat flux density and the thermal affinity, we arrive at Fourier's law:

$$j_q = -k\nabla T \quad (6-2)$$

where  $T$  is the temperature (units of kelvins),  $k$  is the thermal conductivity tensor (units of  $\text{W}/(\text{m}\cdot\text{k})$ ), which, for an isotropic material such as concrete, simplifies to  $k = kI$  where  $I$  is the identity tensor and  $k$  is the scalar thermal conductivity. Combining Eq. (6-1) and Eq. (6-2) while assuming isotropy yields:

$$\frac{dq}{dt} = \text{div}(kI\nabla T) + q_{gen} \quad (6-3)$$

The rate of the volume-specific thermal energy may be expressed by:

$$\frac{dq}{dt} = \frac{d}{dt}(T\rho c_p) \quad (6-4)$$

where  $\rho$  is the density (units of  $\text{kg}/\text{m}^3$ ) and  $c_p$  is the mass-specific heat capacity at constant applied pressure (units of  $\text{J}/(\text{kg}\cdot\text{k})$ ). Substituting Eq. (6-4) into Eq. (6-3) results in an alternative governing equation for heat transfer according to:

$$\frac{d}{dt}(T\rho c_p) = \text{div}(kI\nabla T) + q_{gen} \quad (6-5)$$

If we approximate that  $\rho$  and  $c_p$  are time-independent and that  $k$  is spatially independent, then Eq. (6-5) simplifies to:

$$\frac{1}{\alpha} \frac{dT}{dt} = \text{Idiv}(\nabla T) + \frac{1}{k} q_{gen} \quad (6-6)$$

where  $\alpha = k/(\rho c_p)$  is the thermal diffusivity. With appropriate boundary conditions, Eq. (6-6) may be solved to determine the time and spatially dependent distribution of temperatures within a conductive body.

In this project, the cross-sectional dimensions of the concrete elements allowed approximation of the heat flow as one dimensional. Thus, Eq. (6-6) simplifies to:

$$\frac{1}{\alpha} \frac{dT(x,t)}{dt} = \frac{\partial^2 T(x,t)}{\partial x^2} + \frac{1}{k} q_{gen}(x,t) \quad (6-7)$$

where  $x$  is the linear position across the element cross-section. In order to enhance the temperature rise in the concrete due strictly to heat of hydration, the concrete elements were insulated with 6 inches ( $\sim 15$  cm) of fiberglass batt insulation (see Figure 6-1). Therefore, in order to effectively model the temperature rise throughout the concrete cross-section, it was necessary to apply Eq. (6-7) to the concrete and also to the insulation on either side of the concrete. The boundary conditions were assumed to be such that the temperature on the outer surface of the insulation was the average laboratory temperature (73 °F or 23 °C). At the interface between the insulation and the concrete, the divergence of the heat flux in the  $x$  direction was assumed to be zero. That is, any heat leaving the concrete was assumed to be entering the neighboring insulation. With these boundary conditions, governing equations were generated for both layers of insulation as well as the concrete; the three equations were then solved simultaneously (in the Laplace transform domain). By numerically inverting into the time domain,  $T(x,t)$  was determined for the concrete beam.

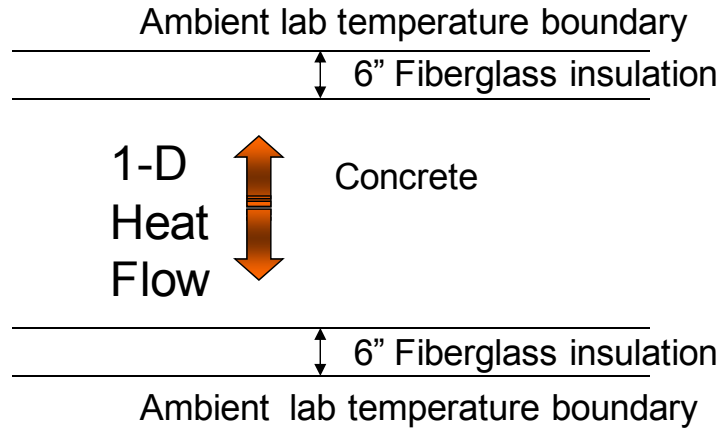
The heat of hydration is accounted for in the term  $q_{gen}(x,t)$ . To estimate the temperature rise in the insulated concrete element due to heat of hydration alone, it was approximated that the rate of hydration was independent of spatial position (i.e.,  $q_{gen}(x,t) = q_{gen}(t)$ ). Furthermore, it was

assumed that the heat of hydration could be expressed as a two-term Gaussian series according to:

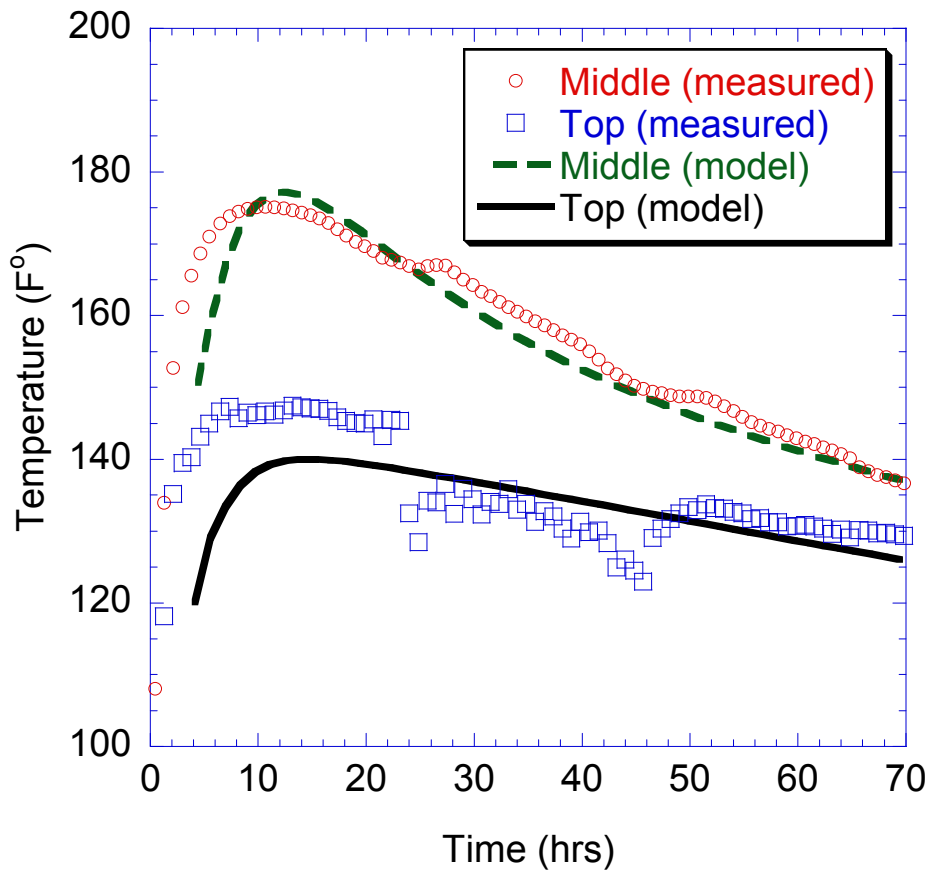
$$q_{gen}(t) = \sum_{i=1}^2 a_i \exp\left(-\left(\frac{t-b_i}{c_i}\right)^2\right) \quad (6-8)$$

where  $a_i$ ,  $b_i$ , and  $c_i$  are empirical constants determining the magnitude, rate, and shape of the heat generation curve. To determine appropriate values for the empirical constants, the total heat of hydration expected at 24 hours was approximated using values found in the literature. Based on values found in Černý and Rovnaníková (2002), for a typical Portland cement the total heat expected to be produced at full hydration is about 410,000 J/kg. Based on the cement content of the concrete mixture used in this research (i.e., 752 lb/yd<sup>3</sup>), if the degree of hydration at 24 hours is approximated as 0.6, then the total heat of hydration expected to be produced during the first 24 hours after casting is about 0.116 kWh/gal (110 MJ/m<sup>3</sup>) of concrete. Values for  $a_i$ ,  $b_i$ , and  $c_i$  were determined by integrating Eq. (6–8) from  $t=0$  to  $t=24$  hours and setting the function equal to 110 MJ. Other restrictions on the empirical constants were prescribed based on the expected shape of the heat of hydration curve. Finally, the empirical constants were fine-tuned by comparison of the final expected temperatures in the concrete to model predictions. The final values used in the modeling are given in Table 6–1. For the complete heat analysis program, which was written in *Mathematica*, see Appendix A.

Figure 6–2 shows the measured and modeled concrete temperatures (at the middle and top of the concrete element) when no efforts were made to increase or control the concrete temperatures. The concrete used was the same concrete mixture that would be used for each structural element produced in this study. First, one sees in the Figure 6–2 that without additional measures the concrete temperature will not be sustained at high enough levels to promote DEF. This is true at both the surface of the concrete and within the center of the concrete cross-section, indicating that in the controlled laboratory environment the heat of hydration is insufficient to generate the necessary temperature history for DEF promotion. This is, of course, dependent on the specimen size and the concrete mixture design utilized. Alternative geometries, laboratory conditions, or concrete mixtures may produce different results.



**Figure 6–1: Model Conditions for Heat Flow Analysis Used to Predict Temperature History in Hydrating Concrete Beams.**



**Figure 6–2: Measured and Modeled Concrete Temperatures When No External Devices Were Used to Increase/Control Internal Temperature.**

Second, one sees in Figure 6–2 that the modeled temperature history agrees fairly well with the measured history at both the top and middle locations. It appears that the measured temperature increases faster than that predicted by the model, but this might be due to the fact that the concrete placed in the forms had already started to react during initial mixing and placement, whereas the model time zero was at the moment of concrete placement (rather than initial mixing). In any event, the model was determined to give a reasonably accurate prediction of peak temperature and temperature distributions within the concrete. Therefore, the model was used to investigate what measures could be implemented in order to control and increase the internal temperature in concrete such that DEF would be promoted.

**Table 6–1: Material Properties and Empirical Constants Utilized in Predicting Concrete Temperature History.**

	Concrete	Insulation
$c_p$ (J/(kg-k))	1000	-
$k$ (W/(m-k))	2	-
$\rho$ (kg/m <sup>3</sup> )	2400	-
$\alpha$ (m <sup>2</sup> /s)	$8.3 \times 10^{-7}$	$4.9 \times 10^{-7}$
$a_1$	1650	-
$a_2$	1580	-
$b_1$	18500	-
$b_2$	41000	-
$c_1$	10500	-
$c_2$	30000	-



### 6.3 NOVEL METHOD FOR SUPPLYING INTERNAL HEAT

In order to increase the internal temperature of the concrete to promote DEF, there are several potential options. First, one might attempt to increase the initial temperature of concrete constituents (e.g., the aggregates) prior to mixing. Second, one might try to increase the temperature of the fresh concrete prior to casting. Third, one might try to apply an external source of heat to the concrete in the forms after casting.

The first idea – increasing the temperature of the concrete constituents – was seriously considered. However, the expense and the number of potential challenges (e.g., controlling set, vaporization of mix water, etc.) led to the consideration of alternatives. Increasing the temperature of the fresh concrete also poses considerable challenges and thus this idea was likewise discounted. In the end, it was decided to apply an external source of heat to the concrete once it was cast in the forms.

In order to determine how much heat must be added (and at what locations) to achieve the proper temperature history, the model described in the previous section was used. Basically, simulations were run considering point heat sources at different distances from the surface of the concrete. The model can incorporate such heat sources by adding in additional  $q_{gen}(x,t)$  beyond that contributed through hydration. Simulations showed that due to the fairly low thermal conductivity of concrete, if only the surfaces of the concrete were heated, they would need to be heated to very high temperatures (i.e., above boiling temperature of water) to achieve a high enough sustained temperature in the middle of the concrete element. Therefore, it was determined to be necessary to include heat sources at the surfaces and at the center of the concrete element.

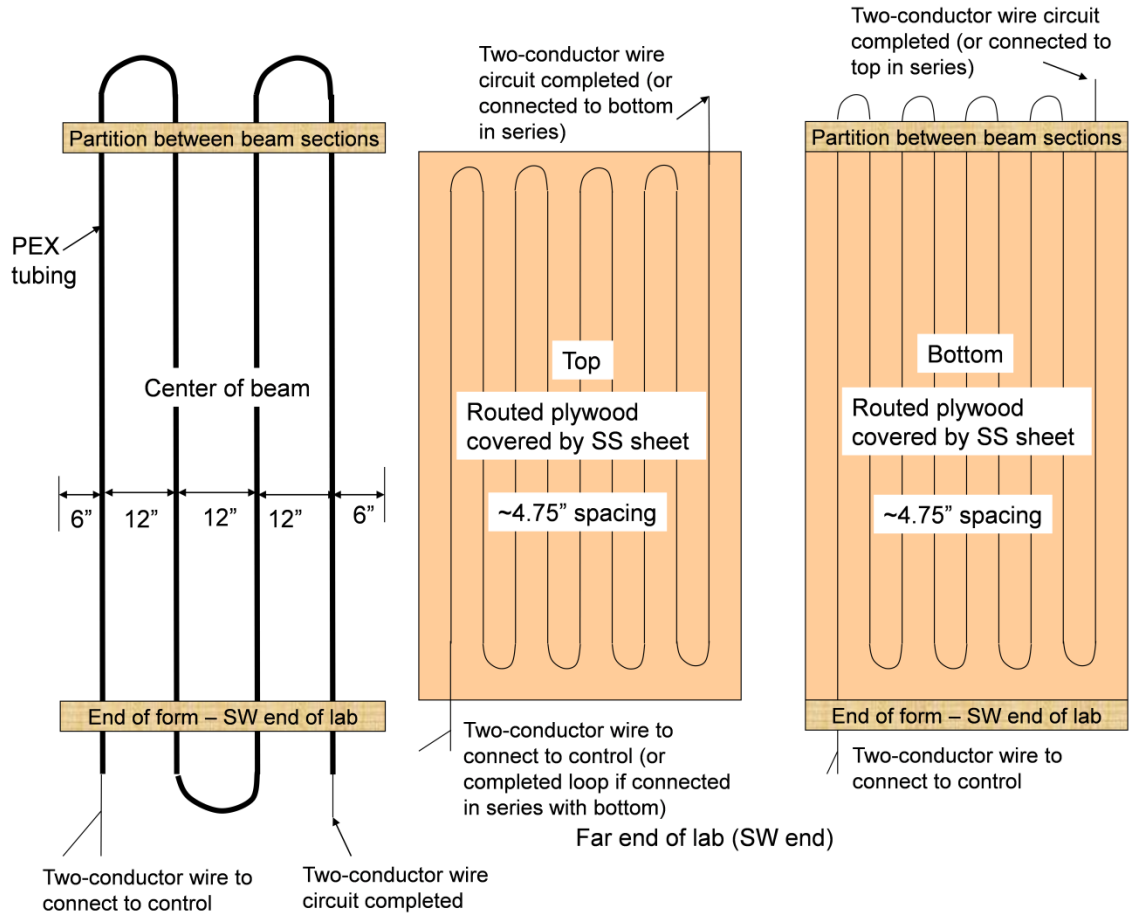
The model was also used in order to determine the magnitude of heat required per unit area at the top, bottom, and middle of the concrete element. The model results indicated that  $700 \text{ W/m}^2$  would be necessary on the surfaces and  $100 \text{ W/m}^2$  in the center of the concrete. While there are likely several ways for one to achieve the required thermal energy density, it was desirable to have an easily controllable supply of thermal energy to make any adjustments that might be necessary to accurately control the concrete temperature. Therefore, it was decided to use electrical resistive heating cables to supply heat to the concrete. In addition to being highly

controllable, electrical resistive heating cables (and their control units) are relatively inexpensive and reusable.

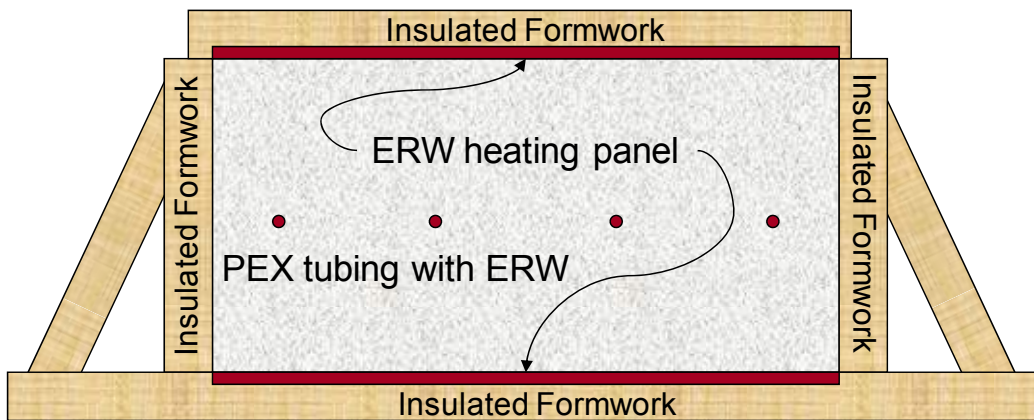
Suitable electrical resistive wire that had a maximum output of 20 W/ft was located on the top and bottom, and wire that had a maximum output of 10 W/ft was located at the center of the concrete. In order to achieve the correct total required heat supply, several runs of each wire were used at the top, bottom, and center of the concrete (Figure 6–3 and Figure 6–4). In order to reuse the resistive wire where possible (since there were multiple concrete elements to be cast), the top and bottom wiring was embedded within special forms. The forms were made from plywood that was routed to accept the wiring, then covered with a thermally conductive stainless steel (SS) sheet to protect the wiring from the fresh concrete. In the center of the concrete element, PEX tubing was mounted running through the length of the element. The wiring was routed through the PEX tubing, which allowed heat transfer from the wire to the concrete without allowing the wires to be in contact with the fresh concrete. Immediately after concrete was cast into the forms, the top form was placed on the fresh concrete and then covered by insulation. The heating wires were then immediately activated.

#### **6.4 RESULTS**

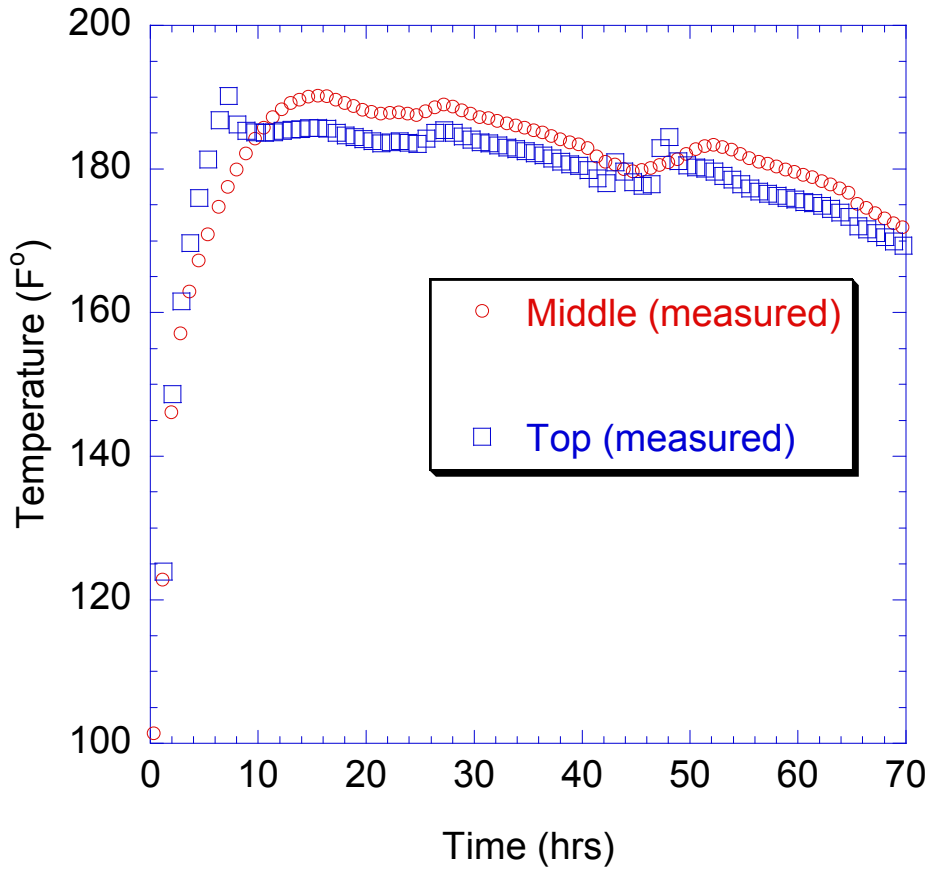
Figure 6–5 shows the measured temperature history from the time of casting for one of the concrete elements where the previously described method for heating the concrete beam was used. It is clear from Figure 6–5 that the use of electrical resistive wiring is an effective means for increasing the temperature of concrete in a controlled fashion. The temperatures were able to be increased above 180 °F for a sustained period (greater than 20 hours). Additionally, by applying greater heat to the surface and less heat to the center of the concrete, nearly uniform temperatures were achieved; that is, both the surface and center of the concrete were heated to above 180 °F for sustained periods. The measured temperature history of each beam is similar to that shown in Figure 6–5, demonstrating the repeatability of the temperature history produced by the novel heating technique.



**Figure 6-3: Layout of Electrical Resistive Wiring to Raise Concrete Temperature.**  
 Note: Wiring was placed in top and bottom plywood forms (with stainless steel (SS) sheets covering the wires) and in PEX tubing in the middle of the concrete element.



**Figure 6-4: Cross-Section View of ERW Heating Plan for Increasing/Controlling Concrete Temperature in Order to Promote DEF.**



**Figure 6-5: Measured Temperature History at the Top and Middle of Concrete Element Heated with Electrical Resistive Wiring.**

## **6.5 CLOSURE AND KEY FINDINGS**

A novel method of modeling and controlling the internal temperature of concrete elements in the laboratory is described. The model was used to determine the magnitude and appropriate location of externally supplied heat needed to achieve the necessary sustained internal concrete temperatures to promote DEF. Based on the model results, electrical resistive wiring was selected, placed on the outer forms, and routed through the center of the concrete elements to heat the concrete to the appropriate temperature.

The key observations from this study are summarized below:

- The measured concrete temperatures of unheated and heated beams shows that the novel heating method developed in this research project is effective at controlling and increasing the internal temperature of concrete elements in the laboratory.
- This technique was so effective, inexpensive, and simple that it is a recommended means of increasing concrete temperature in a controlled manner either in the laboratory or even in the field.



## 7 EXPERIMENTAL INVESTIGATION OF LARGE-SCALE SPECIMENS WITHOUT AND WITH ASR/DEF DETERIORATION EFFECTS

### 7.1 BACKGROUND AND SCOPE

This chapter presents the findings from the experimental testing of large-scale reinforced concrete D-region specimens that have undergone varying levels of premature concrete deterioration due to ASR and DEF (Specimen 1, control; Specimen 2, minor ASR/DEF damage; and Specimen 4, moderate ASR/DEF damage).

As discussed in the previous chapter, four specimens were designed and constructed with a special concrete mix and curing conditions for promoting and accelerating ASR/DEF effects. Three of the specimens (Specimen 2, 3, and 4) were used to investigate the structural performance under varying levels of ASR/DEF (minor, moderate, and severe ASR/DEF damage). These specimens, shortly after construction, were preloaded to mimic prototype gravity load effects and developed a moderate amount of hairline cracking that permits future moisture ingress. These specimens were then conditioned outdoors in an open field at the Texas A&M University Riverside campus. Supplemental watering was provided via a sprinkler system that applied four wetting and drying cycles per day.

One of the specimens (Specimen 2) was categorized as having *minor* ASR/DEF damage and was structurally load tested to failure after eight months of deterioration exposure, while another specimen (Specimen 4) was categorized as having *moderate* ASR/DEF damage and was structurally load tested to failure after a two-year deterioration exposure period. One of the constructed specimens (Specimen 1) was constructed and then stored in the structural testing lab, which has an air-conditioned controlled environment without supplemental water. This specimen was also structurally load tested to failure and represented the baseline structural behavior without ASR/DEF deterioration effects. The final specimen (Specimen 3) that remains at the outdoor facility under deterioration exposure conditions is continually being monitored under further ASR/DEF expansion.

The large-scale structural test results showed that the ASR/DEF-induced damage had no detrimental effects on the structural performance in terms of the ultimate strength, initial stiffness, and deformability for both the minor and moderately damaged specimens as compared to the control specimen. Post-test petrographic analysis of concrete cores taken from the specimen categorized with minor damage showed that the primary cause of distress in the concrete was due to ASR, although small accumulation of ettringite was found, but thought to be too small to create distress in the concrete. The ASR/DEF induced damage of the specimens categorized as minor and moderate damage was concentrated in the concrete cover. It is believed that the confining effect from the reinforcing steel cage under the concrete expansion due to ASR/DEF offset any detrimental effects of the concrete deterioration. The reporting of the petrography analysis of concrete cores taken from specimen categorized as moderate damage and the structural load testing of the final specimen will be shown in a later date.

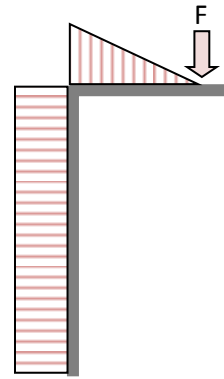
## **7.2 EXPERIMENTAL INVESTIGATION**

### **7.2.1 Representative Prototype, Test Setup, and Deterioration Conditions**

As discussed in the previous chapter and shown in Figure 7–1, the two bridge bents selected for designing the specimens for the experimental investigation were based on current bridge structures in Texas. Figure 7–2 presents the experimental specimens adopted for this research, as addressed in the previous chapter. Due to the large specimen size, an important feature was to ensure that each specimen could be structurally tested using a self-reacting system as shown in Figure 7–2a. Therefore, four “C” shape specimens, consisting of two D-regions, were designed and constructed. Figure 7–2b presents the specimen dimensions and the reinforcing details.

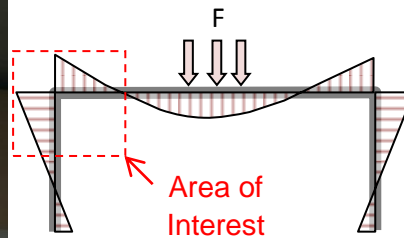
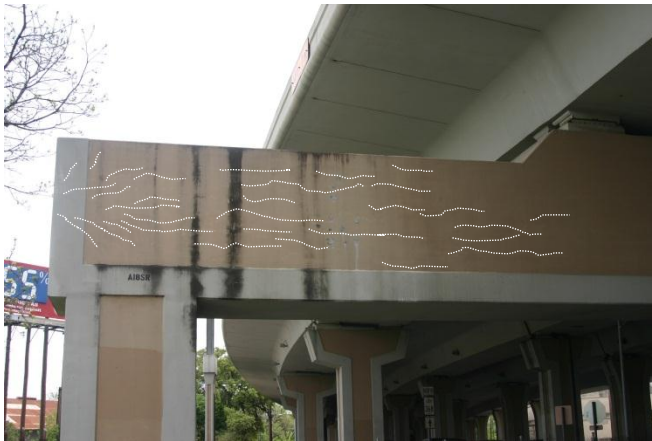
In order to investigate the effects of ASR/DEF, the specimens were constructed using a special concrete mix and curing conditions ideal for promoting both ASR and DEF effects. One of the four constructed specimens was stored in the structural testing lab under stable and dry climate-controlled conditions without external water. The other specimens were used to investigate the effects of varying levels of ASR/DEF damage on D-regions. Due to the initial applied loading that mimicked prototype gravity effects, a moderate amount of hairline cracking that permitted moisture ingress resulted. The specimens were conditioned outdoors in an open





Schematic BMD

(a) *Cantilevered bent*

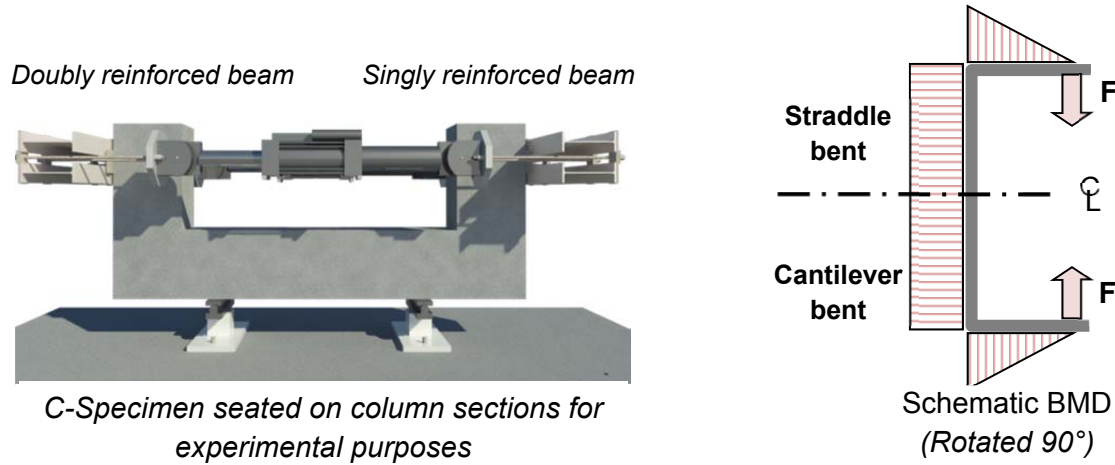


Schematic BMD

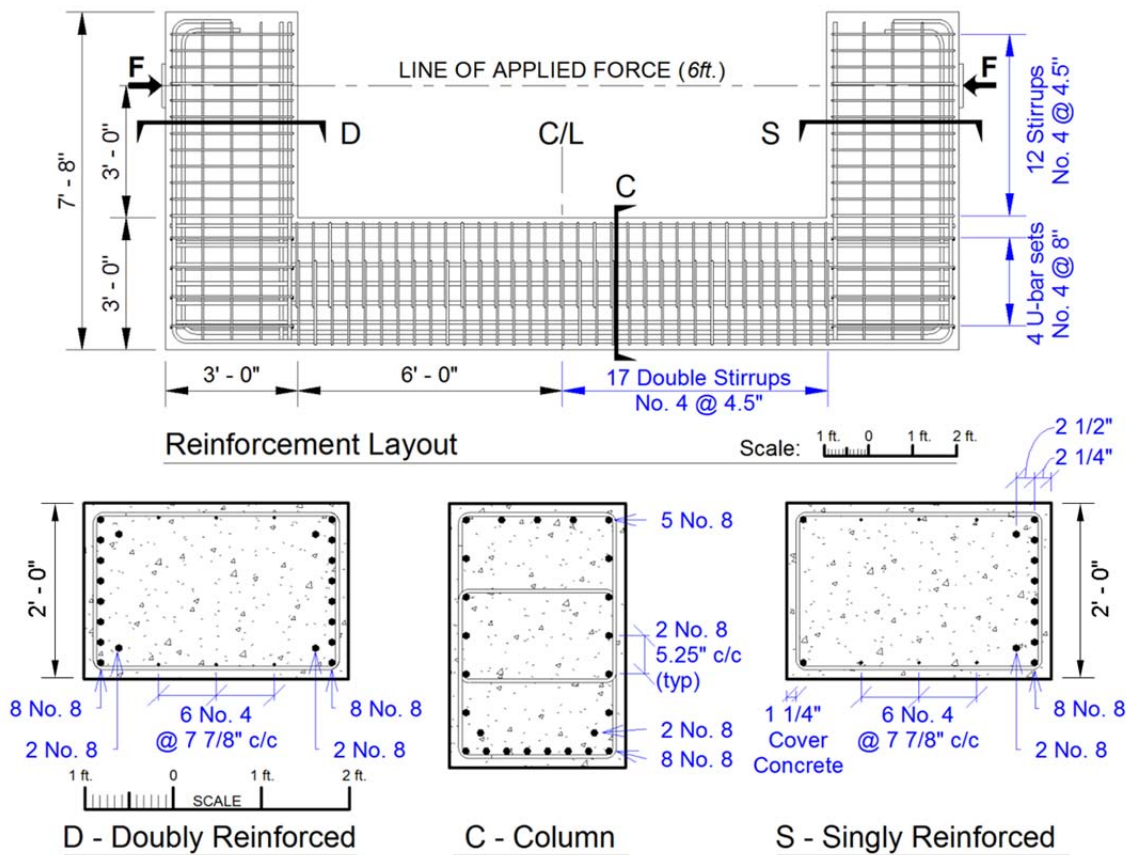
Note that the white dotted lines signify concrete cracking

(b) *Straddle bent*

**Figure 7–1: Prototype Reinforced Concrete Bridge Bents with ASR/DEF Deterioration.**



(a) Experimental C-specimen



(b) Reinforcement details

Figure 7-2: Experimental Specimens.

field at the Texas A&M University Riverside campus and with supplemental watering via a sprinkler system for four wetting and drying cycles per day. Structural testing was undertaken after eight months and two years when minor and moderate ASR/DEF damage was observed in Specimen 2 and 4, respectively.

### 7.2.2 Concrete Compressive Strength

During the construction of each specimen, standard 4 inch by 8 inch concrete cylinders were also made according to ASTM Standard C31 (ASTM-C31, 2008) so that concrete compression strength data of cylinder tests in accordance with ASTM C39 (ASTM-C39, 2008) and some tensile strength data of cylinder tests in accordance with ASTM C496 (ASTM-C496, 2008) could be determined by accepted practices. Half of these cylinders were stored in a curing/wet room with 100 percent humidity, and the other half were stored at the same location and conditions as the specimens. The measured compressive strength of standard 4 inch by 8 inch concrete cylinders at 28 days and at the time of testing for Specimens 1, 2, and 4 are presented in Table 7–1. Note that the compressive strength of Specimen 2 from the field at the time of testing varied from 1.4 ksi (9.7 MPa) to 4.1 ksi (28.3 MPa), resulting in an unreliable indication of the compression strength.

Note that in Table 7–1 “curing” means that cylinders were stored in a wet room under 100 percent humidity and temperature of 73.4 °F (23.0 °C). “Lab” means that cylinders were stored adjacent to the specimen in the air-conditioned structural laboratory without supplemental water. “Field” means that cylinders were stored adjacent to the specimens at the Riverside Campus with supplemental watering.

The field-cured concrete cylinders exhibited significant cracking due to ASR/DEF effects, as shown in Figure 7–3. The highly cracked cylinders led to compressive strengths with significant scatter in the results. Therefore, due to the severely cracked state of the field-cured cylinders for Specimen 4 (Figure 7–3b), the compressive strength was considered to be invalid. Concrete tensile strengths were obtained using two test methods: (i) embedded bar tensile (*t*) test with a 0.5 inch coil rod of high strength steel was embedded in a 3 inch by 3 inch by 36 inch prism of the same concrete mix of each specimen; and (ii) splitting tensile (*s-t*) test. Due to the lack of sufficient cylinders and prisms, the tensile strength at the time of testing of Specimen 2

and 4 were not determined. However, due to their severely cracked state, it was presumed that the tensile strength was significantly less than the original uncracked cylinders and prisms.

**Table 7–1: Material Properties of Concrete.**

		Cylinder Compressive Strength for each Specimen Mix								
		Specimen 1				Specimen 2			Specimen 4	
Age (day)		28 days		Time of Testing 392 days		28 days	Time of Testing 499 days		28 days	Time of Testing 888 days
		Curing	Lab	Curing	Lab	Curing	Curing	Field	Curing	Curing
$f'_c$	<i>ksi</i> <i>ind. test</i>	5.0 4.9; 5.1	4.3 4.1; 4.3; 4.6	5.0 4.8; 5.0; 5.1	5.4 5.1; 5.4; 5.9; 5.5; 5.3	4.7 4.6; 4.8; 4.6	5.6 5.3; 5.7; 5.9; 5.5; 5.4	2.3 1.4; 4.1; 1.5	4.8 5.0; 4.6; 4.7	4.0 4.0; 4.8; 3.3
$E_c$	<i>ksi</i>	4030	3740	4030	4190	3910	4265	2735	3950	3605
$f'_t$	<i>ksi</i> <i>ind. test</i>	-	0.43 0.39; 0.46	0.37 0.41; 0.32	0.17 0.19; 0.14	0.46 0.46; 0.45	-	-	0.49 0.49; 0.48	-
$f'_{s-t}$	<i>ksi</i> <i>ind. test</i>	0.65 0.64; 0.66	0.65 0.65; 0.65	0.61 0.63; 0.58	0.57 0.54; 0.60	0.64 0.65; 0.63	-	-	0.53 0.51; 0.58; 0.51	-

### 7.2.3 Experimental Test Setup

#### *Specimens 1 and 2*

The experimental test setup for the C-Specimens was designed to be a self-reacting system. The specimens concurrently represented two bridge bent types, with potentially two comparative



*(a) Cured concrete cylinder (with hairline cracking)*



*(b) Field concrete cylinder*

**Figure 7-3: Comparison of Cured and Field Cylinders.**

results obtained from one sub-assembly test. Figure 7–4 shows a detailed plan and elevation of the experimental test setup. For experimental convenience, the specimens were oriented so that the column was placed horizontally, while the cantilevered beams were oriented vertically. The column was seated on two hinge supports located a distance of  $D/2$  ( $D$ : the depth of the beams = 3 ft) from the beam face. Equal and opposite loads were applied to the beams at a distance of 3 ft from the column face using two 220 kip MTS (model 244.51S) actuators placed in parallel.

The actuators were connected to header beams using 1.375 inch diameter high strength DYWIDAG bars and were operated in displacement control loading using a servo hydraulic system. A third actuator operating in force control was placed between the 220 kip actuators and maintained at 100 kip in order to provide a total capacity of 540 kip.

For Specimen 1, in order to maximize the results of the experimental investigation of the C-Specimen, the beam on one end of the specimen was strengthened using external post-tensioning. This was done to prevent yielding of the longitudinal steel in the beam and minimize cracking in the beam and beam/column joint region, thus focusing the other end of the specimen as the principal “test” subject area. In this way two “tests” could be performed on the one specimen as discussed in subsequent sections. As shown in Figure 7–4, the strengthening consisted of two 1.375 inch high strength (DYWIDAG<sup>TM</sup>) high alloy threadbars, eccentrically positioned 12 inches from the beam centerline toward the tension steel and post tensioned to a total axial load of 300 kip.

For Specimen 2, no strengthening was provided, and only a single test was conducted primarily because of the unknown damage effects of the ASR/DEF effects on the specimen.

#### *Specimen 4*

In order to simplify the test setup, Specimen 4 was tested with only one 220 kip MTS actuator in displacement control. Figure 7–5 presents the plan and elevation of the experimental test setup for Specimen 4. The specimen was oriented the same as in the previous test setup such that the column was placed on two hinge supports, and the beams were oriented vertically. One 220 kip MTS (model 244.51S) actuator was placed at one side of the specimen with a distance of

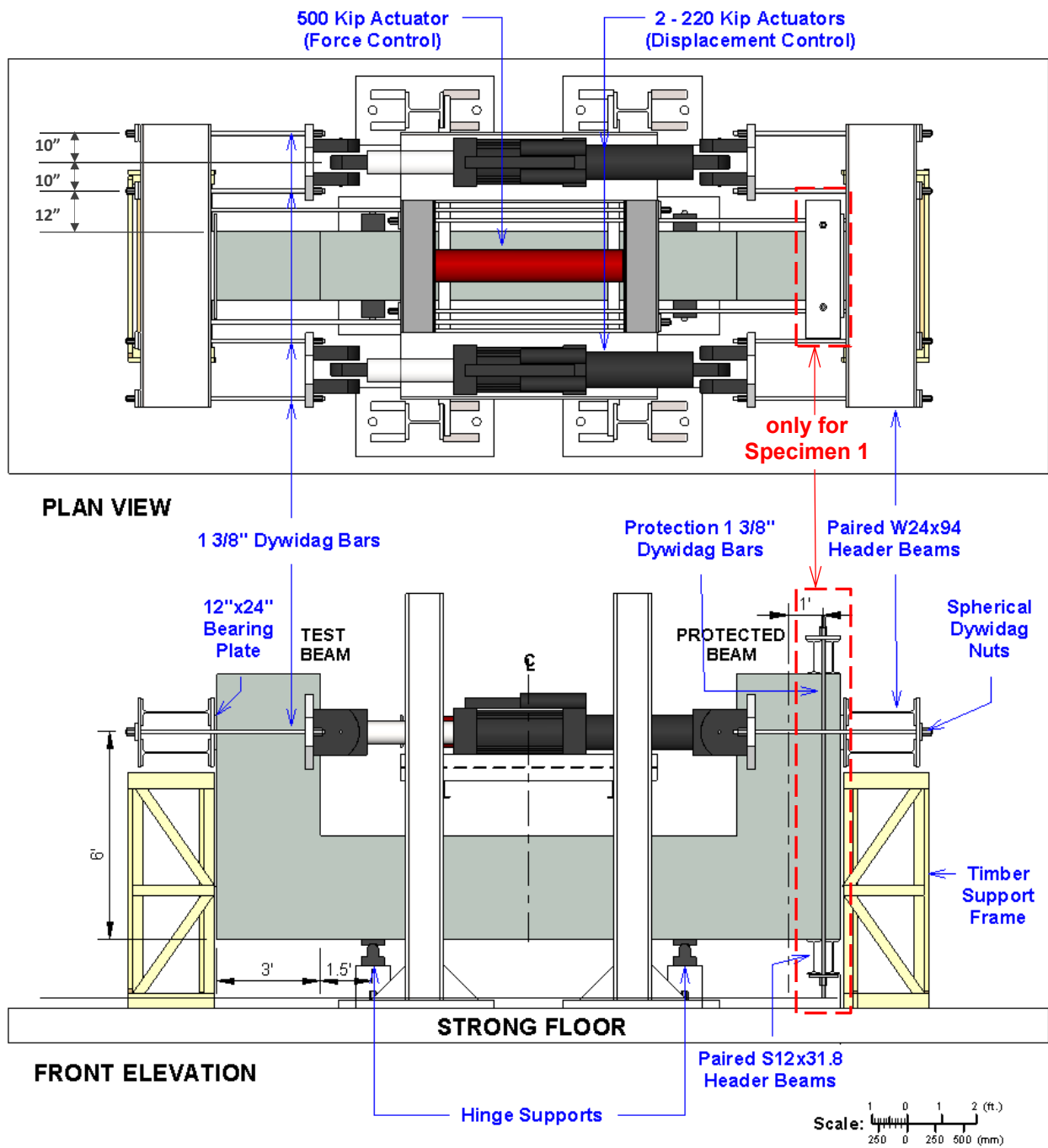


Figure 7-4: Experimental Setup for Specimens 1 and 2.

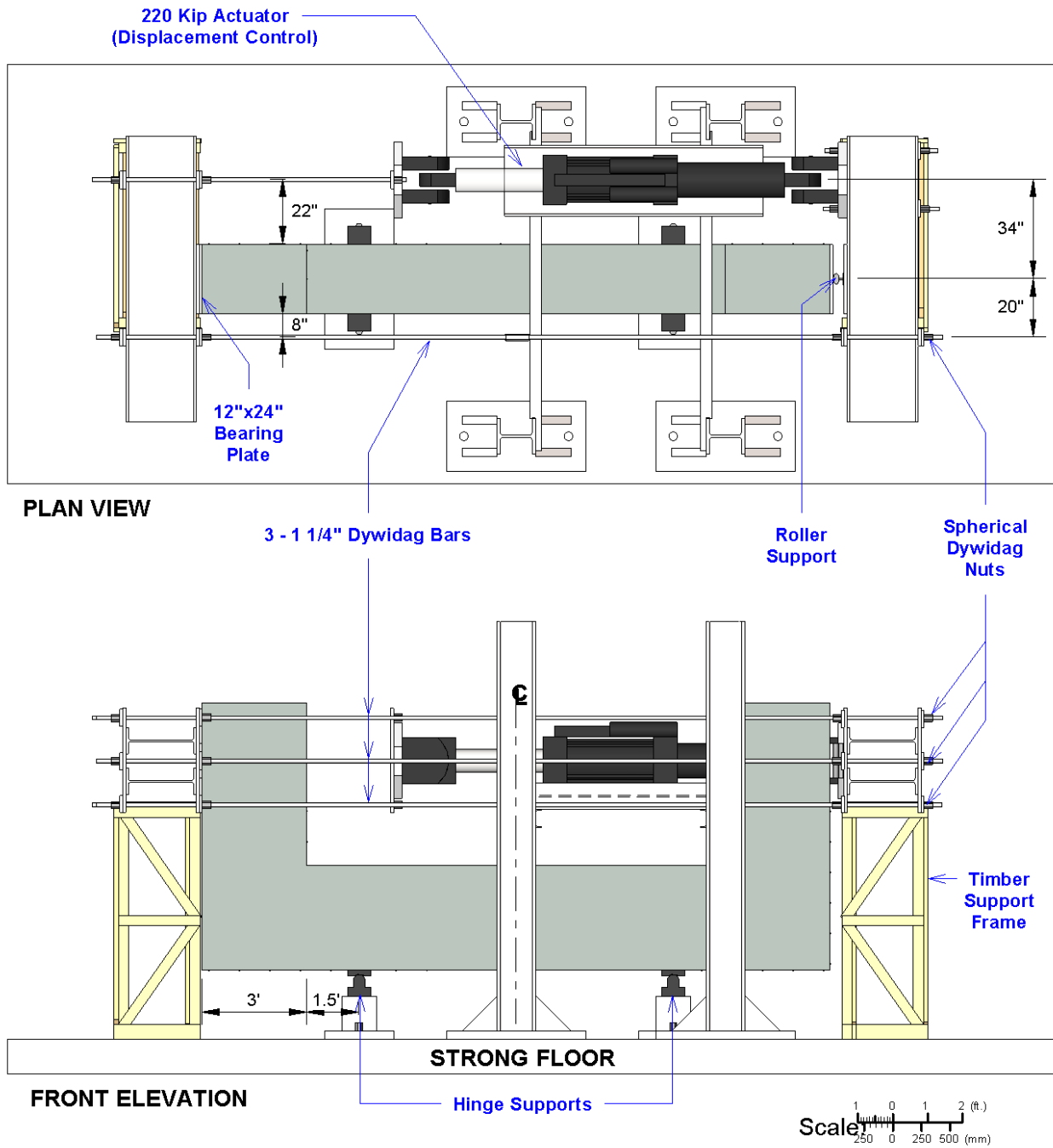


Figure 7-5: Experimental Setup for Specimen 4.



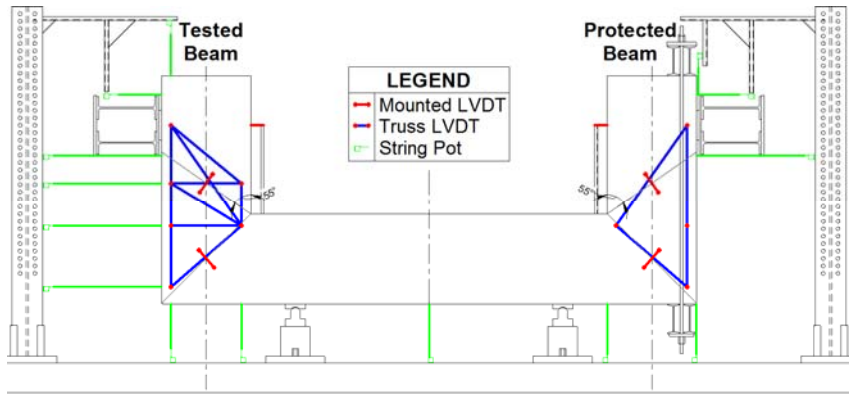
22 inches from the surface of the specimen to the centerline of the actuator. Three 1.25 inch high strength DYWIDAG threadbars were aligned vertically with a distance of 8 inches from the surface of the specimen to the center of the bars. A roller support was used on the one side of the specimen to create a leverage mechanism. The setup takes advantage of using one actuator with a 2.7-to-1 mechanical lever mechanism to create a total capacity of 594 kip. Similar to Specimen 2, by considering the uncertainty of the ASR/DEF effects, only one test was performed to investigate the ultimate strength and behavior of the specimen.

#### **7.2.4 Instrumentation**

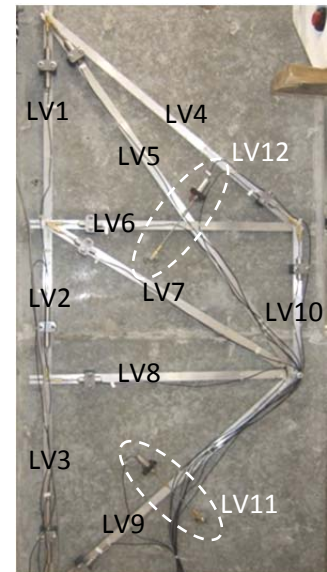
A primary objective of the experimental investigation was to determine the structural performance of the various specimens affected by ASR/DEF and compare these findings with calculations from different modeling approaches using traditional bending theory, SAT modeling, and C-STM. Figure 7–6 and Figure 7–7 show the external and internal instrumentation layout plans used to obtain experimental results that could be used to compare with the analytical modeling results. The specimens were externally instrumented using linear variable differential transformers (*LVDTs*) and string-potentiometers (*SP*), and were internally instrumented using strain gages (*SG*) attached to steel and embedded concrete gages (*KM*). Since only a single test was conducted for Specimens 2 and 4, their external instrumentation layout was different from Specimen 1 due to the available amount of the instrumentation (Figure 7–6).

The global displacements at the applied loading points on the specimen were obtained by taking an average of the measured displacements above and below the header beam. The drift of the beam relative to the column was measured using two LVDTs mounted to a rigid structure that was fixed to the column surface of the specimen and offset from the beam face by 3 inches. The overall deflected shape of the specimen was obtained by externally mounted string pots secured to the external structure or mounted on the strong floor of the laboratory.

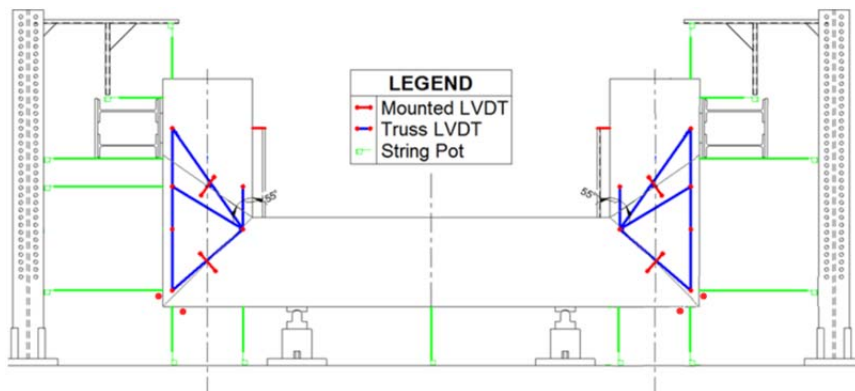
Experimental deformations associated with the SAT and truss modeling were measured using LVDTs mounted to aluminum truss members that were rigidly connected within the specimen between selected nodal points as shown in Figure 7–6b and d. Each node point had an embedded DEMEC connector securely attached into the specimen. Aluminum



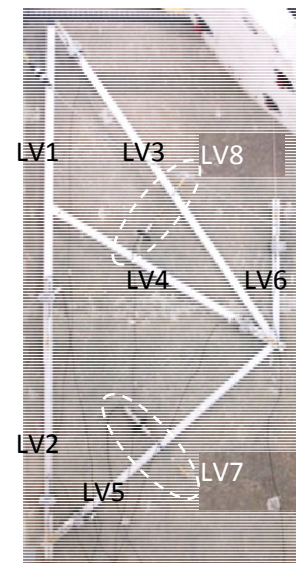
(a) External instrumentation layout of Specimen 1



(b) LVDT truss setup of Specimen 1

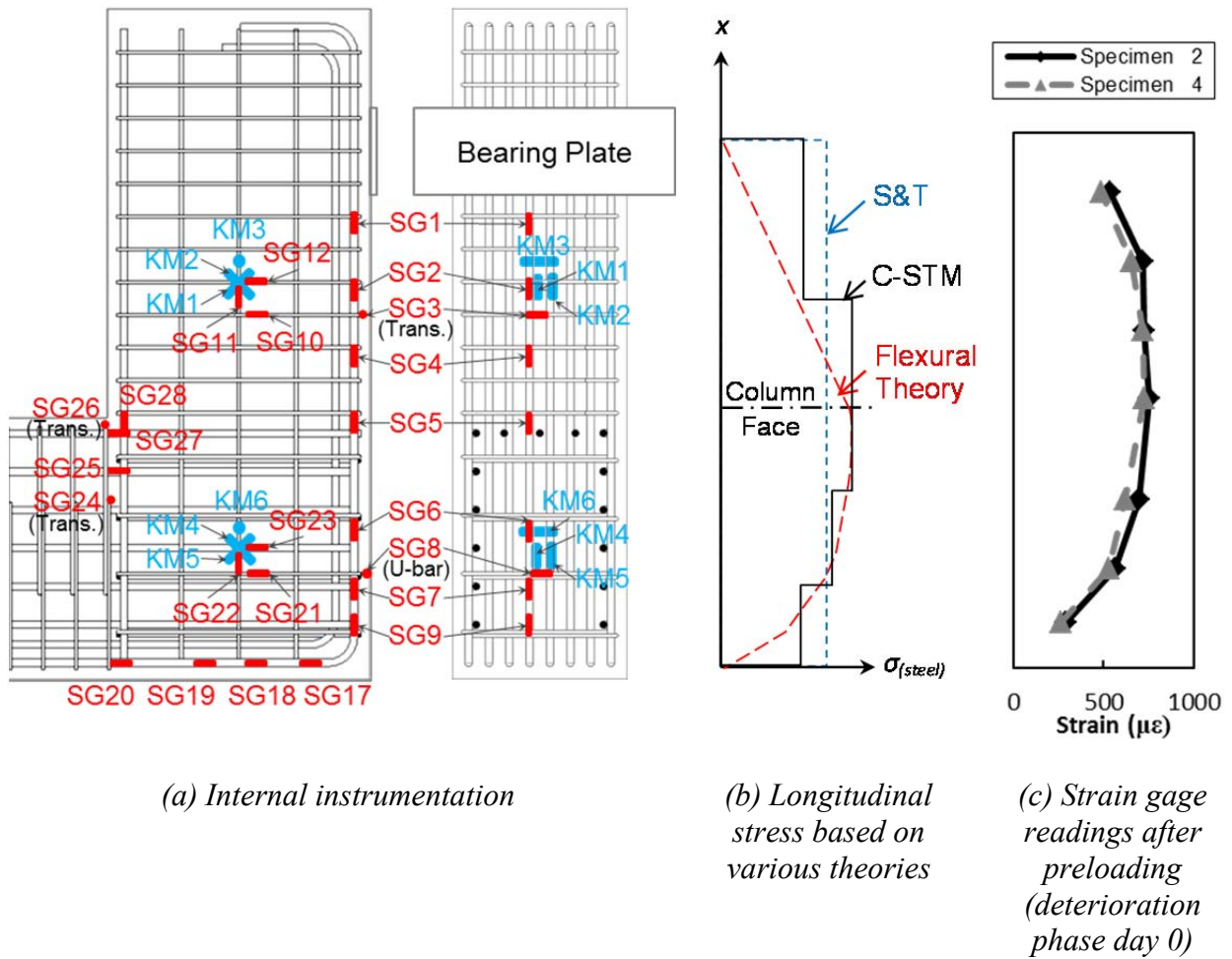


(c) External instrumentation layout of Specimens 2 and 4



(d) LVDT truss setup of Specimens 2 and 4

**Figure 7–6: External Instrumentation Layout.**



**Figure 7-7: Internal Instrumentation Layout.**

members with pin-slotted end connections attached to two DEMEC connectors of interest, and the LVDT was attached to measure the relative deformations at the node points. For Specimen 1, this consisted of 10 members with six node points for the tested beam, and four members with four node points for the protected beam each labeled as LV# (Figure 7–6b). For Specimen 2 and 4, both sides had six members with six node points (Figure 7–6d).

Crack widths or inferred principal tensile strains perpendicular to the corner-to-corner arch struts in the beams and joints were measured with four LVDTs mounted perpendicular to the anticipated crack angles ( $55^\circ$  and  $45^\circ$  in the beam and joint respectively) with a 9 inch gage length.

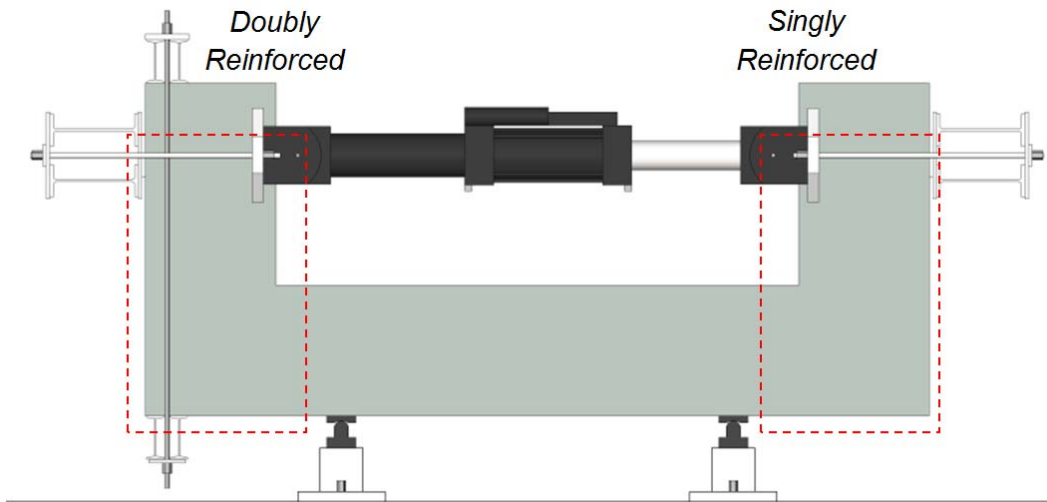
In order to provide insight into the internal deformation strains, an assortment of strain gauges were affixed to the reinforcing steel at locations shown in Figure 7–7a. To measure the strain in the corner-to-corner concrete struts of the beam and joint regions, embedded concrete gages were secured to the center of the cross section and oriented in the three principal directions relative to the arch strut as shown in Figure 7–7a. The concrete strains in the direction of the diagonal struts were denoted as gages KM1 and KM4; the concrete strains perpendicular to these struts were denoted as gages KM2 and KM5; and the concrete strains in the transverse direction were denoted as gages KM3 and KM6 (Figure 7–7a). Figure 7–7b presents the calculated longitudinal strains under preloading based on various theories. The measured longitudinal steel strains of Specimens 2 and 4 after application of the preload to simulate gravity effects are shown in Figure 7–7c.

## **7.2.5 Experimental Testing Procedure and Loading History**

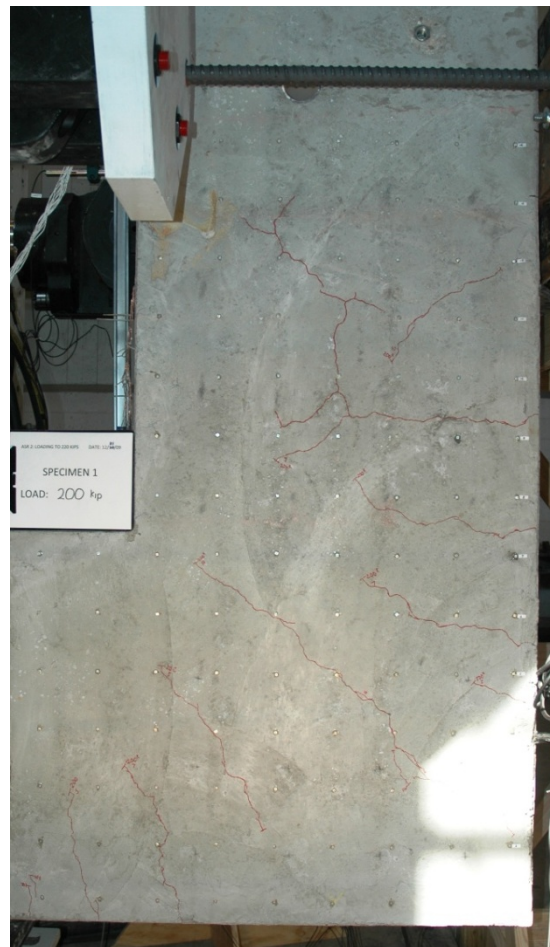
### *Specimen 1*

Experiments were conducted in two phases in order to individually assess the performance of each D-region of Specimen 1 through the effective strengthening using external post-tensioning in the beam on one end of the specimen, as depicted in Figure 7–8 to Figure 7–10.

Phase I focused on the virgin performance of the singly reinforced beam region of the specimen, where the doubly reinforced beam was protected using the external post-tensioning as

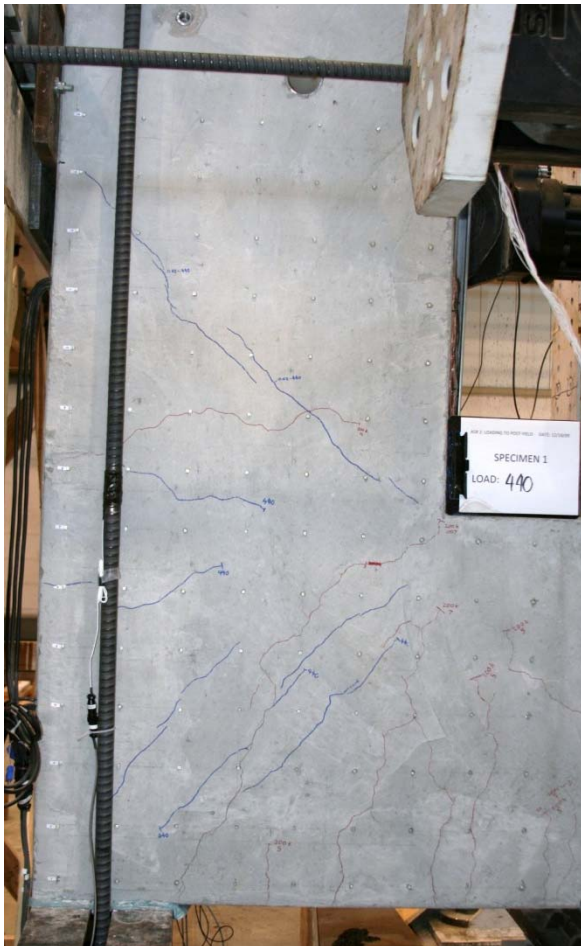
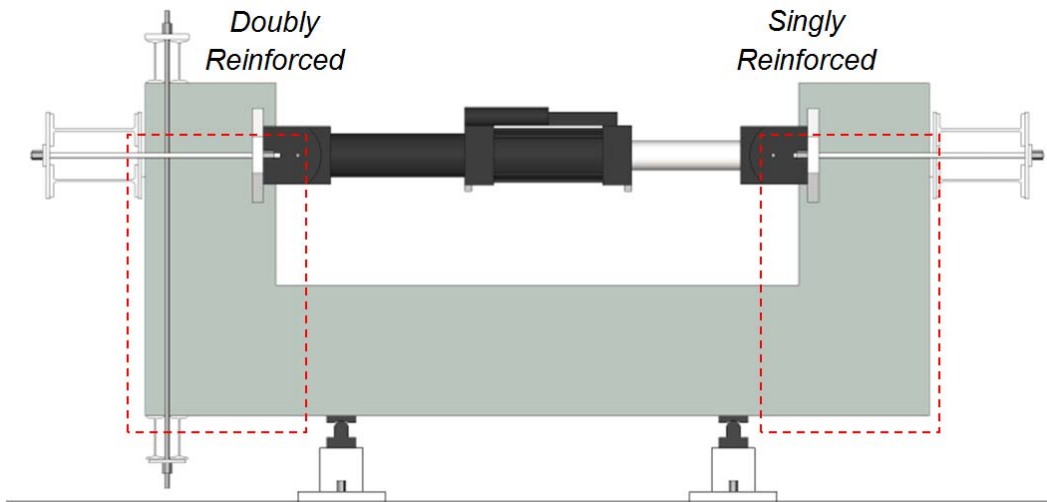


(a) Doubly reinforced beam

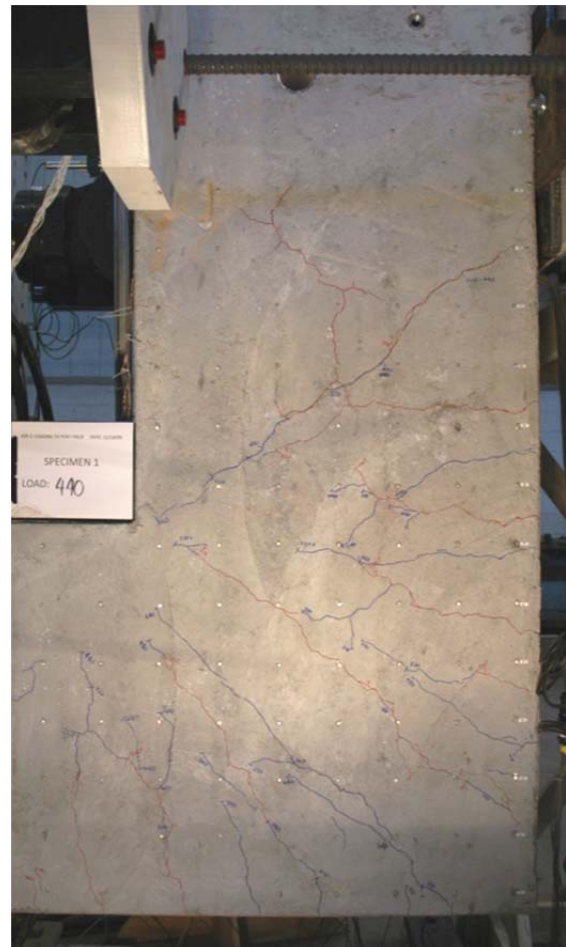


(b) Singly reinforced beam

**Figure 7–8: Test of Specimen 1: Phase I – Serviceability Loading at 200 kip.**

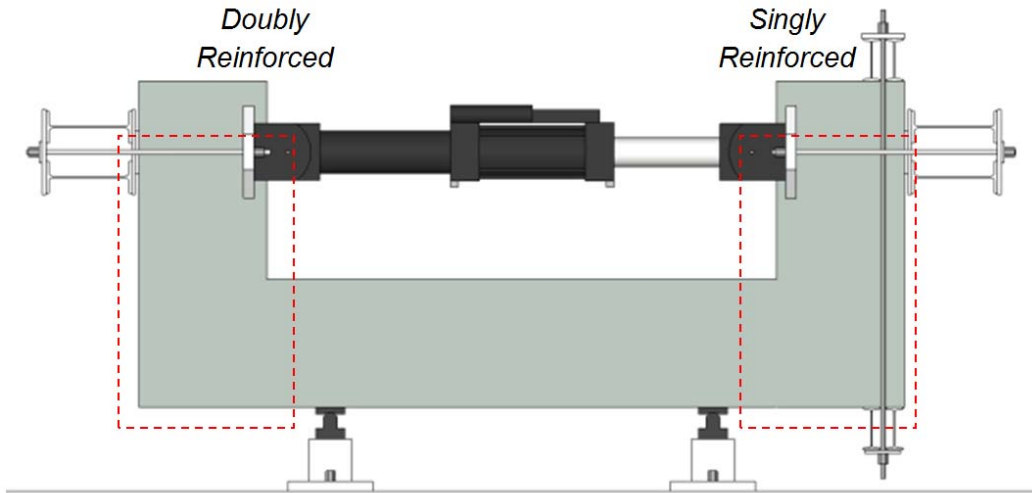


(a) Doubly reinforced beam



(b) Singly reinforced beam

**Figure 7-9: Test of Specimen 1: Phase I – Yield at 440 kip.**



(a) Doubly reinforced beam



(b) Singly reinforced beam

**Figure 7–10: Test of Specimen 1: Phase II – Ultimate Load at 474 kip.**

previously explained. The specimen was gradually loaded to about 200 kip and held for approximately two hours to record crack orientations and width measurements. Then, the specimen was completely unloaded in order to record structural response during service load level reversals. The specimen was reloaded to about the specimen's yield point (440 kip), which was the maximum loading of the test setup at that point, and subsequently unloaded.

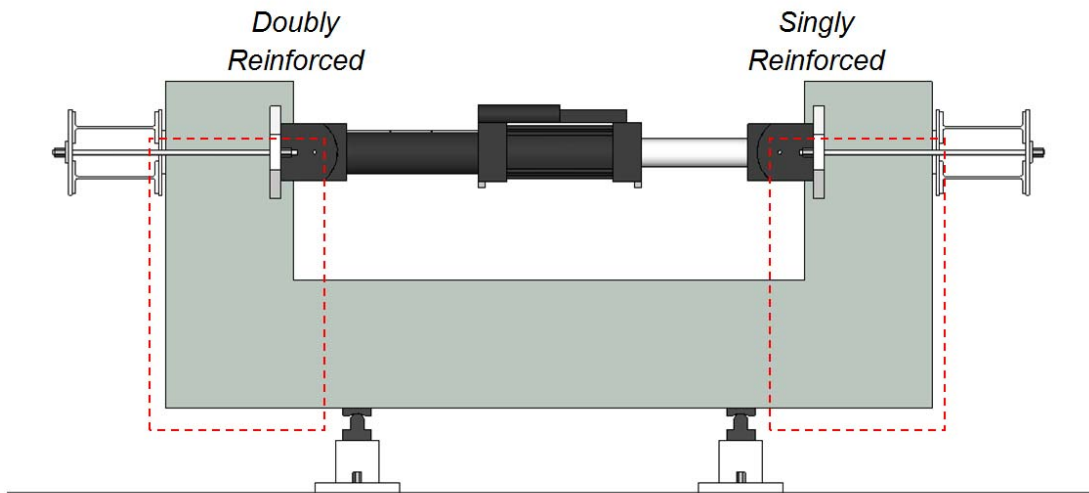
Phase II focused on the pre-cracked performance of the doubly reinforced beam until the ultimate failure load, where the singly reinforced beam region was strengthened via the application of post-tensioning to the beam. In addition, the third actuator in force control loading was implemented in the test setup to increase the maximum loading capability.

#### *Specimens 2 and 4*

Since the ASR/DEF effects on the specimen's structural performance were unclear before the structural testing, only one test was conducted for each of the ASR/DEF damaged specimen (Specimens 2 and 4) instead of having the two-phase testing using post-tensioning strengthening of one beam. The test setup for Specimen 2 consisted of three actuators as in the phase II test setup for Specimen 1, while only one actuator in the leverage mechanism was used for Specimen 4.

Figure 7–11 to Figure 7–13 show both sides of the critical areas of Specimen 2 at particular load levels during experimental testing. The specimen was gradually loaded to 200 kip and held for the crack width measurements and then loaded to 400 kip and held for visual investigations. Note that map cracking was previously observed during the deterioration program. Then the specimen was loaded to the ultimate load without any unloading during the experimental testing. Figure 7–14 to Figure 7–16 present both sides of the critical areas of Specimen 4 during the testing. Similar with Specimen 2, severe map cracking was observed during the deterioration program prior to the structural testing. Using the leverage mechanism test setup, Specimen 4 was gradually loaded to 450 kip, the test was stopped due to lack of mechanism travel. Following unloading and some adjustments of the test setup, the specimen was reloaded to ultimate failure.



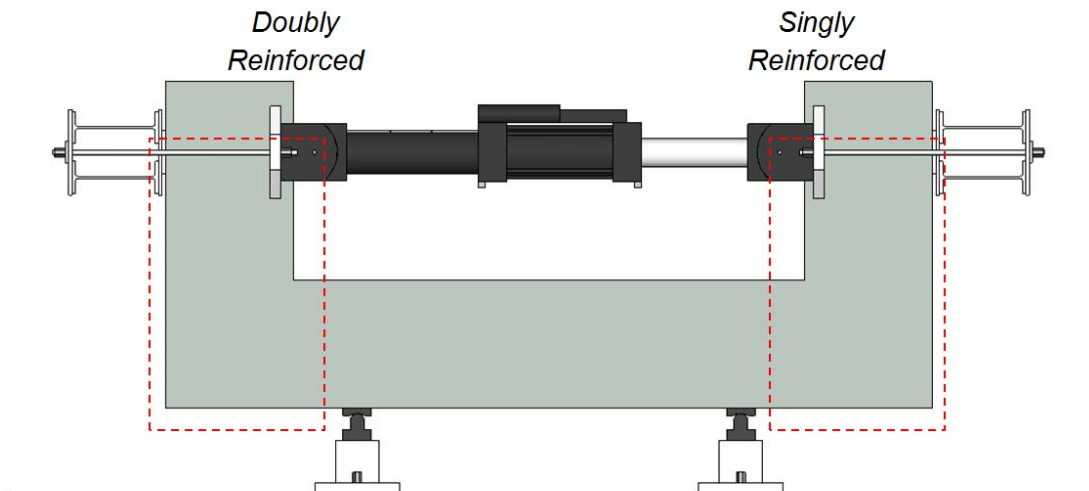


(a) Doubly reinforced beam



(b) Singly reinforced beam

**Figure 7–11: Test of Specimen 2: Serviceability Loading at 200 kip.**

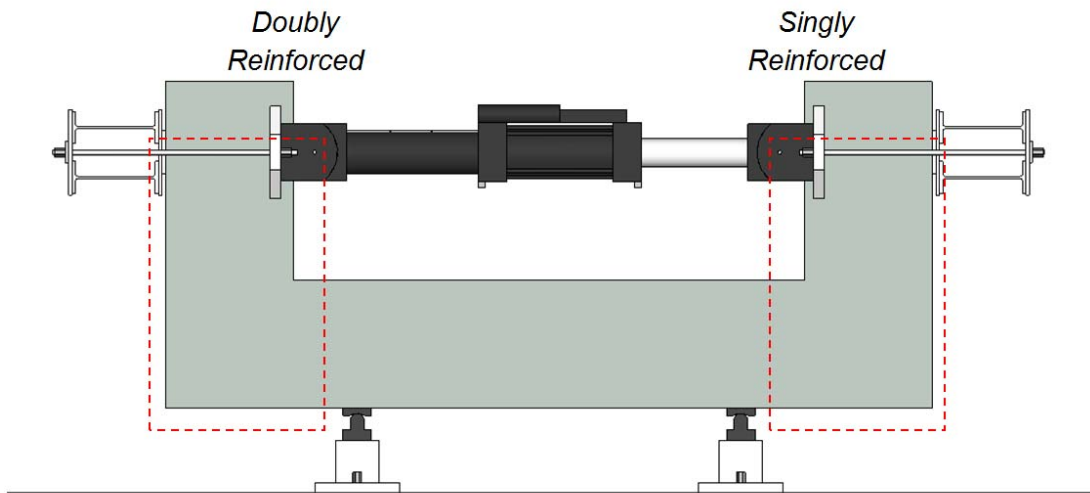


(a) Doubly reinforced beam



(b) Singly reinforced beam

**Figure 7-12: Test of Specimen 2: Load at 400 kip.**

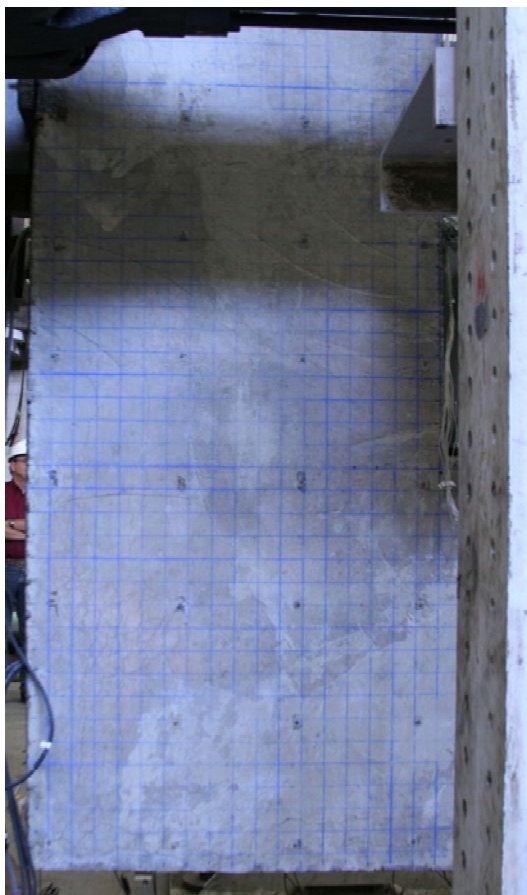
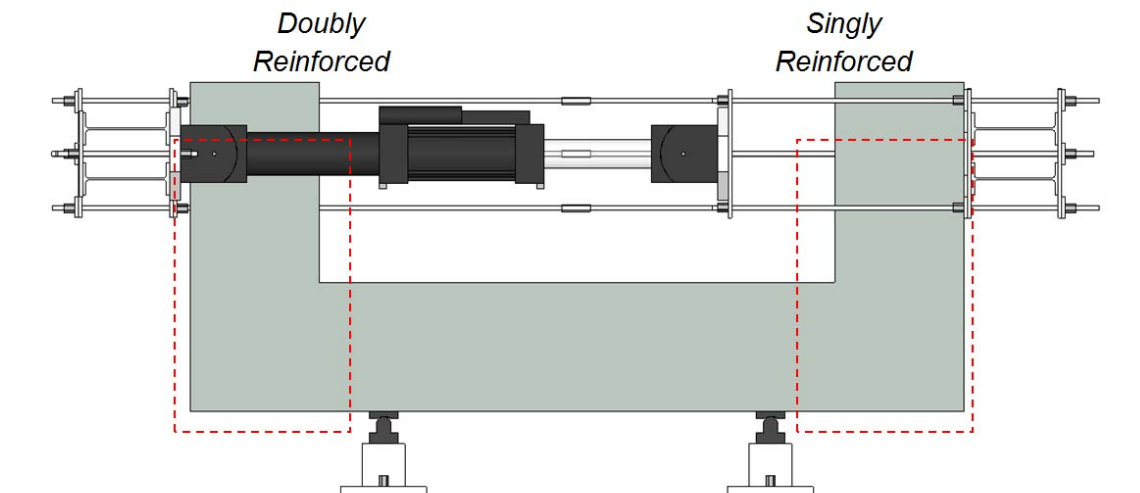


(a) Doubly reinforced beam

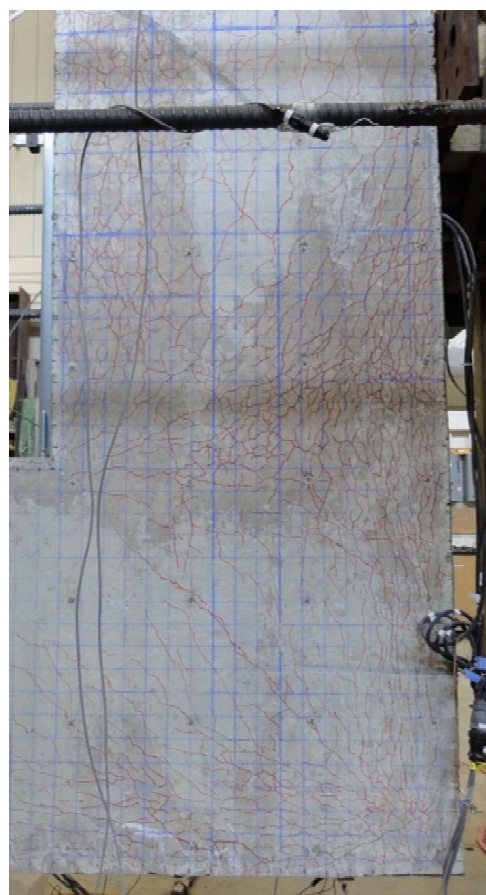


(b) Singly reinforced beam

**Figure 7–13: Test of Specimen 2: Ultimate Load at 500 kip.**

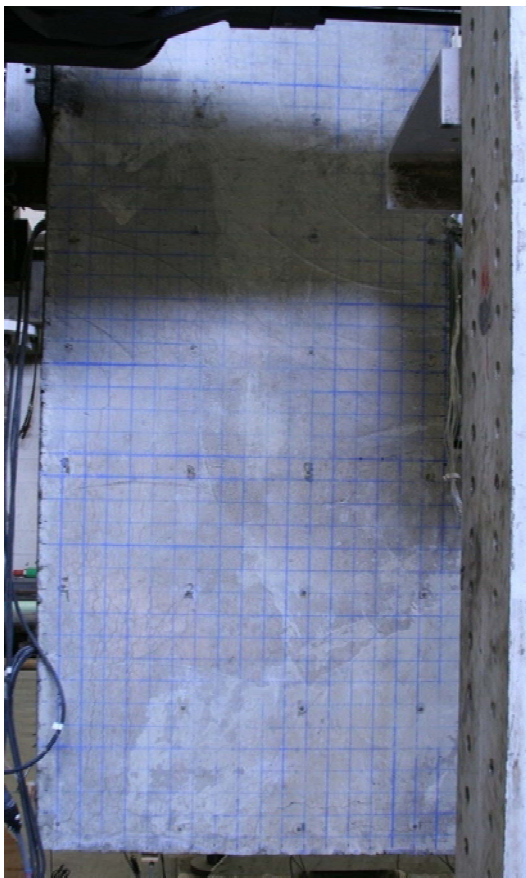
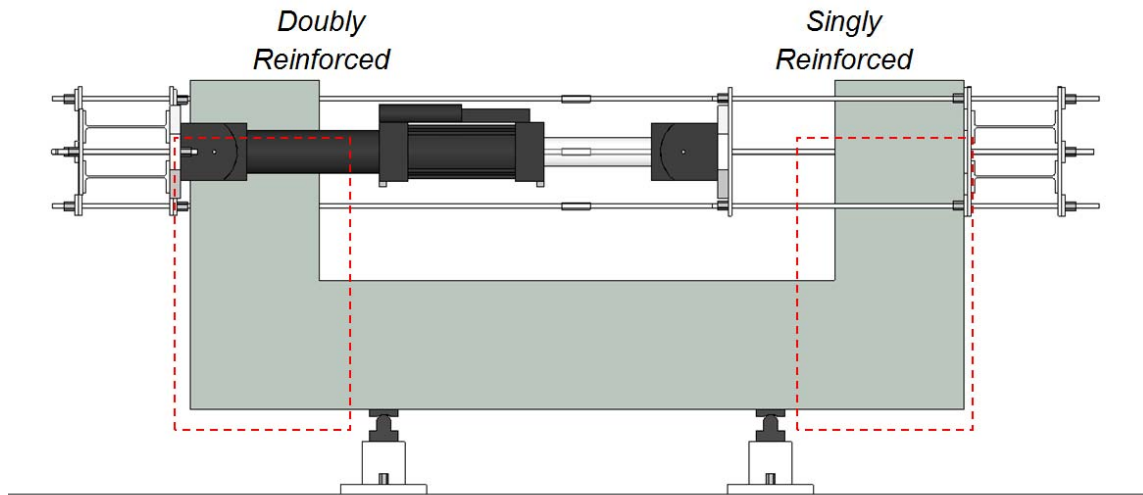


(a) Doubly reinforced beam

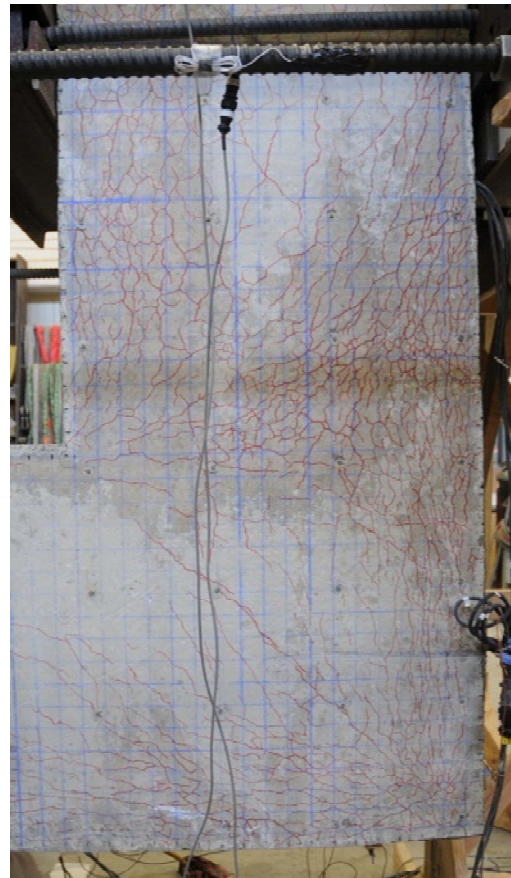


(b) Singly reinforced beam

**Figure 7–14: Test of Specimen 4: Serviceability Loading at 200 kip.**

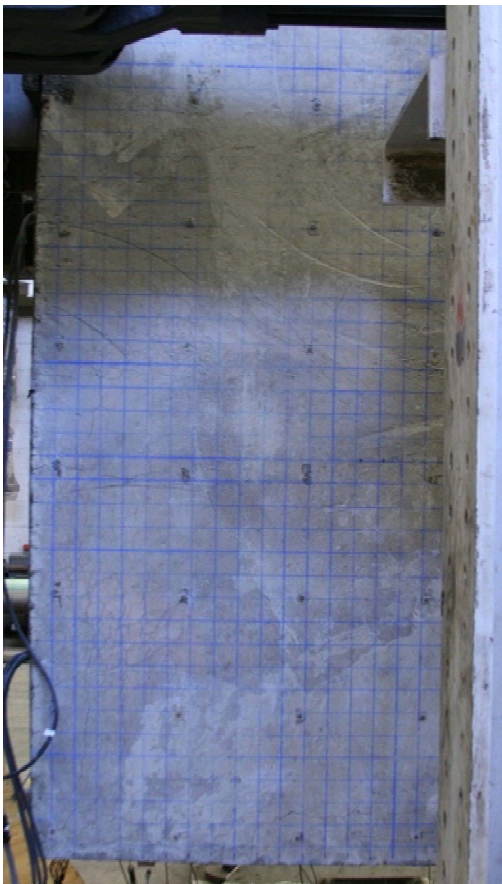
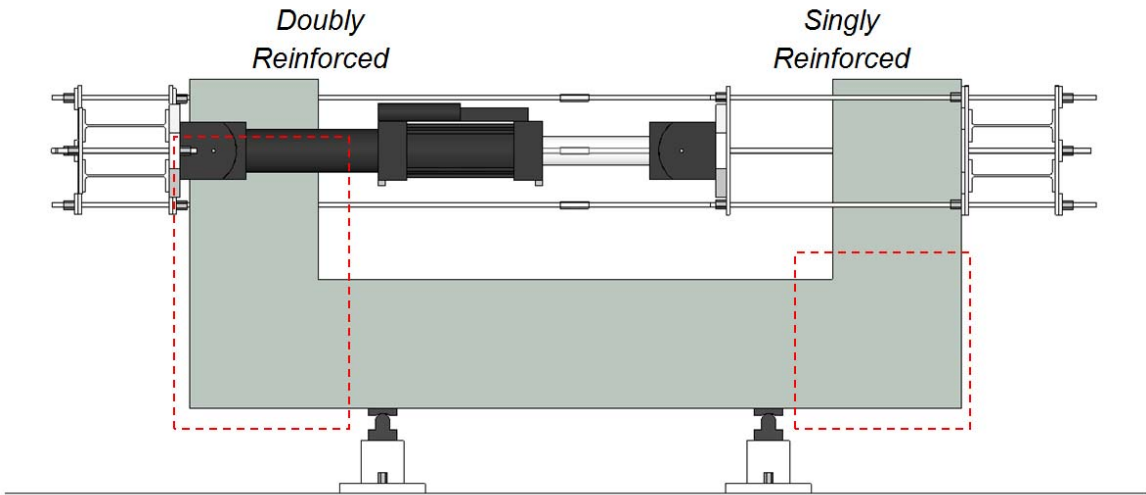


(a) Doubly reinforced beam

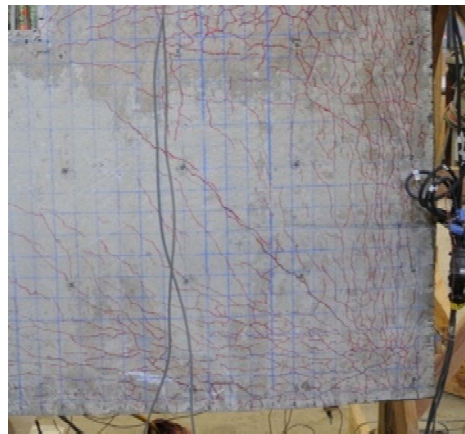


(b) Singly reinforced beam

**Figure 7–15: Test of Specimen 4: Load at 400 kip.**



(a) Doubly reinforced beam



(b) Singly reinforced beam (before failure)



(c) Singly reinforced beam (after failure)

**Figure 7-16: Test of Specimen 4: Ultimate Load at 503 kip.**

## 7.2.6 Experimental Performance

### *Specimen 1*

Phase I: In Phase I of the test, the doubly reinforced beam was protected using external post-tensioning and the singly reinforced beam was subjected to the test. In the unstrengthened region of the specimen (i.e., the region excluding the doubly reinforced beam), flexural cracking in the critical bending regions of the beam was first observed at about 110 kip, shortly followed by small flexural cracking throughout the column of the specimen. Distinct diagonal cracking in the same beam/column joint region was observed at approximately 170 kip. Diagonal cracking through the beam from the loading point to the supporting column slowly propagated when held at a loading of about 200 kip. Upon reloading to 440 kip, existing cracks in the beam and joint propagated toward the internal knee joint (CCC node) with the largest crack width observed in the beam of 0.05 inches at a load of 440 kip.

In the protected region of the specimen (i.e., the doubly reinforced beam of the specimen), some minor flexural cracking was first observed in the column at approximately 120 kip shortly followed by diagonal cracking in the joint propagating from the post-tensioning header beam to the internal knee joint. One hair line crack was observed in the beam-column face toward the internal knee joint at 200 kip. A distinct diagonal crack formed in the beam between the load point and the supporting column at approximately 360 kip with a crack width of 0.02 inches.

Phase II: In Phase II of the test, the singly reinforced beam of the specimen was protected by means of external post-tensioning, and the doubly reinforced beam was tested. Due to the pre-cracked state of the ends of the specimen, existing cracks propagated with the formation of a few new cracks in the joint and beam at higher loads. At 440 kip, the largest diagonal cracks in the beam and joint were approximately 0.025 inch and 0.035 inch, respectively. The ultimate failure mechanism of the specimen occurred in the tested beam-column joint region along the main corner-to-corner diagonal in a sudden, brittle failure near the maximum applied loading of about 470 kip.

The applied post-tensioning at the other end of the specimen, i.e., the singly reinforced beam, successfully protected the beam longitudinal reinforcement from prematurely yielding by

offsetting the measured strain to approximately zero at the applied service load of 200 kip. This not only protected the beam steel from yielding, but also delayed the concrete cracking in the beam. This resulted in a stiffer response of the doubly reinforced beam in Phase II compared to Phase I as seen in the force-displacement responses given in the following section.

#### *Specimens 2 and 4*

As discussed in the previous chapter, the specimens that were exposed to the aggressive deterioration program were preloaded to simulate gravity and service load conditions. The intention of the preload was to ensure that the specimens endured a moderate amount of normal service cracking during exposure to the environmental conditions as part of the field-deterioration program. During this deterioration phase, the preload-induced cracks grew in both length and width over time. Significant new cracking also developed throughout the specimens as a result of the ASR/DEF effects.

Prior to shipping the specimens back to the structural testing lab for experimental load testing, the preloading that mimicked the gravity effects was released. An important observation made at that time was that the existing cracks in the specimens did not fully close after the releasing of the preload. This inelastic response confirmed that some amount of damage had been done as a consequence of concrete expansion in the specimen from ASR/DEF effects.

Since the ASR/DEF effects on the deteriorated specimen's structural performance were unclear before the structural testing, only one test was conducted for each of the ASR/DEF damaged specimen (Specimens 2 and 4) instead of having the two-phase testing by strengthening one beam using external post-tensioning as in the case of Specimen 1.

Specimen 2 was slowly loaded to the ultimate failure load of about 500 kip without unloading. The largest measured crack widths of the diagonal cracking through the beam were 0.013 inch and 0.016 inch at loads of 200 kip and 400 kip, respectively. The largest crack widths measured in the beam/column joint were 0.013 inch and 0.016 inch at the same loads of 200 kip and 400 kip. To minimize pauses in the test, for Specimen 4 no crack width measurements were made during loading. Both Specimen 2 and 4 failed at the singly reinforced side of the specimen.



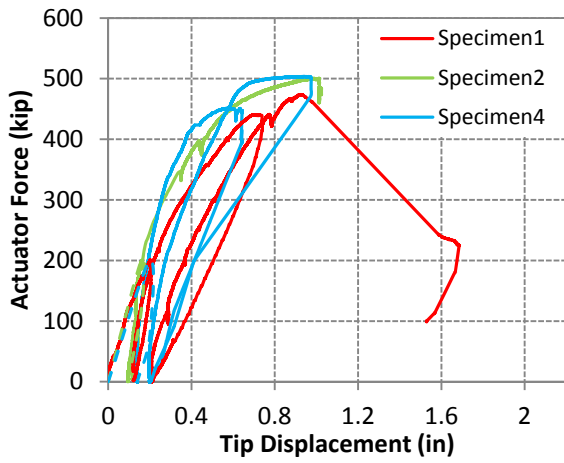
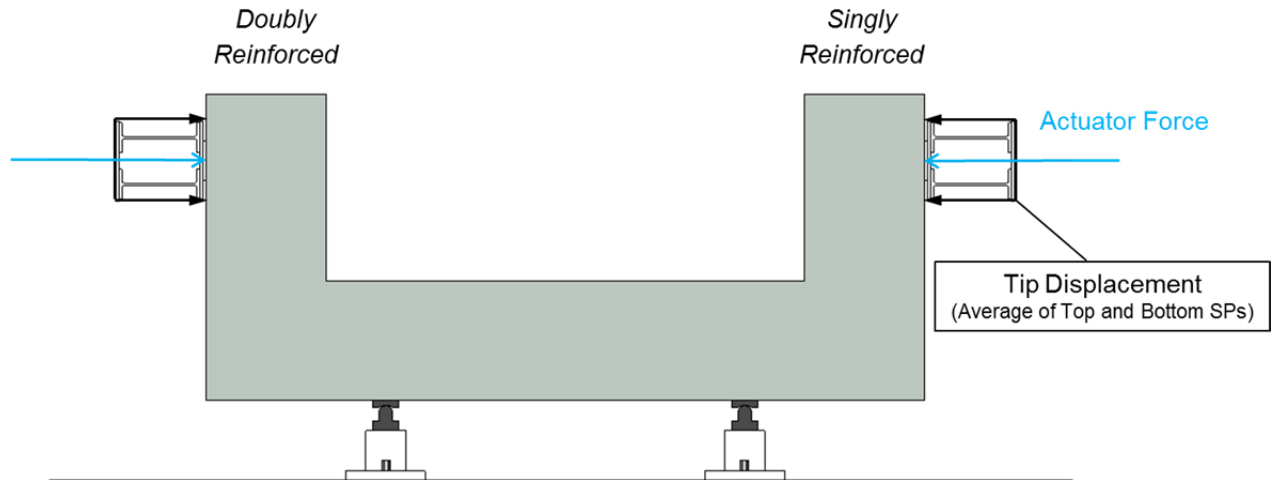
### 7.2.7 Force-Displacement Behavior

Figure 7–17 presents the measured force-displacement behavior for the singly and doubly reinforced regions of Specimens 1, 2, and 4. Specimen 1 reached a peak load of 474 kip and then failed shortly thereafter, while the peak loads for Specimens 2 and 4 were 500 kip and 503 kip, respectively. Some levels of ductility were observed in Specimens 2 and 4 prior to failure that was not observed in Specimen 1. Despite ASR/DEF effects, Specimens 2 and 4 were stronger than Specimen 1 in terms of the ultimate peak loading. In addition, the initial and overall general stiffness of both Specimens 2 and 4 were greater than that of Specimen 1. This was attributed to the beneficial prestressing effects of the concrete from the longitudinal and transverse reinforcement arising from concrete expansion due to ASR/DEF effects. Although significant map cracking on the surface of the specimens was evident due to ASR/DEF effects, this did not appear to impair the structural performance. However, one specimen still remains in the deterioration program with the expectation of developing *severe* ASR/DEF damage; it remains to be seen if the strength capacity can be maintained in a more deteriorated specimen.

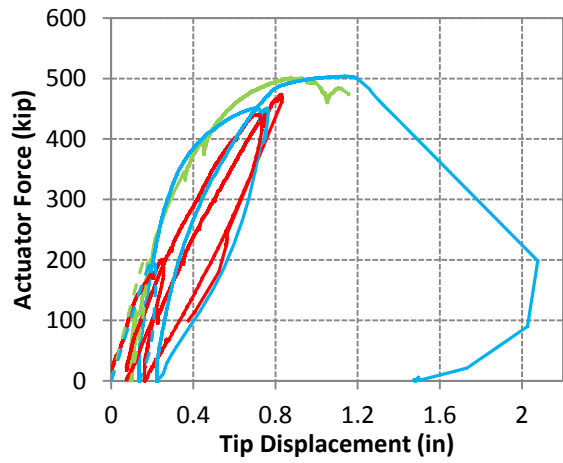
## 7.3 DISCUSSION

### 7.3.1 Failure Assessment

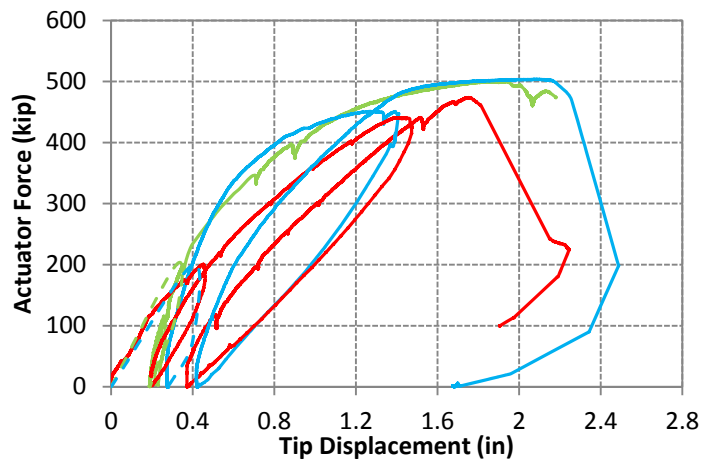
The ultimate failure mechanism in the control specimen and the two specimens with varying levels of ASR/DEF deterioration was common to all specimens. These failures may be classified as brittle joint shear failure through the beam-column joint region. Evidently, the failure mechanism was initially triggered by concrete softening of the joint corner-to-corner diagonal strut (arch action) (KM11, Figure 7–18c; KM5, Figure 7–18d and e). Note that initial readings of the ASR/DEF affected specimens resulted from the deterioration phase. Immediately following this incipient failure mode, a redistribution of the joint forces to the transverse reinforcement in the joint (truss action) was necessary. Because the transverse reinforcement in the joint region had limited capacity, overall failure was sudden with a rapid drop in resistance (Figure 7–18f, g, and h). No strain gages were attached to the U-bar set closest to the corner. SGs 8 and 32 were on the second closest set of U-bars, and no significant increase in strains was observed during the tests. These readings are not representative of the U-bars closest to the corner. The brittle nature



(a) Doubly reinforced beam

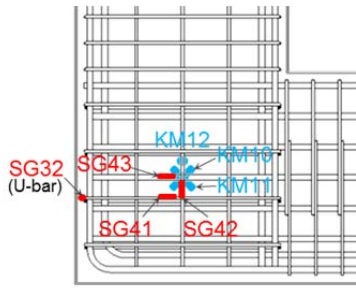


(b) Singly reinforced beam

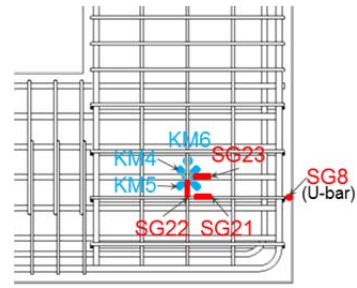


(c) Total tip displacement

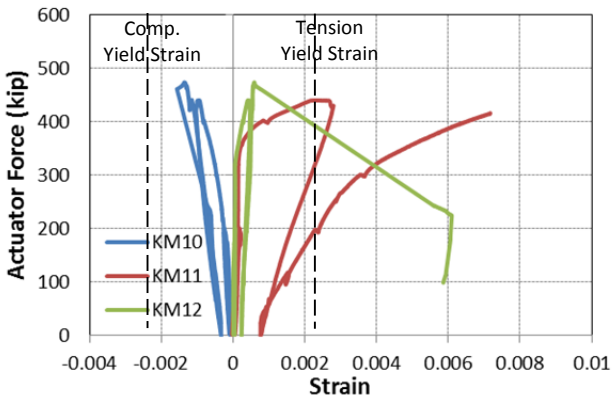
**Figure 7–17: Force-Displacement Behavior of Specimens 1, 2, and 4.**



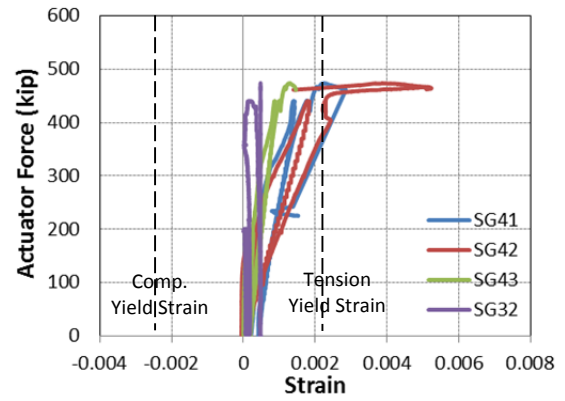
(a) Failure joint of Specimen 1



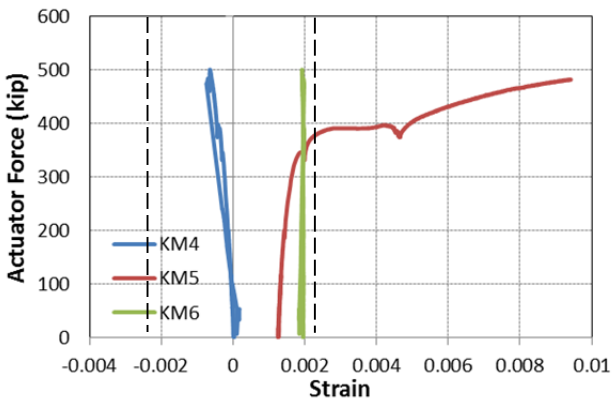
(b) Failure joint of Specimens 2 and 4



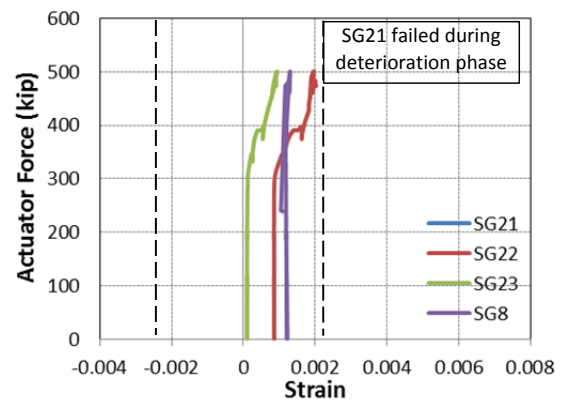
(c) Internal Concrete Strain – Specimen 1



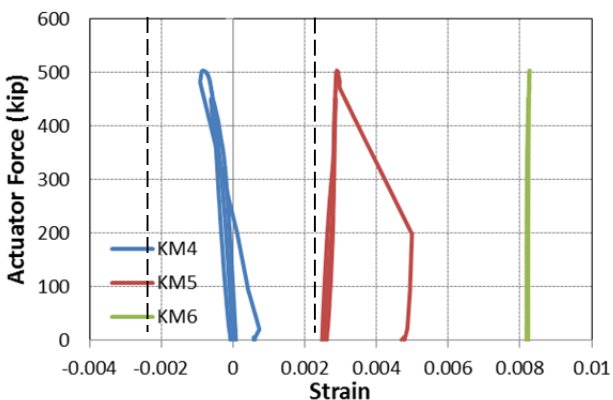
(f) Reinforcing Strain – Specimen 1



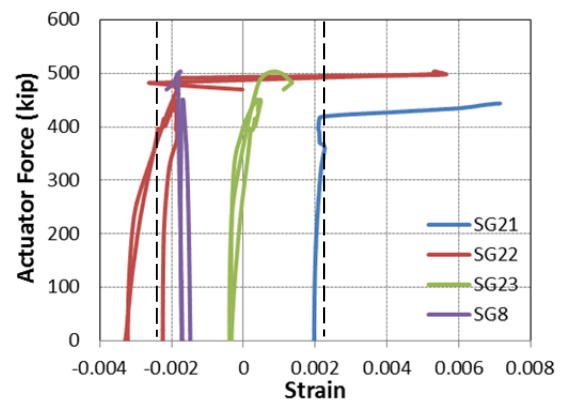
(d) Internal Concrete Strain – Specimen 2



(g) Reinforcing Strain – Specimen 2



(e) Internal Concrete Strain – Specimen 4



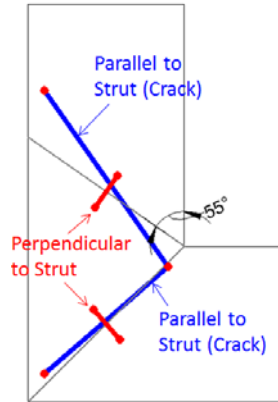
(h) Reinforcing Strain – Specimen 4

**Figure 7–18: Joint Behavior of Specimens 1, 2, and 4.**

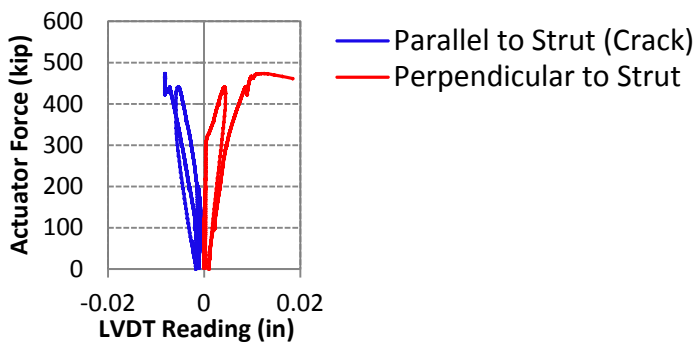
of failure was attributed to the insufficient anchorage of the limited overlapping transverse reinforcement (U-bars) in the joint region within the plane of loading and also the lack of out-of-plane reinforcement along the back face of the joint region. Evidently, the bursting pressures on the concrete were sufficiently high to cause the cover concrete to suddenly spall, promoting a complete and sudden failure mechanism to form.

Crack widths prior to failure were unable to be measured due to safety considerations. However, the size of the cracks can be inferred via the computational model and physical measurements transverse to the principal strut orientations. Figure 7–19 presents the parallel and perpendicular to strut (crack) LVDT readings in both joint and beam regions. Crack widths were measured by LVDTs mounted perpendicular to strut (crack) with a gage length of 9 inches. For Specimen 1, slightly greater crack width in the joint than in the beam region was measured at ultimate load (Figure 7–19b and c). A significantly greater crack width increment in the joint was observed indicating joint failure for Specimens 2 and 4, as shown in Figure 7–19d and e, and Figure 7–19f and g, respectively. It should also be noted that the cracks pre-existed prior to the main failure load tests. The pre-existence of these cracks was first due to the initial preload (emulating self-weight effects), and secondly due to field exposure for Specimens 2 and 4. The computational modeling and significance of these results are discussed in Chapter 8.

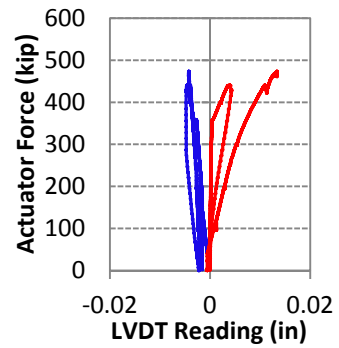
The joint reinforcement consisted of 4 overlapping U-bars and straight side-face longitudinal distribution steel from the beam and column that were not sufficient to transfer the shear forces in the joint and confine the beam-column joint region (Figure 7–20a). Additionally, the beam side-face reinforcements continuing into the joint were terminated at the column longitudinal reinforcement face and were not hooked, thereby making them ineffective in the shear transfer mechanism. Overlapping U-bars rely on bond strength in the spliced regions of the cover concrete to transfer the confining force. In cracked cover sections, the anchorage is markedly reduced, and the ability of the U-bars to provide a shear transfer (truss) can ultimately result in a very rapid and brittle failure mechanism. Figure 7–20 shows the joint failure of Specimen 1 before and after removal of the loose and spalled concrete. Upon closer examination, debonding was observed around the U-bars, and signs of pullout were evident from the direction of the steel ties (Figure 7–20e) as a result of the cover concrete spalling. In addition, due to the forces from the concrete strut in the joint region, the U-bars bulged and bent (Figure 7–20f).



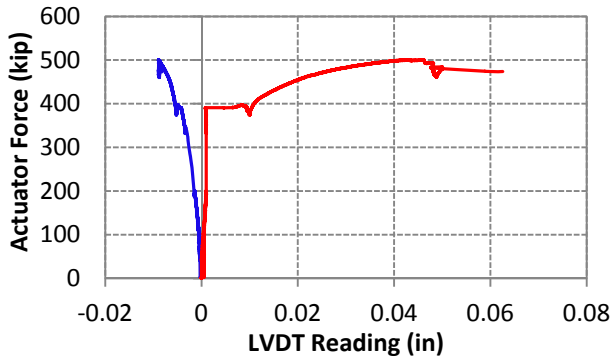
(a) Parallel and perpendicular to strut (crack) LVDT layout



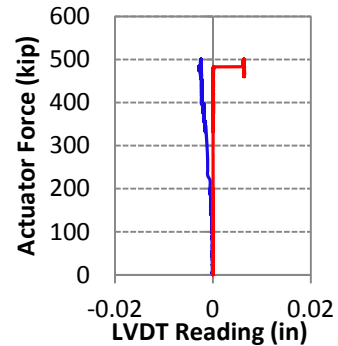
(b) Joint – Specimen 1



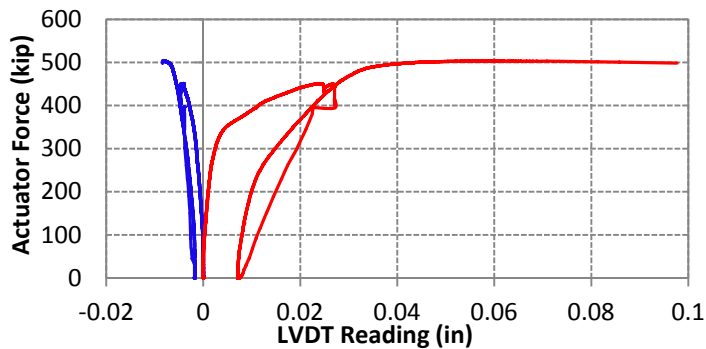
(c) Beam – Specimen 1



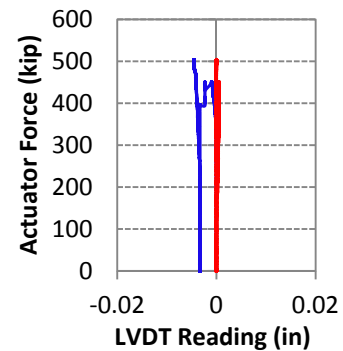
(d) Joint – Specimen 2



(e) Beam – Specimen 2

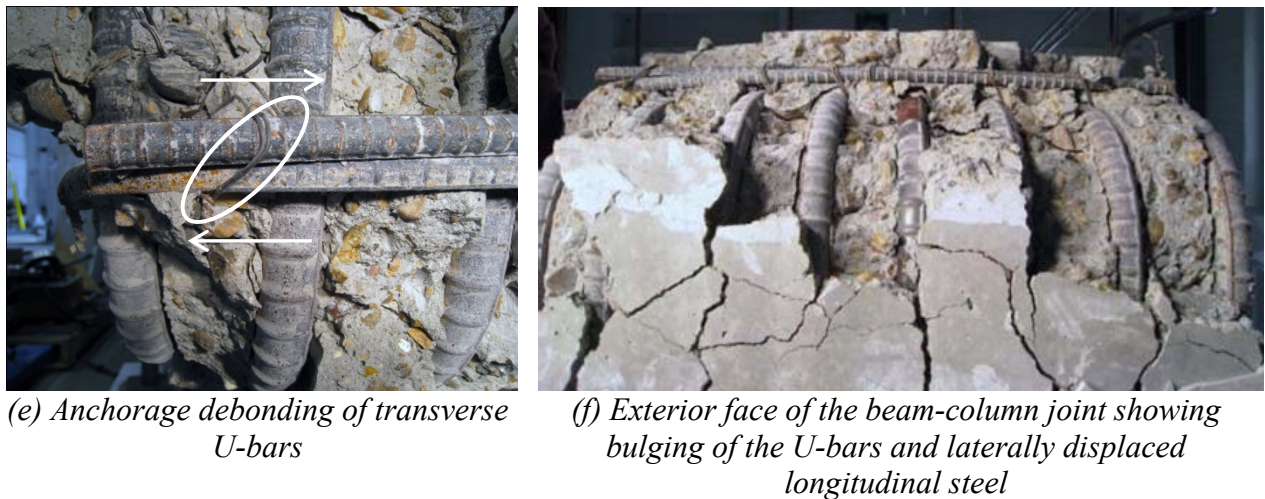
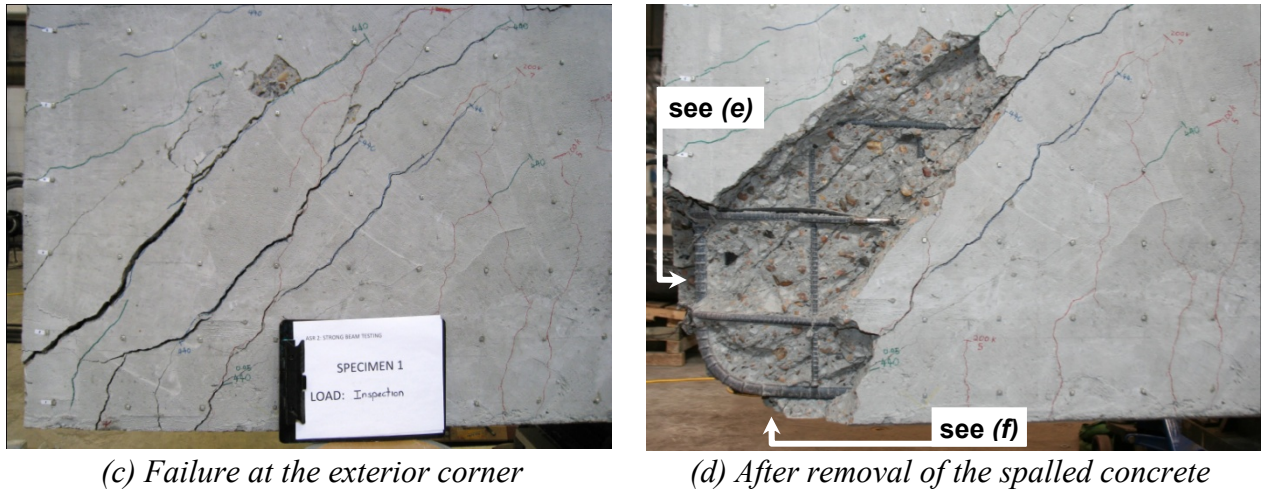
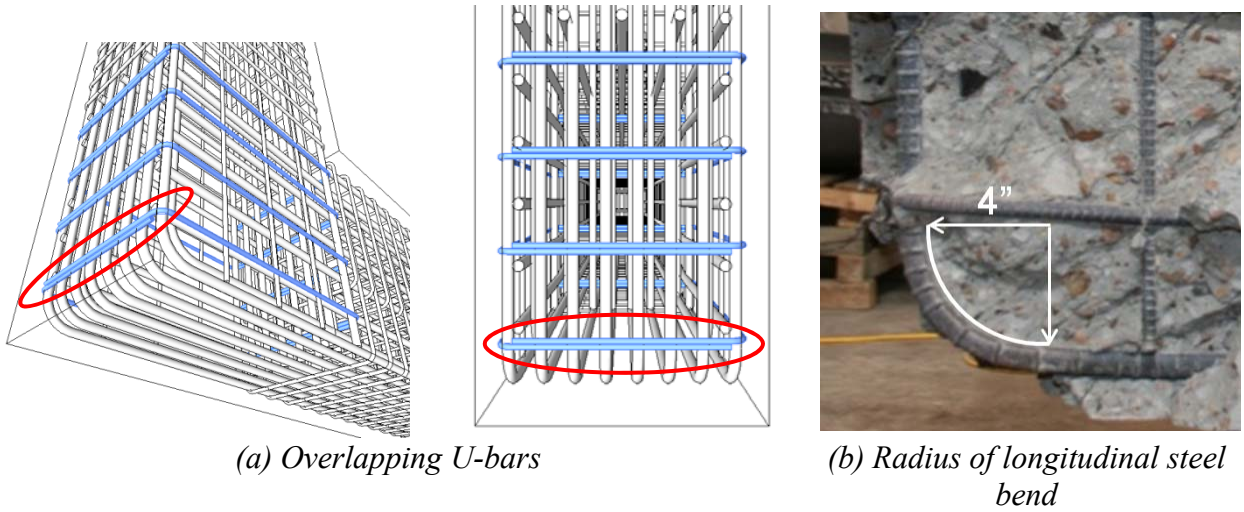


(f) Joint – Specimen 4



(g) Beam – Specimen 4

Figure 7–19: Parallel and Perpendicular to Strut (Crack) LVDT Readings.



**Figure 7-20: Failure Mechanism of Specimen 1.**

The bend of longitudinal bars at the outer corner was pulled into concrete, leading to splitting and bursting of the joint region. Out-of-plane splitting and bursting of the joint region was also observed as evidenced by the crack patterns on the exterior face of the column and the out-of-plane bending of the column reinforcing steel (Figure 7–20f).

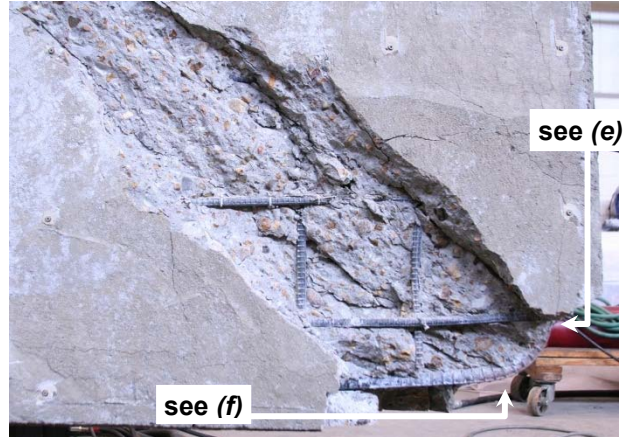
The same failure mechanism was observed in the end of the singly reinforced beam of Specimens 2 and 4 (Figure 7–21a and b, and Figure 7–22a and b). The measured maximum displacement at the loading point of the end of the singly reinforced beam was greater than the maximum displacement at the end of the doubly reinforced beam. Due to the lack of compression reinforcing steel that can slightly contribute to the stiffness of the beam, the singly reinforced side tended to fail prior to the doubly reinforced side. The cover concrete of the inner knee joint (CCC node) for both Specimens 2 and 4 commenced crushing prior to the ultimate brittle failure in the outer joint (Figure 7–21c and d, and Figure 7–22c and d), which was not observed in the testing of Specimen 1. At the outer joint areas, the debonding, pullout, bulging of the U-bars, and slicing into concrete of the longitudinal bars were observed, and this promoted out-of-plane bursting in the joint (Figure 7–21e and f, and Figure 7–22e and f). In addition, significant corrosion of the reinforcing steel bars of Specimen 4 was observed after the removal of the spalled concrete (Figure 7–22e and f). While the reinforcing steel bars showed the commencement of significant corrosion over a 2 year exposure period to field weathering conditions, it is expected that this may become significantly worse over time. The later testing of Specimen 3, which currently remains in the field exposure conditions under supplemental watering, should indicate additional damage from ASR/DEF effects and additional corrosion can lead to deteriorated structural behavior.

### **7.3.2 Longitudinal Steel Behavior**

Figure 7–23 presents the longitudinal steel strains of the end of the singly reinforced beam at variable loading levels during the test. Figure 7–23b presents the longitudinal steel strains of the control specimen (Specimen 1) that show the pattern of the strains based on the flexural theory (Figure 7–7b). Note that the singly reinforced beam region was strengthened in phase II testing such that the longitudinal steel strain at failure loading appears to be less than at a loading of 400 kip. The longitudinal steel strains of the damaged specimens (Specimens 2 and 4) varied



(a) Failure at the exterior corner



(b) After removal of the spalled concrete



(c) Crush cover at the interior corner of the joint



(d) After removal of the spalled concrete



(e) Anchorage debonding of transverse U-bars



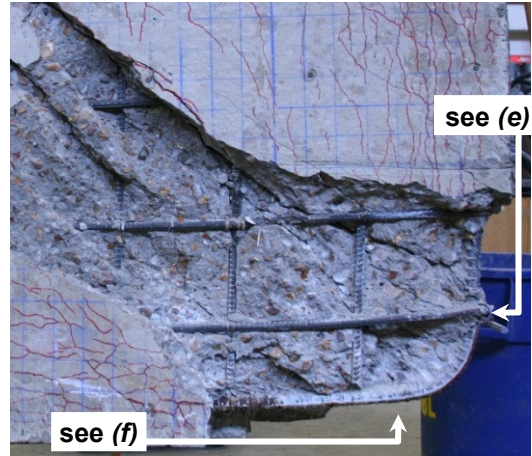
(f) Exterior face of the beam-column joint showing bulging of the U-bars and laterally displaced longitudinal steel

**Figure 7–21: Failure Mechanism of Specimen 2.**





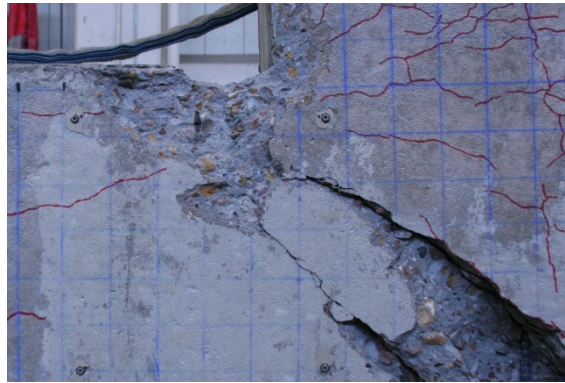
(a) Failure at the exterior corner



(b) After removal of the spalled concrete



(c) Crush cover at the interior corner of the joint



(d) After removal of the spalled concrete



(e) Anchorage debonding of transverse U-bars



(f) Exterior face of the beam-column joint showing bulging of the U-bars, laterally displaced longitudinal steel, and reinforcing steel corrosion

**Figure 7–22: Failure Mechanism of Specimen 4.**

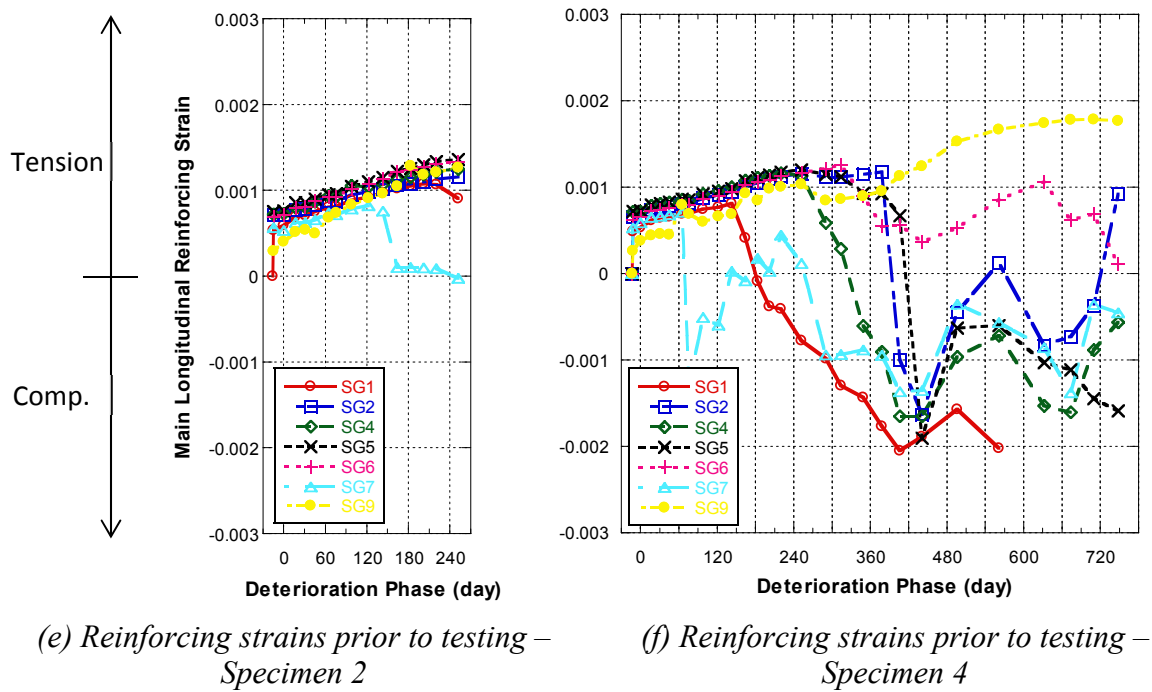
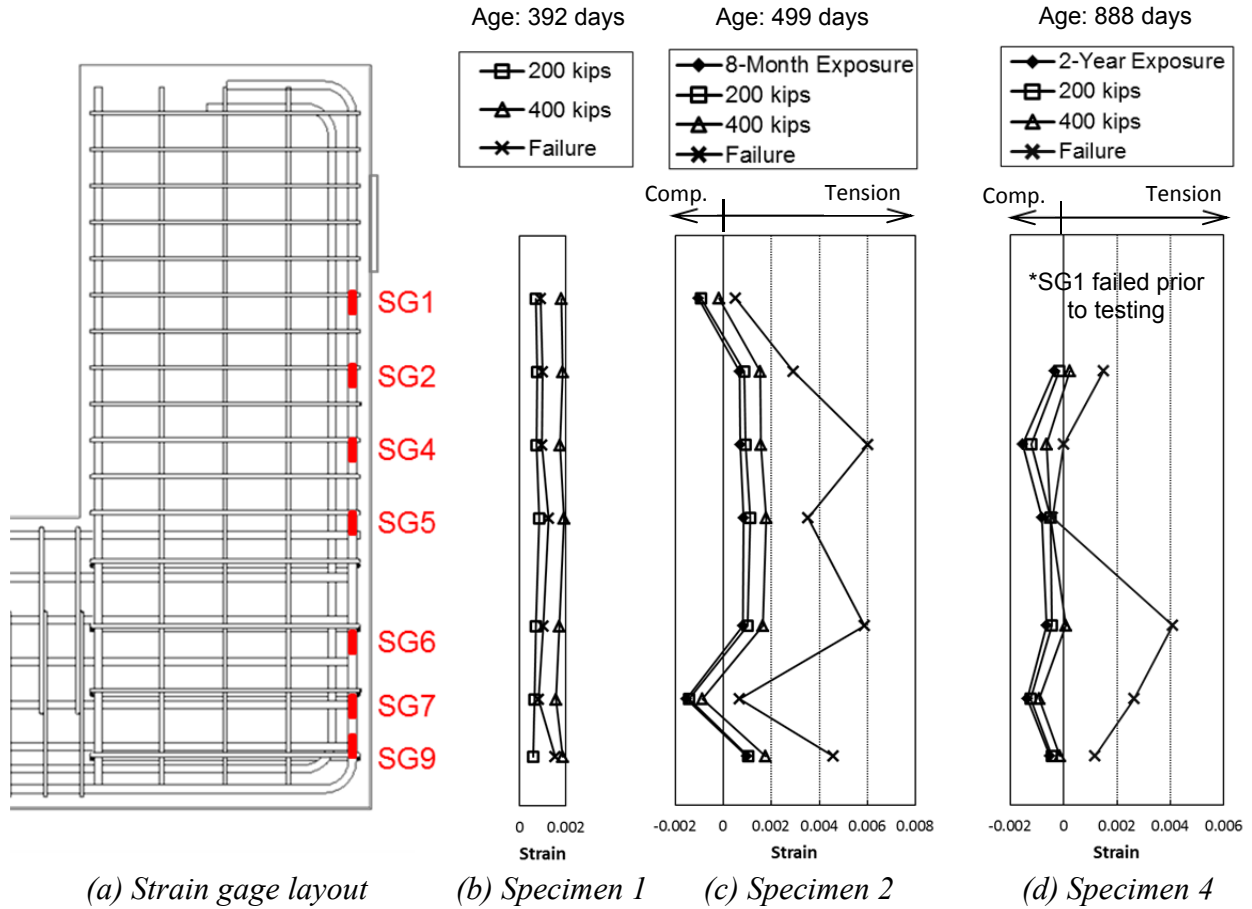


Figure 7-23: Strain Gage Readings in Main Flexural Reinforcing Steel.

over time in the deterioration phase as compared to the strains after preload (deterioration phase day 0, Figure 7-7c). During the deterioration program, the measured reinforcing strains gradually increased in the first four-month exposure (Figure 7-23e). In the subsequent period, compression strains were recorded (Figure 7-23e). This most likely indicated force redistribution between the main longitudinal rebars. Also, formation of ASR gel around the rebars may cause de-bonding between the concrete and steel and result in local compression strains. Note that there was a longitudinal crack right above the longitudinal rebar that was instrumented with strain gages. This crack possibly introduced more moisture, promoted local formation of ASR gel, and caused the unpredictability of measured reinforcing steel strains. Also, faulty readings may have been recorded due to the development of faulty gages over time from the ASR/DEF deterioration. However, the longitudinal steel strains increased during the testing (Figure 7-23c and d).

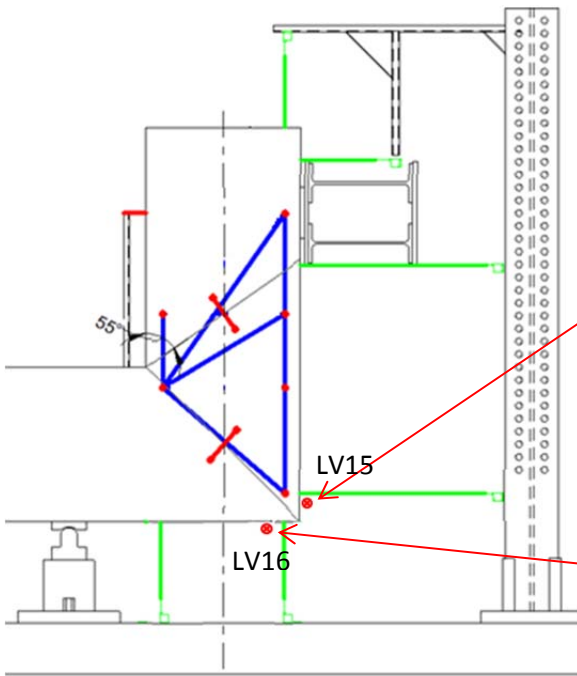
### **7.3.3 Out-of-Plane Behavior**

The failure mechanism of Specimen 1 drew attention to the out-of-plane bursting strains in the joint region. Therefore for Specimens 2 and 4, out-of-plane strains in the joint region were measured on the end surface of the first U-bar set (6 inches from the outer corner) and the column face of the first set of longitudinal distribution steel (9 inches from the outer corner) as shown in Figure 7-24a and b. The out-of-plane strains in the joint region of Specimens 2 and 4 were obtained by averaging the measured displacements over a 22 inch span. The out-of-plane strains were observed on the end and column surface and evidently support the bursting behavior in the joint region shown in Figure 7-24c and d. The out-of-plane strains on the column surface were greater than cap surface for both Specimens 2 and 4.

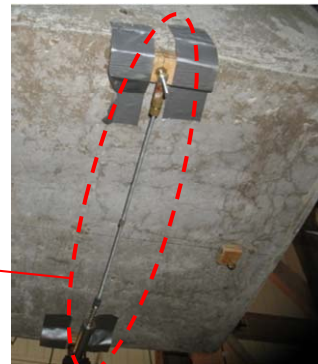
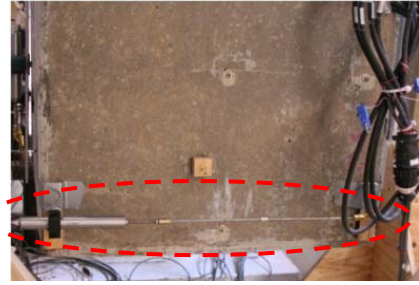
## **7.4 KEY FINDINGS FROM THE EXPERIMENTAL OBSERVATIONS**

In Chapter 5 it was shown that over time concrete specimens, when subjected to ASR/DEF effects, swell considerably in size. In turn this swelling effectively prestresses the reinforcing steel in both the longitudinal and transverse directions.

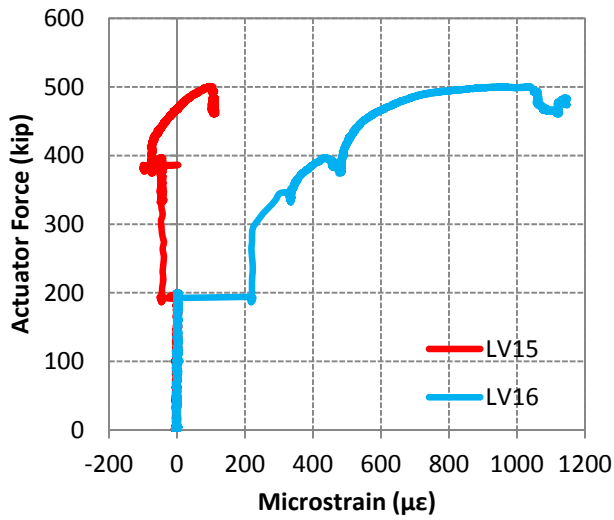
Based on the experimental investigation where three specimens were tested to failure, the key findings are summarized as follows:



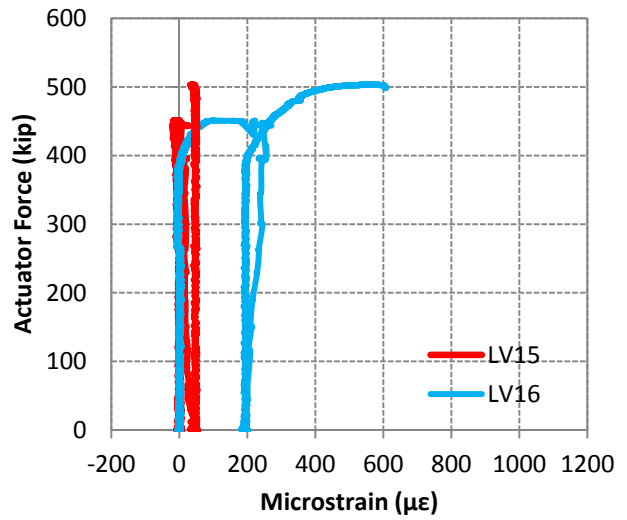
(a) External Instrumentation Layout



(b) Out-of-Plane LVDTs



(c) Specimen 2



(d) Specimen 4

Figure 7-24: Out-of-Plane Strains of Specimens 2 and 4.

- In contrast to the control case (Specimen 1) when loaded to failure, Specimens 2 and 4 with minor (eight months exposure) and moderate (two years exposure) ASR/DEF deterioration and associated swelling effects, led to greater stiffness and strength. Slightly more ductility was also observed in Specimens 2 and 4.
- Similar ultimate failure mechanisms in the control specimen and the two damaged specimens with varying levels of ASR/DEF deterioration were observed. These failures may be classified as *brittle joint shear failure* within the beam-column joint region. The failure mechanism resulted from the insufficient anchorage of the limited overlapping transverse reinforcement (U-bars) in the *joint region* within the plane of loading and also the lack of out-of-plane reinforcement along the back face of the joint region.
- Some corrosion of the reinforcing steel bars was observed in Specimen 4, which had two years of field exposure. Although in this case the deterioration from ASR/DEF and corrosion did not appear to impair the structural performance, it is unknown whether more severe ASR/DEF deterioration and additional corrosion as a by-product of the ASR/DEF deterioration would affect the structural capacity over time. Thus, one specimen still remains in the deterioration program with the expectation of developing severe ASR/DEF deterioration and corrosion damage. Therefore the final conclusion about the performance of D-regions under the influence of severe ASR/DEF deterioration cannot yet be declared.



## **8      FORCE-DEFORMATION MODELING OF EXPERIMENTAL RESULTS**

### **8.1   SCOPE**

Over the past decade, the structural longevity of a large number of reinforced concrete bridge bent caps has been compromised as a result of premature concrete deterioration. A thorough understanding of the structural behavior in disturbed regions is required in order to assess the integrity of bridges that show premature concrete deterioration. Current code design methods are purely force-based approaches that are conservative lower-bound solutions (AASHTO, 2010; ACI 318-08). Hence, they are not appropriate for modeling the complex behavior of D-regions as a means of assessing the degradation in strength. Additionally, the different analysis methodologies within a code have different levels of inherent conservatism. Although this may be justifiable from a design point of view, when design provisions are applied in an inverse form to analyze a structure, the methods may lead to deceptive results.

Clearly it is desirable to have an advanced method of analysis that can be adopted by practicing engineers and implemented as a means of assessing the structural nonlinear behavior of reinforced concrete bridges and D-regions.

The experimental investigation described in earlier chapters herein was specifically designed to replicate typical bridge bents currently used. A key aim of the experiments was to study the structural performance of large-scale reinforced concrete specimens without and with ASR/DEF induced damage. To extend the value of these experimental tests it is essential that the results can be captured and replicated with rigorous mathematical or computational structural models. To that end, this section uses the C-STM, as advanced in Chapter 4. The aim is to analyze each specimen through the same displacement path and compare the modeled force-deformation response with the experimental observations. Another key objective here, is not only to capture the overall force-deformation behavior, but also the ability to model the effect of premature concrete deterioration in bridge bents currently used.

Thus, this chapter first uses beam theory and SAT model, from which it is demonstrated that it is not possible to capture the overall performance. The structure is then modeled using the

C-STM technique without and with the effects of ASR/DEF, and the results are compared with the experimental results.

## 8.2 THE STRUCTURE

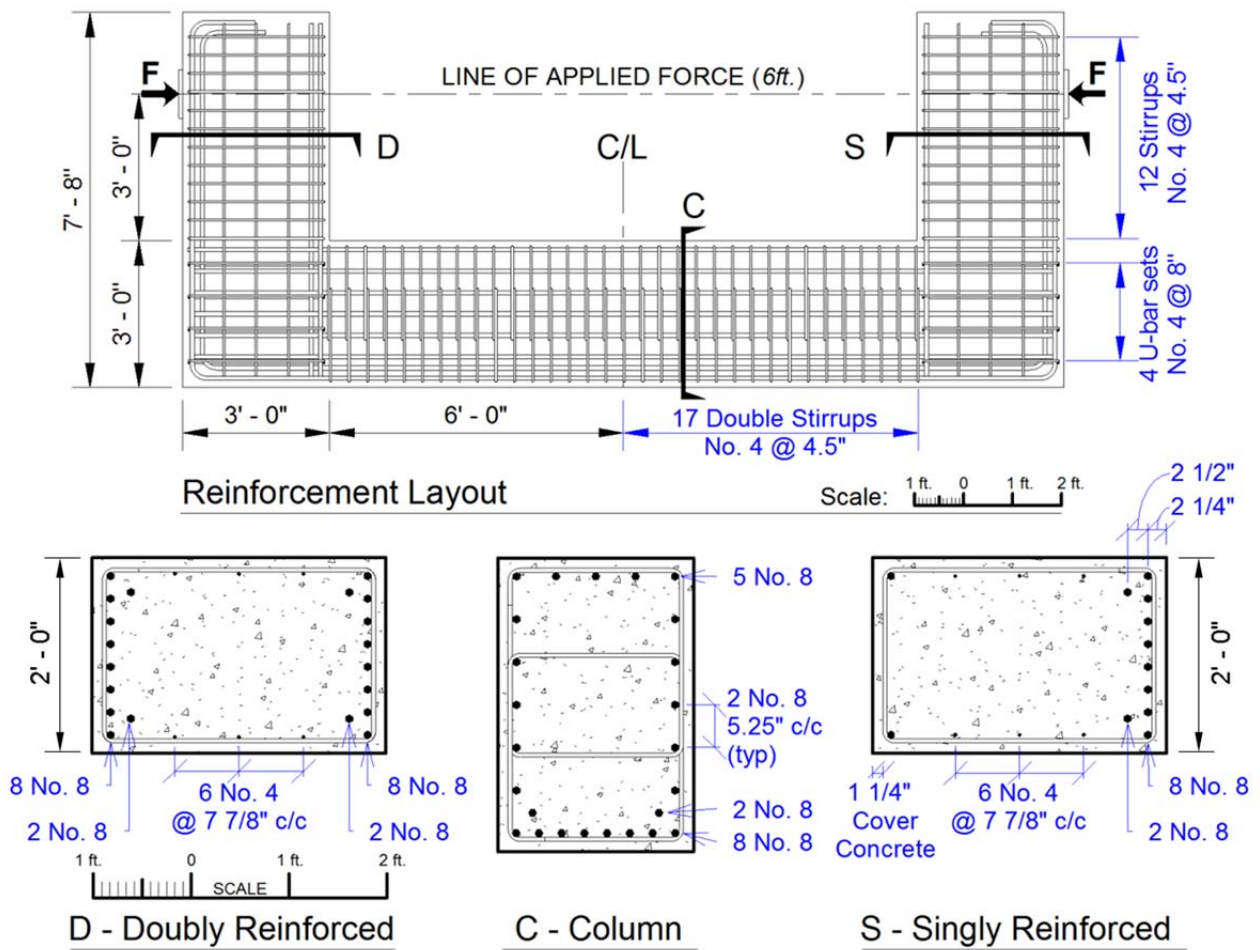
The experimental specimen was designed as a “C” shape sub-assembly such that two large-scale bridge bent components were placed back-to-back, so they could be tested as a self-reacting system. The C-Beam specimen had a constant cross-section of 3 ft deep and 2 ft wide that was symmetrical with the exception of the beam compression steel. More specifically, the physical model scale factors representing the singly reinforced cantilevered bent and the doubly reinforced straddle bent were approximately 0.5 and 0.75, respectively.

Figure 8–1 presents the reinforcing layout and cross-section of C-Beam Specimen. The longitudinal reinforcement consisted of 10 No. 8 bars running continuously around the outside and hooked at the end of each beam. The singly reinforced beam had two No. 8 straight compression bars for construction purposes. The doubly reinforced beam had symmetrical compression and tension reinforcement.

The longitudinal beam distribution steel (distributed along the beam web) consisted of three sets of No. 4 straight bars equally spaced. Transverse beam reinforcement consisted of closed stirrups with a center-to-center spacing of 4.5-inches starting at the column face. The longitudinal column distribution steel consisted of five sets of No. 8 bars equally spaced. Transverse column reinforcement had overlapping No. 4 stirrups spaced 4.5 inch centers. The beam-column joint was reinforced with four No. 4 U-bars at 8 inch centers continuing from the transverse beam reinforcement.

Table 8–1 presents the reported material strength data on the test day and experimental test results. Specimen 1 was the control specimen. This specimen was not conditioned under alternate wetting and drying cycles outdoors; therefore, it did not have any ASR/DEF induced damage. Specimen 2 and 4, which were respectively conditioned outdoors for 8 months and 24 months, showed *slight* and *moderate* amounts of damage due to ASR/DEF effects.





**Figure 8–1: Elevation and Cross-Section of the C-Beam Specimens.**

Full details of the experimental setup, testing procedures, and the general observations from the experiments are detailed in Chapter 7.

### 8.3 PRESENT CODE-BASED STRENGTH PREDICTIONS

The code-based design approaches that use the AASHTO *LRFD Bridge Design Specifications* (2010) (that were also described in detail in Chapter 3) are used to predict the response of C-Beam Specimens 1, 2, and 4.

Analysis results are presented in Table 8–1 and discussed as follows. Detailed computations can be found in Appendix C

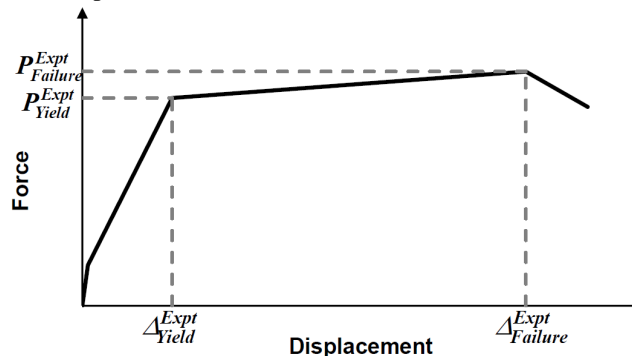
*Stage 1: Normal beam theory:*

- The yield moment ( $M_y^b$ ) and the externally applied load causing first yield ( $P_y^b$ ) are calculated using Eqs. (3–1) and (3–3), respectively. For Specimen 1, the analysis resulted in a yield moment of  $M_y^b = 1290$  kip-ft and a yield force of  $P_y^b = 430$  kip for the doubly reinforced beam. Results for Specimen 2 and 4 are presented in Table 8–1.
- The nominal flexural moment ( $M_n^f$ ) was calculated by normal practice as per the AASHTO *LRFD Bridge Design Specifications* (2010) and Eq. (3–4). Based on the nominal flexural moment  $M_n^f$ , and knowing that the shear span to the face of the column  $L_b = 36$  inch, the externally applied load causing flexure on the bent cap is found to be  $P_n^f = 481$  kip for the doubly reinforced beam of Specimen 1. Results for Specimen 2 and 4 are presented in Table 8–1.
- The shear capacity ( $V_n^s$ ) is calculated from Eq. (3–7). Since there are no prestressing tendons, the component of shear carried by tendons  $V_p = 0$ . The parameters  $\beta$  and  $\theta$  are calculated based on Method 1 specified in the AASHTO *LRFD Bridge Design Specifications* (2010). For Specimen 1, the shear capacity for the doubly reinforced beam was found to be  $V_n^s = 281$  kip and for the joint (using Eq. (3–17)) was found to be

**Table 8–1: Material Properties, Stage 1 and 2 Analyses, and Experimental Results.**

		Specimen 1		Specimen 2		Specimen 4		Comments
Material Properties	$f'_c$ (ksi)	5.40		5.60		4.00		
	$f'_t$ (ksi)	0.30		0.23		0.23		
	$E_c$ (ksi)	4190		4265		3605		
	Age at testing (months)	13		16		29		
Stage 1 Analyses (Sectional)	<b>Beam reinforcement</b>	<b>Double</b>	<b>Single</b>	<b>Double</b>	<b>Single</b>	<b>Double</b>	<b>Single</b>	
	$M_y^b$ (kip.ft)	1290	1276	1290	1277	1285	1269	Eq. (3–1)
	$P_y^b$ (kip)	<b>430</b>	<b>425</b>	<b>430</b>	<b>426</b>	<b>428</b>	<b>423</b>	Eq. (3–3)
	$M_n^f$ (kip.ft)	1442	1416	1443	1420	1428	1383	Eq. (3–4)
	$P_n^f$ (kip)	<b>481</b>	<b>472</b>	<b>481</b>	<b>473</b>	<b>476</b>	<b>461</b>	Eq. (3–6)
	$\phi_f P_n^f$ (kip)	433	425	433	426	428	415	$\phi_f = 0.9$
	$V_n^s$ (kip)	<b>281</b>	<b>285</b>	<b>283</b>	<b>287</b>	<b>266</b>	<b>270</b>	Eq. (3–7)
$V_n^j$ (kip)	<b>532</b>	<b>539</b>	<b>540</b>	<b>547</b>	<b>472</b>	<b>478</b>	Eq. (3–17)	
Stage 2 Analyses (SAT)	$P_y^{SAT}$ (kip)	429		429		429		Based on longitudinal steel yield.
	$\phi_y P_y^{SAT}$ (kip)	300		300		300		
	$P_n^{SAT}$ (kip)	<b>318*</b>		<b>330*</b>		<b>236*</b>		Based on node capacity.
	$\phi_y P_n^{SAT}$ (kip)	223		230		165		
Experimental Results	$P_{Yield}^{Expt}$ (kip)	440		440		440		
	$P_{Failure}^{Expt}$ (kip)	<b>474</b>		<b>485</b>		<b>503</b>		
	$\Delta_{Yield}^{Expt}$ (in)	1.49		0.92		1.1		
	$\Delta_{Failure}^{Expt}$ (in)	1.69		1.94		2.17		
	$\mu$	1.13		2.11		1.97		
Theory/ Experiment	$P_n^{SAT} / P_{Failure}^{Expt}$	0.67		0.68		0.47		

\*Expected critical failure mode capacity. Superscript: *b*=beam; *f*=flexure; *s*=shear; *j*=joint; SAT=strut-and-tie; *Expt*=Experiment. Notation for experimental results:



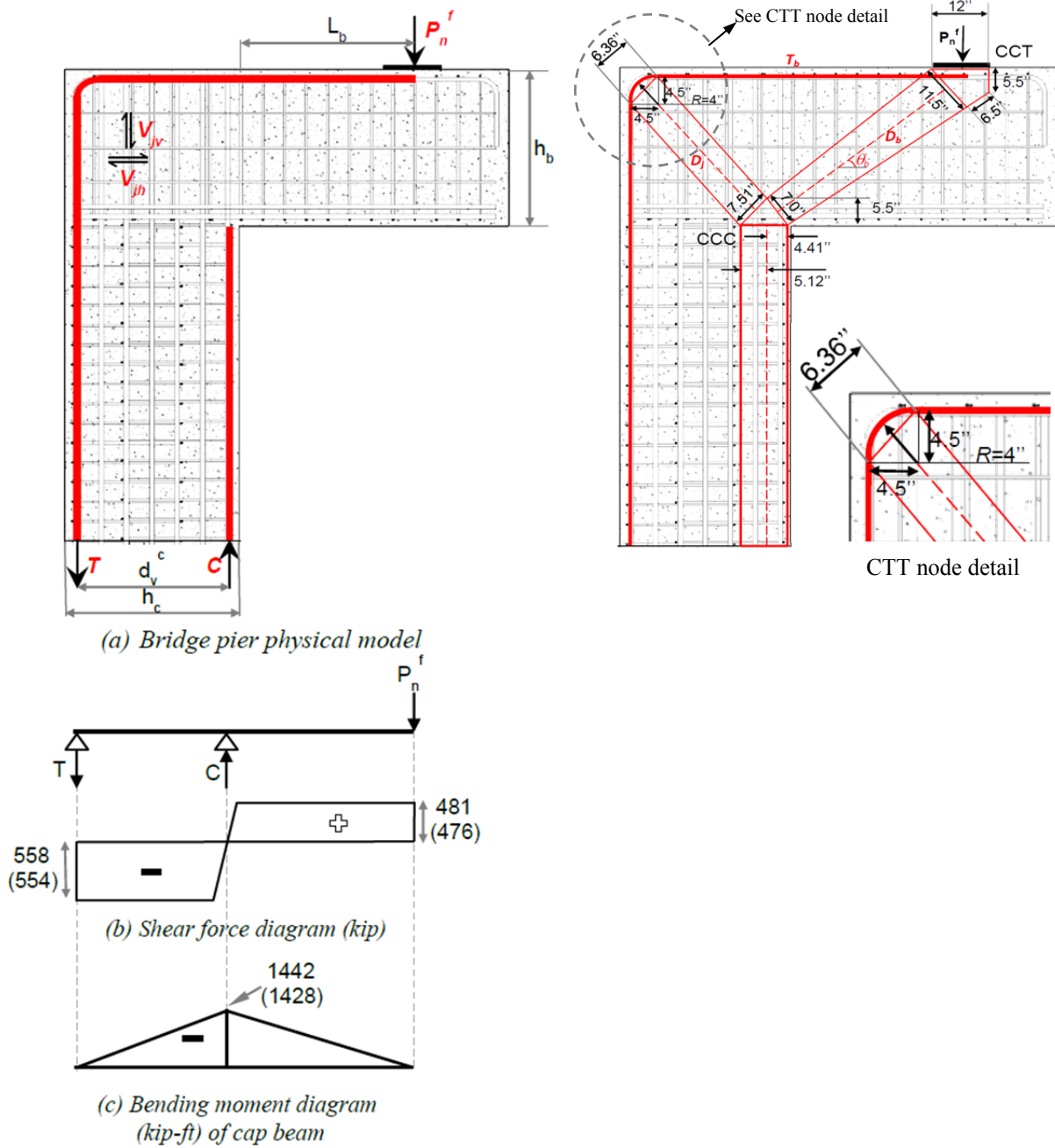
$V_n^j = 532$  kip. Results for Specimen 2 and 4 are presented in Table 8–1.

- The next step of the analysis is to determine the strength hierarchy. The strength reduction factor for shear and flexure are  $\phi_v = 0.90$  and  $\phi_f = 0.90$ , respectively. It is observed that for the doubly reinforced beam of Specimen 1,  $\phi_v V_n^s = 0.90 \times 281 = 253$  kip is less than  $\phi_f P_n^f = 0.90 \times 481 = 433$  kip. Similar outcomes are obtained for Specimen 2 and 4, implying that the factored shear capacity for the beam is insufficient, which can lead to a potentially brittle shear failure in the beam.
- It is important to investigate the shear in the beam-column joint, as this can be a critical section. Shear in the beam-column joint can be found from the shear force diagram of the equivalent beam model of the C-Beam specimen shown in Figure 8–2. The vertical joint shear for Specimen 1 was found to be  $V_{jv} = 558$  kip. The joint shear capacity of the joint is calculated based on Eq. (3–17) considering the contribution of the hoops/ties within the joint ( $V_{truss}$ ) and the corner-to-corner joint arch ( $V_{arch}$ ) as described in Chapter 3, and was found to be  $V_n^j = 532$  kip for the doubly reinforced side of Specimen 1. Thus for Specimen 1, for the joint  $\phi_v V_n^j = 0.90 \times 532 = 479$  kip is less than  $\phi_f V_{jv} = 0.90 \times 558 = 502$  kip. The results for Specimen 2 and 4 are presented in Table 8–1.

From Stage 1 analysis it can be concluded that the factored shear capacity for both the beam and the joint are insufficient. Given that beam-column joints are strictly D-regions where beam theory is insufficient to explain the performance, this warrants further investigation and a SAT analysis is performed.

#### *Stage 2: SAT analysis:*

Stage 2 of this analysis considers a SAT model developed for C-Beam Specimen 1 as shown in Figure 8–2. The steps involved are described below.



Note: Values for Specimen 1 and (Specimen 4)

**Figure 8-2: Modeling Approach Based on Code-Based Beam and SAT Methods.**

- As an important first step in the strut-and-tie analysis to construct the SAT model, it is necessary to determine the truss and node geometry. The width of the bottom face of the CCC node is equal to the depth of compression zone of the column ( $kd$ ) which is determined based on the equation for the elastic compression zone coefficient  $k$  Eq. (3–2). Based on the shear force diagram of the equivalent beam model of the bridge pier (Figure 8–2), the bottom face of the CCC node can be proportioned based on the ratio of  $V_{jv} / P_n^f = 558 / 481 = 1.16$  for Specimen 1. As per the AASHTO LRFD Bridge Design Specifications (2010) the width of the CCT node is taken to be equal to the width of the bearing pad, which is 12 inches in this case. The width of the CTT node is based on the bar bending radius ( $R = 4"$  Figure 7–20b) and the radius ( $d_b / 2$ ) of the longitudinal column reinforcement.
- The height of the CCC node is assumed to be equal to the depth of the back face of the CCT node (which equals two times the distance from the tension face to the centroid of the tension reinforcement). The crack angle in the beam-column joint is assumed to be  $45^\circ$ . After the node geometries are determined, all the SAT model dimensions and inclination angle can be obtained.
- Once the truss geometry is obtained, the determinate truss needs to be solved to obtain the member forces. Assuming that the tension tie has yielded, that is  $T = A_s f_y$ , all the member forces can be determined based on joint equilibrium. Based on steel yield, the externally applied load required to cause yielding is determined. However, this is most unlikely to be the critical load, as the critical node needs to be identified.
- Based on the node geometries (Figure 8–2d), the CTT node becomes the most critical node, and from Eq. (3–20) the allowable stress at the node face is  $f_{cu} = 0.65 f_c'$ . The node strength of the CTT node based on the concrete strength ( $f_c'$ ) of the specimen at the time of testing was found to be  $F_{cu} = 536$  kip for Specimen 1,  $F_{cu} = 556$  kip for Specimen 2, and  $F_{cu} = 397$  kip for Specimen 4.

- The external load required to cause failure based on the node capacity of the CTT node for Specimens 1, 2, and 4 was back calculated and found to be  $P_n^{SAT} = 318$  kip, 330 kip, and 236 kip, respectively. For all the specimen it is noted that  $P_n^{SAT} < P_n^f$  and also  $\phi_v P_n^{SAT} < \phi_f P_n^f$ . Therefore, the joint capacity is technically undependable for all three specimens. The results of the SAT analysis are summarized in Table 8–1.

It can be seen from the results presented in Table 8–1 that the load at failure for Specimen 1 is  $P_{Failure}^{Expt} = 474$  kip. However, the capacity of Specimen 1 obtained from flexure and SAT analysis are found to be  $P_n^f = 481$  kip and  $P_n^{SAT} = 318$  kip, respectively. Similar results can be seen for Specimen 2 and 4. Both methods (beam flexure and SAT) completely miss the actual failure mode (joint shear failure).

Figure 8–3 shows the experimental force-deformation curves of the three C-Beam specimens. Also plotted on these graphs are the strength capacities obtained from the code-based analyses. For Specimens 2 and 4, the prestress applied to mimic gravity effects while the specimens were conditioned in the field was not accurately captured. Hence the experimental results are shown with an initial offset. The dashed lines show the computed (assumed) behavior of this initial prestress effect prior to release of the prestress. As can be seen from Figure 8–3, the analysis results do not give any indication of the overall behavior of the structure, and hence the strength-only predictions are represented as horizontal lines.

From the above analyses, the externally applied load causing yielding based on beam flexure ( $P_y^b$ ) and the SAT ( $P_y^{SAT}$ ) methods agree well with the experimental observations. However, the sectional shear approach ( $V_n^s$ ) had the largest discrepancy and did not accurately represent the specimen capacity. These predictions are unduly harsh because the shear capacity is calculated in a D-region where the sectional theory breaks down. It is for this reason a SAT analysis needs to be conducted. This analysis would imply that the beam-column joint would fail even before the beam yielded, thus suggesting that the structure fails in a very brittle manner. However, this is not the case as can be seen from the experimental results (Figure 8–3) and hence the SAT analysis predicts a somewhat faulty picture about the expected structural behavior.

- $P_y^b$  = External load causing flexural yield
- $P_n^f$  = External load causing beam flexure
- $V_n^s = V_s + V_c$  = Nominal beam shear
- $V_n^j = V_{truss} + V_{arch}$  = Joint shear
- $P_y^{SAT}$  = External load based on longitudinal steel yield from SAT
- $P_n^{SAT}$  = External load based on node capacity from SAT

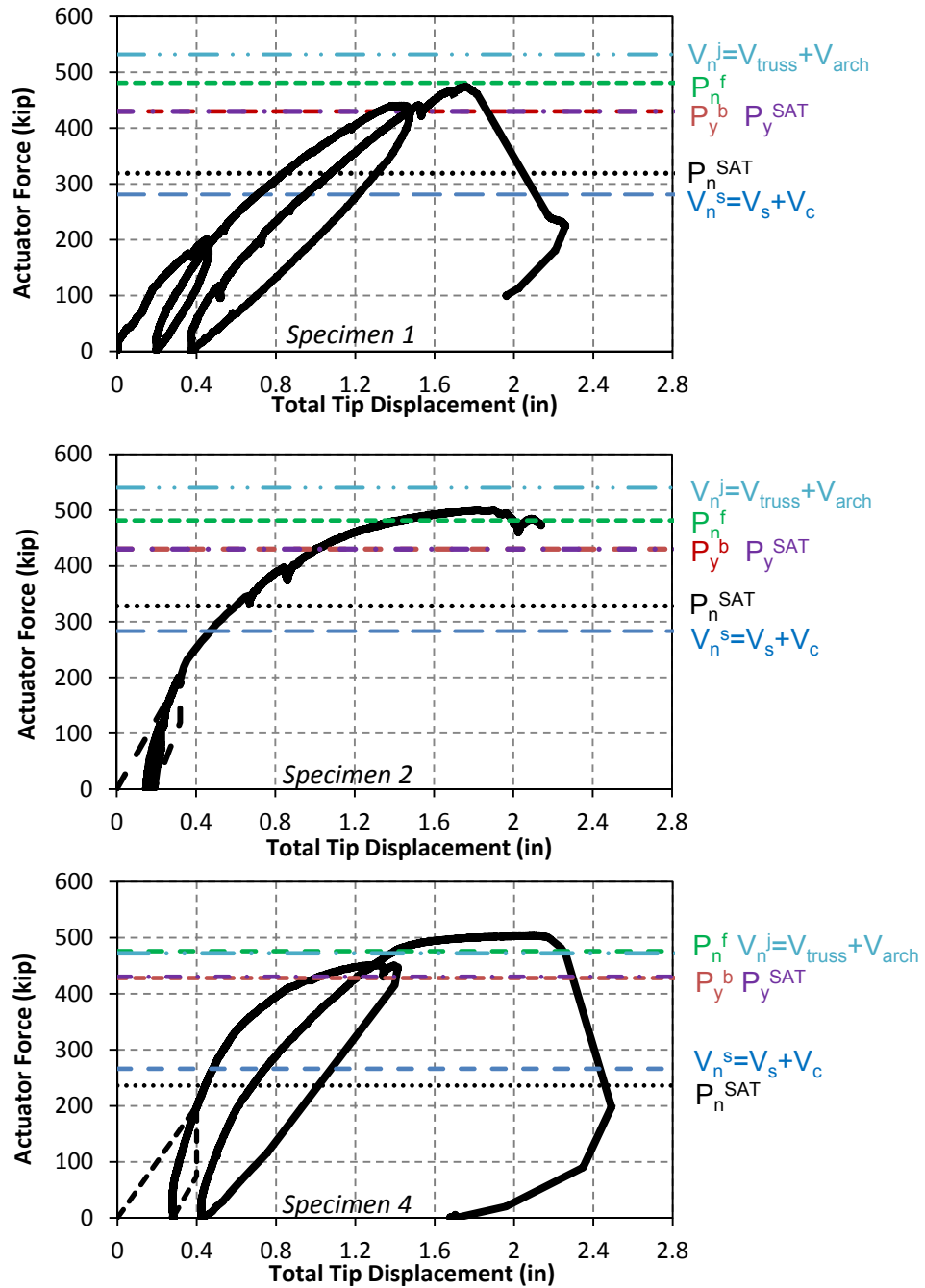


Figure 8-3: Experimental, Stage 1, and Stage 2 Results.



Moreover, it is not clear how the observed effects of ASR/DEF damage can be included in these simple methods.

It can be concluded from these results that it is somewhat inconclusive as to what will be the failure mode of the specimen, as it is observed that the joint capacity is technically undependable. Additionally, the SAT analysis does not take into account the effects of ASR/DEF damage. This justifies the use of a more advanced analysis technique such as the C-STM method as proposed in Chapter 4.

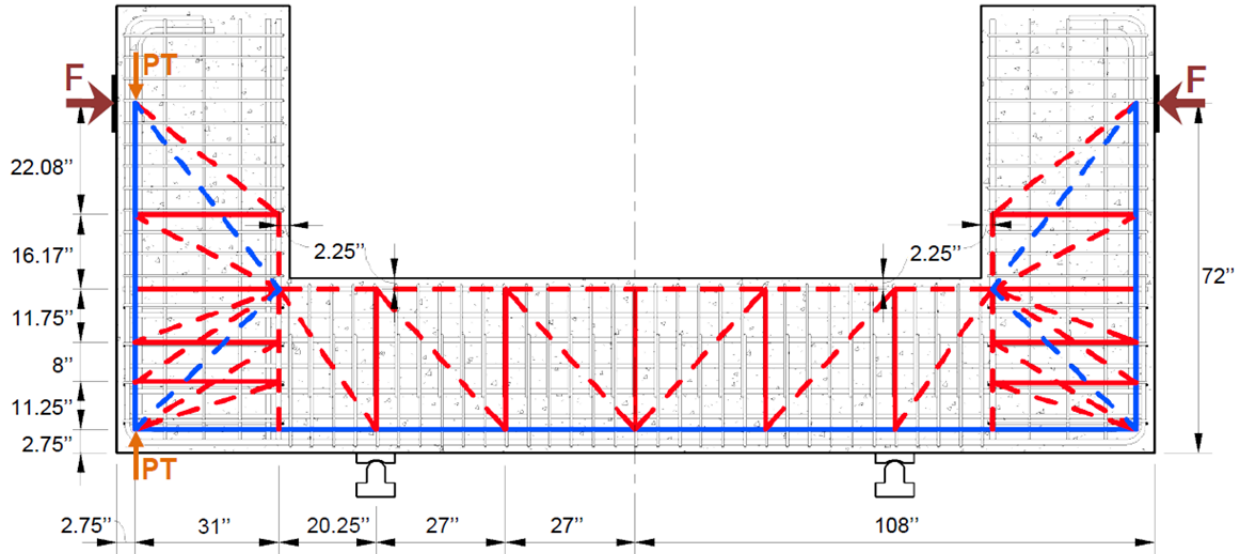
## **8.4 STRENGTH AND DEFORMATION CAPACITY USING C-STM**

### **8.4.1 The C-STM Model**

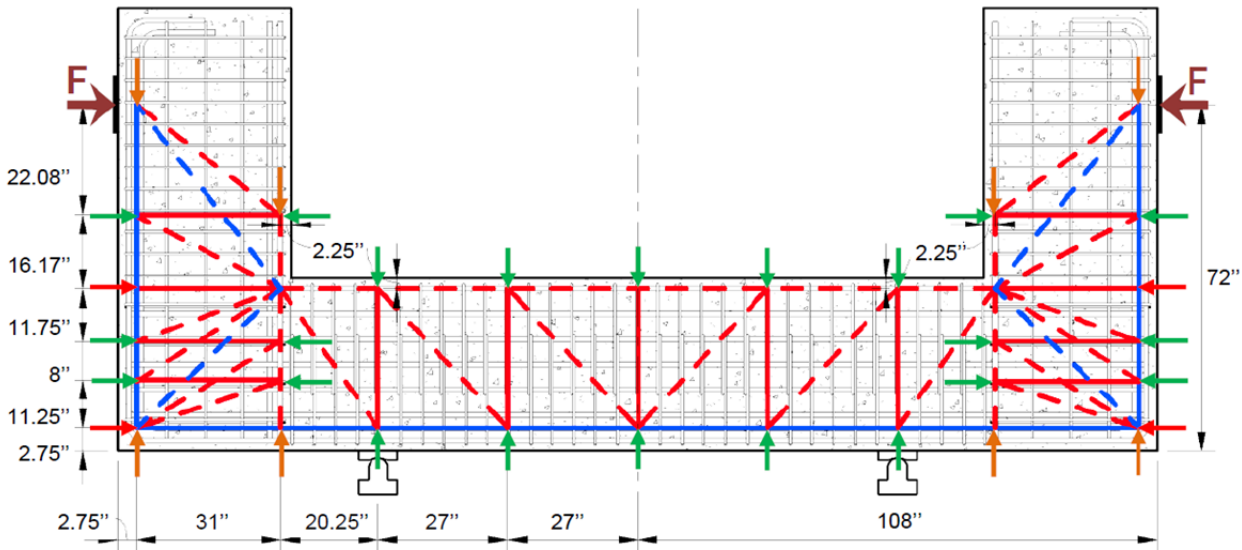
To obtain a better insight into the overall force-deformation behavior of the three C-Beam specimens and to understand the mechanics within the structure that lead to different behavior modes and eventually failure, the C-STM analysis described in Chapter 4 is implemented.

Figure 8–4 shows the C-STM model for C-Beam specimen (a) without and (b) with ASR/DEF damage. The cantilever beams were modeled using a single-point Gauss quadrature model. The joints were modeled using a two-point Gauss model (Kim and Mander, 1999) where the transverse ties were aligned with the U-bar reinforcement to provide a more exact representation of the reinforcement. The representative areas of reinforcement for the tension chord were defined as the sum of longitudinal steel and three sets of web distribution steel for tension. The compression chord was defined as the compression longitudinal steel.

Figure 8–4a shows the C-STM model that was developed for Specimen 1, which was the control specimen and had no ASR/DEF induced damage. To simulate the experimental test setup as accurately as possible, initial loads (shown as PT in Figure 8–4a) were applied to the tension chord members of the protected beam in order to replicate post-tensioning effects in accordance with Phase I and Phase II of testing as described in Chapter 7. This model essentially represents the C-STM analysis *without* any ASR/DEF effects. Row 2 of Figure 8–5 shows the nonlinear concrete stress-strain relations that were derived for the constituent elements of the C-STM model of Specimen 1.



(a) Specimen 1: Without ASR/DEF damage

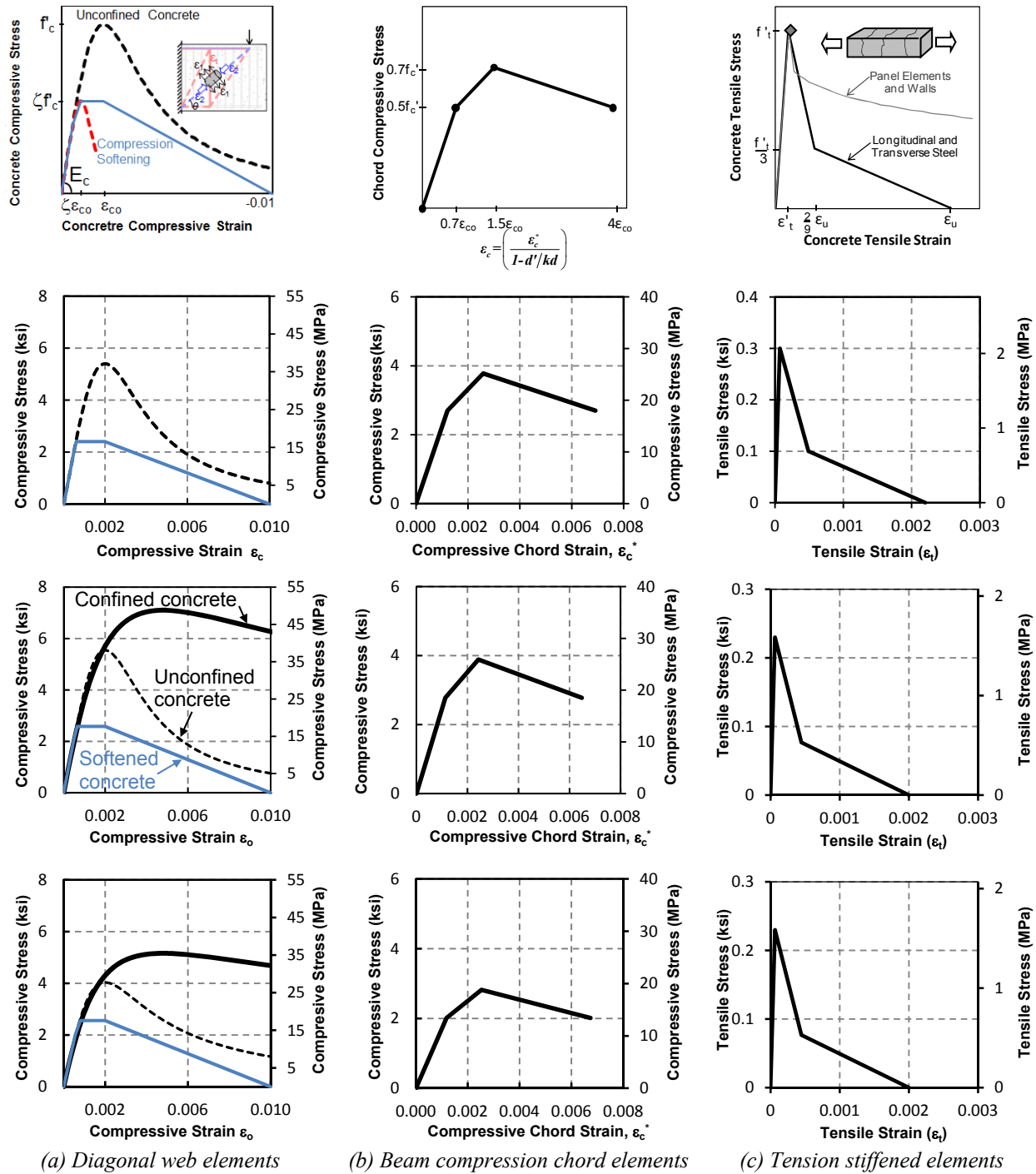


(b) Specimen 2 & 4: With ASR/DEF damage

- Primary tension reinforcement
- Ties representing bundles of hoops
- - - Concrete struts for "truss"
- - - Central concrete "arch"
- Initial confinement effect in hoops and longitudinal steel due to concrete swelling, modeled as a set of externally applied nodal forces
- 
- 

**Figure 8–4: Modeling the C-Beam Specimens without and with ASR/DEF Damage.**

Note: The additional forces in (b) represent the prestress effect actively induced in the reinforcing steel caused by ASR/DEF induced concrete swelling.



**Figure 8-5: Cracked Reinforced Concrete Material Properties.**

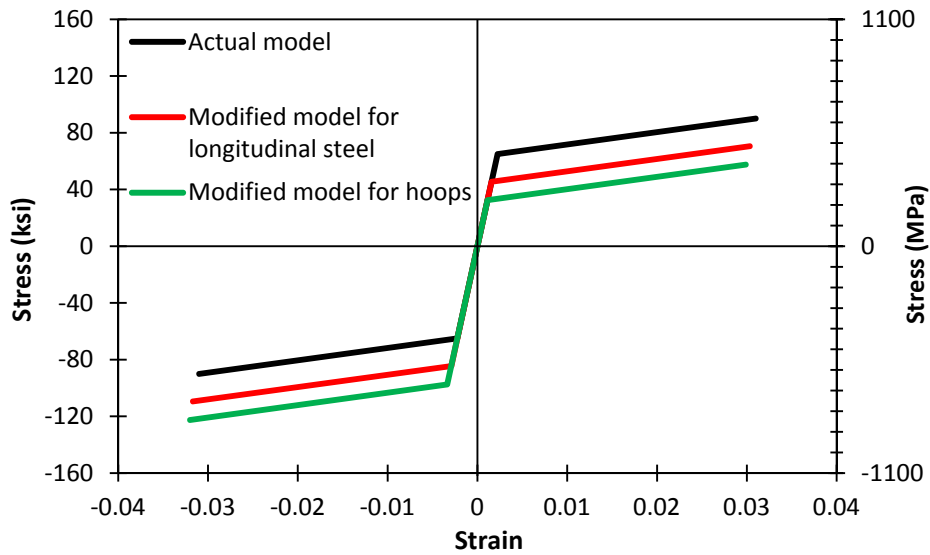
- Row 1: Theoretical nonlinear behavior.**
- Row 2: Specimen 1 modeled behavior.**
- Row 3: Specimen 2 modeled behavior.**
- Row 4: Specimen 4 modeled behavior.**

Specimen 2 and 4 showed *slight* and *moderate* damage due to the effects of ASR/DEF. Figure 8–4b shows the C-STM model for C-Beam Specimen 2 and 4. Prestressing forces were applied on the longitudinal and transverse reinforcement in the beam and column in order to replicate the prestress effects that arise as a consequence of the swelling within the core concrete due to ASR/DEF effects. From the recommendations made in Section 4.8.5, the strength reduction factor for cover concrete is taken as  $\lambda = 0.85$  for Specimen 2 with *slight* damage, and  $\lambda = 0.70$  for Specimen 4 with *moderate* damage due to ASR/DEF effects. The confinement ratio (Mander et al., 1988) was calculated to be  $K_{cc} = f'_{cc} / f'_{co} = 1.20$  for the beam and  $K_{cc} = 1.28$  for the column for Specimen 2. For Specimen 4, the confinement ratio was calculated as  $K_{cc} = 1.28$  for the beam and  $K_{cc} = 1.35$  for the column. The prestress in the longitudinal reinforcement was taken as  $0.3 f_y$  and  $0.5 f_y$  for Specimen 2 and 4, respectively. The prestress in the hoops was taken as  $0.5 f_{yh}$  and  $1.0 f_{yh}$  as per the recommendations for slight and moderate damage due to ASR/DEF for Specimens 2 and 4, respectively. The modified stress-strain relation of longitudinal and transverse reinforcing steel due to prestressing effects is shown in Figure 8–6.

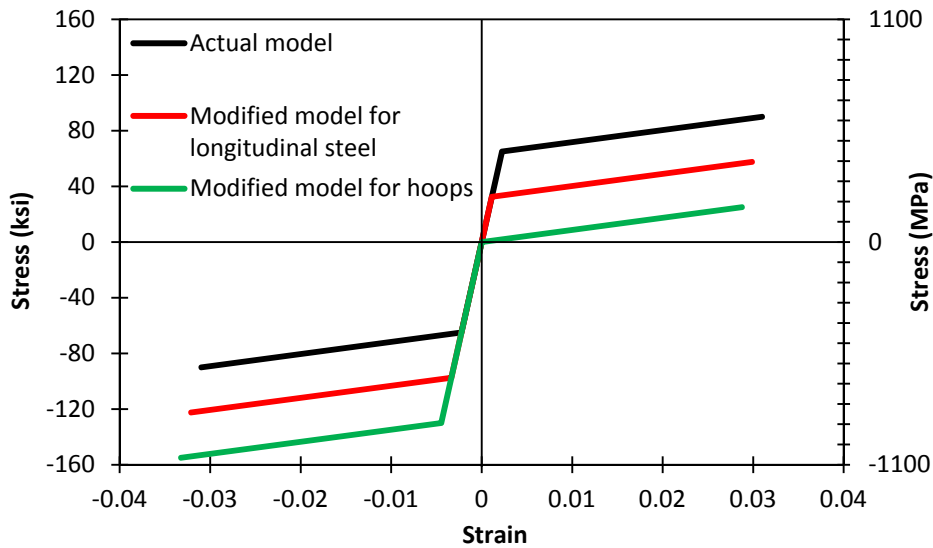
Rows 3 and 4 of Figure 8–5, respectively, show the different nonlinear concrete stress-strain relationships that were derived for Specimens 2 and 4 from the material properties presented in Table 8–1.

#### 8.4.2 Results of C-STM Analysis

Figure 8–7 presents the overall force-deformation results obtained from the C-STM for the three C-Beam specimens; these results may be compared to the experimental behavior. As noted earlier, Specimen 1 was the control specimen and had no damage arising from adverse ASR/DEF effects, whereas Specimen 2 and 4, respectively, showed slight and moderate damage due to ASR/DEF effects. The C-STM provides results that simulate the overall behavior of each specimen quite well. The initial tension-stiffening effects observed are captured well by the C-STM. The ASR/DEF damage effects caused by the swelling of concrete put the reinforcing steel into a state of tension—this in effect prestresses the concrete. When this prestress effect is

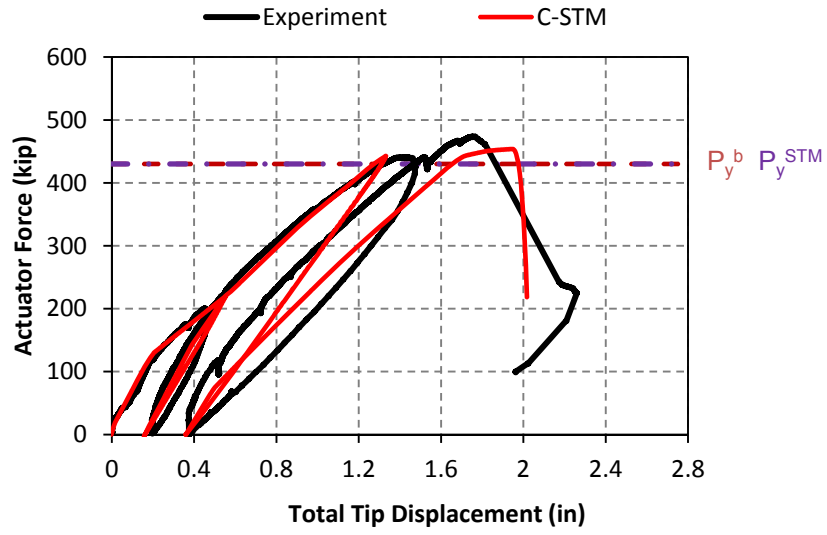


(a) Specimen 2

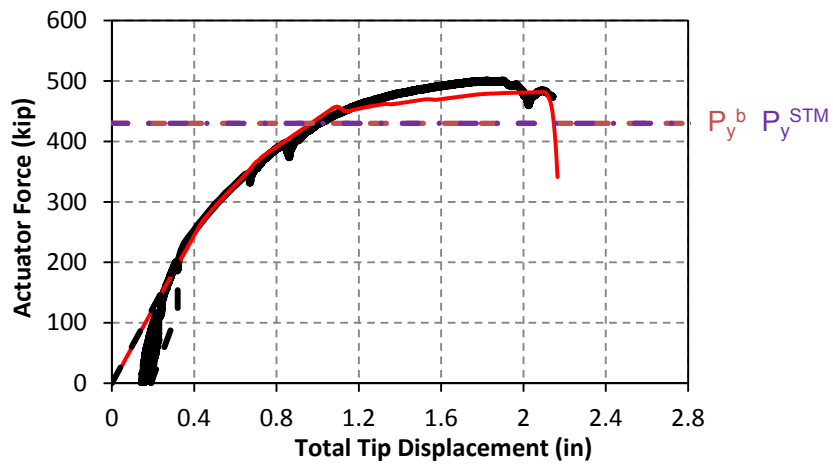


(b) Specimen 4

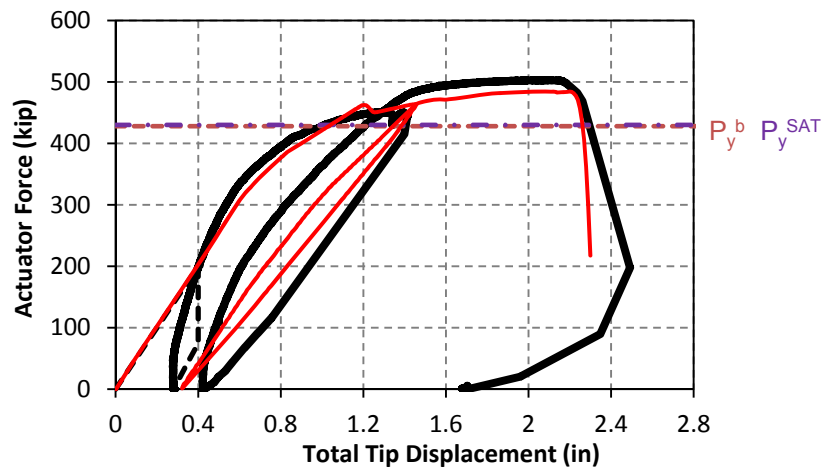
**Figure 8–6: Actual and Modified Stress-Strain Models for Reinforcing Steel to Account for Prestressing Effects in C-Beam Specimens.**



(a) Specimen 1



(b) Specimen 2



(c) Specimen 4

Figure 8-7: Comparison of Experimental and C-STM Results for C-Beam Specimens.

modeled accordingly by applying external loads and modifying the steel stress-strain relations (Figure 8–6), the behavior modification is accurately captured.

The main difference between the modeled and the observed behavior is when unloading and reloading occurs. The partial opening/closing of cracks in the presence of shear deformations leads to a greater hysteresis in the experimental results than obtained through the C-STM modeled results, where concrete opening/closing is crisp and tight.

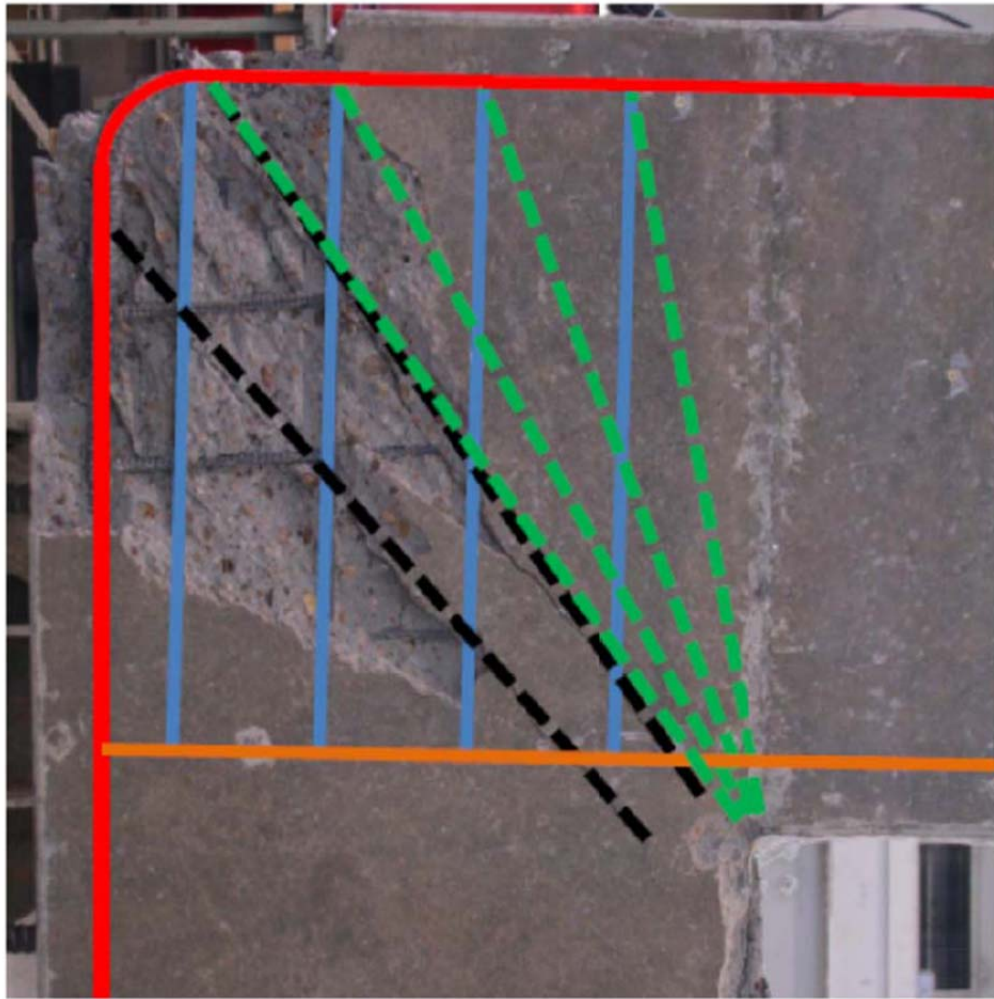
The experimental results confirm that for all tests, as shown in Figure 8–8, the beam-column joint was most critical, and the CTT node is the most critical node. The joint is overlaid with the truss and the arch members as was observed from the crack pattern.

#### **8.4.3 Interrogation of Internal Strains from C-STM and Comparison with Experimental Results**

To further substantiate the veracity of the C-STM approach, it is of interest to compare the strains in the individual C-STM members to the strain data obtained through the instrumentation in the experimental setup. This permits confirmation of the C-STM modeling strategy, and in particular replicates the micro-level behavior of the structure as well as possible.

Figure 8–9 and Figure 8–10 present the development of the nonlinear behavior in the C-STM with increasing levels of force. The modeled behavior is compared with experimentally observed instrumental results. The notation in the left-hand column first describes the type of nonlinear mechanism in parentheses (a description of each follows) followed by the member it refers to (e.g., beam, joint, or column). The instrumentation used for each graph is labeled in the bottom corner of each graph and can be referred to in Figure 7–7.

The first nonlinear mechanism is concrete cracking of the concrete truss elements as shown in Figure 8–9. Subsequent nonlinear mechanisms are shown in Figure 8–10, consisting of concrete arch and chord inelastic compression, followed by steel yielding. The progression of nonlinear behavior can be described as follows:



- Tension ties
- Beam chord
- Transverse ties
- - - Truss action
- - - Arch action

**Figure 8–8: Failure Pattern Observed at the Beam-Column Joint of C-Beam Specimen 1.**



*LC*: Longitudinal Cracking (rows 1 and 2 of Figure 8–9) first occurred in the beam, shortly followed by the column. This is when the member stress exceeds the concrete tensile strength  $f_t'$ , thus initiating flexural cracking in the beam at the column face and along the column, respectively. Tension softening refers to the concrete's ability to resist tensile strains after the development of the primary cracks.

*TC*: Transverse Cracking (rows 3 and 4 of Figure 8–9) then occurred in the transverse concrete elements, starting in the beam-column joint and then in the beam element. This corresponds with diagonal shear cracking observed as a result of the flexure-shear interaction and is in agreement with experimental observations.

*CC*: Chord Compression (row 1 of Figure 8–10) occurred in the column compression chord elements, indicating that the concrete had exceeded the elastic limit. It is evident that the results from the C-STM agree well with the strain gage observations located on the column compression steel at the beam face.

*LY*: Longitudinal Yielding (row 2 of Figure 8–10) occurred in the longitudinal beam reinforcement when the stress exceeds the specified yield stress  $f_y$ . The C-STM results agreed well with the steel strain gage response of *SG5\_D* and the corresponding *LV2\_D* truss member response.

*TY*: Transverse joint steel Yielding (row 3 of Figure 8–10) in the joint U-bars was the next member in the C-STM to respond nonlinearly. The result from the C-STM is in good agreement with the strain gage data *SG21\_D*.

*AC*: Arch Crushing (row 4 of Figure 8–10) ultimately leads to the failure of Specimen 1. The ultimate strength of the specimen is reached when concrete reaches its limiting strain of 0.002. The simulated response is in good agreement with the embedded strain gages and the external LV truss member response.

In a similar manner, Figure 8–11 and Figure 8–12 present the development of nonlinear behavior in the C-STM for Specimens 2 and 4, respectively. As in the earlier case, the simulated behavior is compared with experimentally observed instrumental results. The instrumentation

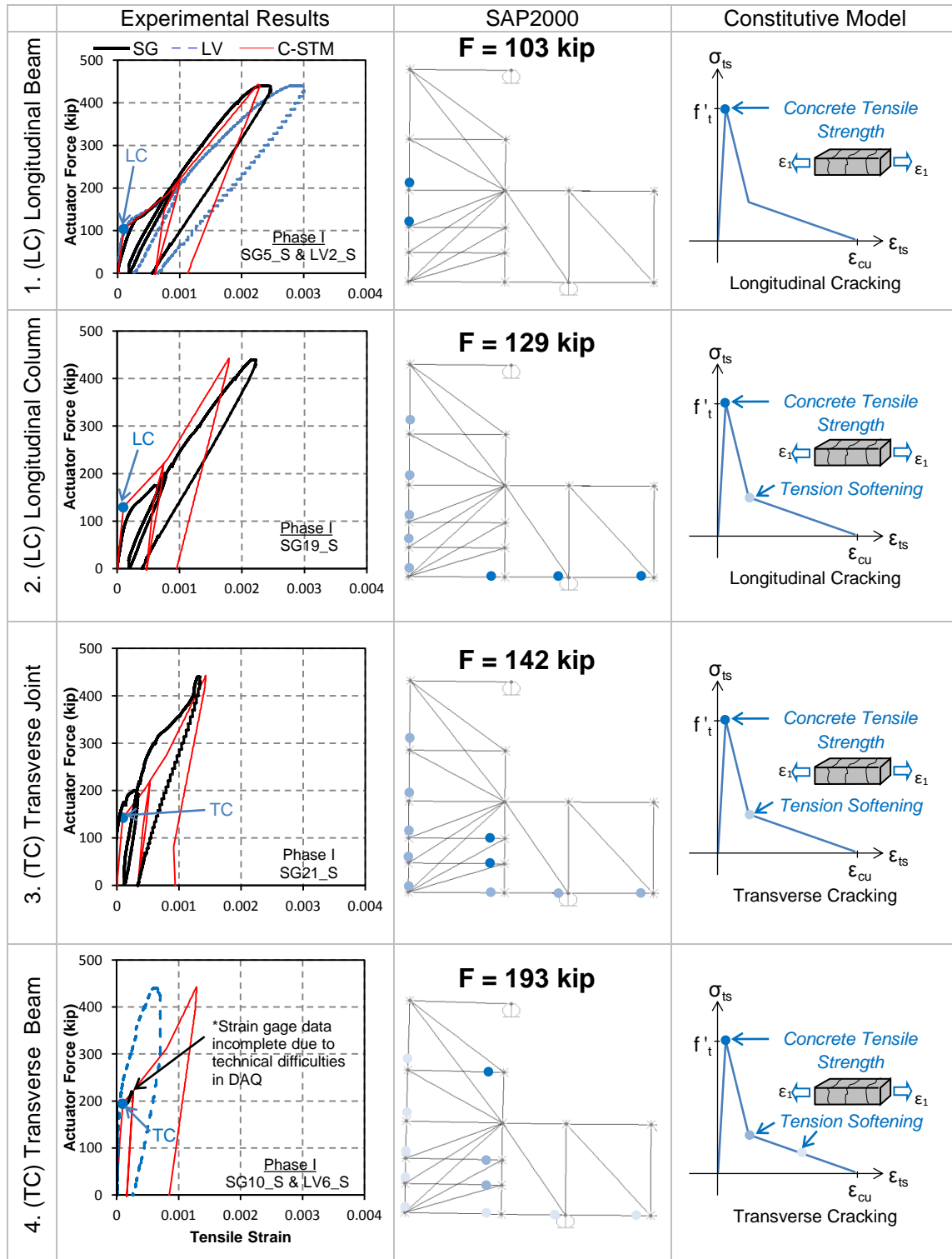


Figure 8-9: Experimental vs. C-STM Comparison of Nonlinear Response and Early Concrete Cracking Effects: Specimen 1.

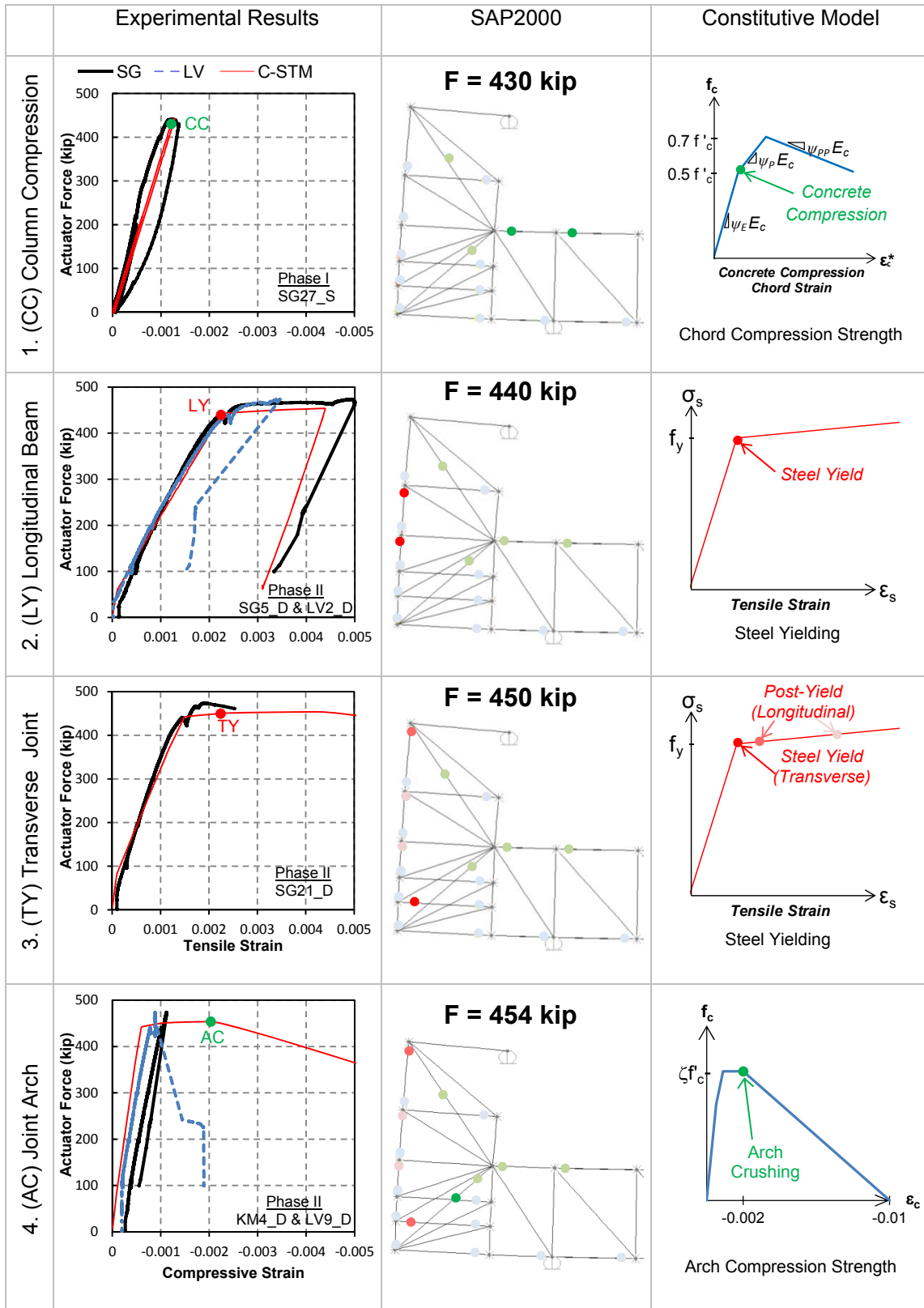
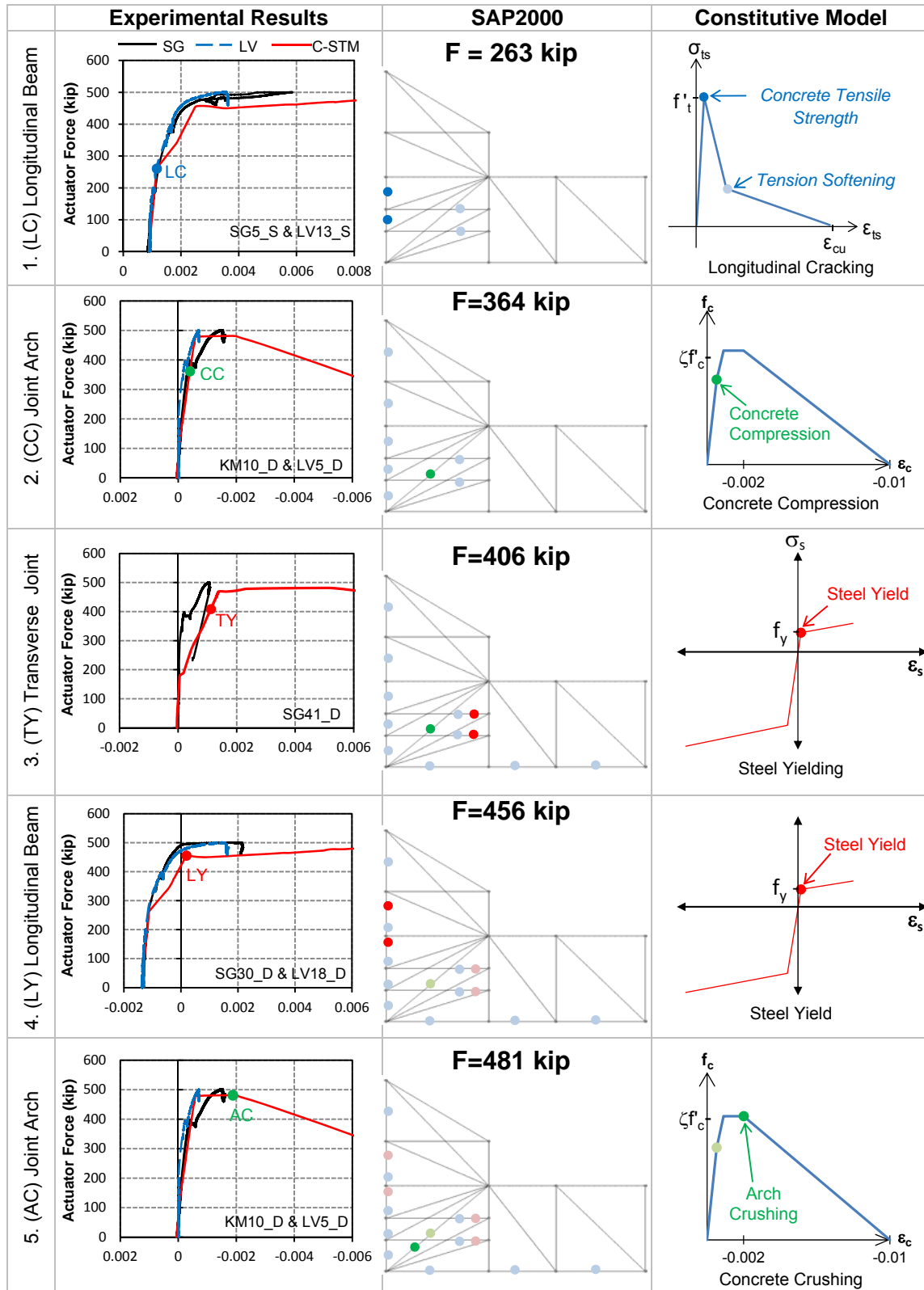
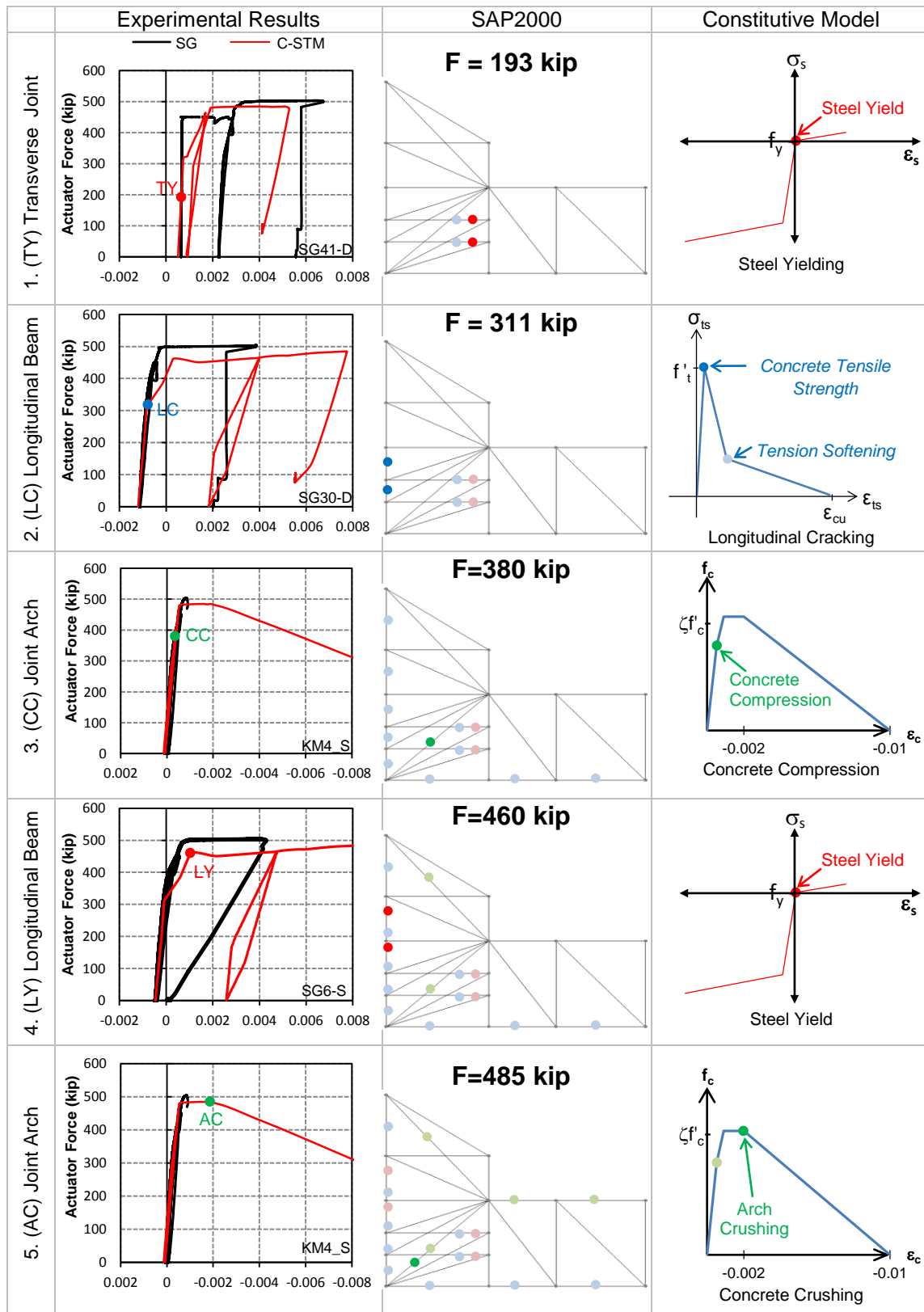


Figure 8–10: Experimental vs. C-STM Comparison of Nonlinear Concrete and Steel Response: Specimen 1.



**Figure 8–11: Experimental vs. C-STM Comparison of Nonlinear Concrete and Steel Response: Specimen 2.**



**Figure 8–12: Experimental vs. C-STM Comparison of Nonlinear Concrete and Steel Response: Specimen 4.**

used for each graph is labeled in the bottom corner of the graph and can be referred to in Figure 7–7.

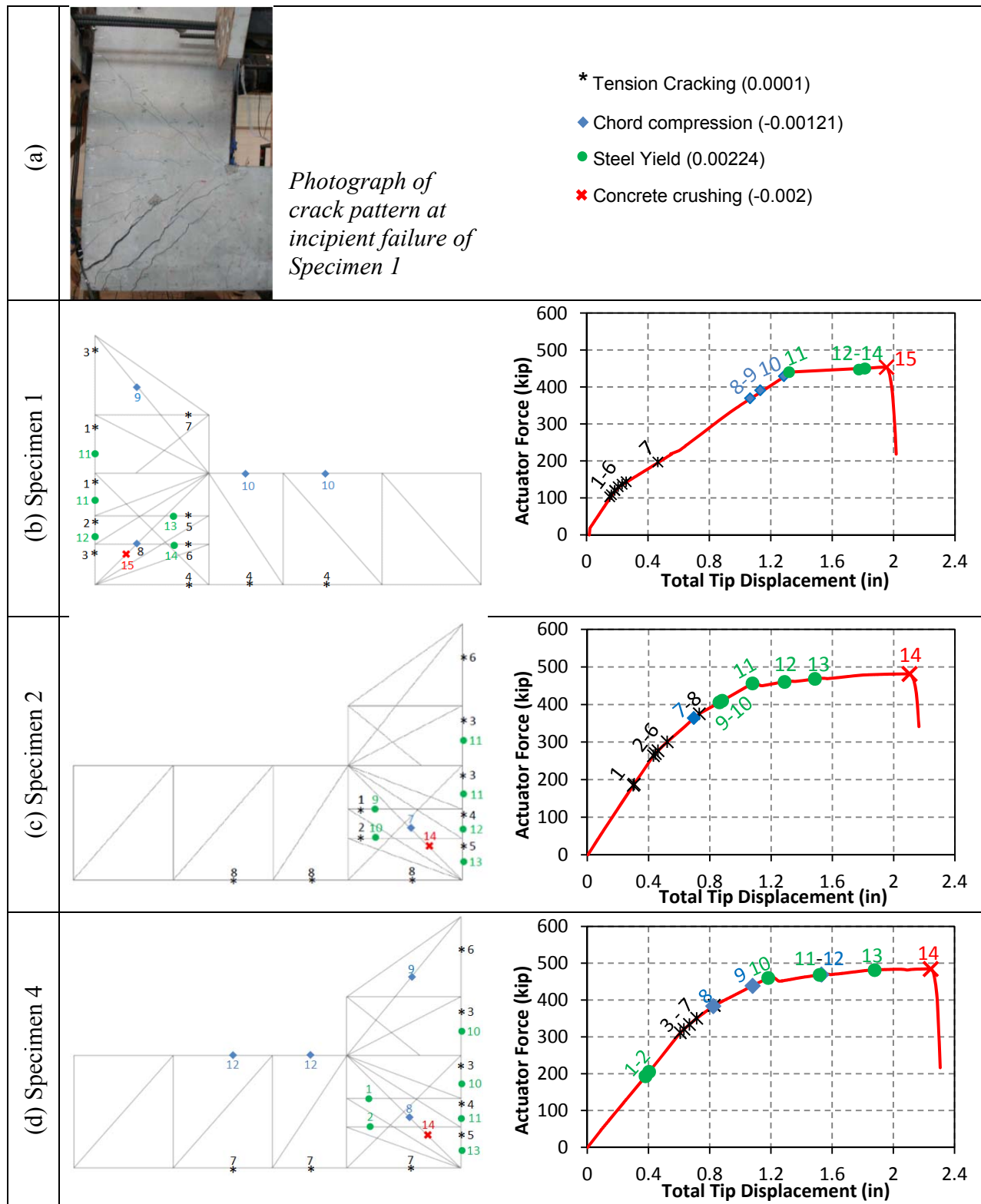
In the case of Specimens 2 and 4, the transverse steel yields ahead of the longitudinal flexure yielding of reinforcing steel. This is in agreement with the experimental results, where it was observed from field strain gage measurements that the hoop bars were subjected to significant strains due to the effects of ASR/DEF, which leads to the early yielding of hoops. As in the case of Specimen 1, the final event that eventually leads to the failure of the specimens is the crushing of the joint arch member when a compressive concrete strain of 0.002 was achieved. Beyond this point, when the deformations on the specimens increased, the arch was unable to sustain the load, and as a consequence “softening” occurred. This leads to physical instability during the experiment and a sudden failure. In a similar manner, during computational modeling, the post-peak behavior of the arch led to numerical instability and thus sudden failure.

In Figure 8–12, the C-STM shows similar trends with the experimentally obtained strain gage data. Although the strains do not precisely match with the experimental data, the trends are nevertheless indicative. Differences can be ascribed to the fact that strain gages were located across cracks, and hence the data obtained from the strain gages may not necessarily be truly indicative of the average strains between the nodes in the structure.

It is evident from Figure 8–9 through Figure 8–12 that the trends of the strain modeled by C-STM are in satisfactory agreement with the experimentally obtained data. This provides evidence that the C-STM not only models the macro-behavior well, but also represents quite well the behavior at the micro-level.

#### **8.4.4 Failure Analysis**

In this sub-section all the nonlinear mechanisms that developed progressively in the various constituent members of the C-STM are presented. The photograph showing the crack pattern on the doubly reinforced beam of C-Beam Specimen 1 is presented in Figure 8–13a. Figure 8–13b–d shows the development of nonlinear hinges formed during the C-STM analysis (left column of Figure 8–13) of the three specimens. When this information is combined with the overall force-deformation behavior of the specimens (the graphs in Figure 8–13), some insight into the



**Figure 8–13: Computed Sequence of Non-Linear Behavior Events.**  
 (Note: Specimens 1, 2, and 4, respectively, had no, minor, and moderate ASR/DEF damage).

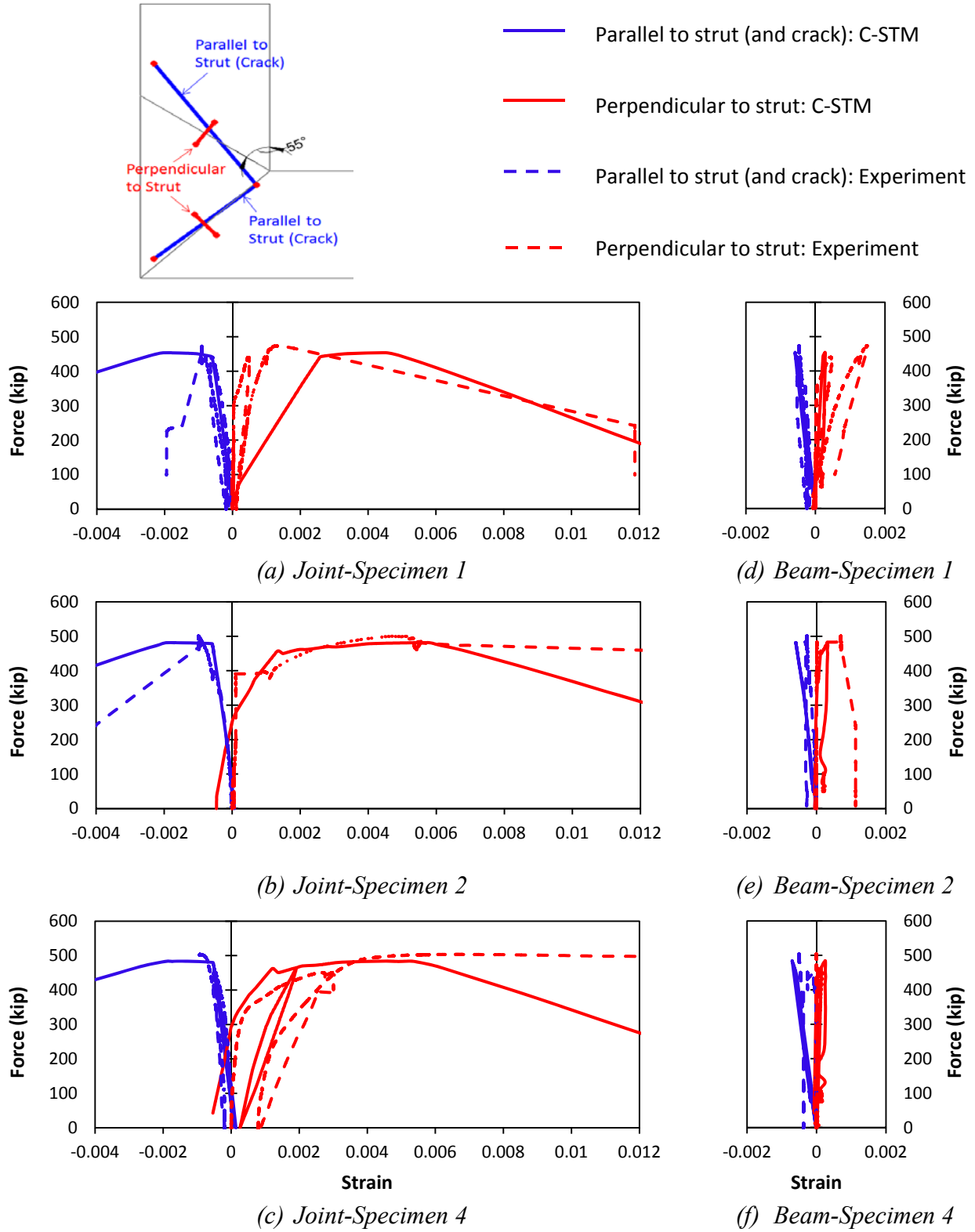
progression of nonlinear hinge formation with respect to the global force-deformation behavior of the structure is obtained. These modeled outcomes shown in Figure 8–13 agree remarkably well with the visual observations made during each experiment.

It is also of interest to investigate the actual cause of failure in order to avoid any misconceptions about the failure mode. Due to the extent of relatively serious damage at the CTT node of the knee joint, it is tempting to surmise this led to the failure of the structure. However, an in-depth forensic analysis into the strains parallel and perpendicular to the arch strut in the beam-column joint is instructive in shedding some light into the actual cause of failure of the structure. Figure 8–14 shows the strains measured parallel to the strut (and crack) along with the strains measured perpendicular to the crack from the experiment and the C-STM analysis. Given the vagaries of strain measurements in highly cracked concrete elements, satisfactory agreement between the experimental observations and the computed response is evident. This agreement provides some further vindication of the adopted C-STM minimalist model.

It is evident from Figure 8–14 that the strains measured perpendicular to the cracks are significantly higher in the beam-column joint when compared to the beam region. The tensile strain acting orthogonal to the compression member results in the concrete softening phenomenon, which causes a reduction in the compressive strength of the concrete arch. This fully explains why the failure occurred in the beam-column joint and not in the beam region of the structure. Based on the experimental and computational evidence, the final sequence of events is postulated as follows:

- The concrete softening phenomenon causes the concrete arch to fail in the beam-column joint.
- Significant out-of-plane concrete dilation concurrently results.
- The hoops in the beam-column joint attempt to restrain this dilation.
- However, as the hoops are lapped and not adequately hooked between the two outer faces of steel, the lack of transverse confining action causes large dilation to develop with consequent failure of the core concrete near the CTT node region.
- Being entirely unconfined, the cover concrete outside the CTT node region crushes and spalls off.





**Figure 8–14: Comparison of Strains Parallel and Perpendicular to Crack in the Joint and Beam Region.**

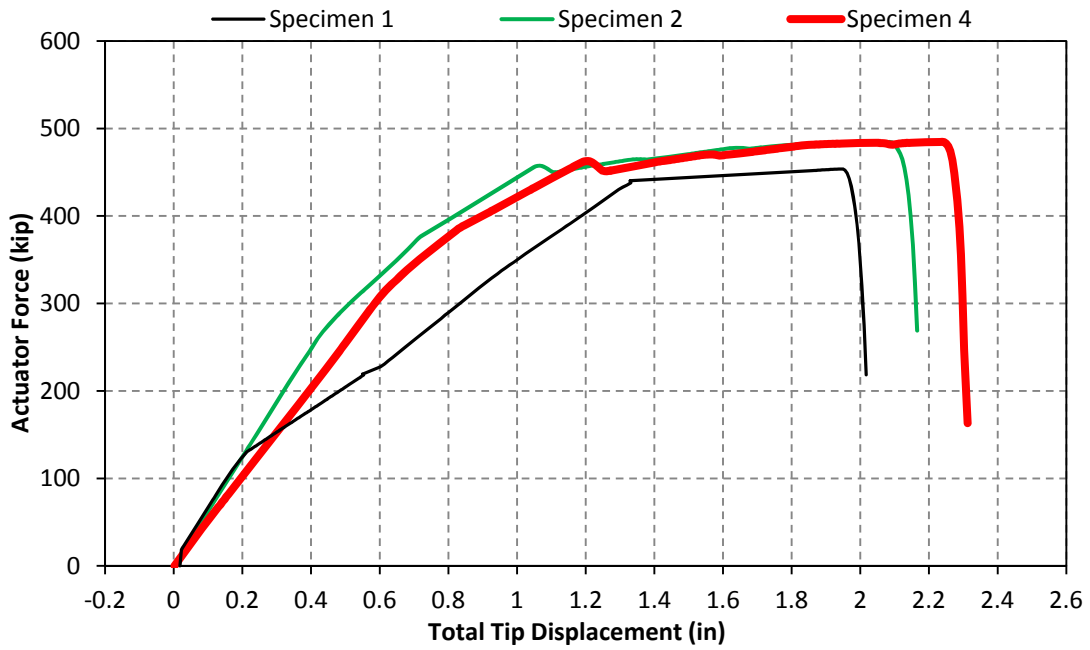
In summary, it is clearly evident from the above that the final event which results in the collapse of the C-Beam specimens with and without ASR/DEF damage was the compression softening of the corner-to-corner (arch) strut in the beam-column joint and the CTT node failure was an outcome of that failure mechanism.

## 8.5 DISCUSSION

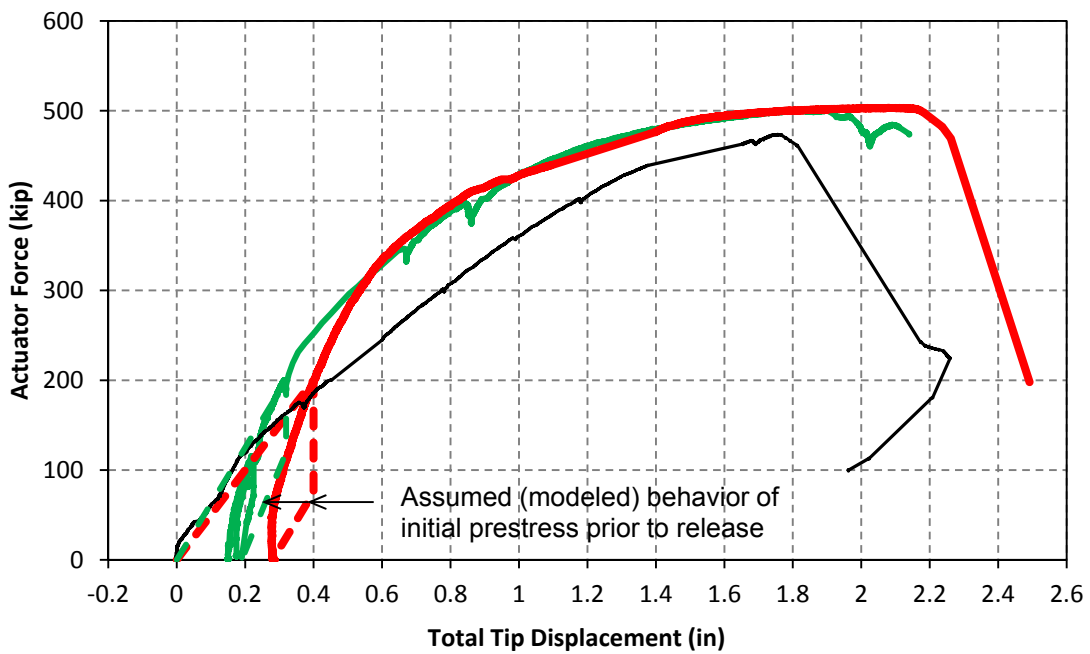
Figure 8–15a shows the overall modeled force-deformation results for the C-STM response for each of the three specimens. In Specimen 1 it is evident that there is a stiffness change at about 100 kip; this is due to first cracking in concrete. For Specimen 2, however, this apparent stiffness change is at about 240 kip, and for Specimen 4 the change occurs at 310 kip. This higher level of apparent “cracking” is strictly when the decompression of the prestress effect at the critical cross sections occur.

Note that after “cracking”/decompression occurs, and prior to yield of the specimens at about 450 kip, the cracked stiffness for each of the specimens appears similar. These computationally modeled results with C-STM are in agreement with the experimental observations for the specimens in Figure 8–15b. Note that the initial prestress (field) loading in the experiments for Specimen 2 and 4 were not accurately captured. It is for this reason the starting point of the laboratory experiment commences at a displacement of 0.15 inch and 0.28 inch for Specimen 2 and 4, respectively.

The computational C-STM results along with the experimental observations for Specimens 1, 2, and 4 are summarized in Table 8–2. The C-STM simulates the behavior of the specimen quite well and also overcomes the difficulties associated with trying to identify the failure mechanism using present conventional Bernoulli beam or SAT strength-based analysis techniques used in the *AASHTO LRFD Bridge Design Specifications* (2010). The effects of ASR/DEF were modeled into the C-STM analysis technique, and the results are in quite good agreement with the experimental observations. Additionally, C-STM provides the additional insight in terms of the sequence of behavior modes and whether the final failure mode is ductile or brittle.



(a) C-STM results



(b) Experimental performance

Figure 8-15: Force-Deformation Results for C-Beam Specimens.

**Table 8–2: Result for C-Beam Specimens.**

		Stage 3: C-STM	Experiment
		$P_{C-STM}^{++}$	$P_{Failure}^{\#}$
<b>Specimen 1</b>	Capacity (kip)	<b>454</b> *	474
	Factored Capacity (kip)	318 <sup>+</sup>	---
<b>Specimen 2</b>	Capacity (kip)	<b>481</b> *	485
	Factored Capacity (kip)	337	---
<b>Specimen 4</b>	Capacity (kip)	<b>485</b> *	503
	Factored Capacity (kip)	339	---

<sup>++</sup> Compression failure due to diagonal splitting/compression in the beam-column joint zone.  $\phi = 0.70$  (assumed).

<sup>#</sup> Maximum load at incipient failure due to failure in beam-column joint zone.

\* Bold typeface = critical case.

<sup>+</sup> Value assumed for overall structural load rating.

Finally, providing the applied factored loads  $1.25D+1.75(L+I)$  are less than  $\phi P_{C-STM} = 318$  kip, then the performance of the structure can be deemed *acceptable*. This is in spite of the moderate level of ASR/DEF damage observed in Specimen 4.

## 8.6 KEY FINDINGS FROM C-STM MODELING

As discussed and shown in this chapter, although the beam methods and the SAT method give some indication of the strength of the structure, they are unable to predict the overall behavior of the structure. It is also not possible to model the damage caused by effects of ASR/DEF on the structure into these methods. The C-STM technique has definite advantages and is summarized below:

- Incorporates a method for apportioning the interaction of different truss and arch shear resistance mechanisms.
- Models the overall performance including the cyclic effects and the internal behavior of the structure remarkably well and compares well with the experimental observations. The ability of C-STM technique to simulate the internal behavior of the structure with good accuracy confirms that the C-STM modeling is conceived on a theoretically sound basis.

- Incorporates a direct method of modeling the softened constitutive relations of cracked reinforced concrete struts, which does not require an iterative process to obtain convergence.
- When an engineer observes damage in a structure, it is natural to assume that the structure would be weaker and more flexible. One would not expect to find the structure to be stronger and stiffer, as observed in the experimental tests. The additional strength and stiffness is attributed to the concrete swelling due to ASR/DEF effects, which in turn puts the reinforcement steel into a state of active prestress. These effects, when appropriately modeled in the C-STM, capture well the overall behavior of the structure.
- The C-STM approach gives the engineer/analyst insight into the complexities of the internal behavior throughout the structure and the D-regions in particular, and finally identifies the actual cause of failure.



## **9 C-STM APPLICATION TO TEXAS BRIDGE PIERS**

### **9.1 BACKGROUND AND SCOPE**

A significant number of D-regions in large concrete structures in Texas exhibit premature concrete deterioration. This is attributed to the effects of ASR/DEF on concrete. As noted earlier, existing code-based analysis and design techniques are based on the performance of sound concrete and have limitations in assessing the performance of these structures that show signs of potential premature deterioration. Therefore, it is important to assess the performance of these large structures subjected to premature concrete deterioration due to ASR/DEF effects.

For the purpose of this study, two bridge piers that are part of the downtown San Antonio Y, located along I-10 and I-35 in Bexar County, were chosen. The two large bridge piers, I5C and H19C, were chosen because of the moderate amount of damage that is evident due to the effects of ASR/DEF. The scope of this study is to assess whether the D-regions of these large bridge piers are in jeopardy of losing a measure of their strength capacity due to ASR/DEF effects, and hence if the general safety of the bridge is impaired.

### **9.2 ANALYSIS OF PIER I5C**

#### **9.2.1 The Structure**

Figure 9–1 presents the reinforcing layout and cross-section of pier I5C. The overall height of the pier from the column footing is 35 ft. The hammerhead portion of the pier has an overall length of 22 ft 9 inches with a free cantilever portion extending 12 ft 3 inches from the column face. The longitudinal reinforcement for the column consists of a total of 50 No. 11 bars with 11 bars along each of the two short faces and 14 bars along each long face. The hammerhead pier cap beam consists of two layers of 13 No. 11 bars as the top (tensile) reinforcement and one layer of 13 No. 5 bars for the bottom (compressive) reinforcement, with No. 8 bars distributed along the side faces of the beam to provide torsional strength. Transverse reinforcement in the column is provided by No. 4 closed stirrups with a center-to-center spacing of 12 inches. For the cap beam, No. 6 closed double stirrups with a center-to-center spacing of 6 inches is used.

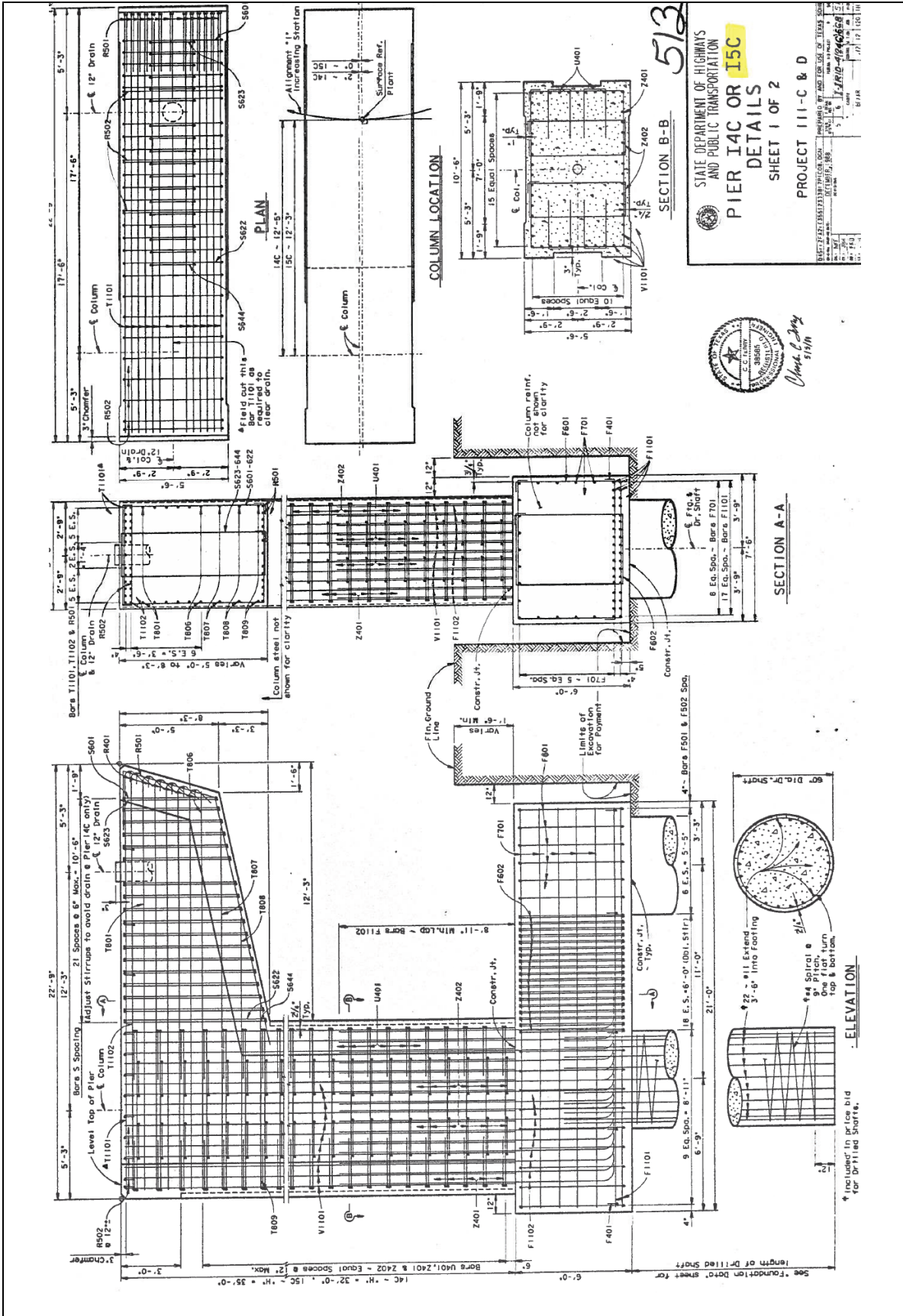


Figure 9-1: Layout and Reinforcement Detail of Pier I5C.



Grade 60 steel ( $f_y = 60$  ksi) for the reinforcement and Class C concrete ( $f'_c = 3.6$  ksi) were specified for constructing this structure. In the absence of more precise information on the existing in situ strength of steel and concrete, the specified strengths have been adopted for the analyses.

### 9.2.2 The C-STM Model

Figure 9–2 shows the C-STM model that was developed for pier I5C. The span that this pier supports is seated on two bearing pads near the outer part of the cantilever. These two pad locations are used to analyze the load capacity of the pier.

The cantilever portion of the pier is modeled using the single point Gauss truss model up to the bearing pad close to the column face, while the rest of the model is completed with a corner-to-corner diagonal arch from the outermost point of application of loads to the column face. The beam-column joint of the pier is modeled using a truss based on Boole's rule, where the ties clustered are at quarter points. This model was chosen to better represent the flow of stresses within the beam-column joint. The column was modeled using a simple truss model as shown in Figure 9–2.

The pier is analyzed without and with damage due to ASR/DEF effects. To model the effects of ASR/DEF concrete deterioration, prestressing forces were applied on the longitudinal and transverse reinforcements in the beam and the column in order to replicate the prestress effects that arise as a consequence of the swelling within the core concrete due to ASR/DEF effects. As per the recommendations made in Section 4.8.5, the strength reduction factor for cover concrete is taken as  $\lambda = 0.70$ . The confinement ratio was calculated to be  $K_{cc} = 1.37$  for the beam and  $K_{cc} = 1.06$  for the column core concrete. The prestress in the longitudinal and transverse reinforcement was taken as  $0.5 f_y$  and  $1.0 f_{yh}$ , respectively.

Figure 9–3 shows the different nonlinear concrete stress-strain relationships that were derived for pier I5C without and with ASR effects. Due to the prestressing effects, concrete shows delayed cracking. This effect is taken into consideration by assigning a higher tensile stress to the prestressed C-STM members.

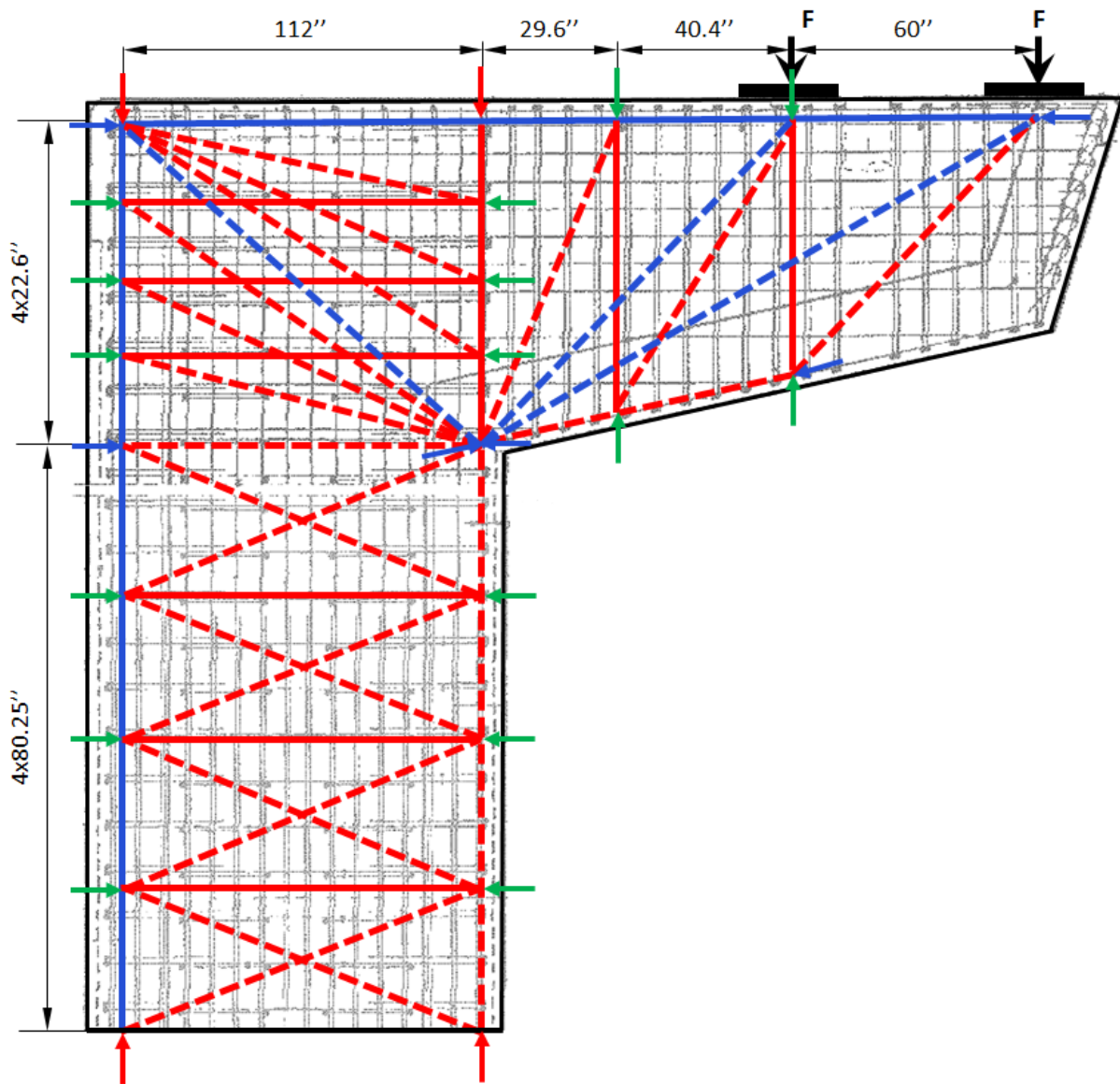
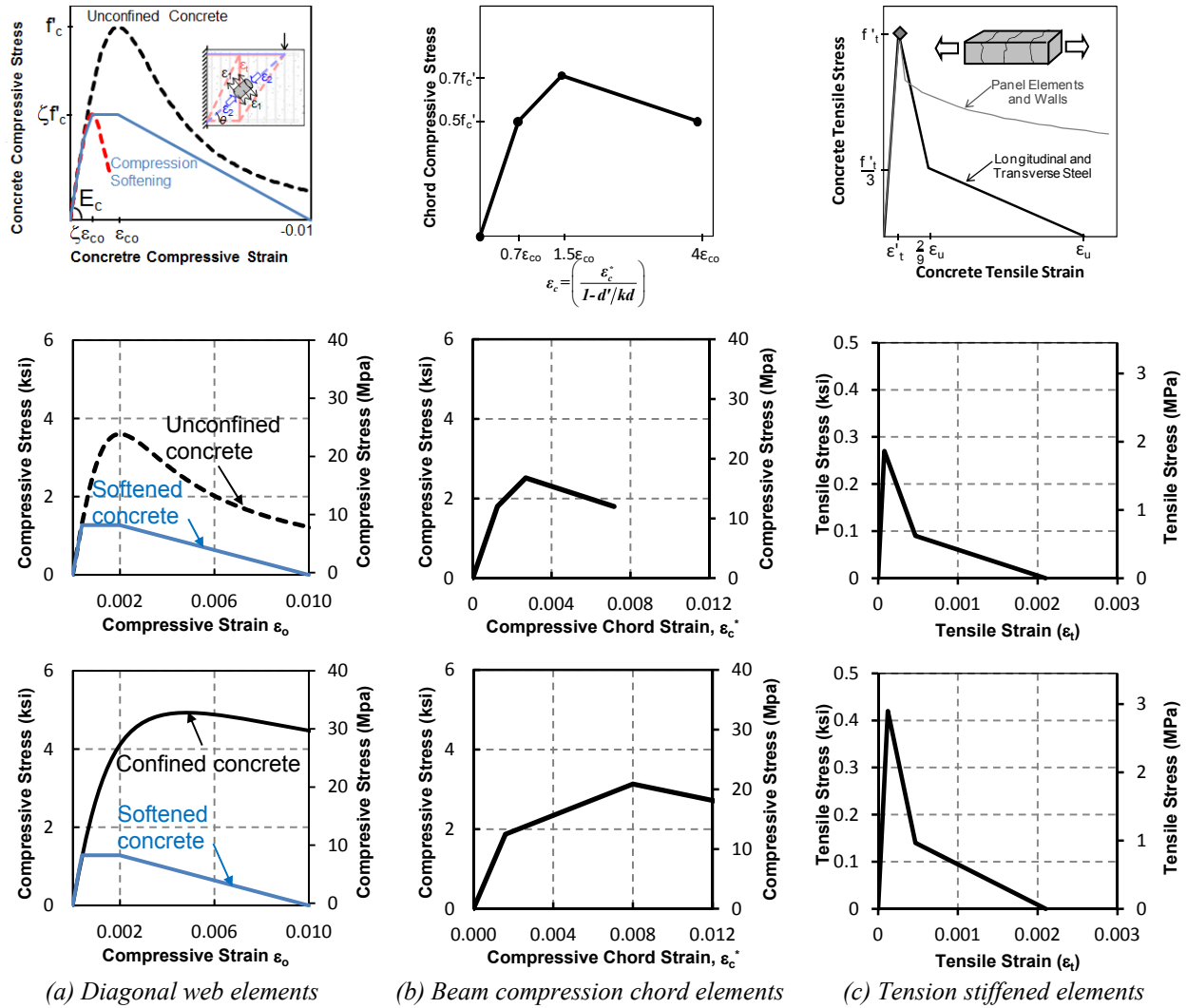


Figure 9-2: C-STM Model of Pier I5C.



**Figure 9-3: Cracked Reinforced Concrete Material Properties.**

**Row 1: Theoretical nonlinear behavior.**

**Row 2: Pier I5C modeled behavior, without ASR effects.**

**Row 3: Pier I5C modeled behavior, with ASR effects.**

### 9.2.3 C-STM Results and Discussion

Figure 9–4 shows the results obtained from C-STM analysis. Results without and with ASR/DEF damage are presented. The critical events that occur are marked as points along the force-deformation curve. The model captures the initial tension stiffening effects well, which leads to the first major change in slope in the force-deformation curve. The next major nonlinear event that has a significant effect on the behavior of the structure is the flexural yielding of longitudinal beam reinforcement. The final event that leads to the failure of the pier is the crushing of the softened beam-column arch.

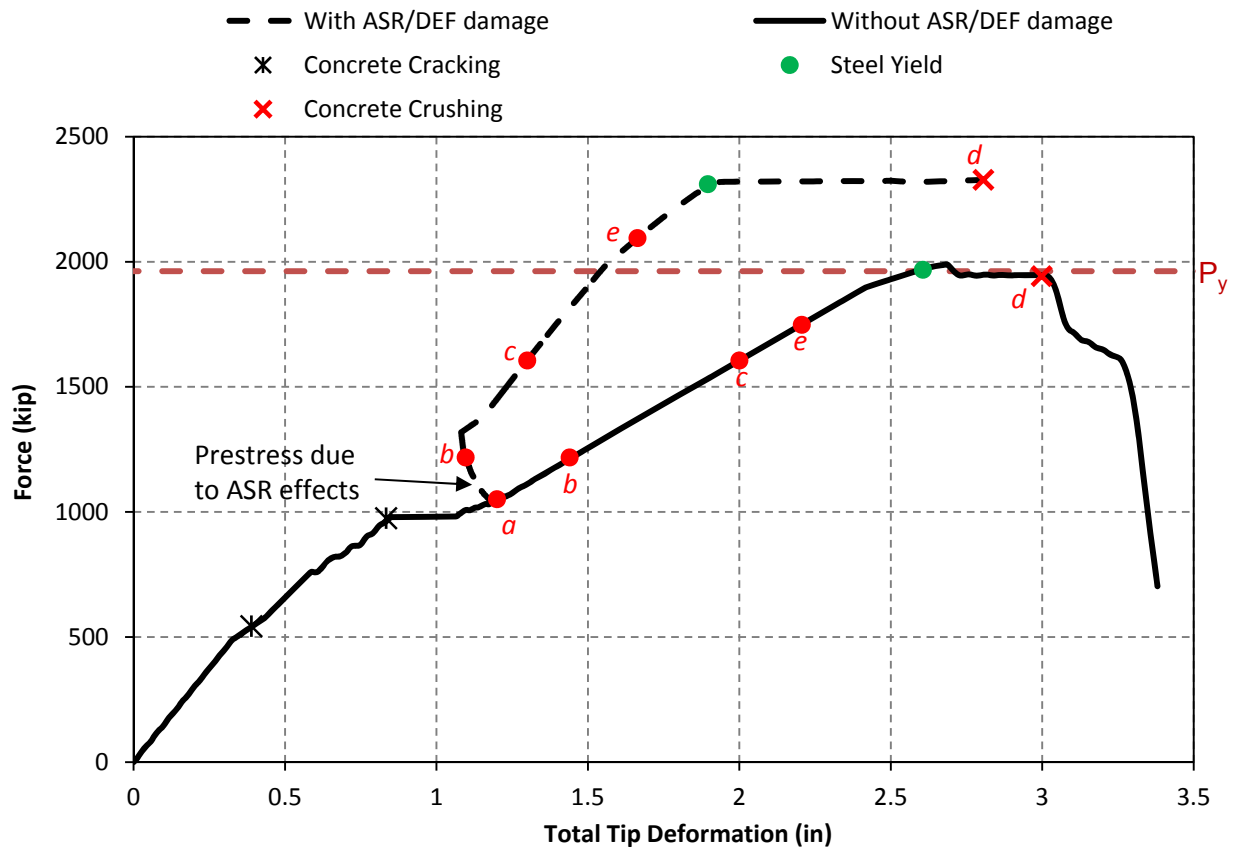
From the C-STM analysis, the nominal capacity ( $P_n$ ) of the bridge pier without ASR/DEF damage was found to be equal to the flexural yield strength ( $P_y$ ) of the cantilever beam. However, for the case with ASR/DEF damage, due to the confining effects, the nominal strength of the bridge pier ( $P_n^{ASR}$ ) was found to be 20 percent higher than ( $P_n$ ), that is,  $P_n^{ASR} = 1.20P_n$ .

Although counterintuitive, the analysis shows that there could be significant stiffening and strengthening of the pier when subjected to ASR/DEF damage due to the effects of the swelling of core concrete, which in turn puts the reinforcement in a state of active prestress. This is in agreement with the experimental observations made in Chapter 7.

The overstrength factor provided can be defined as:

$$\Omega = \frac{\text{Factored capacity}}{\text{Factored (code) load demand}} = \frac{\phi M_n}{M_u} \quad (9-1)$$

Though the final mode of failure of the structure is due to the failure of the joint arch, the structure can be deemed non-serviceable after the yield of longitudinal reinforcement as can be seen from Figure 9–4. The ultimate load at failure due to flexural yield of steel was found to be  $P_n = 2310$  kip and the factored capacity  $\phi F_n = 0.9 \times 2310 = 2080$  kip. From this the overstrength factor is determined to be  $\Omega = 1.30$ .



- $P_y$  = Shear force at first yield.
- (a) D = Self-weight.
- (b) D + (L+I) = Maximum service load.
- (c) 1.25 D + 1.75 (L+I) = Ultimate load demand.
- (d)  $P_n$  = Nominal maximum capacity.
- (e)  $\phi P_n$  = Factored capacity (where  $\phi = 0.9$  for flexure).

**Figure 9–4: Force-Deformation of Pier I5C without and with ASR/DEF Damage.**

## 9.3 ANALYSIS OF PIER H19C

### 9.3.1 The Structure

Figures 9–5 and 9–6 present the reinforcing layout and cross-section of pier H19C. The overall height of the pier from the column footing is 27 ft. Included in this height is the cap beam whose overall length is 40 ft 3 inches. The free cantilever portion that extends from the face of the column is 24 ft 3 inches long. The longitudinal reinforcement for the column consists of a total of 44 No. 18 bars with eleven bars along each of the short and long faces. The cantilever portion consists of two different rectangular cross-sections with overall depths of 8 ft 9 inches and 6 ft. The top (tensile) and bottom (compressive) reinforcement consist of seven No. 8 and No. 11 bars, respectively, with additional No. 8 bars distributed along the side faces of the beam to provide torsional strength. Transverse reinforcement in the column is provided by No. 4 closed stirrups with a center-to-center spacing of 12 inches. For the bent cap beam, No. 6 closed double stirrups with varying spacing are used. Grade 60 steel ( $f_y = 60 \text{ ksi}$ ) is used for longitudinal and transverse reinforcement, and the compressive strength of concrete specified during construction was  $f'_c = 5 \text{ ksi}$ . Since, existing in situ strength of steel and concrete is not available; the specified strengths have been adopted for the analyses.

The bent cap is post-tensioned using eight tendons, each consisting of 19 0.6 inch diameter strands with an ultimate tensile strength of 270 ksi. The strands were post-tensioned to a total of 5530 kip. The post-tensioning tendons are straight in the free cantilever portion, but have a draped profile over the beam-column joint. At the crown point the draped tendon is 9 inches below the upper face of the concrete pier.

### 9.3.2 Loading

The structure is subjected to three categories of loads:

- Externally applied loads.
- Internal forces from post-tensioning.
- Prestressing forces due to ASR/DEF effects.

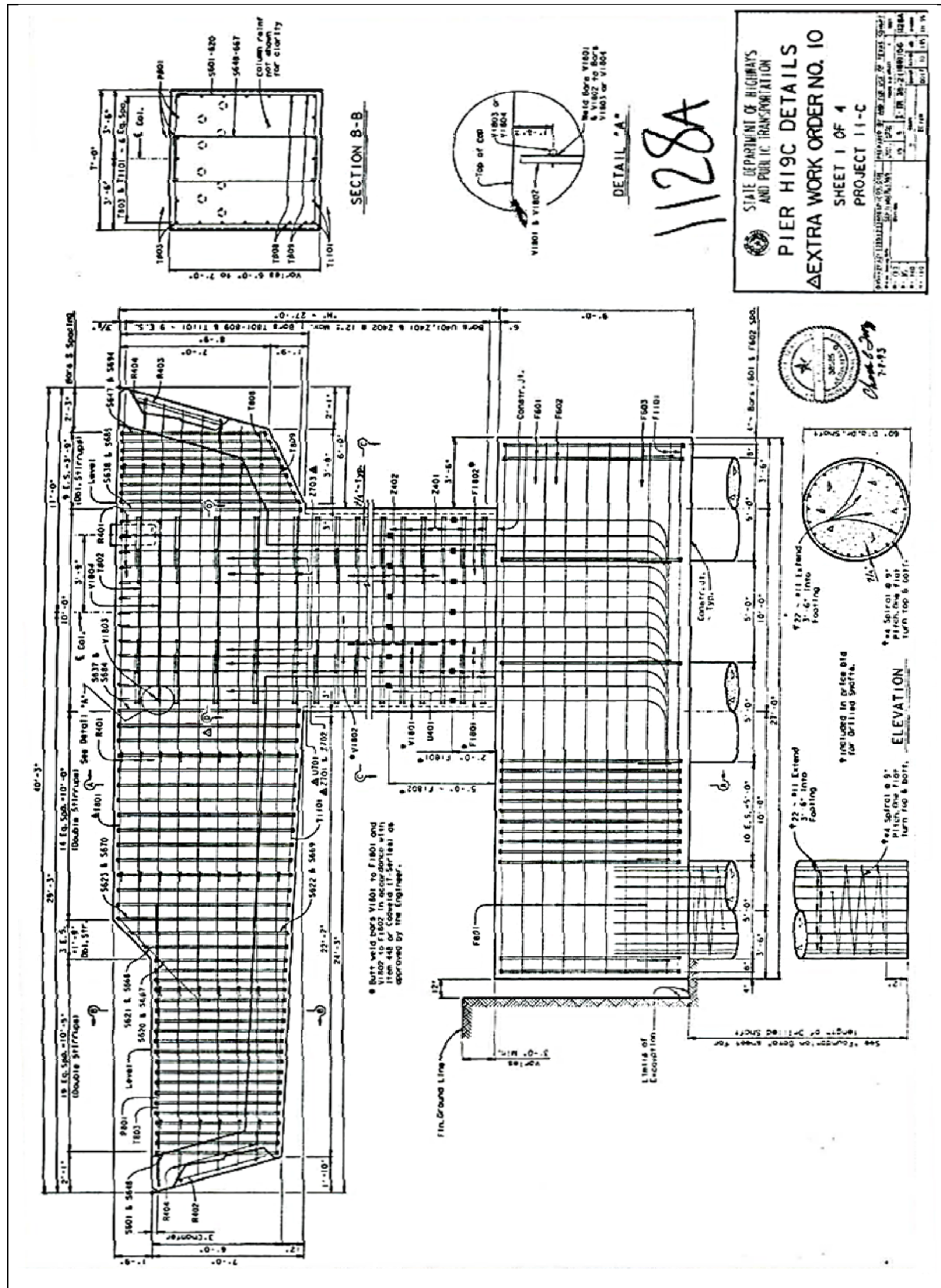


Figure 9-5: Layout and Reinforcement Detail of Pier H19C-Sheet 1.

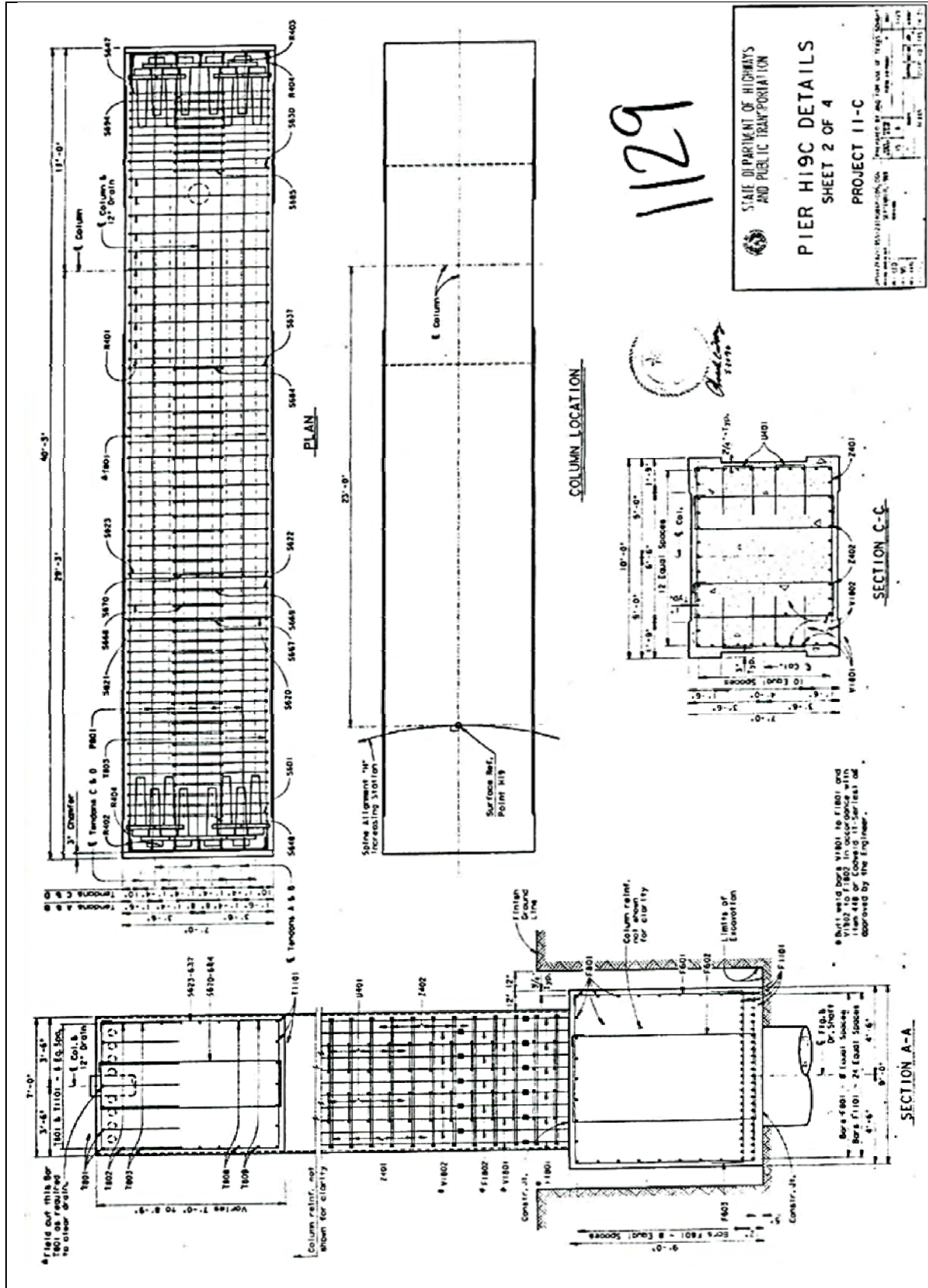


Figure 9-6: Layout and Reinforcement Detail of Pier H19C-Sheet 2.



The externally applied loads are the live loads due to traffic on the bridge deck. Pier H19C supports two girders, one on each side of the bent cap. Each girder supports two lanes of traffic. Two AASHTO design trucks spaced 50 ft apart are used for the moving load case to calculate the maximum shear in the interior support. Using an impact factor of 33 percent, the axial load on each point of support of the girder was determined to be 163 kip. Two cases of the externally applied live loads are considered as shown in Figure 9–7.

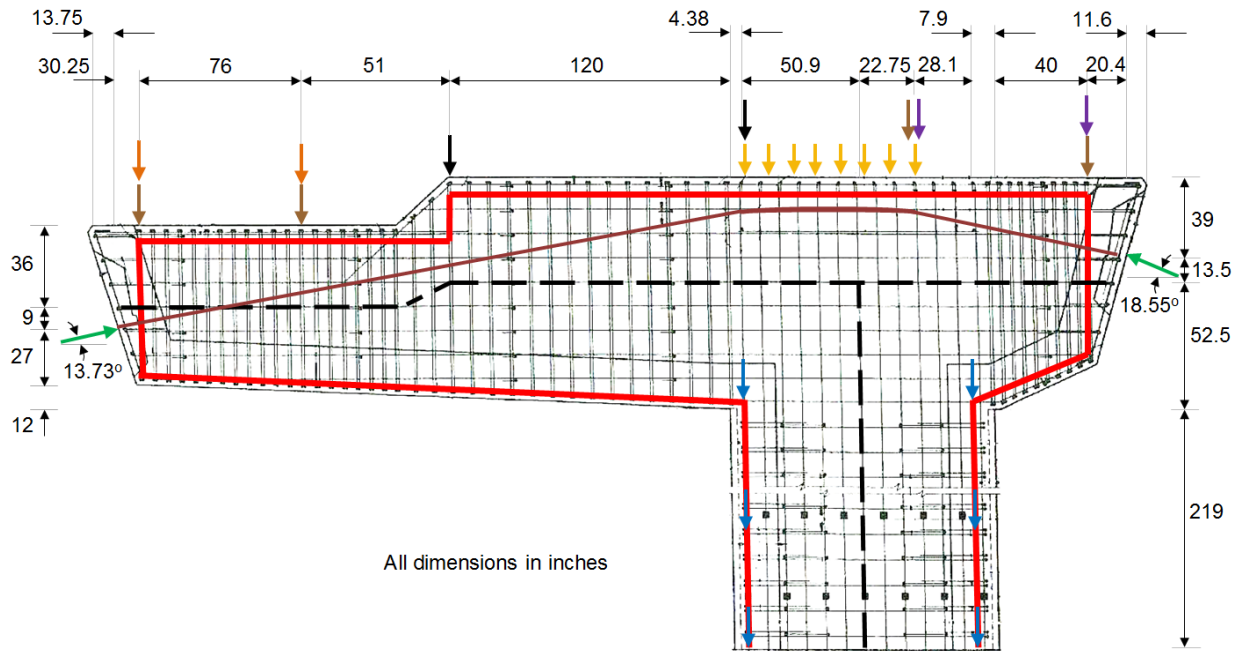
The self-weight from the girders are applied as point loads on the bent cap at the bearing pads where the girders are supported, and the self-weight of the pier is applied as point loads distributed across the different node points.








The post-tensioned tendons are straight in the beam overhangs, but have a curvature over the beam-column joint. The bearing forces between the post-tensioning tendons and the concrete must be accounted for, and this is achieved by a system of equivalent transverse distributed loads over the beam column joint. The system of post-tensioning forces must be such that the system is in internal-equilibrium. The internal forces from post-tensioning was determined to be 4433 kip after long-term losses. The bent cap with the externally applied loads and internal forces is shown in Figure 9–7.

There are additional loads on the structure due to compatibility requirements arising from the ASR/DEF effects. These loads are induced due to the prestressing effects that are caused by the swelling of core concrete due to ASR/DEF. These prestressing forces are applied on the longitudinal and transverse rebars in the beam and column in order to account for the effects caused by the swelling of core concrete.

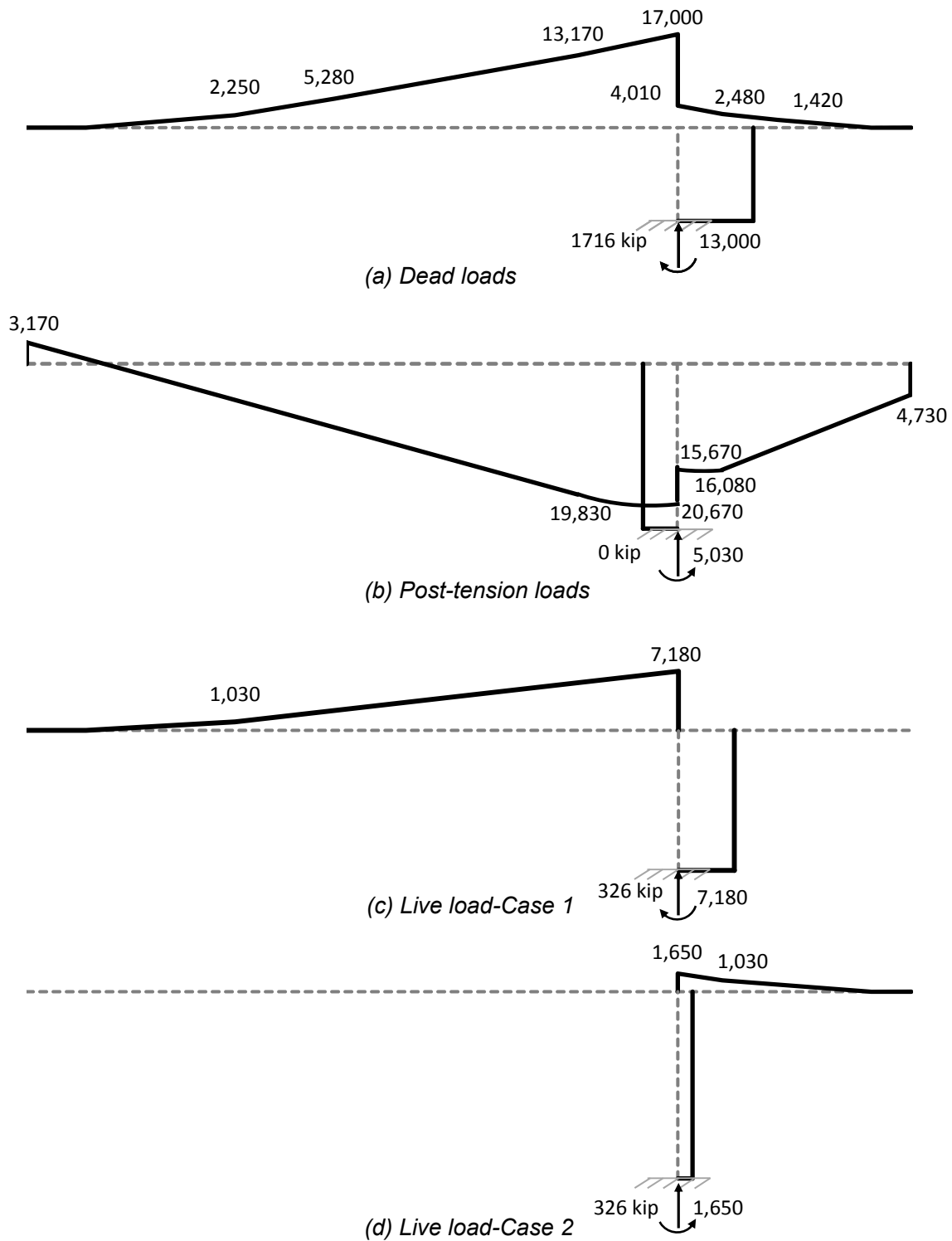
Considering a center-line model for the structure and based on the dead loads, live loads, and post-tensioning forces, the bending-moment diagram for the normal service regime of the structure was determined. Figure 9–8 shows the resulting bending moment diagram for:

- Dead loads only.
- Post-tension forces only.
- Live loads only – Case 1.
- Live loads only – Case 2.



  	356 kip 50 kip 32 kip	Dead loads
	4433 kip	Post-tension force after losses
	33.50 kip/ft	Downward post-tension reaction force over column region
	163 kip	Live load-Case 1
	163 kip	Live load-Case 2

**Figure 9–7: Loads on Pier H19C.**



*All moments in kip-ft*

**Figure 9–8: Bending Moment Diagrams for Normal Service Regime.**

For the different load cases in the normal service range, the axial load and moment at the base of the column can be determined. These loads are then factored to obtain a combination of the different factored load cases as presented in Table 9–1.

**Table 9–1: Column Axial Load and Moment for Various Load Combinations.**

Load case	Axial load (kip)	Moment (kip-ft)
D + P	1716	7970
1.25D + P	2145	11250
1.25D + P + 1.75(L + I)	2715	23830
D = Dead loads; P = post-tensioning loading effects; L = Live load and I=Impact load		

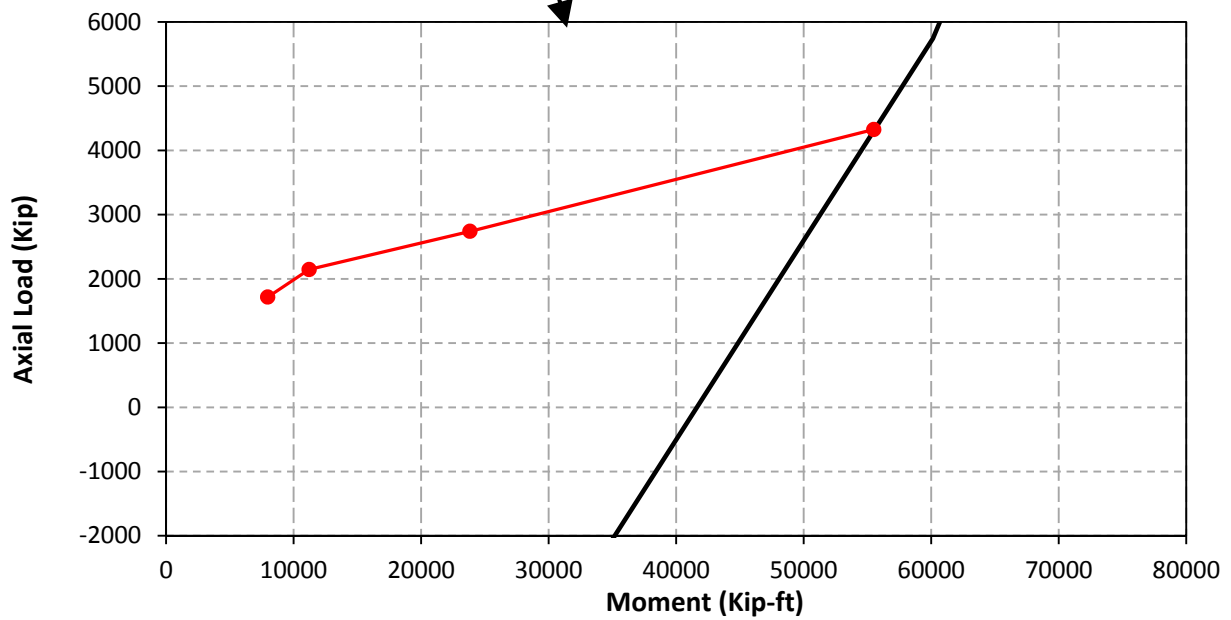
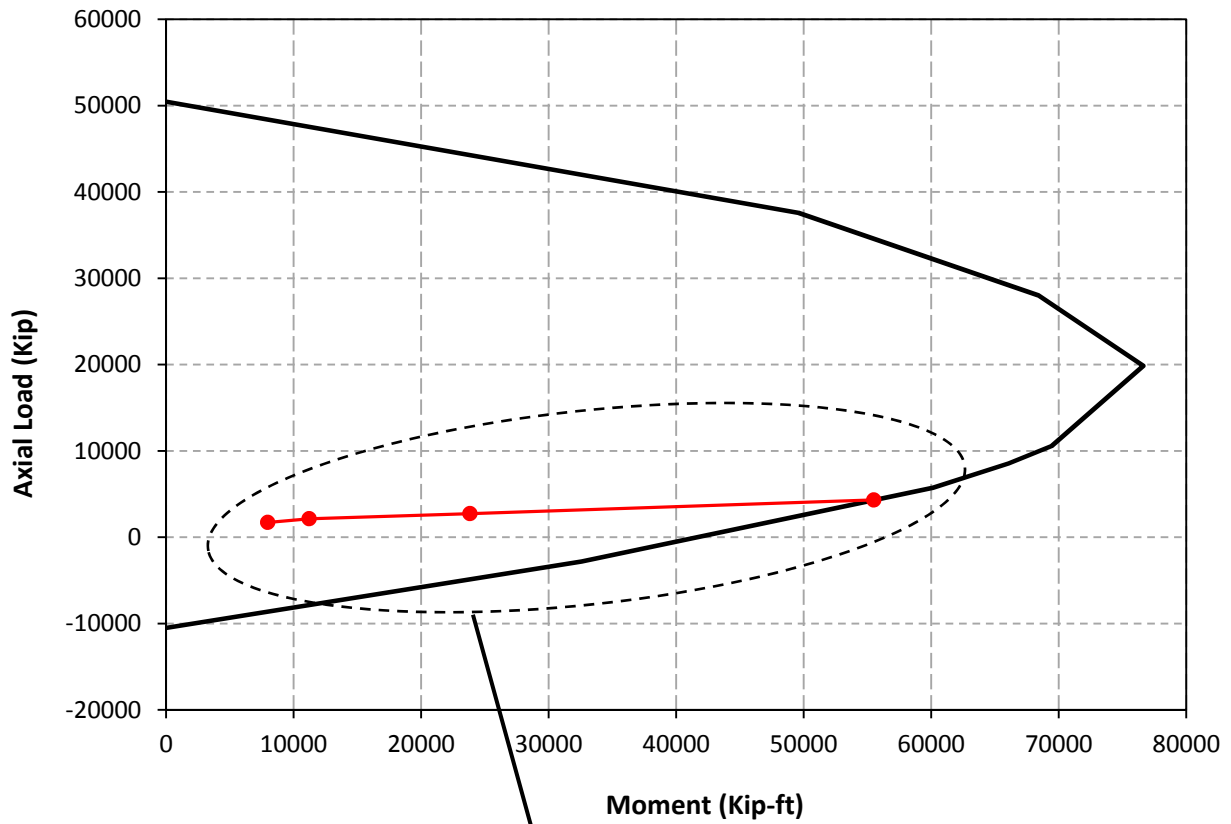
The axial load and moment for the different load cases shown above are plotted as points on the column interaction diagram as shown in Figure 9–9. By extending this line, the axial load at the point of intersection on the column interaction diagram may be obtained.

Thus, from the interaction diagram for the column the overstrength factor is determined to be  $\Omega = \phi P_n / P_u = 1.43$ . This shows that the column has sufficient capacity and is expected to form a flexural mechanism due to yielding of tensile column steel; the overhang is less likely to fail mainly due to the load balancing effect of the large post-tensioning force. Although Case 1 of (L+I) is applied near a disturbed region at the end of the cantilever, since flexure is shown to govern for the cantilever and as no signs of distress are expected in the anchorage zone, a C-STM analysis is not warranted. Figure 9–10 shows the bending moment diagram for the factored load cases.

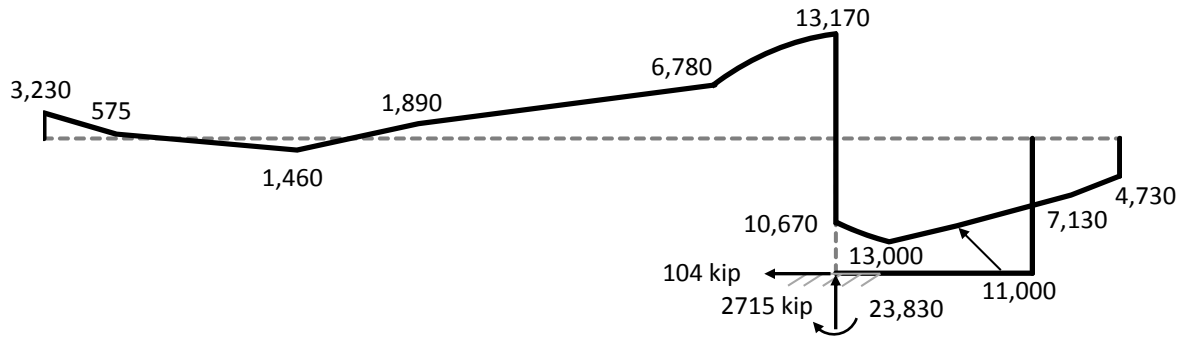
For Case 2 of (L+ I) load, the loads are applied externally to a region near the beam-column joint; a highly disturbed region. Hence, it is best to analyze this load case using the C-STM analysis method as presented next.

### 9.3.3 The C-STM Model

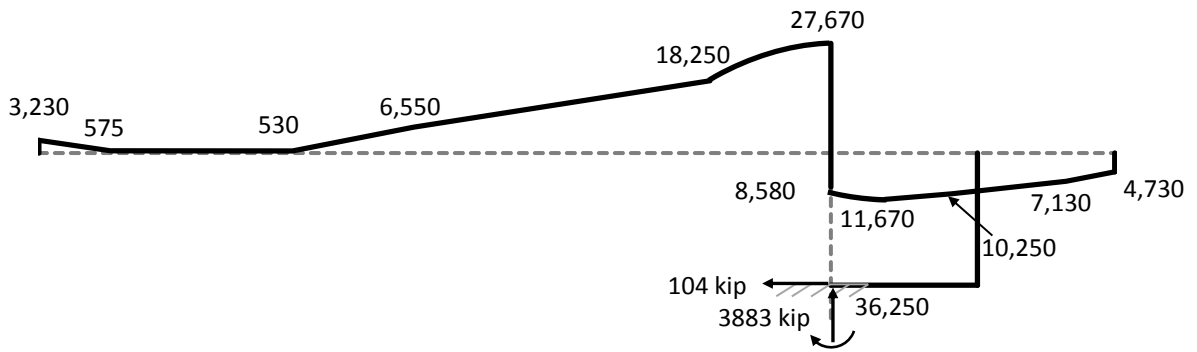
Figure 9–11a and b, respectively, show the truss and arch action of the C-STM model that was developed for pier H19C. (The truss and the arch mechanism function together, but are shown separate for clarity.) The C-STM technique is primarily used to analyze Case 2 of (L+I) where



**Figure 9-9: Column Interaction Diagram with Different Load Cases.**



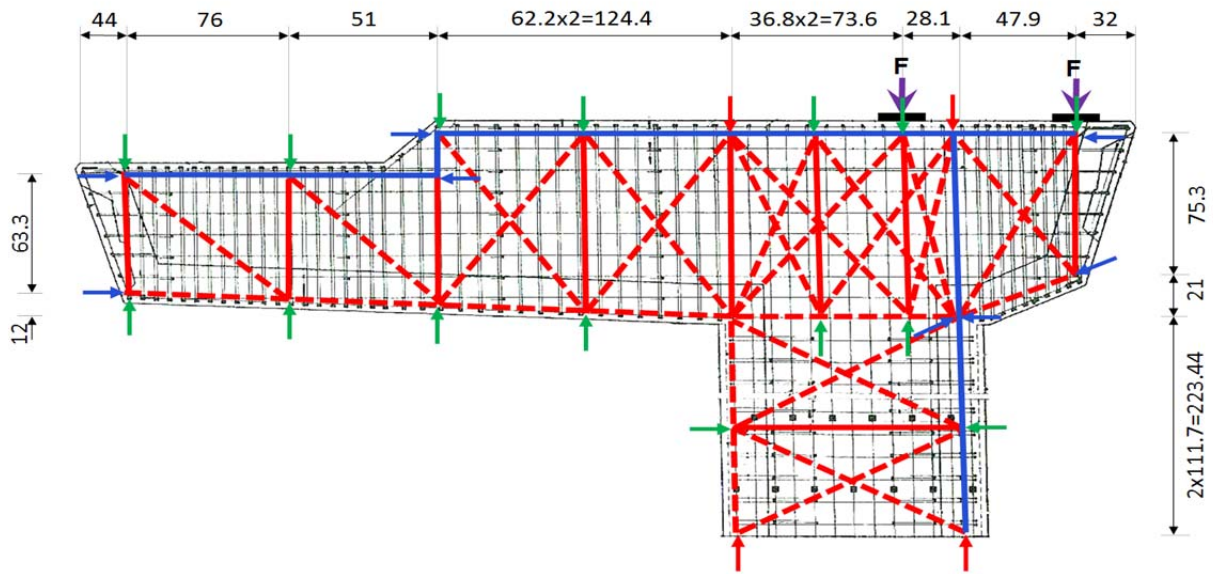
(a)  $1.25D + P + 1.75(L+I)$



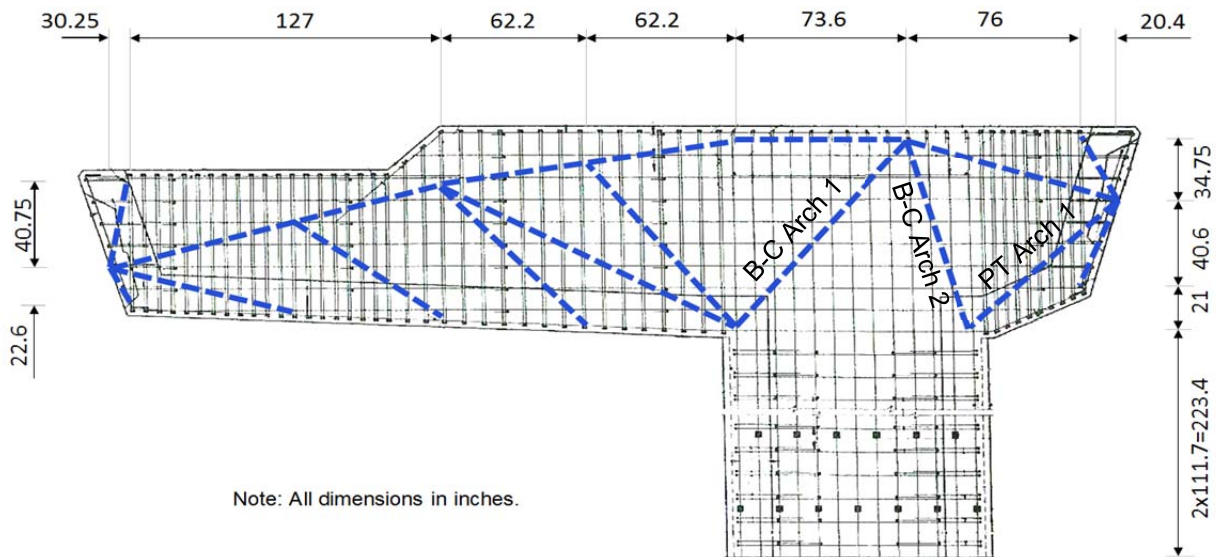
(b)  $1.43[1.25D + 1.75(L+I)] + P$

*All moments in kip-ft*

**Figure 9–10: Bending Moment Diagrams for (a) the Design Ultimate Strength and (b) for Overload at Incipient Mechanism Formation.**



(a) C-STM Truss action



(b) C-STM Arch action

**Figure 9–11: C-STM Model for Pier H19C.**

live loads are applied via the two bearing pads resting on the right-hand side (shorter) cantilever portion of the pier as shown in Figure 9–11a.

The beam-column joint of the pier was modeled using the *Three-Point Gauss* truss model. The arch mechanisms formed due to the compressive force in the post-tensioned tendons were positioned along the centroid of the tendons for simplicity. The rest of the truss and arch action were modeled based on the probable stress flow paths in the structure. As there was no local failure observed at the anchorage zone, the C-STM was modeled to replicate this observation at the end zones.

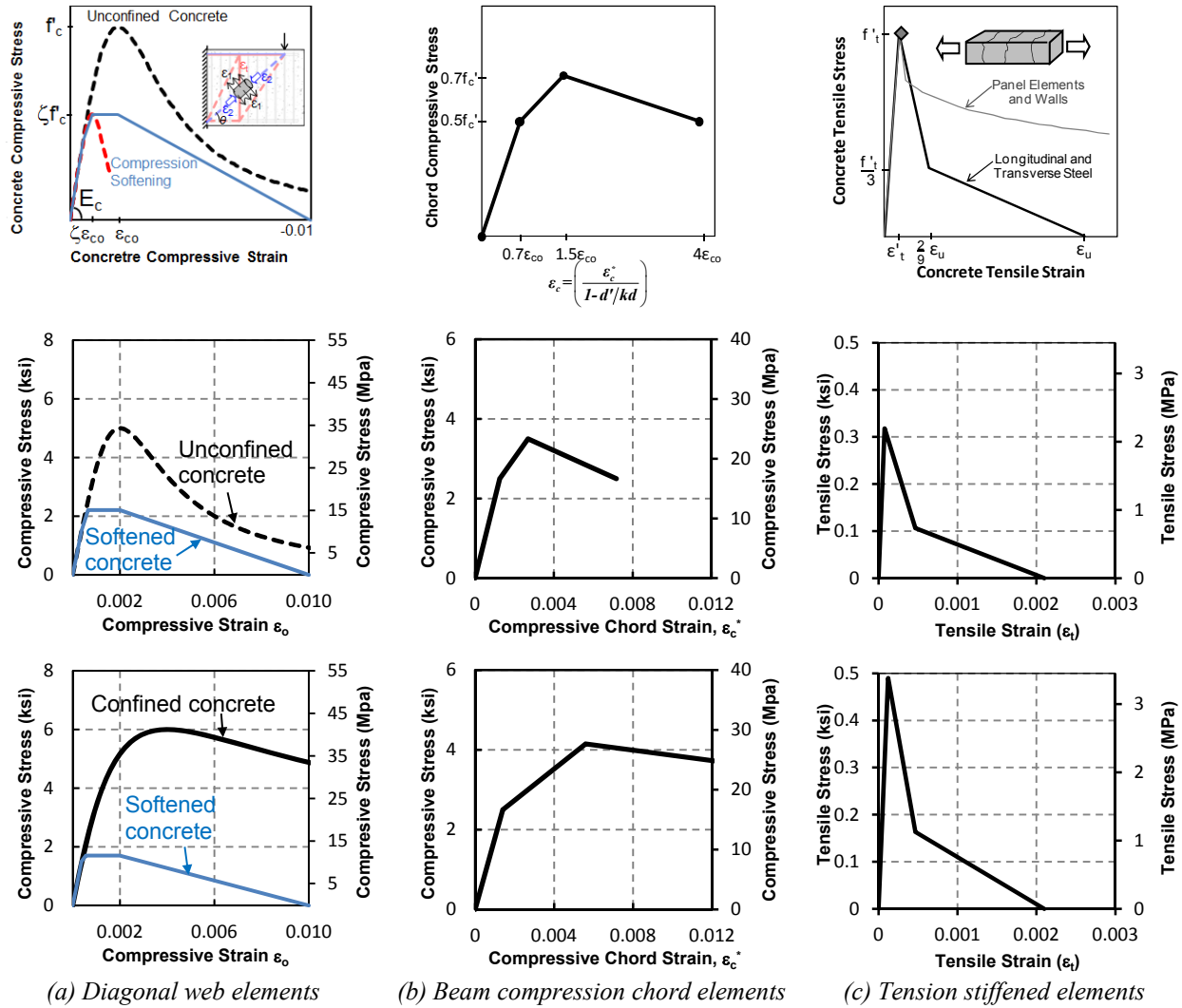
Due to the moderate level of observed damage due to ASR/DEF effects, as per the recommendations made in section 4.8.5, a strength reduction factor for cover concrete was taken as  $\lambda = 0.70$ . The confinement ratio was calculated to be  $K_{cc} = 1.20$  for the beam and  $K_{cc} = 1.04$  for the column core concrete. The prestress in the longitudinal and transverse reinforcement was taken as  $0.5 f_y$  and  $1.0 f_{yh}$ , respectively.

Figure 9–12 shows the different nonlinear concrete stress-strain relationships that were derived for pier HI9C without and with ASR/DEF effects. Again it is to be noted that due to the prestressing effects, concrete shows delayed cracking, and this effect is taken into consideration by assigning a higher tensile stress to the prestressed C-STM members.

#### **9.3.4 C-STM Results and Discussion**

The C-STM model was used to analyze both scenarios of the live load cases. The analysis was subjected to the different load cases in a sequence that best replicates the actual loading of the structure. The model was first loaded by the dead loads of the pier followed by the post-tensioning forces. This is followed by the application of (L + I) loads. This completes the analysis due to normal service loads. The prestressing effect due to ASR/DEF is applied on the structure next, as a result of which there is a change in stiffness between the structure without and with ASR/DEF damage. The model is then subjected to the factored loads and finally loaded to failure.





**Figure 9-12: Cracked Reinforced Concrete Material Properties.**

**Row 1: Theoretical nonlinear behavior.**

**Row 2: Pier HI9C modeled behavior-without ASR effects.**

**Row 3: Pier HI9C modeled behavior-with ASR effects.**

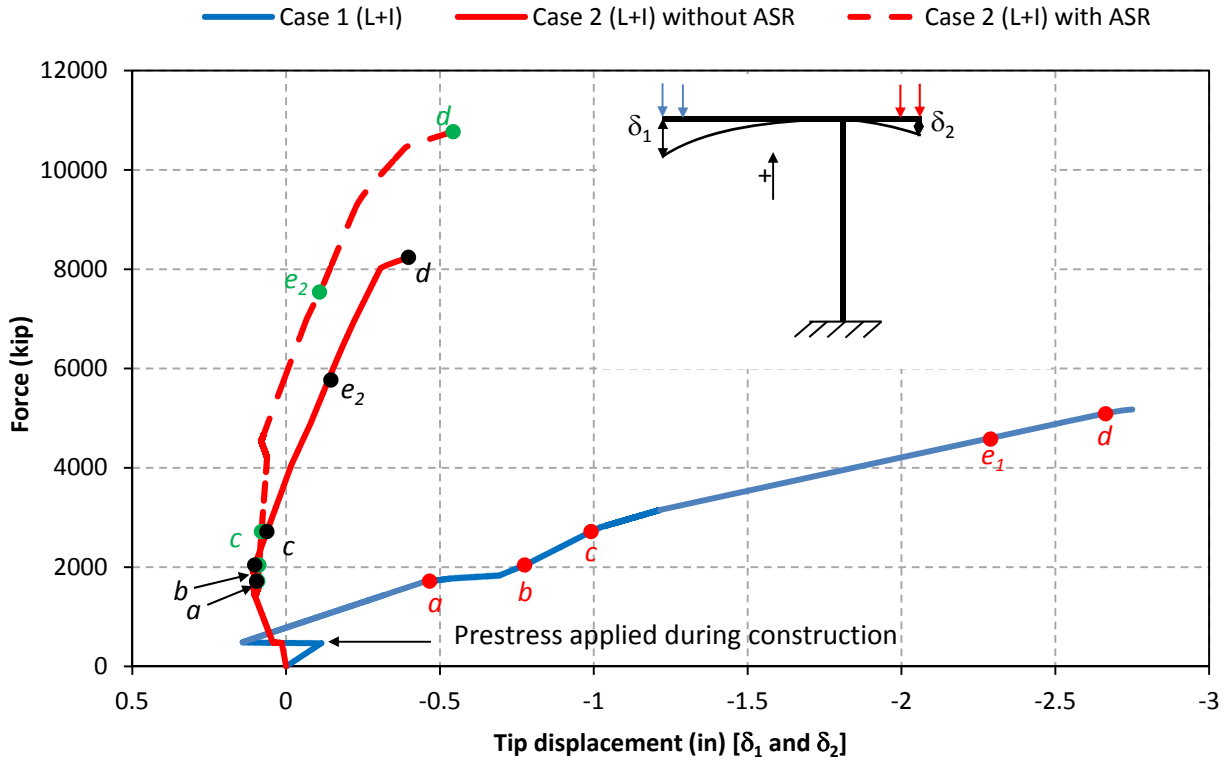
Figure 9–13 shows the force-deformation plot from the C-STM analysis. The tip deformations  $\delta_1$  and  $\delta_2$  are measured positive upward and are as shown in the inset in Figure 9–13.

For Case 1 of (L + I) loads, flexural yielding of the column tensile steel was determined to be the cause of structural failure. The column axial loads computed for the different load combinations (Table 9–1) are presented as points along the force-deformation curve. The maximum nominal capacity of the pier  $P_n = 5087$  kip. It is observed that the factored capacity  $\phi P_n = 0.9 \times 5087 = 4578$  kip is well over the factored axial load demand of  $P_u = 1.25D + P + 1.75(L + I) = 2715$  kip. Thus, the over-strength factor provided is obtained as  $\Omega = \phi P_n / P_u = 1.68$ . The prestressing effects due to ASR will not have a profound effect on this case, as the structure is predominantly governed by flexure in the column.

For Case 2 of (L + I), the measured tip displacements ( $\delta_2$ ) are much smaller. It may be observed from the analysis that the B-C Arch 2 and P-T Arch 1 shown in Figure 9–11b were subjected to maximum compressive strains. The tensile strains transverse to the arches were evaluated, and the softened concrete stress-strain relation was obtained for these members. Based on the softened concrete model, it was observed that the final mode of failure was the crushing of the softened joint arch (B-C Arch 2) underneath the (L + I) load in the beam-column joint.

The maximum nominal capacity  $P_{n2} = 8238$  kip and the factored capacity  $P_{n2} = 0.7 \times 8238 = 5767$  kip.

For the analysis case with ASR/DEF damage on the structure, additional prestressing forces were applied on the longitudinal and transverse steel in the beam and the column. The structural response was found to be stiffer and stronger than without the effects of ASR/DEF. The ultimate load at failure due to the crushing of the joint arch was found to be  $P_{n2} = 10770$  kip and the factored capacity  $\phi P_{n2} = 0.7 \times 10770 = 7539$  kip. For this case it was found that the overstrength factor  $\Omega = 2.78$ . This is a shear-brittle failure. In spite of the observed ASR/DEF effects, it can be concluded from this analysis that the structure remains safe due to the high reserve strength (overstrength) capacity.



- (a)  $D + P$  = Self-weight + Post-tension (after losses).
- (b)  $D + P + (L+I)$  = Maximum service load.
- (c)  $1.25 D + 1.75 (L+I)$  = Ultimate load demand.
- (d)  $P_n$  = Nominal maximum capacity.
- (e<sub>1</sub>)  $\phi P_{n1}$  = Factored capacity (where  $\phi = 0.9$  for flexure).
- (e<sub>2</sub>)  $\phi P_{n2}$  = Dependable capacity (where  $\phi = 0.7$  as for SAT modeling requirements).

**Figure 9–13: Force-Deformation for Case 1 and Case 2 Live Load.**

## 9.4 KEY FINDINGS

The key observations that may be made from the analysis of the two bridge piers are as follows:

- Pier I5C was found to be critical at the beam-column joint. The final mode of failure was due to the crushing of the corner-to-corner arch in the beam-column joint zone.
- For pier H19C it was observed that the factored capacity due to Case 1 loading causing flexural yielding of the column is less than the factored capacity due to Case 2 loading, which causes shear failure at the beam-column joint. Both load cases had large overstrength factors.
- Field observations have indicated a moderate degree of damage from ASR/DEF effects, but the analyses show that because of these effects the strength is not adversely affected.
- It should be noted that the joint zones are not part of a careful design process in the U.S. practice. Normally either the column or beam hoop steel is merely continued into the joints and a pass/fail check is made (clause 5.10.11.4 AASHTO LRFD *Bridge Design Specifications*, 2010).
- Premature joint failure could be avoided by using a more thorough joint design process, which will inevitably require more joint steel and improved anchorage of the longitudinal bars and hoop steel.
- Although the C-STM process is intended primarily as an analysis method to check the performance of a structure, when a design is deemed to be deficient via such an analysis, alternative remedial measures can be explored—in particular providing more hoop steel in the critical beam-column joints. The analysis can then be successively repeated until the desired satisfactory performance is obtained.

## **10 SUMMARY, CONCLUSIONS, AND RECOMMENDATIONS**

### **10.1 SUMMARY**

It has been observed in Texas that a significant number of D-regions in large concrete bridge piers exhibit premature concrete deterioration. The deterioration has been attributed to the detrimental effects of ASR and DEF. The excessive cracking on these reinforced concrete piers due to ASR/DEF effects has been a major concern for the TxDOT engineers and creates uncertainty about the strength and hence safety and longevity of the bridges affected. It is of utmost importance to assess the effects that ASR/DEF deterioration of concrete can have on the structural performance of the reinforced concrete bridge piers.

In this research the effects of ASR/DEF on the D-regions of structures were investigated by means of a dual experimental and analytical modeling program. The following were the main tasks identified in this project to study the behavior and assess the performance of reinforced concrete bridge piers subjected to the detrimental effects of ASR/DEF:

1. Design laboratory specimens that are representative of typical bridge bents in Texas.
2. Use construction material and curing conditions to promote deterioration of the specimens due to ASR/DEF effects.
3. Subject the specimens to varying periods of exposure to typical Texas weather conditions and constantly monitor the deterioration phase, both through visual observations and mechanical measurements.
4. Perform a destructive test on the control specimen (without ASR/DEF deterioration) and the ASR/DEF deteriorated specimens and compare their performance.
5. Establish any effect ASR/DEF deterioration may have on the load carrying capacity of the bridge bents and investigate their causes.
6. Determine the cause of failure of the bridge bent specimens from instrument measurements and visual observations made during the destructive testing phase.

7. Develop and verify an analytical model that can be used to analyze bridge bents with significant D-regions.
8. Apply the developed model to the current experimental program, and devise a method to simulate the effects of ASR/DEF concrete deterioration on the structure.

A brief summary of the experimental and analytical program follows:

*Experimental specimen design and construction:*

- For the experimental investigation on the effects of ASR/DEF on reinforced concrete bridge bents, a specimen design was established being representative of two typical bridge bents in Texas: (i) the cantilever bent; and (ii) the straddle bent. The cantilever and straddle bents are characterized, respectively, by the singly reinforced side and the doubly reinforced side of the test specimen.
- Special aggregates and chemicals were used to promote ASR deterioration effects in the concrete mix. Supplemental heating was applied to concrete during curing of the specimens to promote DEF effects.
- Four near full-scale specimens (with the same design) were constructed and conditioned over time, and three have been tested to failure.
- Specimen 1 served as the control specimen (without ASR/DEF deterioration) and was tested in an undamaged condition. Specimens 2 and 4, respectively, were tested after eight months and two years of field conditioning through the Texas heat along with supplemental water aimed at promoting ASR/DEF.

*Deterioration phase:*

- Based on visual observations, Specimen 2 and 4, respectively, were categorized to display slight and moderate amount of damage due to ASR/DEF effects. The fourth specimen (Specimen 3) remains to be tested within the next three years (2014) and at just over five years of age, Specimen 3 is expected to show heavy damage due to the effects of ASR/DEF.

- In the specimens subjected to deterioration, early formation of ASR gel was observed, and with time, load-induced cracks along with other additional cracks were observed. These additional cracks were a result of the continued formation of ASR gel that caused the concrete to swell, and in turn put the reinforcing steel into a state of active prestress.

*Destructive laboratory testing:*

- *Specimen 1:* Specimen 1 was tested in two phases as follows:

*Phase I:* In Phase 1 of testing, the doubly reinforced beam was protected by external post-tensioning, and the singly reinforced beam was loaded to 440 kip and unloaded.

*Phase II:* In Phase 2 of the test the singly reinforced beam was protected by post-tensioning, and the doubly reinforced beam was tested to failure. In this manner two tests were conducted on the same specimen.

- *Specimen 2 and 4:* The effects that the ASR/DEF deterioration had on the specimen's structural performance were unknown. Therefore, in the case of Specimen 2 and 4, no post-tension was applied, and a single test was conducted. It was observed that the singly reinforced side of the beam failed in both Specimen 2 and 4. However, the failure mechanism in all three specimens (Specimen 1, 2, and 4) was found to be same.
- From the experimental tests, it was observed that the failure mechanism in both the control and the age-deteriorated specimens was a brittle shear failure within the beam-column joint zone. This was initiated by concrete softening of the joint corner-to-corner diagonal strut (arch action). In contrast to the control specimen, when loaded to failure, the specimens with ASR/DEF deterioration showed greater stiffness and strength and slightly greater ductility.
- In spite of the disturbing appearances of the ASR/DEF damage arising from concrete swelling and cracking, the performance and strength of the specimens were not impaired.

- **A caution from the test results:** At the end of destructive testing of the moderately damaged specimen (Specimen 4), onset of corrosion on the longitudinal rebars was observed. While this did not have any significant effect on the load carrying capacity of this specimen, it is possible that such corrosion over time could rapidly lead to a more accelerated deteriorated condition with a reduced strength capacity.

*Analytical modeling–C-STM:*

- A C-STM technique was developed as a suitable minimalist analysis technique to model the force-deformation behavior of reinforced concrete bridge piers with significant D-regions that may be deteriorated through ASR/DEF effects. In addition to the normal SAT force equilibrium requirements, the model accounts for non-linear behavior through displacement compatibility using inelastic constitutive laws of cracked and softened reinforced concrete.
- The C-STM takes into account the combined shear resistance provided by the truss and arch action. The model was implemented into widely used commercial structural analysis software (SAP2000) and validated against results from previously conducted large scale experiments.
- For the specimens in the current experimental program, though it is evident from the  $a/d$  ratio ( $= 36/33.25 = 1.08$ ) that the arch (direct strut) action will be the predominant behavior, the C-STM models both the truss action and the arch action to model the structure as close to reality as possible. The model automatically takes care of the principal shear mechanism that takes place in the structure.
- The effects of ASR/DEF on the structure were modeled into the C-STM by applying prestress forces at nodes to mimic the effects caused by the swelling of concrete and appropriately modifying the material properties. Material modification factors are recommended based on the field and experimental observations and engineering judgment. It was observed that the C-STM modeled the overall and the internal behavior of the structure without and with ASR/DEF deterioration very well.



## 10.2 CONCLUSIONS

The key conclusions that can be drawn from the experimental testing and analytical modeling follows:

*Cracking induced due to ASR/DEF:*

- From the experimental program, it was observed that there are two main types of cracking that are induced on a structure: thermal cracking due to thermal shock and normal service-load cracking.
- Map cracking was observed on all the specimens at an early age. However, when the specimen was thermally shocked during its early age by means of a sudden change in temperature, the map cracks were more pronounced.
- These cracks act as a point of ingress of moisture into the specimen, which accelerates the formation of ASR/DEF.

*Effect of ASR/DEF formation on the structure:*

- The formation of ASR gel in concrete causes the concrete to swell. However, the swelling of concrete is restrained by the reinforcement which causes tensile strains in the longitudinal and transverse reinforcement. This effectively puts the longitudinal and transverse reinforcement in a state of active prestress which causes the core concrete to be confined.
- The damage that appeared in the cover concrete region was offset by the mild level of confinement to the core concrete induced by the reinforcing steel.

*Observation from the destructive testing:*

- From the destructive testing of the control and the age-deteriorated specimens it was observed that failure in all the specimens was caused by a brittle shear failure through the beam-column joint.

- The failure was initially triggered by concrete softening of the joint's corner-to-corner diagonal strut. Immediately following this incipient failure mode, a redistribution of the joint forces to the transverse reinforcement in the joint was necessary.
- Since the transverse reinforcement in the joint region had limited capacity, overall failure was sudden with a rapid drop in resistance.
- The brittle nature of the failure may be attributed to the insufficient amount of transverse shear reinforcement and the insufficient anchorage of the limited overlapping transverse reinforcement (U-bars) in the joint region.
- The joint reinforcement consisted of 4 overlapping U-bars and straight side-face longitudinal distribution steel from the beam and column. The side-face reinforcements continuing into the joint from the beam or the column were not hooked to the longitudinal reinforcement, and therefore, they were found to be ineffective in contributing to the shear transfer mechanism in the beam-column joint region. Any increase in the side-face reinforcement without proper hook details would have been inefficient in contributing toward the shear capacity of the test specimen.
- Interestingly, however, a stiffening and strengthening effect was observed in the specimens with ASR/DEF damage. This is attributed to swelling of the core concrete due to ASR/DEF effects, which in turn puts the reinforcing steel into a state of active prestress.

*Inferences from code-based analysis:*

- An analysis procedure was used to evaluate the C-Beam specimens based on the current code based methods, i.e., the flexural beam theory and the SAT method. It was observed that the beam theory and the SAT technique were able to predict the yield loads of all three specimens with good accuracy.
- The ultimate load at failure for Specimen 1, 2, and 4 from the experimental testing was found to be 474 kip, 485 kip, and 503 kip, respectively. The ratio of the factored

externally applied load ( $\phi_f P_n^f$ ) obtained from the nominal moment to the experimental results were found to be 0.91, 0.88, and 0.83, respectively, for Specimen 1, 2, and 4.

- The factored shear capacity ( $\phi_v V_n^s$ ) was found to be close to 50% of the ultimate load obtained from the experiments for all three specimens.
- A similar observation was made from the SAT analysis, where the ratio of the factored externally applied load leading to node failure ( $\phi_v P_n^{SAT}$ ) to the experimental results were found to be 0.47 for Specimen 1 and 2 and 0.33 for Specimen 4.
- Thus it was concluded that the code-based analysis techniques could not give a satisfactory estimate of the failure load for any of the three specimens.

*Observations from the C-STM analysis:*

- The C-STM model was developed and validated against previously conducted large-scale experiments. The C-STM method shows much promise in the analysis of reinforced concrete structures possessing substantial D-regions.
- The C-STM was then used to model the experimental specimen in this study and was shown to simulate quite well the overall force-deformation behavior of the control specimen (without any ASR/DEF effects) and the specimens with varying amounts of ASR/DEF deterioration.
- Additionally, the C-STM was able to model the internal behavior of the specimen quite well and also provided an insight into the complexities of the internal behavior throughout the structure and the D-regions in particular.
- The C-STM was also able to identify the final mode of failure accurately and was consistent with the experimental test observations.

### **10.3 RECOMMENDATIONS AND FUTURE WORK**

From the experimental and analytical results and observation it is clear that the joint detailing of the specimen was insufficient to prevent failure of the beam-column joint. It is recommended that a greater amount of transverse reinforcement be provided in the beam-column joint to enable better shear transfer mechanism. It is also recommended that where practicable, 135° hooks at the ends of all hoops and ties within the joint region be used to prevent any pull-out of the transverse reinforcement.

From the tests it was observed that the specimen with the most ASR/DEF damage revealed the onset of corrosion. Additional corrosion could become quite a serious threat over time. Moreover, the effects of corrosion coupled with ASR/DEF effects on the overall performance of the structure are unknown. While some mild to moderate amount of ASR/DEF deterioration may appear to provide a beneficial strength gain, as evidenced in this study, it is postulated that as time proceeds there would be corresponding loss in capacity due to the corrosion of rebars. This deserves further investigation, particularly if ASR/DEF is associated with a marine environment or if deicing salts are used during the winter months.

## REFERENCES

- AASHTO. (2002). “Standard Specifications for Highway Bridges.” 17th edition, *American Association of State Highway and Transportation Officials*, Washington DC.
- AASHTO. (2010). “LRFD Bridge Design Specifications and Commentary.” Third edition, *American Association of State Highway and Transportation Officials*, Washington DC, 1264.
- ACI Committee 318. (2008). “Building Code Requirements for Structural Concrete (ACI 318–08) and Commentary.” *American Concrete Institute*, Farmington Hills, MI.
- Ahmed, T., Burley, E., and Rigden, S. (1998). “The Static and Fatigue Strength of Reinforced Concrete Beams Affected by Alkali-Silica Reaction.” *ACI Structural Journal*, V. 95, No. 4, July-August, 376–388.
- Ahmed, T., Burley, E., and Rigden, S. (1999a). “Effect of Alkali-Silica Reaction on Tensile Bond Strength of Reinforcement in Concrete Tested under Static and Fatigue Loading.” *ACI Structural Journal*, V. 96, No. 4, July-August, 419–428.
- Ahmed, T., Burley, E., and Rigden, S. (1999b). “Effect of Alkali-Silica Reaction on Bearing Capacity of Plain and Reinforced Concrete.” *ACI Structural Journal*, V. 96, No. 4, July-August, 557–570.
- Alcocer, S.M., and Uribe, C.M. (2008). “Monolithic and Cyclic Behavior of Deep Beams Designed Using Strut-and-Tie Models.” *ACI Structural Journal*, 105(3), 327–337.
- Arnold, D.M. (2004). *Development and experimental testing of a seismic damage avoidance designed beam to column connection utilizing draped unbonded post-tensioning*. M.S. Thesis, University of Canterbury: Christchurch, New Zealand.
- ASCE-ACI committee 445 on shear and torsion (1998). “Recent Approaches to Shear Design of Structural Concrete. State-of-the-art Report by ASCE-ACI Committee 445 on Shear and Torsion.” *Journal of Structural Engineering*, ASCE, 124(12), 1375–1417.

- ASTM-C31 (2008). “Standard Practice for Making and Curing Concrete Test Specimens in the Field.” *American Society for Testing and Materials*, West Conshohocken, PA.
- ASTM-C39 (2008). “Standard Test Method for Compressive Strength of Cylindrical Concrete Specimens.” *American Society for Testing and Materials*, West Conshohocken, PA.
- ASTM-C496 (2008). “Standard Test Method for Splitting Tensile Strength of Cylindrical Concrete Specimens.” *American Society for Testing and Materials*, West Conshohocken, PA.
- Barbarulo, R., Peycelon, H., Prene, S., and Marchand, J. (2005). “Delayed Ettringite Formation Symptoms on Mortars Induced by High Temperature Due to Cement Heat of Hydration or Late Thermal Cycle.” *Cement and Concrete Research*, 35(Compendex) 125–131.
- Bentz, E.C., Vecchio, F.J., and Collins, M.P. (2006). “Simplified Modified Compression Field Theory for Calculating Shear Strength of Reinforced Concrete Elements.” *ASCE J Struct Div*, 104(4), 649–666.
- Berube, M-A, Chouinard, D., Pigeon, M., Frenette, J., Boisvert, L., and Rivest, M. (2002). “Effectiveness of Sealers in Counteracting Alkali-Silica Reaction in Plain and Air-Entrained Laboratory Concretes Exposed to Wetting and Drying, Freezing and Thawing, and Salt Water.” *NRC Research Press, Can. J. Civ. Eng.*, 29, 289–300.
- Bracci, J.M., Keating, P.B., and Hueste, M.B.D. (2000). “Cracking in RC Bent Caps.” *Texas Transportation Institute*, Texas A&M University.
- Černý, R. and Rovnaníková, P. (2002). “Transport Processes in Concrete.” London: Spon Press.
- Chana, P.S., and Korobokis, G.A. (1991). “Structural Performance of Reinforced Concrete Affected by Alkali Silica Reaction.” Contractor Report 267, Transport and Road Research Laboratory, 77.
- Collins, M.P. (1978). “Towards a Rational Theory for RC Members in Shear.” *ASCE J Struct Div*, 104(4), 649–666.

- Collins, M.P., and Mitchell, D. (1980). "Shear and Torsion Design of Prestressed and Non-prestressed Concrete Beams." *Journal - Prestressed Concrete Institute*, 25(5), 32–100.
- Collins, M.P., and Mitchell, D. (1991). *Prestress Concrete Structures*. Prentice Hall, Englewood Cliffs, NJ.
- Collins, M.P., Bentz, E.C., and Sherwood, E.G. (2008). "Where Is Shear Reinforcement Required? Review of Research Results and Design Procedures." *ACI Structural Journal*, 105(5), 590–600.
- Deschenes, D.J., Bayrak, O., and Folliard, K.J. (2009). "ASR/DEF-Damaged Bent Caps: Shear Tests and Field Implications." Technical Report 12–8XXIA006, The University of Texas at Austin.
- Dilger, W. (1966). "Veränderlichkeit der Biege- und Schubsteifigkeit bei Stahlbetontragwerken und ihr Einfluß auf Schnittkraftverteilung und Traglast bei statisch unbestimmter Lagerung." Deutscher Ausschuss für Stahlbeton, Heft 179, Berlin, Germany.
- Drucker, D.C. (1961). "On Structural Concrete and the Theorems of Limit Analysis." *International Association for Bridge and Structural Engineering (IABSE)*, Zürich, Abhandlungen 21.
- Fan, S., and Hanson, J.M. (1998a). "Length Expansion and Cracking of Plain and Reinforced Concrete Prisms due to Alkali-Silica Reaction." *ACI Materials Journal*, V. 95, No. 4, July–August, 480–487.
- Fan, S., and Hanson, J.M. (1998b). "Effect of Alkali Silica Reaction Expansion and Cracking on Structural Behavior of Reinforced Concrete Beams." *ACI Structural Journal*, V. 95, No. 5, September–October.
- FIP-Commission 3. (1996). "Practical Design of Structural Concrete." SETO, distributed by fib, London, UK.

- Fu, Y., Xie, P., Gu, P., and Beaudoin J.J. (1994). "Effect of Temperature on Sulphate Adsorption/Desorption by Tricalcium Silicate Hydrates." *Cement and Concrete Research*, 24(Compendex), 1428–1432.
- Fu, Y., Xie, P., Gu, P., and Beaudoin J.J. (1995). "A Kinetic Study of Delayed Ettringite Formation in Hydrated Portland Cement Paste." *Cement and Concrete Research*, 25(Compendex), 63–70.
- Grattan-Bellew, P.E., Beaudoin, J.J., and Vallee, V.G. (1998). "Effect of Aggregate Particle Size and Composition on Expansion of Mortar Bars due to Delayed Ettringite Formation." *Cement and Concrete Research*, 28(8), 1147–1156.
- Holden, T., Restrepo, J., and Mander, J.B. (2003). "Seismic Performance of Precast Reinforced and Prestressed Concrete Walls." *Journal of Structural Engineering*, 129(3), 286–296.
- Hsu, T.T.C. (1994). "Unified Theory of Reinforced Concrete-A Summary." *Structural Engineering and Mechanics*, 2(1), 1–16.
- Hsu, T.T.C. (1996). "Toward a Unified Nomenclature for Reinforced-Concrete Theory." *Journal of Structural Engineering*, 122(3), 275–283.
- Hsu, T.T.C., and Zhang, L.X. (1997). "Nonlinear Analysis of Membrane Elements by Fixed-Angle Softened-Truss Model." *ACI Structural Journal*, 94(5), 483–492.
- Hwang, S.J., Lu, W.Y., and Lee, H.J. (2000) "Shear Strength Prediction for Deep Beams." *ACI Structural Journal*, 97(3), 367–376.
- Jensen, V. (2003). "Elgeseter Bridge in Trondheim Damaged by Alkali Silica Reaction: Microscopy, Expansion and Relative Humidity Measurements, Treatment with Mono-Silanes and Repair." 9th Euroseminar on Microscopy Applied to Building Materials, September 9–12, Trondheim, Norway.
- Karthik, M.M., and Mander, J.B. (2011). "Stress-Block Parameters for Unconfined and Confined Concrete Based on a Unified Stress-Strain Model." *ASCE Journal of Structural Engineering*, 137(28), 270–273.



- Kelham, S. (1996). "Effect of Cement Composition and Fineness on Expansion Associated with Delayed Ettringite Formation." *Cement & Concrete Composites*, 18(3), 171–179.
- Kim, J.H., and Mander, J.B. (1999). *Truss Modeling of Reinforced Concrete Shear-Flexure Behaviour*. Technical Report MCEER - 99–0005, University at Buffalo, New York.
- Kim, J.H., and Mander, J.B. (2000). "Cyclic Inelastic Strut-Tie Modeling of Shear-Critical Reinforced Concrete Members." *American Concrete Institute*, V. SP Vol. 193, 707–728.
- Kim, J.H., and Mander, J.B. (2007). "Influence of Transverse Reinforcement on Elastic Shear Stiffness of Cracked Concrete Elements." *Engineering Structures*, 29(8), 1798–1807.
- Lawrence, C.D. (1995). "Mortar Expansions Due to Delayed Ettringite Formation. Effects of Curing Period and Temperature." *Cement and Concrete Research*, 25(Compendex), 903–914.
- Ley, M.T., Riding, K.A., Widiyanto, Bae S., and Breen, J. (2007). "Experimental Verification of the Strut and Tie Model Design Method." *ACI Structural Journal*, Vol. 104, No. 6, 749–755.
- MacGregor, J.G. (1992). *Reinforced Concrete Mechanics and Design*. 2<sup>nd</sup> Ed., Prentice-Hall, Englewood Cliffs, NJ.
- Mander, J.B., Priestley, M.J.N., and Park, R. (1988). "Theoretical Stress-Strain Model for Confined Concrete." *ASCE Journal of Structural Engineering*, 114(8), 1804–1826.
- Marti, P. (1985). "Basic Tools of Reinforced Concrete Beam Design." *Journal of the American Concrete Institute*, 82(1), 46–56.
- Marti, P. (1999). "How to Treat Shear in Structural Concrete." *ACI Structural Journal*, 96(3), 408–414.
- Mau, S.T., and Hsu, T.T.C. (1987). "Shear Strength Prediction for Deep Beams with Web Reinforcement." *ACI Structural Journal*, 84(6), 513–523.
- Mörsch, E. (1909). *Concrete-Steel Construction*, McGraw-Hill, NY, 368.

- Odler, I., and Chen, Y. (1996). "On the Delayed Expansion of Heat Cured Portland Cement Pastes and Concrete." *Cement and Concrete Composites*, 18, 181–185.
- Park, R., and Paulay, T. (1975). *Reinforced Concrete Structures*. Wiley, NY.
- Paulay, T. (1971). "Coupling Beams of Reinforced Concrete Shear Walls." *Journal of the Structural Division, ASCE*, 97(ST3), 843–862.
- Petersson, P.E. (1980). "Fracture Energy of Concrete: Practical Performance and Experimental Results." *Cement and Concrete Research*, 10(1), 91–101.
- Poole, A.B. (1992), "Introduction to Alkali-Aggregate Reaction in Concrete." The Alkali-Silica Reaction on Concrete, Blackie, Glaskow, Scotland, and London, and Van Nostrand Reinhold, NY.
- Powanusorn, S., and Bracci, J.M. (2006). "Behavior of Reinforced Concrete Members Prone to Shear Deformations: Part I - Effect of Confinement." *ACI Structural Journal*, 103(5), 736–46.
- Ritter, W. (1899). "Die Bauweise Hennebique (The Hennebique system)." *Schweizerische Bauzeitung* (Zürich).
- Ronne, M., and Hammer, T.A. (1999). "Delayed Ettringite Formation (DEF) in Structural Lightweight Aggregate Concrete: Effect of Curing Temperature, Moisture, and Silica Fume Content." *Cement, Concrete and Aggregates*, 1999. 21(Compendex) 202–211.
- Rots, J.G., Nauta, P., Kusters, G.M.A., and Blaauwendraad, J. (1985). "Smearred Crack Approach and Fracture Localization in Concrete." *Heron*, 30(1), 1–48.
- Salem, H.M., and Maekawa. K. (2006). "Computer-Aided Analysis of Reinforced Concrete Using a Refined Nonlinear Strut-and-Tie Model Approach." *Journal of Advanced Concrete Technology*, 4(2), 325–336.
- SAP2000™ (1995). Advanced 14.0.0, Computer and Structures, Inc, Berkeley, CA.

- Schlaich, J., Schaefer, K., and Jennewein, M. (1987). "Toward a Consistent Design of Structural Concrete." *PCI Journal*, 32(3), 74–150.
- Scott, R.M. (2010). *Experimentally validated compatibility strut and tie modeling of reinforced concrete bridge piers*. M.S. Thesis, Texas A&M University: College Station, TX.
- Scrivener, K., and Lewis, M. (1997). "A Microstructural and Microanalytical Study of Heat Cured Mortars and Delayed Ettringite Formation." *Proceedings of the 10th International Congress on the Chemistry of Cement*, Gothenburg, Sweden.
- Shimada, Y., and Young, J.F. (2004). "Thermal Stability of Ettringite in Alkaline Solutions at 80 °C." *Cement and Concrete Research*, 34(Compendex): p. 2261–2268.
- Sritharan, S., and Ingham, J.M. (2003). "Application of Strut-and-Tie Concepts to Concrete Bridge Joints in Seismic Regions." *PCI Journal*, 48(4), 66–90.
- Swamy, R.N. (1992). "Testing for Alkali-Silica Reaction." *The Alkali-Silica Reaction on Concrete*, Blackie, Glaskow, Scotland, and London, and Van Nostrand Reinhold, NY.
- Swamy, R.N., and Al-Asali, M.M. (1989). "Effect of Alkali-Silica Reaction on the Structural Behavior of Reinforced Concrete Beams." *ACI Structural Journal*, V. 86, No. 4, July-August., 451–459.
- Swamy, R.N., and Al-Asali, M.M. (1998). "Engineering Properties of Concrete Affected by Alkali-Silica Reaction." *ACI Materials Journal*, V. 85, No. 5, 367–370.
- Taylor, H.F.W., Famy, C., and Scrivener, K.L. (2001). "Delayed Ettringite Formation." *Cement and Concrete Research*, 31(Compendex), 683–693.
- Thomas, M., Folliard, K., Drimalas, T., and Ramlochan, T. (2008). "Diagnosing Delayed Ettringite Formation in Concrete Structures." *Cement and Concrete Research*, 38(Compendex), 841–847.

- Thörlimann, B., Marti, P., Pralong, J., Ritz, P., and Zimmerli, B. (1983). “Application of the Theory of Plasticity to Reinforced Concrete (Anwendung der plastizitätstheorie auf stahlbeton).” *Institute of Structural Engineering*, ETH Zürich.
- To, N.H.T., Ingham, J.M., and Sritharan, S. (2001). “Monotonic Nonlinear Strut-and-Tie Computer Models.” *Bulletin of the New Zealand Society for Earthquake Engineering*, 34(3), 169–190.
- To, N.H.T., Ingham, J.M., and Sritharan, S. (2002). “Strut-and-Tie Computer Modelling of Reinforced Concrete Bridge Portal Frames.” *Bulletin of the New Zealand Society for Earthquake Engineering*, 35(3), 165–189.
- To, N.H.T., Ingham, J.M., and Sritharan, S. (2003). “Strut-and-Tie Computer Modelling of Reinforced Concrete Bridge Joint Systems.” *Journal of Earthquake Engineering*, 7(4), 581–590.
- To, N.H.T., Sritharan, S., and Ingham, J.M. (2009). “Strut-and-Tie Nonlinear Cyclic Analysis of Concrete Frames.” *Journal of Structural Engineering*, 135(10), 1259–1268.
- Vecchio, F.J. (2000). “Analysis of Shear-Critical Reinforced Concrete Beams.” *ACI Structural Journal*, 97(1), 102–110.
- Vecchio, F.J., and Collins, M.P. (1986). “The Modified Compression-Field Theory for Reinforced Concrete Elements Subjected to Shear.” *Journal of the American Concrete Institute*, 83(2), 219–231.
- Vecchio, F.J., and Collins, M.P. (1993). “Compression Response of Cracked Reinforced Concrete.” *Journal of Structural Engineering*, 119(12), 3590–3610.
- Young, B.S., Bracci, J.M., Keating, P.B., and Hueste, M.B.D. (2002). “Cracking in Reinforced Concrete Bent Caps.” *ACI Structural Journal*, 99(4), 488–498.
- Yun, Y.M. (2000). “Nonlinear Strut-Tie Model Approach for Structural Concrete.” *ACI Structural Journal*, 97(4), 581–590.

Zhang, Z., Olek, J., and Diamond, S. (2002), "Studies on Delayed Ettringite Formation in Early-Age, Heat-Cured Mortars I. Expansion Measurements, Changes in Dynamic Modulus of Elasticity, and Weight Gains." *Cement and Concrete Research*, 32, 1729–173.

Zhu, R.R.H., Wanichakorn, W., Hsu, T.T.C., and Vogel, J. (2003). "Crack Width Prediction Using Compatibility-Aided Strut-and-Tie Model." *ACI Structural Journal*, 100(4), 413-421.



## APPENDIX A: DETAILS OF HEAT FLOW ANALYSIS

The program below solves the 1D heat flow equation simultaneously for concrete and bounding insulation. It allows one to incorporate heat of hydration along with other point sources of heat. In this case, heat was added at the interface between concrete and the insulative forms and in the center of the concrete element.

**Heat flow analysis in concrete beams** (  [Created with Wolfram Mathematica 8.0](#) )

### Summary

This program is intended to predict the temperature distribution in concrete as a function of time during the first two days (approximately) as a result of heat generated by the hydration reaction and also from discrete point (line) heat sources. The model assumes 1D heat flow (either top to bottom only or side to side only). The model solves the 1D heat flow equation for the concrete beam and the insulation on each boundary.

The heat flow equation for non-steady state may be expressed as:

$$\nabla^2 T(x,t) - \frac{1}{\alpha} \times \frac{\partial T(x,t)}{\partial t} = \frac{-1}{k} \times q_{gen}(x,t) \quad (\text{A-1})$$

where  $T(x,t)$  is the temperature,  $\alpha$  is the thermal diffusivity,  $k$  is the thermal conductivity,  $x$  is the linear position,  $t$  is time, and  $q_{gen}(x,t)$  is additional heat supplied either through hydration or through point (line) heat sources. For 1D heat flow, we can simplify the equation to:

$$\frac{\partial^2 T(x,t)}{\partial^2 x} - \frac{1}{\alpha} \times \frac{\partial T(x,t)}{\partial t} = \frac{-1}{k} \times q_{gen}(x,t) \quad (\text{A-2})$$

To solve this equation, we utilize Laplace Transforms to eliminate the time derivative to get:

$$\frac{\partial^2 T(x,s)}{\partial^2 x} - \frac{1}{\alpha} \times (T(x,s) - T(x,t=0)) = \frac{-1}{k} \times qgen(x,s) \quad (\text{A-3})$$

where the overbars denote Laplace Transformed parameters, and s is the transform variable. The parameter  $qgen(x,s)$  is the Laplace transform of  $qgen(x,t)$ , which includes a function for heat of hydration and the point (line) heat sources.

Once the heat flow equation is solved for both of the insulation layers and the concrete cross-section, we can find the unknown interface boundary temperature by using the principle of conservation of energy, which requires that the heat flowing into the concrete at one of the boundaries must be equal to the heat flowing out of the insulation at that boundary (and vice versa).

Once the boundary temperature  $T_{bound}(s)$  is known, we can then invert concrete temperature function  $T_{concr}(x,s)$  into the time domain. This must be done numerically and is accomplished using the Stehfest algorithm.

## Load modules

The following command sets the search directory for modules to the directory in which this file is located.

```
thisDir = ToFileName[
    ("FileName" /. NotebookInformation[EvaluationNotebook[]])
    [[1]]];
SetDirectory[thisDir];
```

The following command loads a module for numerical transform inversion. Copyright Arnaud Mallet.

```
<< NumericalInversion.m;
<< NumericalInversionmodified.m;
Off[General::spell1]

$TextStyle = {FontFamily -> "Times", FontSize -> 16};
{FontFamily -> "Arial", FontSize -> 16};
```

## Inputs



$Q_{\text{supplied}}$  is the heat supplied on the surface of the specimen by the heating elements (in Watts /  $m^2$ )

**$Q_{\text{supplied}} = -700;$**

**$Q_{\text{suppliedinner}} = -100;$**

$h$  is the width or thickness (in m) of the concrete specimen.

**$h = .6;$**

$thick$  is the thickness of the fiberglass insulation (in inches) for the left or right (or the top or bottom).

**$thickleft = 6;$**

**$thickright = 6;$**

**$thickright = thickright * .0254;$**

**$thickleft = thickleft * .0254;$**

$T_{\text{concinital}}$  is the initial temperature of the concrete (in  $^{\circ}\text{C}$ ), and  $T_{\text{ambient}}$  is the ambient temperature (in  $^{\circ}\text{C}$ ).  $T_{\text{insinital}}$  is the initial temperature of the insulation (in  $^{\circ}\text{C}$ ).

**$T_{\text{concinital}} = 25;$**

**$T_{\text{ambient}} = 23;$**

**$T_{\text{concinital}} = 273 + T_{\text{concinital}};$**

**$T_{\text{ambient}} = T_{\text{ambient}} + 273;$**

**$T_{\text{insinital}} = T_{\text{ambient}};$**

$c_{\text{conc}}$  is the thermal capacity of the concrete (J/kg-K).

**$c_{\text{conc}} = 1000;$**

$k_{\text{conc}}$  is the thermal conductivity of the concrete (Watt/m-K).

**$k_{\text{conc}} = 2;$**

$\rho_{\text{conc}}$  is the density of concrete ( $\text{kg}/\text{m}^3$ )

**$\rho_{\text{conc}} = 2400;$**

HydrationHeat is the heat of hydration output by the concrete ( $\text{W}/\text{m}^2/\text{m}$ ) or ( $\text{W}/\text{m}^3$ ) as a function of time.

$$\text{HydrationHeat} = \left( a_1 * e^{-\left(\frac{t-b_1}{c_1}\right)^2} + a_2 * e^{-\left(\frac{t-b_2}{c_2}\right)^2} \right);$$

$$a_1 = 1650; b_1 = 18500; c_1 = 10500; a_2 = 1580; b_2 = 41000; c_2 = 30000;$$

Joules is the net heat output of the concrete over the first 24 hours after casting. This value is used to verify the parameters for the hydration heat model.

$$\text{Joules} = \text{N}[\text{Integrate}[\text{HydrationHeat}, \{t, 0, 86400\}]]$$

$$1.10931 \times 10^8$$

$$\text{JperKgcementatFullHyd} = 410000;$$

$$\text{CemContentlbperyd3} = 752;$$

$$\text{CemContentkgperm3} = \text{CemContentlbperyd3} / 1.68;$$

$$\text{degHydat24hrs} = 0.6;$$

$$\text{JperKgcement} = \text{degHydat24hrs} * \text{JperKgcementatFullHyd};$$

$$\text{Jperm3cement} = \text{CemContentkgperm3} * \text{JperKgcement}$$

$$1.10114 \times 10^8$$

$\alpha_{\text{conc}}$  is the thermal diffusivity of concrete and  $\alpha_{\text{ins}}$  is the thermal diffusivity of the fiberglass insulation ( $\text{m}^2/\text{s}$ )

$$\alpha_{\text{conc}} = \left( \frac{k_{\text{conc}}}{c_{\text{conc}} * \rho_{\text{conc}}} \right);$$

$$\alpha_{\text{ins}} = 49 * 10^{-8};$$

## Analysis

### *Insulation left*

The following equations solve the heat transfer equation for the insulation on the left (or top) of the specimen assuming a boundary temperature of  $T_{\text{bound}}$  at the interface between the insulation and concrete.

$$\text{eq1} = s * \text{Tbar}[x] - \text{Tinsinitial} == \alpha_{\text{ins}} * \text{D}[\text{Tbar}[x], \{x, 2\}];$$

$$\text{Sol1} = \text{DSolve}[\{\text{eq1}, \text{Tbar}[-\text{thickleft} - h/2] == \text{Tambient} / s, \text{Tbar}[-h/2] == \text{Tboundbar}\}, \text{Tbar}[x], x];$$

$$\text{Tleftbar}[x_, s_] = \text{Simplify}[\text{Tbar}[x] /. \text{Sol1}];$$

$$\text{qleftbar}[x_, s_] = \text{D}[\text{Tleftbar}[x, s], x];$$

### *Insulation right*

The following equations solve the heat transfer equation for the insulation on the right (or bottom) of the specimen assuming a boundary temperature of Tbound at the interface between the insulation and concrete.

```
Sol2 = DSolve[{eq1, Tbar[thickright + h/2] == Tambient/s, Tbar[h/2] == Tboundbar}, Tbar[x], x];
```

```
Trightbar[x_, s_] = Tbar[x] /. Sol2;
```

```
qrightbar[x_, s_] = D[Trightbar[x, s], x];
```

### *Concrete beam*

The following equations solve the heat transfer equation for the concrete beam assuming a boundary temperature of Tbound at both interfaces between insulation and concrete.

```
qgen[x_, t_] = ((UnitStep[t] - UnitStep[t - 30 * 60 * 60]) * (DiracDelta[x - h/2 + .001] + DiracDelta[x + h/2 - .001]) * Qsupplied + HydrationHeat + (UnitStep[t - 0]) * (DiracDelta[x - 0]) * Qsuppliedinner;
```

```
qgenbar[x_] = LaplaceTransform[qgen[x, t], t, s];
```

```
eq2 = s * Tconcbar[x] - Tconcinitial == aconc * D[Tconcbar[x], {x, 2}] +  $\frac{aconc}{kconc}$  * qgenbar[x];
```

```
Sol3 = DSolve[{eq2, Tconcbar[-h/2] == Tboundbar, Tconcbar[h/2] == Tboundbar}, Tconcbar[x], x];
```

```
Tconcbar[x_, s_] = Tconcbar[x] /. Sol3;
```

```
qconcbar[x_, s_] = D[Tconcbar[x, s], x];
```

The following equations solve for the unknown boundary condition Tboundbar based on conservation of energy; the heat flow into the concrete must equal the heat flow out of the insulation (and vice versa).

```
Sol4 = Solve[qleftbar[-h/2, s] == qconcbar[-h/2, s], Tboundbar];
```

```
Tboundbar = Simplify[Tboundbar /. Sol4];
```

The following equations invert the solutions for the temperature in concrete (Tconc) and insulation (Tright, Tleft) from the Laplace transform domain (Tconcbar, Tleftbar, Trightbar) into the time domain. This is done numerically utilizing the Stehfest algorithm.

```
Tconc[x_, t_] = Stehfest[Tconcbar[x, s], s, t, 8] - 273;
```

`Tright[x_, t_] = Stehfest[Trightbar[x, s], s, t, 8] - 273;`

`Tleft[x_, t_] = Stehfest[Tleftbar[x, s], s, t, 8] - 273;`

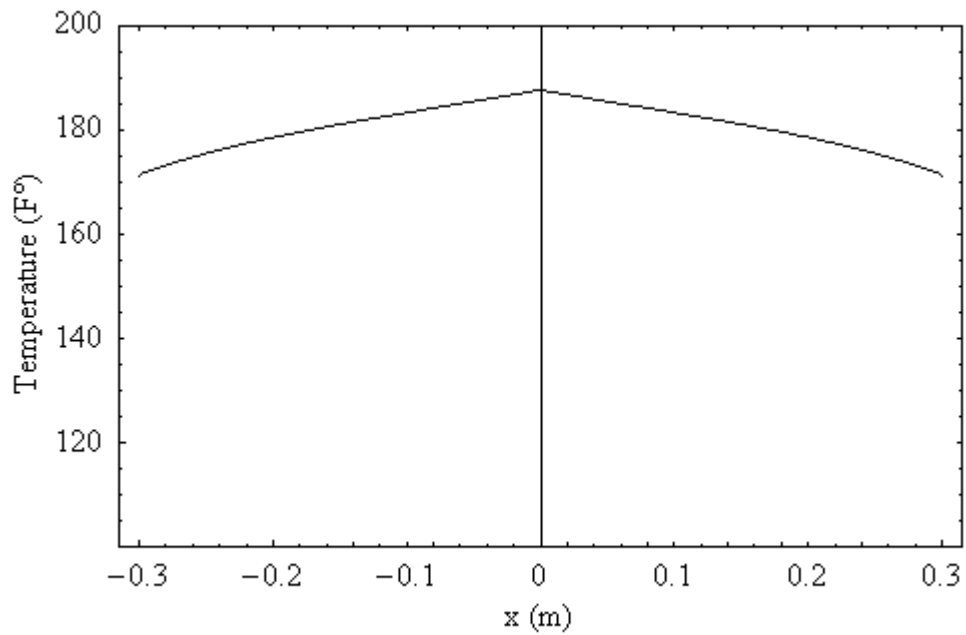
The following equations convert the temperature from Celsius into Fahrenheit.

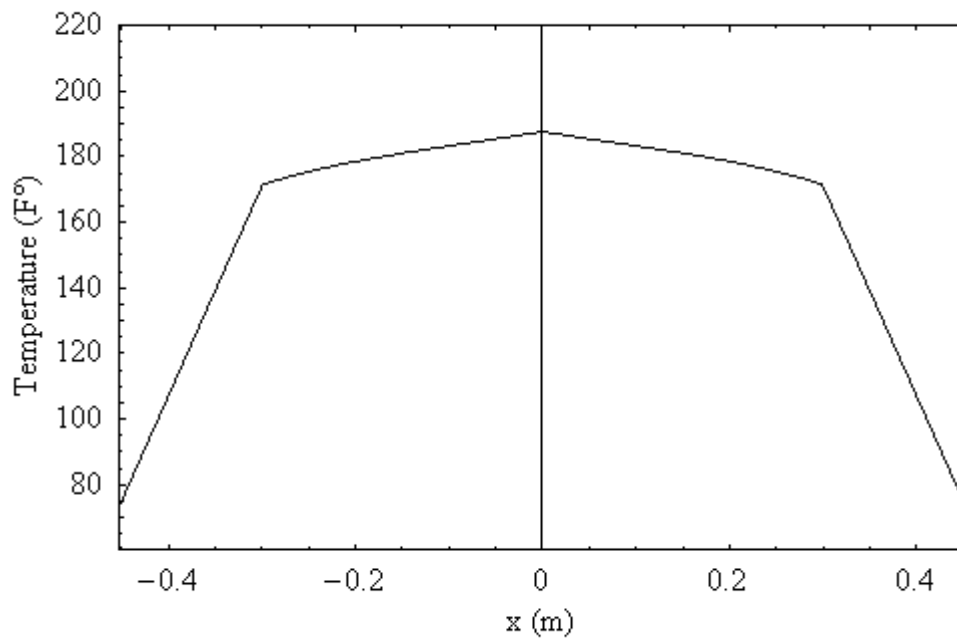
`Tfright[x_, t_] = Tright[x, t] * 9 / 5 + 32;`

`Tfconc[x_, t_] = Tconc[x, t] * 9 / 5 + 32;`

`Tfleft[x_, t_] = Tleft[x, t] * 9 / 5 + 32;`

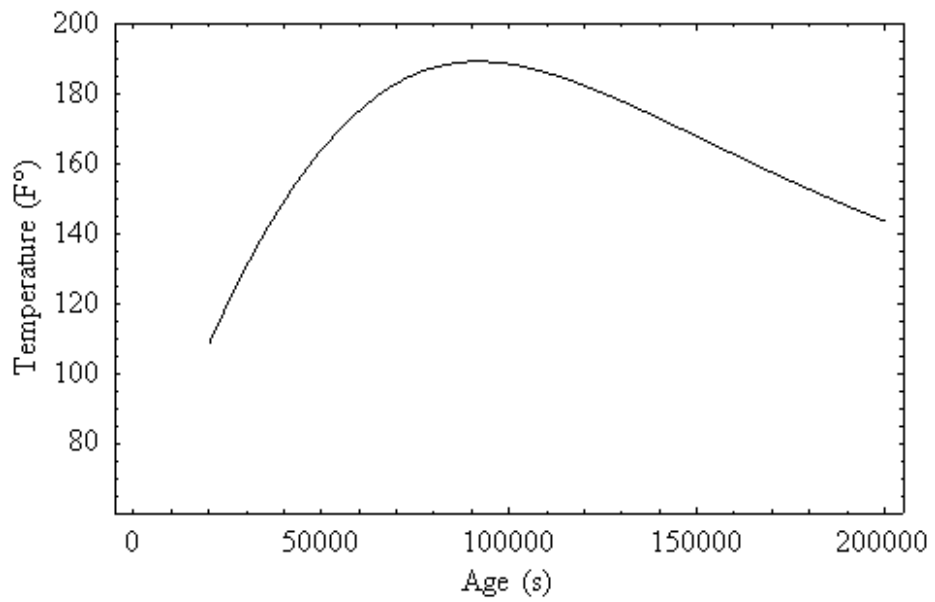
The graph below shows the temperature distribution in the concrete alone at about 1 day age.



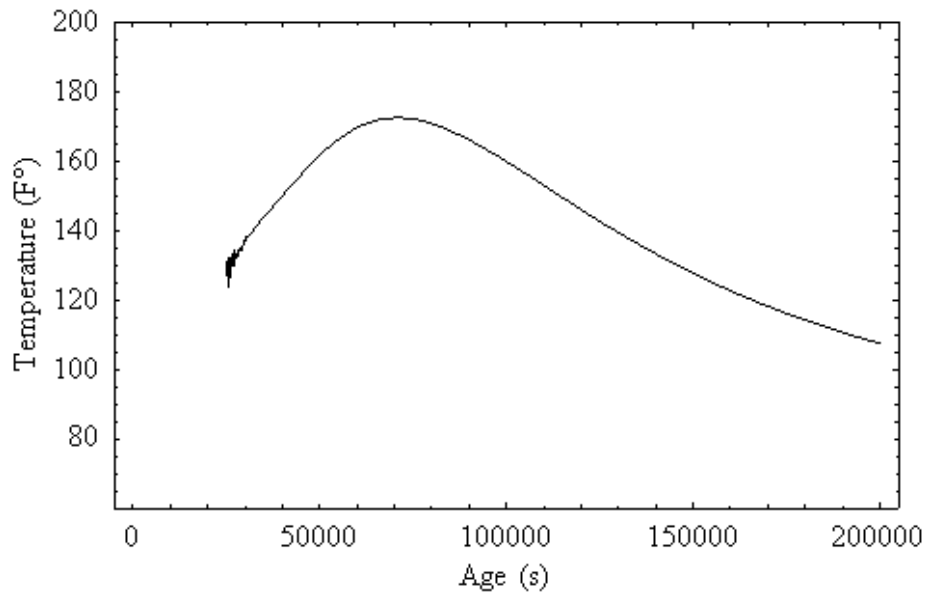


The outer portions of the graph above are the temperature distributions (at ~1 day age) in the insulation, while the inner portions are the temperature distribution in the concrete. The left side would be the top, the right side the bottom.

The graph below plots the temperature evolution in the center of the specimen.



The graph below plots the temperature evolution on the surface of the concrete.



## APPENDIX B: STAGE 1–3 ANALYSIS–BENT CAP SPECIMEN

*Results of Stage 1 and 2 analyses of bent cap specimens*

**Table B–1: Results for Stage 1 Flexure Analysis.**

	Specimen 2A	Specimen 5D	Specimen 8G	
$L_b(in)$	39	39	39	
$b_w(in)$	33	33	33	
$d'(in)$	3 1/4	3 1/4	3 1/4	
$\rho_L'$	0.00581	0.00581	0.00581	
$d(in)$	32 3/4	32 3/4	32 3/4	
$\rho_L$	0.00581	0.00799	0.00581	
$n$	6.46	6.86	7.31	
$k$	0.222	0.261	0.232	<i>Eq. (3–2)</i>
$C_c(kip)$	-344	-472	-338	
$C_s(kip)$	-64	-89	-71	
$T(kip)$	408	562	408	
$M_y^b(kip.in)$	12332	<i>16755</i>	<i>12289</i>	<i>Eq. (3–1)</i>
$P_y^b(kip)$	<b>316</b>	<i>430</i>	<i>315</i>	<i>Eq. (3–3)</i>
$\beta_1$	0.74	0.78	0.79	<i>Eq. (3–5)</i>
$M_n^f(kip.in)$	14365	18795	14364	<i>Eq. (3–4)</i>
$P_n^f(kip)$	<b>368</b>	482	368	<i>Eq. (3–6)</i>

**Table B-2: Results for Stage 1 Shear Analysis.**

	Specimen 2A	Specimen 5D	Specimen 8G	
$d_v$ (in)	29.36	29.36	29.36	
$A_{sh}$ (in <sup>2</sup> )	0.614	0.614	1.227	
$f_c'$ (ksi)	6.2	5.5	5.3	
$f_y$ (ksi)	65	65	65	
$V_c$ (kip)	152	144	141	Eq. (3-8)
$V_s$ (kip)	187	187	374	Eq. (3-9)
$V_n^s$ (kip)	<b>339</b>	331	515	Eq.(3-7)

**Table B-3: Results for Stage 2 SAT Analysis.**

	Specimen 2A	Specimen 5D	Specimen 8G	Comments
$a$ (in)	2.35	3.6	2.75	
$\theta_s$ (degrees)	36.8	36.8	36.8	
$T$ (kip)	408	561	408	
$D$ (kip)	510	701	510	
$P_y^{SAT}$ (kip)	306	421	306	Based on longitudinal steel yield.
$\phi_v P_y^{SAT}$ (kip)	214	295	214	
$P_n^{SAT}$ (kip)	368	483	369	Based on node capacity.
$\phi_v P_n^{SAT}$ (kip)	258	338	259	
$\phi_f P_n^f$ (kip)	331	434	331	



**Table B-4: Summary of Results for Bent Cap Specimens.**

		Specimen 2A		Specimen 5D		Specimen 8G		
Stage		Capacity (kip)	Factored Capacity (kip)	Capacity (kip)	Factored Capacity (kip)	Capacity (kip)	Factored Capacity (kip)	Comments
Stage 1: Beam Theory	$P_y^b$	316	---	430	---	315	---	External load based on yield flexural resistance of the beam.
	$P_n^f$	368	331	482	434	368	331	External load based on nominal flexural capacity of the beam.
	$V_n^s$	339	288	331	281	515	438	Beam shear capacity.
Stage 2: SAT	$P_y^{SAT}$	306	214	421	295	306	214	External load based on yield of longitudinal steel in beam.
	$P_n^{SAT}$	368	N/A	483	N/A	369	N/A	External load based on critical CCC node.
Stage 3: C-STM	$P_{C-STM}$	<b>383</b>	268	<b>455</b>	319	---	---	External load based on C-STM analysis.
Experiment	$P_{Failure}$	404	---	465	---	---	---	Maximum load at incipient failure.



## APPENDIX C: STAGE 1–3 ANALYSIS–C-BEAM SPECIMEN

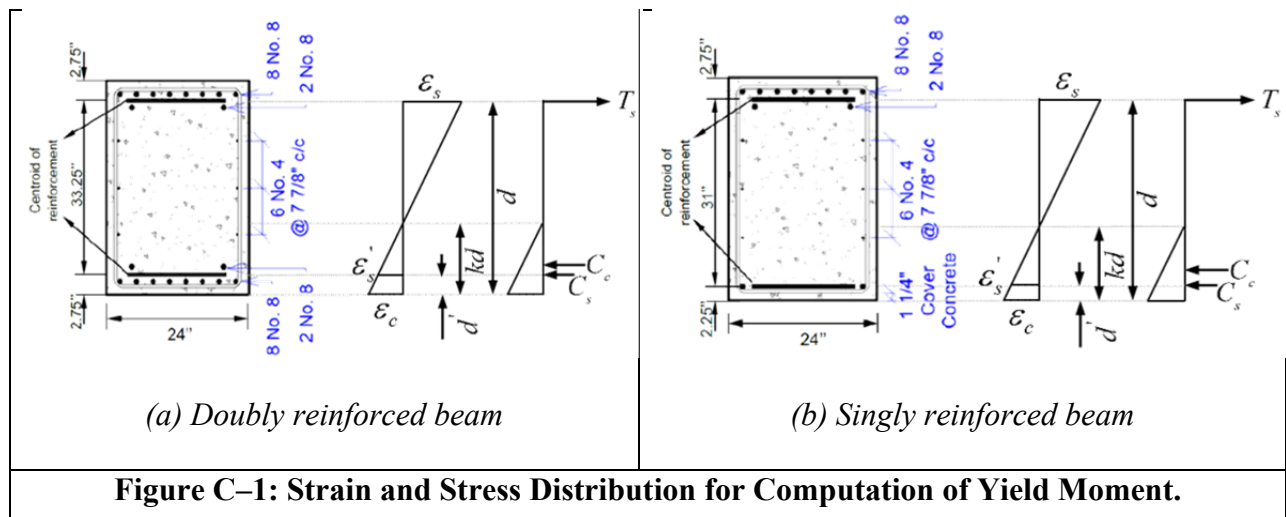
This appendix presents the analysis procedure followed for the C-Beam specimens. The computations for Stage 1 (beam theory), Stage 2 (SAT analysis), and Stage 3 (C-STM analysis) are included.

**Table C–1: Material Properties for C-Beam Specimens.**

	Specimen 1	Specimen 2	Specimen 4
$f'_c$ (ksi) (at time of testing)	5.40	5.60	4.00
$f'_t$ (ksi)	0.30	0.23	0.23
$E_c$ (ksi)	4190	4265	3605
$f_y$ (ksi)	65	65	65
$E_s$ (ksi)	29000	29000	29000

### STAGE 1: ANALYSIS USING BEAM THEORY

Step 1: Determine first yield flexural capacity,  $M_y^b$ .



**Table C-2: Computation of First Yield Flexural Capacity and Corresponding Axial Load.**

	Specimen 1		Specimen 2		Specimen 4	
	Doubly reinforced	Singly reinforced	Doubly reinforced	Singly reinforced	Doubly reinforced	Singly reinforced
$A_s$ (in <sup>2</sup> )	7.854	7.854	7.854	7.854	7.854	7.854
$A'_s$ (in <sup>2</sup> )	7.854	1.571	7.854	1.571	7.854	1.571
$b$ (in)	24	24	24	24	24	24
$d$ (in)	33.25	33.25	33.25	33.25	33.25	33.25
$d'$ (in)	2.75	2.25	2.75	2.25	2.75	2.25
$jd = d - d'$ (in)	30.5	31	30.5	31	30.5	31
$\rho_L = \frac{A_s}{bd}$	0.00984	0.00984	0.00984	0.00984	0.00984	0.00984
$\rho'_L = \frac{A'_s}{bd}$	0.00984	0.00197	0.00984	0.00197	0.00984	0.00197
$n = E_s / E_c$	6.92		6.80		8.04	
$k = \sqrt{(\rho_L + \rho'_L)^2 n^2 + 2(\rho_L + \rho'_L d'/d)n} - (\rho_L + \rho'_L)n$						
$k$	0.271	0.299	0.270	0.297	0.285	0.317
$kd$ (in)	9.01	9.94	8.98	9.88	9.48	10.54
$\varepsilon_c = \frac{\varepsilon_y(kd)}{d - kd}$	0.00083	0.00096	0.00083	0.00095	0.00089	0.00104
$\varepsilon'_s = \frac{\varepsilon_y(kd - d')}{d - kd}$	0.00058	0.00074	0.000575	0.00073	0.00063	0.00082
$C_c(kip) = \frac{1}{2} \varepsilon_c E_c (kd)b$	-377	-480	-381	-480	-366	-474
$C_s(kip) = A'_s \varepsilon'_s E_s$	-132	-34	-131	-33	-144	-37
$T_s(kip) = A_s f_y$	511	511	511	511	511	511
$M_y^b = T_s(d - kd/3) + C_s(kd/3 - d')$						
$M_y^b(kip.in)$	15474	15319	15478	15328	15420	15228
$P_y^b = M_y^b / L_b$ where $L_b = 36$ in						
$P_y^b(kip)$	430	425	430	426	428	423

Step 2 and Step 3: Determine nominal flexural moment,  $M_n^f$  and axial load demand based on flexure,  $P_n^f$ .

For an accurate estimate of the nominal moment, calculations were performed in a spreadsheet considering the contribution of each layer of steel. The spreadsheets are presented below for both doubly and singly reinforced beam for all the three specimens.

**Table C-3: Computation of Flexural Moment and Corresponding Axial Load Demand for Doubly Reinforced Beam: Specimen 1.**

Input Parameters						Calculated Variables	
Section Properties		Reinforcement Details		Reinforcement Properties		$\alpha$	0.85
Breadth (in)	24	Reinforcement	Diameter (in)	Es (ksi)	29000	$\beta$	0.78
a (shear span) (in)	36	Longitudinal	1	fy (ksi)	65		
Concrete Properties		Distribution	0.5			Assume NA depth for equilibrium, c (in)	4.145
f'c (ksi)	5.4	Stirrups	0.5				
Analysis							
Layer	No. of bars	Area (in <sup>2</sup> )	Dist to layers from bottom (in)	Strain	Stress in Steel (ksi)	Force in Concrete/ Steel (kip)	Moment (kip-in)
Concrete (Bottom)	-----	-----	1.617	-0.0030	-----	-356.16	-575.75
1	8	6.28	2.250	-0.0014	-39.77	-249.91	-562.30
Steel 2	2	1.57	4.750	0.0004	12.70	19.95	94.75
Steel 3	2	0.39	10.125	0.0043	64.96	25.51	258.29
Steel 4	2	0.39	18.000	0.0100	64.96	25.51	459.18
Steel 5	2	0.39	25.875	0.0157	64.96	25.51	660.06
Steel 6	2	1.57	31.250	0.0196	64.96	102.04	3188.72
Steel 7	8	6.28	33.750	0.0214	64.96	408.16	13775.26
						$M_n^f$ (kip-ft)	<b>1441.52</b>
						$P_n^f$ (kip)	<b>480.51</b>

**Table C-4: Computation of Flexural Moment and Corresponding Axial Load Demand for Singly Reinforced Beam: Specimen 1.**

Input Parameters						Calculated Variables	
<i>Section Properties</i>		<i>Reinforcement Details</i>		<i>Reinforcement Properties</i>		$\alpha$	0.85
Breadth (in)	24	<i>Reinforcement</i>	<i>Diameter (in)</i>	Es (ksi)	29000	$\beta$	0.78
a (shear span) (in)	36	Longitudinal	1	fy (ksi)	65		
<i>Concrete Properties</i>		Distribution	0.5			Assume NA depth for equilibrium, c (in)	5.845
fc (ksi)	5.4	Stirrups	0.5				
Analysis							
<i>Layer</i>	<i>No: of bars</i>	<i>Area (in<sup>2</sup>)</i>	<i>Dist to layers from bottom (in)</i>	<i>Strain</i>	<i>Stress in Steel (ksi)</i>	<i>Force in Concrete/ Steel (kip)</i>	<i>Moment (kip-in)</i>
Concrete (Bottom)	-----	-----	2.280	-0.0030	-----	-502.23	-1144.86
1	2	1.57	2.250	-0.0018	-53.46	-83.97	-188.93
Steel 2	0	0.00	4.750	-0.0006	-16.30	0.00	0.00
Steel 3	2	0.39	10.125	0.0022	62.08	24.38	246.83
Steel 4	2	0.39	18.000	0.0062	64.96	25.51	459.18
Steel 5	2	0.39	25.875	0.0103	64.96	25.51	660.06
Steel 6	2	1.57	31.250	0.0130	64.96	102.04	3188.72
Steel 7	8	6.28	33.750	0.0143	64.96	408.16	13775.26
						$M_n^f$ (kip-ft)	<b>1416.36</b>
						$P_n^f$ (kip)	<b>472.12</b>

**Table C-5: Computation of Flexural Moment and Corresponding Axial Load Demand for Doubly Reinforced Beam: Specimen 2.**

Input Parameters						Calculated Variables	
<i>Section Properties</i>		<i>Reinforcement Details</i>		<i>Reinforcement Properties</i>		$\alpha$	0.85
Breadth (in)	24	Reinforcement	Diameter (in)	Es (ksi)	29000	$\beta$	0.77
a (shear span) (in)	36	Longitudinal	1	fy (ksi)	65		
<i>Concrete Properties</i>		Distribution	0.5			Assume NA depth for equilibrium, c (in)	4.105
fc (ksi)	5.6	Stirrups	0.5				
Analysis							
<i>Layer</i>	<i>No: of bars</i>	<i>Area (in<sup>2</sup>)</i>	<i>Dist to layers from bottom (in)</i>	<i>Strain</i>	<i>Stress in Steel (ksi)</i>	<i>Force in Concrete/ Steel (kip)</i>	<i>Moment (kip-in)</i>
Concrete (Bottom)	-----	-----	1.580	-0.0030	-----	-361.10	-570.68
1	8	6.28	2.250	-0.0014	-39.31	-247.02	-555.79
Steel 2	2	1.57	4.750	0.0005	13.67	21.47	102.00
Steel 3	2	0.39	10.125	0.0044	64.96	25.51	258.29
Steel 4	2	0.39	18.000	0.0102	64.96	25.51	459.18
Steel 5	2	0.39	25.875	0.0159	64.96	25.51	660.06
Steel 6	2	1.57	31.250	0.0198	64.96	102.04	3188.72
Steel 7	8	6.28	33.750	0.0217	64.96	408.16	13775.26
						$M_n^f$ (kip-ft)	<b>1443.08</b>
						$P_n^f$ (kip)	<b>481.03</b>

**Table C-6: Computation of Flexural Moment and Corresponding Axial Load Demand for Singly Reinforced Beam: Specimen 2.**

Input Parameters						Calculated Variables	
Section Properties		Reinforcement Details		Reinforcement Properties		$\alpha$	0.85
Breadth (in)	24	Reinforcement	Diameter (in)	Es (ksi)	29000	$\beta$	0.77
a (shear span) (in)	36	Longitudinal	1	fy (ksi)	65		
Concrete Properties		Distribution	0.5			Assume NA depth for equilibrium, c (in)	5.721
f <sub>c</sub> (ksi)	5.6	Stirrups	0.5				
Analysis							
Layer	No: of bars	Area (in <sup>2</sup> )	Dist to layers from bottom (in)	Strain	Stress in Steel (ksi)	Force in Concrete/ Steel (kip)	Moment (kip-in)
Concrete	-----	-----	2.203	-0.0030	-----	-503.25	-1108.44
(Bottom) 1	2	1.57	2.250	-0.0018	-52.74	-82.85	-186.41
Steel 2	0	0.00	4.750	-0.0005	-14.77	0.00	0.00
Steel 3	2	0.39	10.125	0.0023	63.57	24.96	252.74
Steel 4	2	0.39	18.000	0.0064	64.96	25.51	459.18
Steel 5	2	0.39	25.875	0.0106	64.96	25.51	660.06
Steel 6	2	1.57	31.250	0.0134	64.96	102.04	3188.72
Steel 7	8	6.28	33.750	0.0147	64.96	408.16	13775.26
						<b><math>M_n^f</math> (kip-ft)</b>	<b>1420.09</b>
						<b><math>P_n^f</math> (kip)</b>	<b>473.36</b>



**Table C-7: Computation of Flexural Moment and Corresponding Axial Load Demand for Doubly Reinforced Beam: Specimen 4.**

Input Parameters						Calculated Variables	
<i>Section Properties</i>		<i>Reinforcement Details</i>		<i>Reinforcement Properties</i>		$\alpha$	0.85
Breadth (in)	24	Reinforcement	Diameter (in)	Es (ksi)	29000	$\beta$	0.85
a (shear span) (in)	36	Longitudinal	1	fy (ksi)	65		
<i>Concrete Properties</i>		Distribution	0.5			Assume NA depth for equilibrium, c (in)	4.555
f <sub>c</sub> (ksi)	4	Stirrups	0.5				
Analysis							
<i>Layer</i>	<i>No: of bars</i>	<i>Area (in<sup>2</sup>)</i>	<i>Dist to layers from bottom (in)</i>	<i>Strain</i>	<i>Stress in Steel (ksi)</i>	<i>Force in Concrete/ Steel (kip)</i>	<i>Moment (kip-in)</i>
Concrete	-----	-----	1.936	-0.0030	-----	-315.93	-611.61
(Bottom) 1	8	6.28	2.250	-0.0015	-44.02	-276.61	-622.38
Steel 2	2	1.57	4.750	0.0001	3.72	5.85	27.79
Steel 3	2	0.39	10.125	0.0037	64.96	25.51	258.29
Steel 4	2	0.39	18.000	0.0089	64.96	25.51	459.18
Steel 5	2	0.39	25.875	0.0140	64.96	25.51	660.06
Steel 6	2	1.57	31.250	0.0176	64.96	102.04	3188.72
Steel 7	8	6.28	33.750	0.0192	64.96	408.16	13775.26
						$M_n^f$ (kip-ft)	<b>1427.94</b>
						$P_n^f$ (kip)	<b>475.98</b>

**Table C-8: Computation of Flexural Moment and Corresponding Axial Load Demand for Singly Reinforced Beam: Specimen 4.**

Input Parameters						Calculated Variables	
<i>Section Properties</i>		<i>Reinforcement Details</i>		<i>Reinforcement Properties</i>		$\alpha$	0.85
Breadth (in)	24	Reinforcement	Diameter (in)	Es (ksi)	29000	$\beta$	0.85
a (shear span) (in)	36	Longitudinal	1	fy (ksi)	65		
<i>Concrete Properties</i>		Distribution	0.5			Assume NA depth for equilibrium, c (in)	6.985
f <sub>c</sub> (ksi)	4	Stirrups	0.5				
Analysis							
<i>Layer</i>	<i>No: of bars</i>	<i>Area (in<sup>2</sup>)</i>	<i>Dist to layers from bottom (in)</i>	<i>Strain</i>	<i>Stress in Steel (ksi)</i>	<i>Force in Concrete/ Steel (kip)</i>	<i>Moment (kip-in)</i>
Concrete	-----	-----	2.969	-0.0030	-----	-484.48	-1438.24
(Bottom) 1	2	1.57	2.250	-0.0020	-58.58	-92.01	-207.03
Steel 2	0	0.00	4.750	-0.0010	-27.84	0.00	0.00
Steel 3	2	0.39	10.125	0.0013	39.11	15.36	155.50
Steel 4	2	0.39	18.000	0.0047	64.96	25.51	459.18
Steel 5	2	0.39	25.875	0.0081	64.96	25.51	660.06
Steel 6	2	1.57	31.250	0.0104	64.96	102.04	3188.72
Steel 7	8	6.28	33.750	0.0115	64.96	408.16	13775.26
						$M_n^f$ (kip-ft)	<b>1382.79</b>
						$P_n^f$ (kip)	<b>460.93</b>

Step 4: Determine beam shear capacity,  $V_n^s$ .

**Table C–9: Computation of Beam Shear Capacity.**

	Specimen 1		Specimen 2		Specimen 4	
$f'_c$ (ksi) (at time of testing)	5.40		5.60		4.00	
$f_y$ (ksi)	65		65		65	
$b_v$ (in)	24		24		24	
$A_v$ (in <sup>2</sup> )	0.393		0.393		0.393	
$s$ (in)	4.5		4.5		4.5	
$\beta$ (per AASHTO Method 1)	2		2		2	
$\theta$ (degrees) (per AASHTO Method 1)	45		45		45	
	<i>Doubly</i>	<i>Singly</i>	<i>Doubly</i>	<i>Singly</i>	<i>Doubly</i>	<i>Singly</i>
$d_v = jd$ (in)	30.5	31	30.5	31	30.5	31
$V_c = 0.0316 \beta \sqrt{f'_c} b_v d_v$ (kip)	108	109	110	111	93	94
$V_s = A_v f_y \frac{d_v}{s} \cot \theta$ (kip)	173	176	173	176	173	176
$V_n^s = V_c + V_s$ (kip)	281	285	283	287	266	270

Step 5: Check strength hierarchy.

**Table C–10: Checking Strength Hierarchy.**

	Specimen 1		Specimen 2		Specimen 4	
	<i>Doubly</i>	<i>Singly</i>	<i>Doubly</i>	<i>Singly</i>	<i>Doubly</i>	<i>Singly</i>
$\phi_v$	0.90 (AASHTO 5.5.4.2)					
$V_n^s$ (kip)	281	285	283	287	266	270
$\phi_f$	0.90 (AASHTO 5.5.4.2)					
$P_n^f$ (kip)	481	472	481	473	476	461
$\phi_v V_n^s$ (kip)	253	256	255	258	239	243
$\phi_f P_n^f$ (kip)	433	425	433	426	428	415

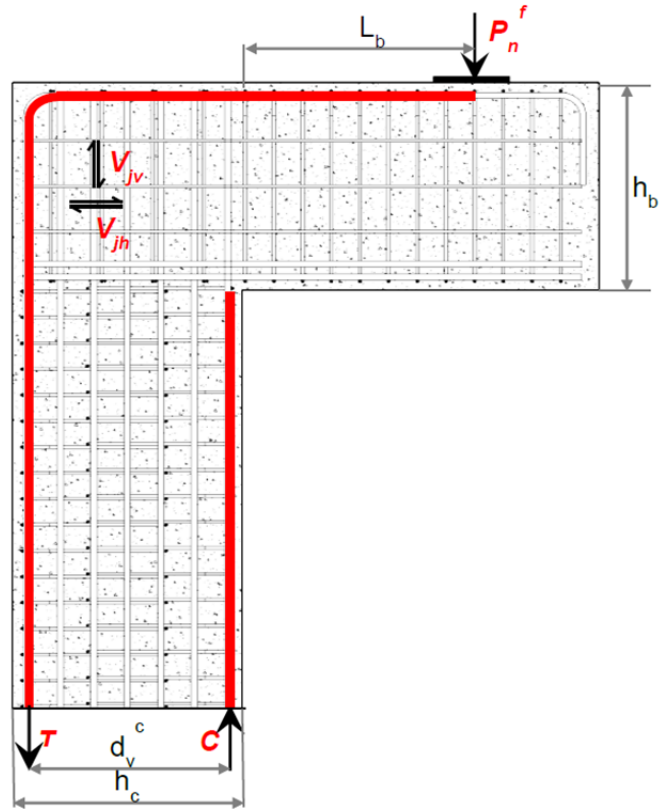
In all of the above cases  $\phi_v V_n^s < \phi_f P_n^f$ , that is the dependable shear capacity may be insufficient leading to a shear failure of the bridge pier.

*Step 6: Determine the shear capacity of the beam-column joint region.*

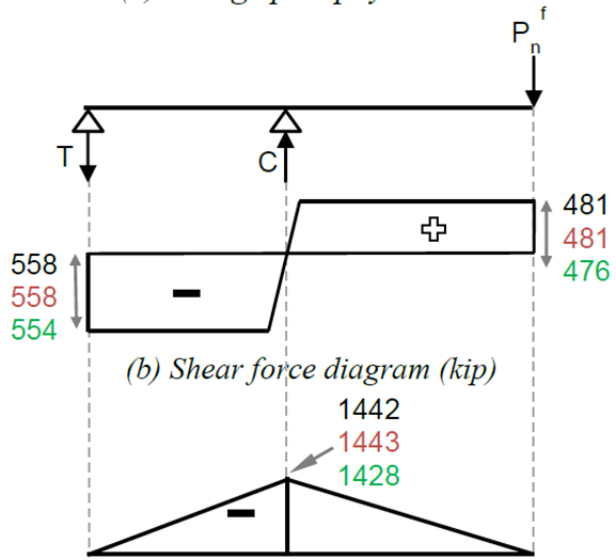
The vertical shear in the joint ( $V_{jv}$ ) caused by the axial load based on flexure can be determined from the shear force diagram of the equivalent beam model of the bridge pier shown in Figure C-2. The horizontal shear  $V_{jh}$  can be computed from  $V_{jv}$ .

**Table C-11: Computing the Vertical and Horizontal Shear in the Beam-Column Joint Caused by Flexural Axial Load Demand.**

	Specimen 1		Specimen 2		Specimen 4	
	<i>Doubly</i>	<i>Singly</i>	<i>Doubly</i>	<i>Singly</i>	<i>Doubly</i>	<i>Singly</i>
$P_n^f$ (kip)	481	472	481	473	476	461
$V_{jv}$ (kip)	558	548	558	550	554	535
$h_c = h_b$ (in)	36		36		36	
$V_{jh} = \frac{h_c}{h_b} V_{jv}$ (kip)	558	548	558	550	554	535



(a) Bridge pier physical model



(b) Shear force diagram (kip)

(c) Bending moment diagram (kip-ft) of cap beam

Figure C-2: Approach to determine shear in the beam-column joint for Specimen 1, Specimen 2 and Specimen 4.

The computation for assessing the joint shear capacity is as follows:

**Table C–12: Assessing the Joint Shear Capacity.**

	Specimen 1		Specimen 2		Specimen 4	
$\sum A_{sv} \text{ (in}^2\text{)}$ (total area of hoops/ties in the joint region)	1.571		1.571		1.571	
$f_y \text{ (ksi)}$	65		65		65	
$f'_c \text{ (ksi)}$	5.4		5.6		4.0	
$b_v \text{ (in)}$	24		24		24	
	<i>Doubly</i>	<i>Singly</i>	<i>Doubly</i>	<i>Singly</i>	<i>Doubly</i>	<i>Singly</i>
$jd \text{ (in)}$	30.5	31	30.5	31	30.5	31
$V_{truss} \text{ (kip)}$	102	102	102	102	102	102
$V_{arch} \text{ (kip)}$	430	437	438	445	370	376
$V_n^j \text{ (kip)} = V_{arch} + V_{truss}$	532	539	540	547	472	478
$\phi_v$	0.90					
$\phi_v V_n^j \text{ (kip)}$	479	485	486	492	425	430
$\phi_f$	0.90					
$\phi_f V_{jv} \text{ (kip)}$	502	493	502	495	498	481

In all of the above cases  $\phi_v V_n^j < \phi_f V_{jv}$ , that is the joint capacity is less than the demand, and hence there could be a shear joint failure.

From the above analysis it is determined that the beam and the beam-column joint are shear critical. Therefore a strut-and-tie analysis is performed. It is also required by the code to perform a SAT as the  $a/d$  ratio for the specimen is 1.08.

## ***STAGE 2: STRUT-AND-TIE ANALYSIS***

*Step 1: Determine the node geometry.*

The computation of the node dimensions and geometry for each of the specimens follows.

*CCT node:*

- The width of the CCT node is taken equal to the width of the bearing pad = 12".
- The depth of the back face of the CCT node =  $2 \times$  distance from the extreme tension face to the centroid of the tension reinforcement =  $2 \times 2.75 = 5.5"$ .

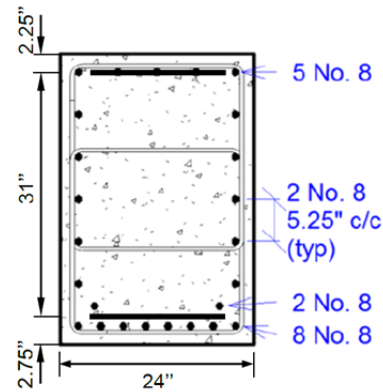
*CTT Node:*

- Width of the CTT node =  $\sqrt{2 \times (R + d_b / 2)^2}$  where  $R$  = bar bending radius = 4" and  $d_b$  = diameter of the column longitudinal rebar = 1".

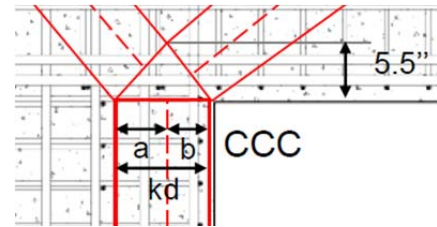
*CCC Node:*

- The width of the bottom face of the CCC node is equal to the depth of compression zone of the column ( $kd$ ) which is determined based on the equation for the elastic compression zone coefficient  $k$ .
- The bottom face is proportioned based on the ratio of  $a/b = V_{jv} / P_n^f$  (Figure in Table C-13) obtained from Stage 1 of the analysis.
- Since the horizontal force in the CCC node is equal to the horizontal force in the CCT node, the height of the CCC node is assumed to be equal to the depth of the back face of the CCT node =  $2 \times 2.75 = 5.5"$ .
- Knowing the above, the other sides of the CCC node can be determined.

**Table C-13: Computations for Sizing the CCC Node.**



(a) Column cross section

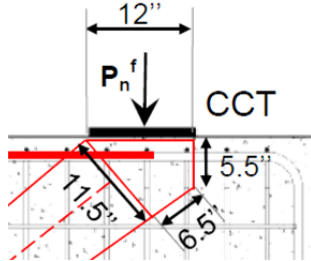
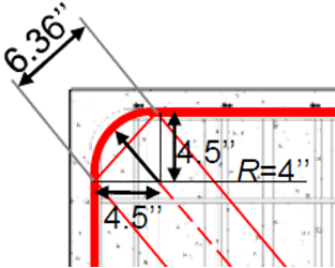

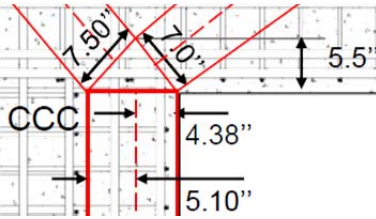
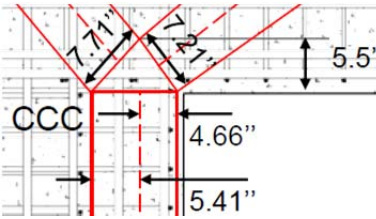


(b) CCC node configuration

	<b>Specimen 1</b>	<b>Specimen 2</b>	<b>Specimen 4</b>
$A_s$ (in <sup>2</sup> )	7.854		
$A'_s$ (in <sup>2</sup> )	3.927		
$b$ (in)	24		
$d$ (in)	33.25		
$d'$ (in)	2.25		
$\rho_L = \frac{A_s}{bd}$	0.00984	0.00984	0.00984
$\rho'_L = \frac{A'_s}{bd}$	0.00492		
$n = E_s / E_c$	6.92	6.80	8.04
$k = \sqrt{(\rho_L + \rho'_L)^2 n^2 + 2(\rho_L + \rho'_L d'/d)n} - (\rho_L + \rho'_L)n$			
$k$	0.287	0.285	0.303
$kd$ (in)	9.5	9.5	10.1
$V_{jv}$ (kip)	558	558	554
$P_n^f$ (kip)	481	481	476
$V_{jv} / P_n^f$	1.16	1.16	1.16
$a$ (in)	5.12	5.10	5.41
$b$ (in)	4.41	4.38	4.66



**Table C-14: Geometry and Dimensions of Nodes.**

<p style="writing-mode: vertical-rl; transform: rotate(180deg);"><b>CCT Node</b></p>			
<p style="writing-mode: vertical-rl; transform: rotate(180deg);"><b>CTT Node</b></p>			
<p style="writing-mode: vertical-rl; transform: rotate(180deg);"><b>CCC Node</b></p>	<p><b>Specimen 1</b></p>	<p><b>Specimen 2</b></p>	<p><b>Specimen 4</b></p>
			

Step 2: Solve the determinate truss and determine strut and tie forces.

**Table C–15: Forces in the Struts and Ties of the SAT Model.**

CCT Node	<b>Node forces based on steel yield</b>		
	$A_s$ (in <sup>2</sup> )	7.854	
	$f_y$ (ksi)	65	
	$\theta_b$ (degrees)	40	
	$\theta_j$ (degrees)	45	
	$T = A_s f_y$ (kip)	511	
	$D_b = T / \cos(\theta_b)$ (kip)	667	
$P^{SAT} = D_b \sin(\theta_b)$ (kip) = $P_y^{SAT}$	429		
CCC Node	$C' = D_b \cos(\theta_b)$ (kip)	511	
	$D_j = C' / \cos(\theta_j)$ (kip)	723	
	$P_v^j = D_j \sin(\theta_j)$ (kip)	511	

Step 3 and Step 4: Determine minimum applied load causing node failure and determine shear demand.

Allowable stresses in the nodes based on AASHTO (2010) are presented in Table C–16. From the allowable node stresses, the CTT node is found to be the critical node. The axial load required to cause the failure of the CTT node can be back calculated based on the allowable nodal stress and the area of the node. The results are presented in Table C–16.

**Table C-16: Allowable Node Stresses and Axial Load Required to Cause CTT Node Failure.**

	<b>Specimen 1</b>	<b>Specimen 2</b>	<b>Specimen 4</b>
$f'_c$ (ksi)	5.40	5.60	4.00
<b>Allowable Stresses</b>			
CCC Node $f_{cu} = 0.85 f'_c$	4.60	4.76	3.40
CCT Node $f_{cu} = 0.75 f'_c$	4.05	4.20	3.00
CTT Node $f_{cu} = 0.65 f'_c$	3.51	3.64	2.60
Node capacity $D_{j(node)} (kip) = F_{cu}$	536	556	397
Axial load that causes nodal failure, $P_n^{SAT} (kip) = P_y^{SAT} D_{j(node)} / D_j$	318	330	236

For all three specimens it is evident that  $P_n^{SAT}$  computed from the SAT analysis is less than  $P_n^f$  calculated from the beam flexure theory. Also,  $\phi_v P_n^{SAT} < \phi_f P_n^f$  for all the specimens. However from the experimental results, it was observed that the load at failure for the three specimens was  $P_{Failure}^{Expt} = 474$  kip, 485 kip, and 503 kip, respectively. It is apparent from Stage 1 and Stage 2 of the analysis that they do not give a good prediction of the load carrying capacity of the specimens. Therefore, a C-STM analysis is performed to evaluate the performance of the structure.

**STAGE 3: ANALYSIS USING COMPATIBILITY STRUT-AND-TIE METHOD**

The computation of member and material properties of the C-STM model are presented below for Specimen 1 (control specimen) followed by Specimen 2 and 4 (with ASR/DEF damage).

**Computation for C-Beam Specimen 1**

A few section properties have to be determined beforehand to set up the C-STM geometry. These computations follow.

*Step 1: Calculate section properties.*

**Table C-17: Computation of Section Properties for C-STM.**

	Doubly Reinforced	Column	Singly Reinforced
<b>CROSS-SECTION</b>			
Compression Chord	8-#8 Bars	5-#8 Bars	2-#8 Bars
$h$ (in)	36	36	36
$d'$ (in)	2.25	2.25	2.25
$d$ (in)	33.25	33.25	33.25
$A_s'$ ( $in^2$ )	6.28	3.93	1.57
Steel contributing to tension chord	10-#8 Bars 2 sets of 2-#4	10-#8 Bars 2 sets of 2-#4	10-#8 Bars 2 sets of 2-#8
$A_{s(total)}$ ( $in^2$ )	8.64	11.00	8.64
$\bar{y}$ (in) (centroid of $A_{s(total)}$ )	3.78	4.86	3.78
$A_s$ ( $in^2$ ) = $A_{s(total)} \frac{h-d'-\bar{y}}{d-d'}$	8.35	10.25	8.35
$jd = d - d'$ (in)	31.0	31.0	31.0

Determine the depth of compression zone ( $kd$ ) of the singly and doubly reinforced beams and column using the equation:

$$k = \sqrt{\left(\rho_L + \rho'_L + \left(\frac{P}{f_c'bd}\right)\left(\frac{f_c'}{f_s}\right)\right)^2 n^2 + 2\left(\rho_L + \rho'_L\left(\frac{d'}{d}\right) + \left(\frac{P}{f_c'bd}\right)\left(\frac{f_c'}{f_s}\right)\right)n - \left(\rho_L + \rho'_L + \left(\frac{P}{f_c'bd}\right)\left(\frac{f_c'}{f_s}\right)\right)n}$$

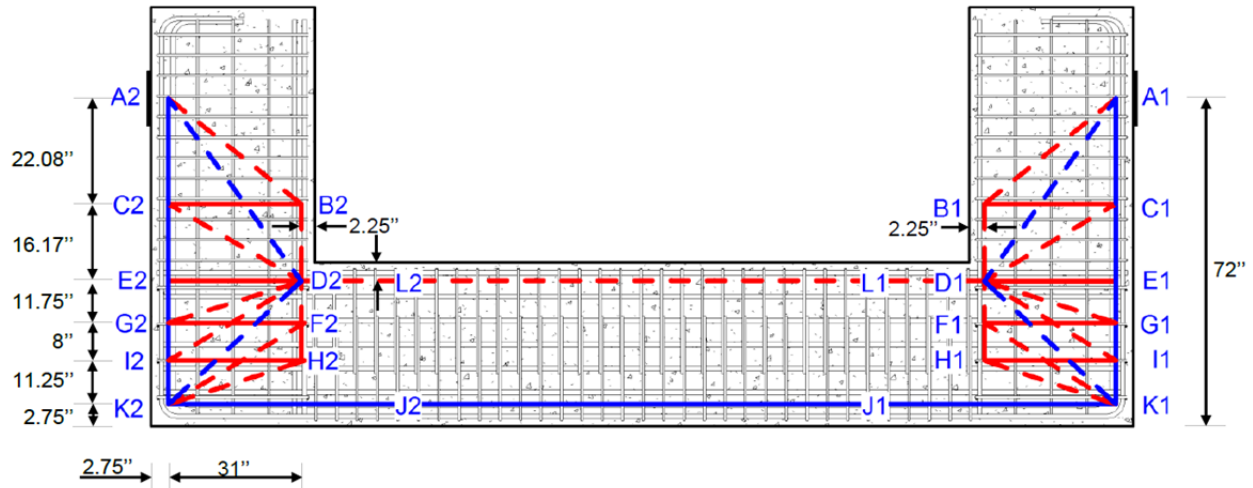
For the beams the axial load  $P$  is zero.

**Table C–18: Determining the Depth of the Compression Zone for Specimen 1.**

$f_c' = 5.4$ ksi	Compression Steel			Tension Steel				Axial Load	Elastic Depth	
	$As'$ (in <sup>2</sup> )	$d'$ (in)	$\rho'$	$As$ (in <sup>2</sup> )	$d$ (in)	$b$ (in)	$\rho$	$P$ (kip)	$k$	$kd$ (in)
Single Beam	1.57	2.25	0.00197	8.35	33.25	24	0.01046	-	0.307	10.19
Double Beam	6.28	2.25	0.00787	8.35	33.25	24	0.01046	-	0.283	9.42
Column	3.92	2.25	0.00492	10.25	33.25	24	0.01284	430	0.394	13.10

*Step 2: Determine C-STM geometry based on Step 1.*

The tension ties (AK and K1K2 in Figure C–3) and compression chords (BH and L1L2 in Figure C–3) in the beams and the column are placed along the centroids of the tension and compression steel determined in Table C–17. The C-STM geometry is the same in both the singly and double reinforced beams. The overhang portion of the specimen is modeled using the single-point Gauss truss model as presented in Chapter 4. The position of tie CB is determined based on the coefficients for the single point Gauss model. In the beam-column joint region, the ties GF and IH are placed along the position of the U-Bars to better represent the specimen. All the dimensions of the C-STM are shown in Figure C–3.



**Figure C-3: C-STM Model for C-Beam Specimen 1.**

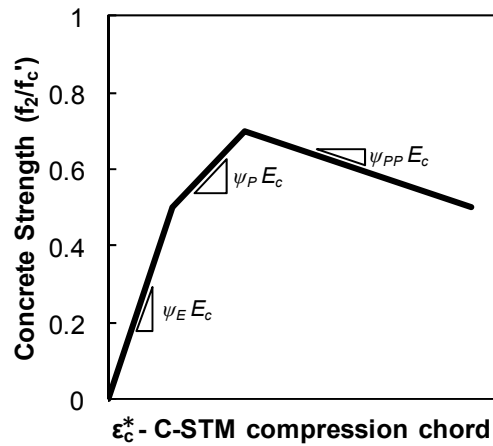
*Step 3: Determine axial rigidities.*

The next step in the C-STM analysis is to determine the axial rigidities of each of the members constituting the C-STM model.

To model the combined response of steel and concrete in the compression chord members, the compatibility correction factor is calculated in Table C-19. Based on these correction scalars, the modified stress-strain relation of the compression chord is determined.

**Table C-19: Computation of Compatibility Correction Scalar for Specimen 1.**

	<b>Singly Reinforced</b>	<b>Double Reinforced</b>	<b>Column</b>
$d' (in)$	2.25	2.25	2.25
$kd (in)$	10.19	9.42	13.10
$f'_c (ksi)$	5.4	5.4	5.4
$\psi_E = \frac{\sqrt{f'_c (psi)}}{168(1-d'/kd)}$	0.561	0.575	0.528
$\psi_P = \frac{\sqrt{f'_c (psi)}}{480(1-d'/kd)}$	0.196	0.201	0.185
$\psi_{PP} = -\frac{\sqrt{f'_c (psi)}}{1500(1-d'/kd)}$	-0.063	-0.064	-0.059



The arch breadth scalar is calculated to determine the area that needs to be assigned to the inclined arch and the struts in the beam and the beam-column joints.

**Table C–20: Computing Arch Breadth Scalar.**

$\eta = \frac{V_{Arch}}{V_{Arch} + V_{Truss}} = \frac{\rho_L f_y}{\rho_L f_y + \rho_T f_{yh} j \cot^2 \alpha}$			
	<b>Singly Reinforced</b>	<b>Double Reinforced</b>	<b>Column</b>
$d$ (in)	33.25	33.25	33.25
$b$	24	24	24
$s$	4.5	4.5	8
$jd$ (in)	31.0	31.0	31.0
$j$	0.93	0.93	0.93
$f_y = f_{yh}$ (ksi)	65	65	65
$A_s$ (in <sup>2</sup> )	8.35	8.35	10.25
$A_{sh}$ (in <sup>2</sup> )	0.393	0.393	0.393
$\rho_T = A_{sh}/b_w s$	0.00364	0.00364	0.00205
$\rho_L = A_s/bd$	0.0105	0.0105	0.0128
$\alpha$ (degrees)	39.02	39.02	45
$\eta$	0.671	0.671	0.87 (0.75 used)

Based on the properties computed above and the theory presented in Chapter 4, the axial rigidities are computed. The equations used are presented in Table 4–2.



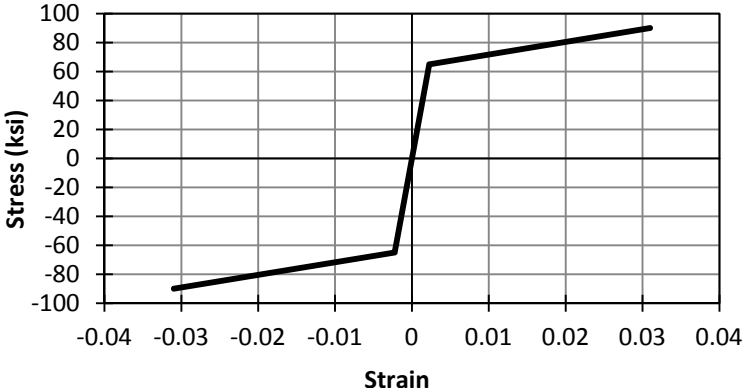
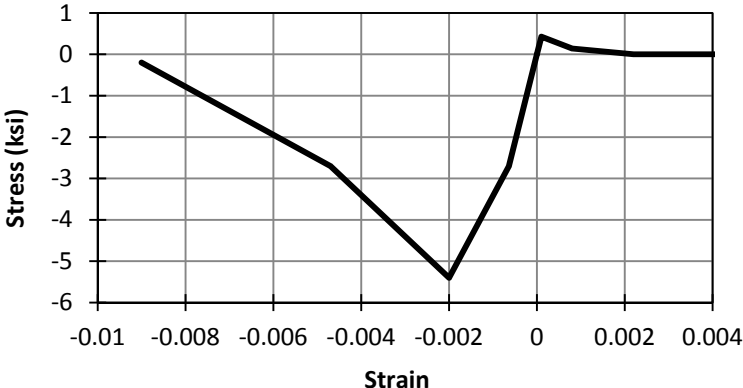
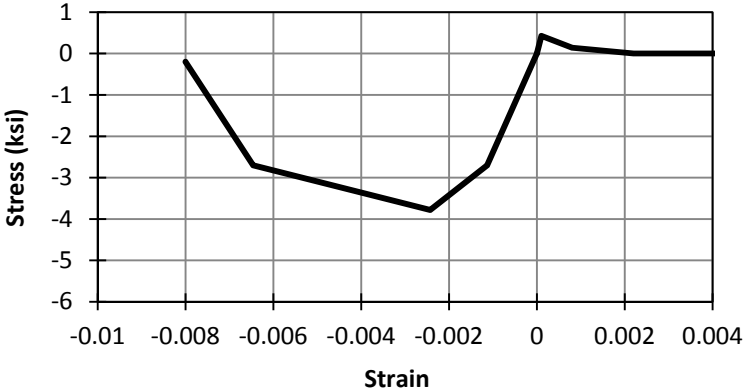
**Table C–21: Axial Rigidities of C-STM Elements: Specimen 1.**

	MEMBER	Steel		Concrete		Comments
		E (ksi)	A (in <sup>2</sup> )	E (ksi)	A (in <sup>2</sup> )	
<b>Beam</b>	A-E (D)	29000	8.35	4190	226.00	Tension Chord
	A-E (S)	29000	8.35	4190	245.00	
	B-D (D)	29000	6.28	2409	226.00	Compression Chord
	B-D (S)	29000	1.57	2351	245.00	
	BC	29000	2.36	4190	162.00	Transverse Steel
	AD	-	-	4190	240.60	Concrete Arch
	AB	-	-	4190	110.52	Concrete Truss
	CD	-	-	4190	118.14	
<b>Beam-Column Joint</b>	E-K (D)	29000	8.35	4190	226.00	Tension Chord
	E-K (S)	29000	8.35	4190	245.00	
	D-H (D)	29000	6.28	2409	226.00	Compression Chord
	D-H (S)	29000	1.57	2351	245.00	
	FG&HI	29000	0.39	4190	54.00	Transverse Steel
	DK	-	-	4190	295.92	Concrete Arch
	DG	-	-	4190	73.64	Concrete Truss
	DI	-	-	4190	78.46	
	FK	-	-	4190	78.15	
HK	-	-	4190	73.90		
<b>Column</b>	JJ	29000	10.25	4190	314.40	Tension Chord
	LL	29000	3.93	2212	314.40	Compression Chord
Beam: $N_h = 6$ and beam-column joint: $N_h = 2$						
<i>(D) Doubly reinforced beam (S) Singly reinforced beam</i>						

*Step 4: Determine constituent material properties.*

The stress-strain models used for the members in Phase 1 of Specimen 1 are as follows. The only difference for Phase 2 of the specimen is that the concrete tensile strength was reduced to 0.2 *ksi* to account for the minor concrete cracking that had occurred in Phase 1 of the experiment.

**Table C-22: Stress-Strain Models Used for C-STM Members: Phase 1 of Specimen 1.**

Member	Stress-Strain Model
All steel members.	
All concrete members, except the beam and column compression chord members. AB, CD, GD, ID, FK, HK, AD, CB, GF, IH, J1J2, and AK.	
Beam compression chord. BH	

**Table C-22: Stress-Strain Models Used for C-STM Members: Phase 1 of Specimen 1 (continued).**

<p>Column compression chord. L1L2</p>	
<p>Softened concrete model for the beam-column joint concrete arch. DK (In Phase 2)</p>	

### ***Computation for C-Beam Specimen 2 and 4.***

C-Beam Specimen 2 and 4 were subjected to slight and moderate amounts of ASR/DEF damage. While the procedure for calculating the member and material properties remains the same as in the case of Specimen 1, certain modifications are required to account for the effects of ASR/DEF in the specimens. The modifications are based on the recommendations made in Chapter 4.

*Step 1: Compute modified material properties to account for ASR/DEF.*

To account for the effects of ASR/DEF on the C-Beam specimens, modified material properties are calculated based on the recommendations presented in Section 4.8.5.

- *Diagonal truss concrete:*

**Table C–23: Modified Concrete Strength for Concrete Truss Members of the C-STM.**

	<b>Specimen 2</b>	<b>Specimen 4</b>
ASR/DEF damage level	Slight	Moderate
$f'_c$ (ksi)	5.6	4.0
$\lambda$	0.85	0.70
$f'_{cASR}$ (ksi) = $\lambda f'_c$	4.76	2.80

The stress-strain of the following members (Figure C–3) is modified based on the reduced concrete strength of the diagonal truss: AK, AB, CD, GD, ID, FK, HK, CB, GF, and IH.

- *Compute prestress in the beam and column ties:*

Based on the recommendations made in 4.8.5 the prestress in the longitudinal bars and the hoops are calculated.

**Table C–24: Prestress in Longitudinal Bars and Hoops Due to ASR/DEF.**

	<b>Specimen 2</b>	<b>Specimen 4</b>
ASR/DEF damage level	Slight	Moderate
$f_y = f_{yh}$ (ksi)	65	65
Prestress in longitudinal bar (ksi)	$f_{ps} = 0.3f_y = 19.5$	$f_{ps} = 0.5f_y = 32.5$
Prestress in hoops (ksi)	$f_{ps} = 0.5f_{yh} = 32.5$	$f_{ps} = 1.0f_{yh} = 65$

Knowing the prestress in the ties and the tie area, the prestress force to be applied in the C-STM model is computed.

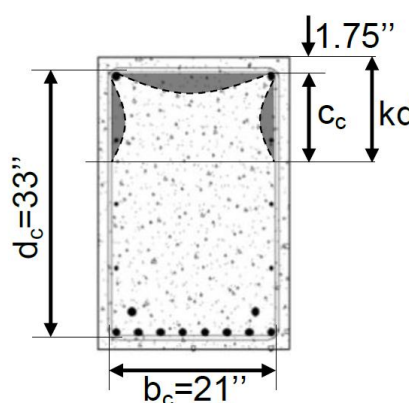
**Table C–25: Prestress Forces Applied to the C-STM Model.**

<b>MEMBER</b>	<b>Prestress Force (kip)</b>	
	<b>Specimen 2</b>	<b>Specimen 4</b>
<b>A-K</b>	$19.5 \times 8.35 = 162.82$	$32.5 \times 8.35 = 271.38$
<b>B-H (D)</b>	$19.5 \times 6.28 = 122.46$	$32.5 \times 6.28 = 204.10$
<b>B-H (S)</b>	$19.5 \times 1.57 = 30.62$	$32.5 \times 1.57 = 51.03$
<b>BC</b>	$32.5 \times 2.36 = 76.70$	$65 \times 2.36 = 153.40$
<b>FG&amp;HI</b>	$32.5 \times 0.393 = 12.67$	$65 \times 0.393 = 25.35$
<b>JJ</b>	$19.5 \times 10.25 = 199.87$	$32.5 \times 10.25 = 333.13$
<b>LL</b>	$19.5 \times 3.93 = 76.64$	$32.5 \times 3.93 = 127.73$

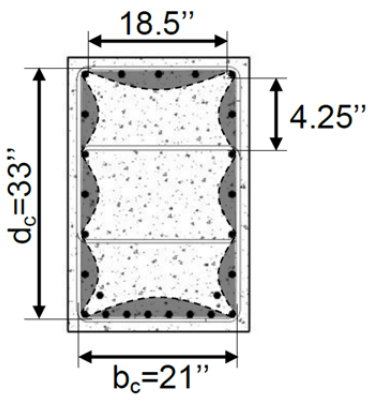
- Compute confinement ratio for the beam and the column:

To account for the confinement caused by the swelling of core concrete, the confinement ratios are computed for the beam and the column.

**Table C–26: Calculating Confinement Ratio of the Beam.**

	<b>Specimen 2</b>	<b>Specimen 4</b>
		
$f'_c$ (ksi)	5.6	4.0
$kd$ (in)	10.25	11.20
$A_{cc}$ (in <sup>2</sup> ) = $(c_c + d_s / 2) \times b_c$	183.75	200.70
$A_e$ (in <sup>2</sup> ) = $(c_c + d_s / 2) \times b_c - \text{area of shaded region}$	107.96	122.86
$k_e = A_e / A_{cc}$	0.5875	0.603
$f_{lx}$ (ksi)	0.190	0.176
$f_{ly}$ (ksi)	0.158	0.162
Smallest confining stress ratio $f_{ly} / f'_c$	0.028	0.041
Largest confining stress ratio $f_{lx} / f'_c$	0.034	0.44
$K = f'_{cc} / f'_c$	1.20	1.28

**Table C–27: Calculating Confinement Ratio of the Column.**



	<b>Specimen 2</b>	<b>Specimen 4</b>
$f'_c$ (ksi)	5.6	4.0
$kd$ (in)	10.25	11.20
$A_{cc}$ (in <sup>2</sup> ) = $b_c d_c$	693	
$A_e$ (in <sup>2</sup> ) = $b_c d_c$ – area of shaded region	560.85	
$k_e = A_e / A_{cc}$	0.81	
$f_{lx}$ (ksi)	0.278	
$f_{ly}$ (ksi)	0.219	
Smallest confining stress ratio $f_{ly} / f'_c$	0.039	0.055
Largest confining stress ratio $f_{lx} / f'_c$	0.049	0.069
$K = f'_{cc} / f'_c$	1.28	1.35

*Step 2: Compute section properties.*

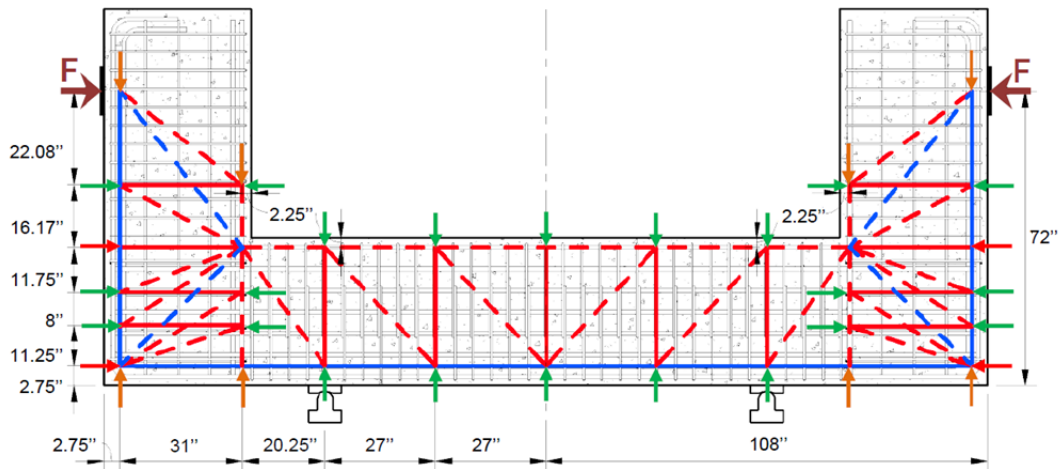
The steel areas computed in Table C–17 for Specimen 1 hold good for Specimen 2 and 4 as well. However, the depth of compression zone ( $kd$ ) has to be recalculated to account for the prestress forces that are applied on the ties.

**Table C–28: Determining the Depth of the Compression Zone for Specimen 2 and 4 With ASR/DEF Damage.**

	Compression Steel			Tension Steel				Axial Load	Elastic Depth	
	$A_s'$ (in <sup>2</sup> )	$d'$ (in)	$\rho'$	$A_s$ (in <sup>2</sup> )	$d$ (in)	$b$ (in)	$\rho$	$P$ (kip)	$k$	$kd$ (in)
<b>Specimen 2</b>										
Single Beam	1.57	2.25	0.00197	8.35	33.25	24	0.01046	30.6	0.311	10.36
Double Beam	6.28	2.25	0.00787	8.35	33.25	24	0.01046	122.5	0.308	10.25
Column	3.92	2.25	0.00492	10.25	33.25	24	0.01284	629.8	0.418	13.89
<b>Specimen 4</b>										
Single Beam	1.57	2.25	0.00197	8.35	33.25	24	0.01046	51.0	0.337	11.21
Double Beam	6.28	2.25	0.00787	8.35	33.25	24	0.01046	204.1	0.343	11.40
Column	3.92	2.25	0.00492	10.25	33.25	24	0.01284	763.1	0.458	15.22

Step 3: Determine C-STM geometry.

The geometry of the C-STM remains the same as Specimen 1. However, axial loads are applied at the nodes to account for the ASR/DEF effects. The C-STM model for Specimen 2 and 4 is shown in Figure C–4.



**Figure C–4: C-STM Model for C-Beam Specimen 2 and 4.**



Step 4: Determine axial rigidities.

The compatibility correction factor for Specimen 2 and 4 are recalculated.

**Table C–29: Computation of Compatibility Correction Scalar for Specimen 2.**

	<b>Singly Reinforced</b>	<b>Double Reinforced</b>	<b>Column</b>
$d'$ (in)	2.25	2.25	2.25
$kd$ (in)	10.36	10.25	13.89
$f'_c$ (ksi)	5.6	5.6	5.6
$\psi_E = \frac{\sqrt{f'_c(\text{psi})}}{168(1-d'/kd)}$	0.570	0.571	0.532
$\psi_P = \frac{\sqrt{f'_c(\text{psi})}}{480(1-d'/kd)}$	0.199	0.200	0.186
$\psi_{PP} = -\frac{\sqrt{f'_c(\text{psi})}}{1500(1-d'/kd)}$	-0.064	-0.064	-0.060

**Table C–30: Computation of Compatibility Correction Scalar for Specimen 4.**

	<b>Singly Reinforced</b>	<b>Double Reinforced</b>	<b>Column</b>
$d'$ (in)	2.25	2.25	2.25
$kd$ (in)	11.21	11.40	15.22
$f'_c$ (ksi)	4.0	4.0	4.0
$\psi_E = \frac{\sqrt{f'_c(\text{psi})}}{168(1-d'/kd)}$	0.471	0.469	0.442
$\psi_P = \frac{\sqrt{f'_c(\text{psi})}}{480(1-d'/kd)}$	0.165	0.164	0.155
$\psi_{PP} = -\frac{\sqrt{f'_c(\text{psi})}}{1500(1-d'/kd)}$	-0.053	-0.053	-0.049

The arch-breadth scalar remains the same as in Table C–20.

The axial rigidities are recomputed based on the modified properties calculated above for Specimen 2 and 4.

**Table C–31: Axial Rigidities of C-STM Elements: Specimen 2.**

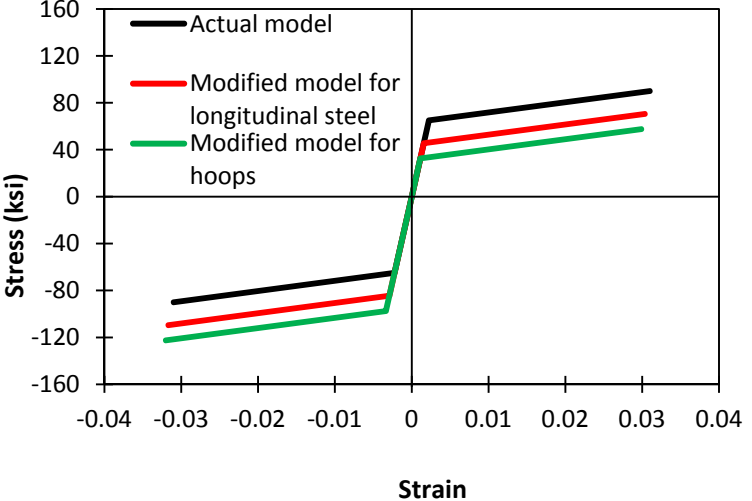
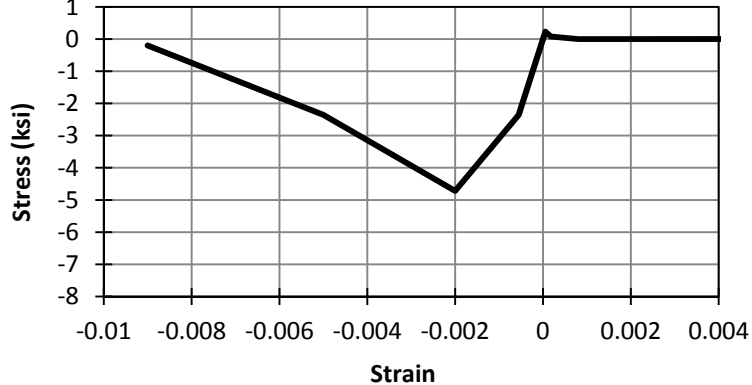
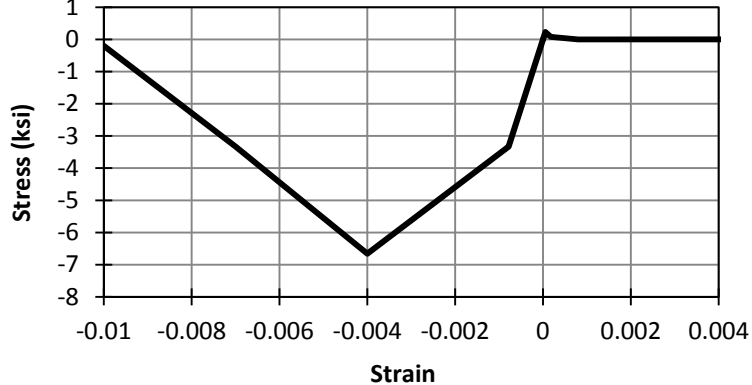
	MEMBER	Steel		Concrete		Comments
		E (ksi)	A (in <sup>2</sup> )	E (ksi)	A (in <sup>2</sup> )	
<b>Beam</b>	A-E (D)	29000	8.35	4190	246.00	Tension Chord
	A-E (S)	29000	8.35	4190	248.64	
	B-D (D)	29000	6.28	2435	246.00	Compression Chord
	B-D (S)	29000	1.57	2431	248.64	
	BC	29000	2.36	4190	162.00	Transverse Steel
	AD	-	-	4190	240.60	Concrete Arch
	AB	-	-	4190	110.52	Concrete Truss
	CD	-	-	4190	118.14	
<b>Beam-Column Joint</b>	E-K (D)	29000	8.35	4190	246.00	Tension Chord
	E-K (S)	29000	8.35	4190	248.64	
	D-H (D)	29000	6.28	2435	246.00	Compression Chord
	D-H (S)	29000	1.57	2431	248.64	
	FG&HI	29000	0.39	4190	54.00	Transverse Steel
	DK	-	-	4190	295.92	Concrete Arch
	DG	-	-	4190	73.64	Concrete Truss
	DI	-	-	4190	78.46	
	FK	-	-	4190	78.15	
	HK	-	-	4190	73.90	
<b>Column</b>	JJ	29000	10.25	4190	333.36	Tension Chord
	LL	29000	3.93	2212	333.36	Compression Chord
Beam: $N_h = 6$ and beam-column joint: $N_h = 2$						
<i>(D) Doubly reinforced beam (S) Singly reinforced beam</i>						

**Table C–32: Axial Rigidities of C-STM Elements: Specimen 4.**

	MEMBER	Steel		Concrete		Comments
		E (ksi)	A (in <sup>2</sup> )	E (ksi)	A (in <sup>2</sup> )	
<b>Beam</b>	<b>A-E (D)</b>	29000	8.35	4190	273.60	Tension Chord
	<b>A-E (S)</b>	29000	8.35	4190	269.04	
	<b>B-D (D)</b>	29000	6.28	1690	273.60	Compression Chord
	<b>B-D (S)</b>	29000	1.57	1698	269.04	
	<b>BC</b>	29000	2.36	4190	162.00	Transverse Steel
	<b>AD</b>	-	-	4190	240.60	Concrete Arch
	<b>AB</b>	-	-	4190	110.52	Concrete Truss
	<b>CD</b>	-	-	4190	118.14	
<b>Beam-Column Joint</b>	<b>E-K (D)</b>	29000	8.35	4190	273.60	Tension Chord
	<b>E-K (S)</b>	29000	8.35	4190	269.04	
	<b>D-H (D)</b>	29000	6.28	1690	273.60	Compression Chord
	<b>D-H (S)</b>	29000	1.57	1698	269.04	
	<b>FG&amp;HI</b>	29000	0.39	4190	54.00	Transverse Steel
	<b>DK</b>	-	-	4190	295.92	Concrete Arch
	<b>DG</b>	-	-	4190	73.64	Concrete Truss
	<b>DI</b>	-	-	4190	78.46	
	<b>FK</b>	-	-	4190	78.15	
<b>HK</b>	-	-	4190	73.90		
<b>Column</b>	<b>JJ</b>	29000	10.25	4190	365.28	Tension Chord
	<b>LL</b>	29000	3.93	1593	365.28	Compression Chord
Beam: $N_h = 6$ and beam-column joint: $N_h = 2$						
<i>(D) Doubly reinforced beam (S) Singly reinforced beam</i>						

Step 5: Determine constituent material properties.

**Table C-33: Stress-Strain Models for the Elements of the C-STM Model: Specimen 2.**

Member	Stress-Strain Model
All steel members.	 <p>The plot shows Stress (ksi) on the y-axis (ranging from -160 to 160) versus Strain on the x-axis (ranging from -0.04 to 0.04). Three curves are shown: a black line for the 'Actual model', a red line for the 'Modified model for longitudinal steel', and a green line for the 'Modified model for hoops'. All curves show a linear elastic region followed by a yield plateau and then strain hardening. The actual model has the highest yield strength and ultimate stress, while the modified models are lower.</p>
Concrete truss members in the beam. AK, AB, CD, GD, ID, FK, HK, CB, GF, and IH.	 <p>The plot shows Stress (ksi) on the y-axis (ranging from -8 to 1) versus Strain on the x-axis (ranging from -0.01 to 0.004). The curve shows a linear elastic region up to a peak stress of approximately 0.5 ksi at a strain of about -0.001. After the peak, the stress drops sharply to zero at a strain of approximately 0.001.</p>
For remaining concrete members in the beam.	 <p>The plot shows Stress (ksi) on the y-axis (ranging from -8 to 1) versus Strain on the x-axis (ranging from -0.01 to 0.004). The curve shows a linear elastic region up to a peak stress of approximately 0.5 ksi at a strain of about -0.001. After the peak, the stress drops sharply to zero at a strain of approximately 0.001.</p>

**Table C-33: Stress-Strain Models for the Elements of the C-STM Model: Specimen 2 (continued).**

<p>Column members.</p>	<p>Stress (ksi)</p> <p>Strain</p>
<p>Softened concrete model for the beam-column joint, DK.</p>	<p>Stress (ksi)</p> <p>Strain</p>

**Table C-34: Stress-Strain Models for the Elements of the C-STM Model: Specimen 4.**

Member	Stress-Strain Model
All members	
Concrete truss members in the beam. AK, AB, CD, GD, ID, FK, HK, CB, GF, and IH.	
For remaining concrete members in the beam.	

**Table C-34: Stress-Strain Models for the Elements of the C-STM Model: Specimen 4 (continued).**

<p>Column members.</p>	<p>Detailed description: This graph plots Stress (ksi) on the vertical axis (ranging from -6 to 1) against Strain on the horizontal axis (ranging from -0.01 to 0.004). The curve starts at approximately (-0.01, -0.5), descends to a peak stress of about -5.5 ksi at a strain of -0.0065. It then rises to a stress of -3.5 ksi at a strain of -0.001, and finally reaches 0 ksi at a strain of 0. For positive strains, the stress remains constant at 0 ksi.</p>
<p>Softened concrete model for the beam-column joint, DK.</p>	<p>Detailed description: This graph plots Stress (ksi) on the vertical axis (ranging from -6 to 1) against Strain on the horizontal axis (ranging from -0.01 to 0.004). The curve starts at approximately (-0.01, -0.5), descends to a peak stress of about -2.5 ksi at a strain of -0.002. It then rises to a stress of -2.5 ksi at a strain of -0.001, and finally reaches 0 ksi at a strain of 0. For positive strains, the stress remains constant at 0 ksi.</p>

